SAPIENZA
UNIVERSITÀ DI ROMA

A Thermomechanical and Electromagnetic Approach For The Design Of High-Intensity Accelerator Components

Ph.D. School in Accelerator Physic

Ph.D. in Accelerator Physics – XXXII Cycle

Candidate

Lorenzo Teofili

ID number 1382460

Thesis Advisors

Prof. Mauro Migliorati (Sapienza)

Eng. Iñigo Lamas Garcia (CERN)

External Referees

Benoit Salvant Ph.D. (CERN)

Ryutaro Nagaoka Ph.D. (Soleil)

A thesis submitted in partial fulfillment of the requirements
for the degree of Doctor of Philosophy in Accelerator Physics

October 2019

Thesis defended on the 19th of February 2020
in front of a Board of Examiners composed by:

Prof. Andy Wolski (chairman)

Prof. Cristina Morone

Prof. Daniele Davino

A Thermomechanical and Electromagnetic Approach For The Design Of High-Intensity Accelerator Components

Ph.D. thesis. Sapienza – University of Rome

This thesis has been typeset by LaTeX and the Sapthesis class.

Version: April 8, 2020

Author's email: lorenzo.teofili@gmail.com

Dedicato a
Mamma e Papà

Abstract

At the European Council for Nuclear Research (CERN) two projects call for an upgrade of the laboratory particle accelerators to find new physics results: the High-Luminosity Large Hadron Collider (HL-LHC) and the LHC Injection Upgrade (LIU). In this context, beam characteristics such as intensity and stored energy will be doubled. Some of the current accelerator components cannot safely perform their main tasks with these new conditions. As an example, it was demonstrated that the majority of the devices responsible for partially or totally absorbing the beam, the so-called beam intercepting devices (BIDs), have to be redesigned to face the new challenging scenario. These devices, because of their specific functional requirements, usually, have strong electromagnetic interaction with the beam, i.e. high impedance. They are among the strongest impedance sources in the CERN accelerators. Devices with high impedance could generate beam instabilities or they could be overheated because of RF-heating. Thus, at CERN, an impedance minimization campaign for the new BIDs was started, and this thesis reports the results of the campaign. In particular, the manuscript analyzes the impedance of LIU and HL-LHC devices via simulations and measurements. It defines a series of guidelines for minimizing the device impedance and shows examples of the successful application of these guidelines. Furthermore, the impedance induced heating thermo-mechanical effects are also discussed, a new method to simulate them is developed and successfully benchmarked against experimental data. Finally, the manuscript tackles the problem of determining the wakefield and the impedance induced heating of two counter-rotating beams passing in the same vacuum chamber. On this topic, some extensions to the present theory are reported.

3D Interactive Figures

This thesis uses 3D interactive figures to allow a better understanding of the 3D CAD model used. An example of 3D interactive figure is shown in Fig. 0.1. If the image does not appear interactive, please enable this function (it may be requested to trust the document first) and click on it. In order to correctly open and manipulate the 3D interactive figures, a recent version of Adobe Reader is recommended. This paragraph is a brief guide on how to handle interactive figures using Adobe Reader.

The author wants to specify that the use of the interactive 3D images is not crucial for understanding the messages of the manuscript, however, it could help.

There are several possible operations to navigate an interactive figure. In this section the main ones are reported. The interested reader can refer to the Adobe Website for further instructions [1]. Once the interactivity is enabled, right clicking the image opens the navigation menu, where the most important entries are "Tools" and "Viewing Options". The former, with the commands "Rotate", "Pan" and "Zoom", allows to interact with the images. In the "Tools" entry there is also the "3D Measurements Tools" to measure lengths and angles directly on the 3D images. The results of the measurements are reported in "model units", in the context of this thesis this means millimeters for lengths and degrees for angles. The important entry in the "Viewing Options" is the "Cross Section Properties" one. Indeed, clicking on this entry and ticking "Enable Cross Section" in the window that appears, one can create a section cut in the figure. It is also recommended to tick the "Add Section Caps" entry in "Display Setting". Finally, in the submenu "Position and Orientation", the entry "Offset" controls the motion of the section cut. Before continuing in the reading, the author invites the reader to familiarise with the commands to navigate 3D images. At the end of every section where a specific device is discussed, a simplified 3D interactive CAD model of the device is reported.

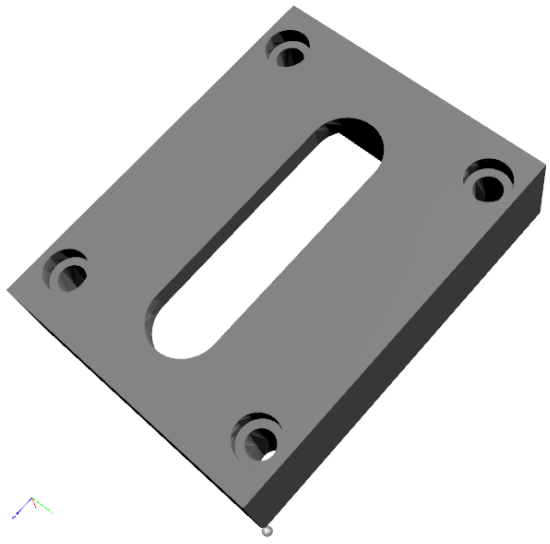

Figure 0.1. Example of a 3D interactive figure. If the figure does not appear interactive, please enable this function and click on the figure or use a recent version of Adobe Reader.

Contents

Chapter 1

Introduction

Particle accelerators are one of the most versatile instruments ever designed by physicist. Their birth and developments have been connected with the major achievements and results obtained in particle and nuclear physics, from the first artificial atomic nucleus splitting performed in 1932 by a Cockcroft-Walton accelerator [2] to the discovery of the Higgs boson in 2012 by the experiments of the Large Hadron Collider (LHC) at CERN (Conseil Européenne pour la Recherche Nucléaire).

Accelerator technology has spread in a huge variety of sectors and fields [3]. In biology and chemistry accelerators are essential tools to study molecular structures or to perform sensitive trace element analysis. Cosmology and astrophysics take advantages from the accelerator capability of reproducing phenomena happening in extreme environments, as the nucleo-synthesis, the process through which stars produce their energy, or generation of quark-gluon plasma.

Further, the possibility of producing beam of accelerated particles is exploited also in industry: ion implantation by accelerated beam is used in electronics to precisely dope semiconductors and in automotive, space and aeronautical industry to modify the surface properties of metals. Moreover, the accelerators capability of generating radiation of tunable intensity, the so-called synchrotron radiation, has dramatically increased the possibility of application of such machines. Indeed, the radiation can be used to preserve food, dispose of dangerous and noxious waste and polymerize plastic.

However, the accelerator forefront machines are, still nowadays, used almost exclusively for fundamental research due to their huge cost and to the enormous effort to keep them operational.

The world biggest particle accelerator at the writing time is the LHC [4], about 27 km of circumference, located at the CERN laboratories. It accelerates protons at energies up to 7 TeV. It is a circular collider machine, i.e. two counter-rotating particle beams run, separately, in the machine to collide each other in four interaction points. At each interaction point is located an experiment ALICE [5], ATLAS [6], CMS [7] and LHCb [8]. The scope of the LHC is to provide high energy particle beam collisions to its experiments.

Before being injected in the LHC, particles are previously accelerated by other machines at CERN, i.e. the LHC injection chain. A schematic of the CERN accelerators and experiments is reported in Fig. 1.1.

1.1 Scope and Structure of the Chapter

The thesis work has been performed at CERN. In this manuscript beam coupling impedance optimization for beam intercepting devices to be installed in the CERN machines is discussed.

This chapter has the aim of introducing the CERN accelerator complex. It presents the two ongoing projects to increase the performance of the accelerator complex and, in this context, the chapter explains the motivations of the work done for this Ph.D. thesis. Furthermore, the chapter briefly describes what is a beam intercepting device, what is the impedance and why it has to be minimized. Finally, it gives an overview of the manuscript organization.

1.2 CERN: Conseil Européen Pour la Recherche Nucléaire

The European Organization for Nuclear Research, best known as CERN (Conseil Européen Pour la Recherche Nucléaire), is the organization that operates the largest particle physics laboratory in the world. It was Established in 1954, it is located in the suburb of Geneva (Switzerland) and, at the writing time, it has 23 member states, 2,667 scientific, technical, and administrative staff members, 839 fellows, 1245 among students and trainees and hosts about 13,000 users [9].

The CERN scope is to provide the particle accelerators needed for high-energy physics research to the numerous experiments that have been constructed at CERN, e.g. ATLAS [6], CMS [7], ALICE [5], LHCb [8], AWAKE [10], AD [11], n_ToF [12], HiRadMat [13] and many others. This is done thanks to the CERN accelerator chain, shown in Fig. 1.1. Protons are first accelerated in the LINAC4 (in 2020 LINAC2 will be replaced by LINAC4), subsequently, they go trough the Proton Syncrotron Booster (PSB), the Proton Syncrotron (PS) and the Super Proton Syncrotron (SPS) to end up into the Large Hadron Collider (LHC). The LINAC4, the Proton Syncrotron Booster (PSB), the Proton Syncrotron (PS) and the Super Proton Syncrotron (SPS) form the already mentioned LHC injection chain. During the transit in each accelerator of the CERN complex the beam characteristics change, in particular, the beam energy is increased up to 7 TeV per nucleon in the LHC [14].

Currently, two projects are ongoing to increase the performance of the CERN complex; they are the High Luminosity Large Hadron Collider project (HL-LHC) [16] and the LHC Injection Upgrade project (LIU) [17].

1.3 The HL-LHC Project

When two beams in a collider intersect their trajectories at the interaction points, the beam particles can collide. Every collision between a couple of particles can generate events that can be observed by the experiment detectors. Every event is characterised by a cross section σ_p, i.e. the probability of the event to happen starting from the given collision energy. A statistically sufficient amount of interesting events have to be observed to announce a discovery. The number of events per unit time that a collider can generate, $d\mathcal{N}/dt$, is [18]:

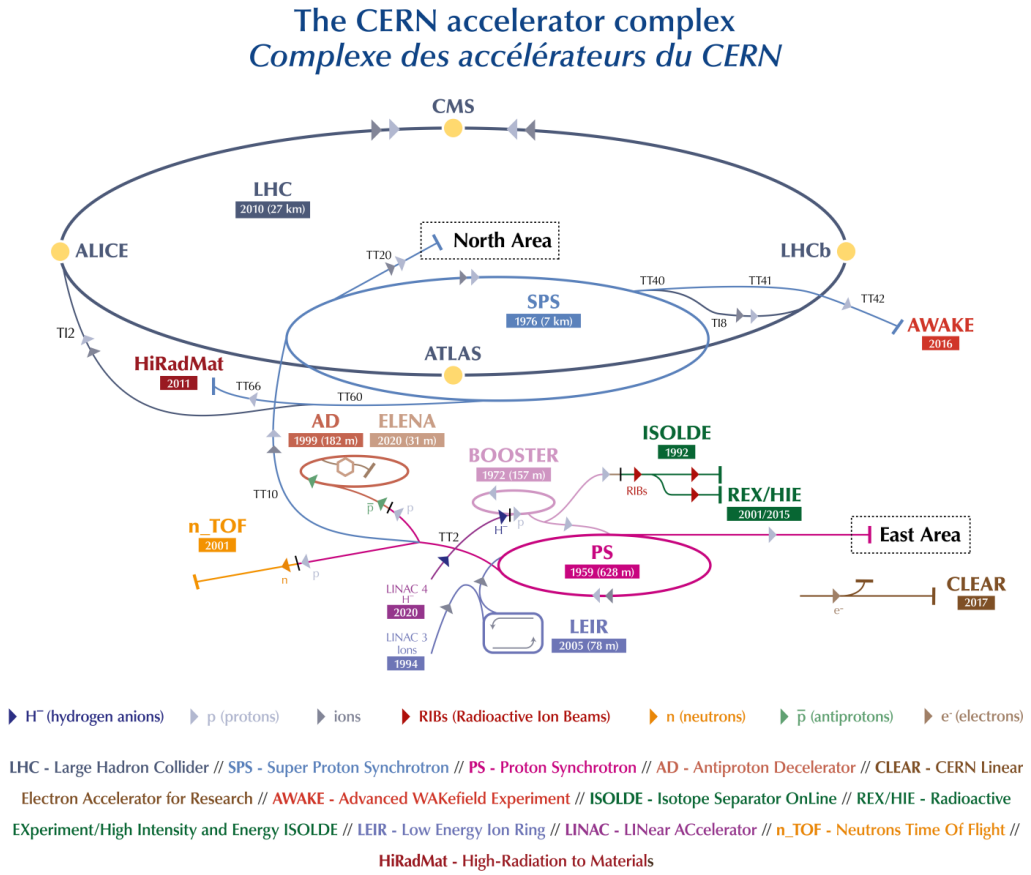

Figure 1.1. CERN accelerator and experiments complex in 2019, courtesy of Mobs [15].

$$\frac{d\mathcal{N}}{dt} = \mathcal{L}\sigma_p. \tag{1.1}$$

In Eq. 1.1, $\mathcal{L}$ is called the instantaneous luminosity. The cross section does not depend on the particle beam characteristics but it is only a function of the particular event and of the colliding particles energy. On the contrary, the instantaneous luminosity $\mathcal{L}$ depends exclusively on the particle beam characteristics that an accelerator can provide. This means that, if one wants to increase the number of events per unit time at fixed energy, since the event cross section cannot be changed, one has to increase the instantaneous luminosity. For two bunched beams with identical Gaussian profile colliding heads-on, the instantaneous luminosity can be calculated as [18]:

$$\mathcal{L} = \frac{N_b^2 f_0 n_b}{4\pi\sigma_x\sigma_y} F, \tag{1.2}$$

where N_b is the number of particles per bunch, n_b is the number of bunches per beam, f_0 is the revolution frequency of the particles around the circular accelerator, σ_x and σ_y are the transverse r.m.s. beam sizes and F is the geometric luminosity

Table 1.1. LHC nominal beam paramenters and HL-LHC nominal beam parameters for proton collision [16].

Parameter	LHC	HL-LHC
Energy per Nucleon [TeV]	7	7
Number of Bunches	2808	2748
Particles per Bunch [10^{11} ppb]	1.15	2.20
Beam intensity [10^{14} p]	3.23	6.05
Maximum Instantaneous Luminosity [10^{34} cm^{-2}s^{-1}]	1	5
Maximum Beam Stored Energy [MJ]	362	678

reduction factor (it takes into account the crossing angles of the beams trajectories at the interaction points).

The current LHC nominal instantaneous luminosity is $\mathcal{L} = 10^{34}$ cm^{-2}s^{-1} [16]. One of the main goals of the HL-LHC project is to increase this instantaneous luminosity by a factor 5. This is planned to be done by a dedicated upgrade of the machine that will transform LHC into HL-LHC and foresees, among others, the following points:

- The beam intensity, i.e. the total number of particles in the beam, will be approximately doubled.
- A new optics has been proposed. It allows to reduce the transverse beam dimensions (σ_x and σ_y) at the interaction points [19].
- The use of special cavities, so called crab cavities, will increase the geometric factor F [20].

In table 1.1 some of the beam parameters for the current LHC and for the future HL-LHC are shown. Of particular importance for this thesis is the beam intensity and the maximum beam stored energy, both will be doubled in the HL-LHC.

1.4 The LIU Project

As already said, the particles, before being injected in the LHC, are accelerated in the LHC injectors chain. This is true also for the HL-LHC, which will rely on the same injection accelerators. However, the current LHC injection chain cannot deliver the beam with the characteristics required by HL-LHC. Thus, the LHC Injection Upgrade project (LIU) was launched. The main goal of this project is to upgrade the LHC injection chain to make the injectors capable of reliably delivering the beams required by the HL-LHC. The project covers LINAC4 and the upgrades of the PS-Booster (PSB), the Proton Synchrotron (PS) and the Super Proton Synchrotron (SPS).

With the LIU projects, several changes are introduced on the beam parameters of the injectors accelerators, they are reported in Fig. 1.2. As can be seen from the figure, also for the injectors the beam intensity will increase of a factor two (the number of bunches in the accelerators does not change but the number of protons

August 25, 2017 – Beam parameters at injection of each accelerator

PSB (H^- injection from Linac4)

		N (10^{11} p)	$\epsilon_{x,y}$ (μm)	E (GeV)	ϵ_z (eVs)	B_l (ns)	$\delta p/p_0$ (10^{-3})	$\Delta Q_{x,y}$
Achieved	Standard	17.73	2.14	0.05	1.0	1100	2.4	(0.51, 0.59)
	BCMS	8.48	1.15	0.05	0.9	1000	2.2	(0.46, 0.56)
LIU target	Standard	34.21	1.72	0.16	1.4	650	1.8	(0.58, 0.69)
	BCMS	17.11	1.36	0.16	1.4	650	1.8	(0.35, 0.43)

PS (Standard: 4b+2b – BCMS: 2× 4b)

		N (10^{11} p/b)	$\epsilon_{x,y}$ (μm)	E (GeV)	ϵ_z (eVs/b)	B_l (ns)	$\delta p/p_0$ (10^{-3})	$\Delta Q_{x,y}$
Achieved	Standard	16.84	2.25	1.4	1.2	180	0.9	(0.25, 0.30)
	BCMS	8.05	1.20	1.4	0.9	150	0.8	(0.24, 0.31)
LIU target	Standard	32.50	1.80	2.0	3.00	205	1.5	(0.18, 0.30)
	BCMS	16.25	1.43	2.0	1.48	135	1.1	(0.20, 0.31)

SPS (Standard: 4 × 72b – BCMS: 5 × 48b)

		N (10^{11} p/b)	$\epsilon_{x,y}$ (μm)	p (GeV/c)	ϵ_z (eVs/b)	B_l (ns)	$\delta p/p_0$ (10^{-3})	$\Delta Q_{x,y}$
Achieved	Standard	1.33	2.36	26	0.35	4.0 (3.0)	0.9 (1.5)	(0.05, 0.07)
	BCMS	1.27	1.27	26	0.35	4.0 (3.0)	0.9 (1.5)	(0.07, 0.12)
LIU target	Standard	2.57	1.89	26	0.35	4.0 (3.0)	0.9 (1.5)	(0.10, 0.17)
	BCMS	2.57	1.50	26	0.35	4.0 (3.0)	0.9 (1.5)	(0.12, 0.21)

LHC (≈10 injections)

		N (10^{11} p/b)	$\epsilon_{x,y}$ (μm)	p (GeV/c)	ϵ_z (eVs/b)	B_l (ns)	bunches/train
Achieved	Standard	1.20	2.60	450	0.47 (0.48)	1.65 (1.21)	288
	BCMS	1.15	1.39	450	0.40 (0.41)	1.50 (1.13)	96
LIU target	Standard	2.32	2.08	450	0.56 (0.58)	1.65 (1.24)	288
	BCMS	2.32	1.65	450	0.56 (0.58)	1.65 (1.24)	240

PSB, PS → Longitudinal emittance and bunch length are values from tomoscope (matched area and foot tangent). Momentum spread is rms value
SPS, LHC → Longitudinal emittance ϵ_z (2σ), momentum spread $\delta p/p_0$ (1σ), bunch length B_l (4σ). Values are given at first turn and after filamentation (in parentheses). Present voltages are $V_{SPS,inj}$=4 MV, $V_{SPS,ext}$=7 MV, $V_{LHC,inj}$=6 MV. Future voltage values are $V_{SPS,inj}$=4 MV, $V_{SPS,ext}$=10 MV, $V_{LHC,inj}$=8 MV. 800 MHz voltage in SPS is assumed 1/10 of the 200 MHz voltage value. Longitudinal emittances at SPS injection and after filamentation are the same because they are measured with different conventions

Figure 1.2. Current injection beam parameters and LIU targets for protons, courtesy of the LIU collaboration [21].

per bunch, N, doubles). This will automatically translate in a doubling of the total beam stored energy.

1.5 HL-LHC and LIU Implications for Beam Intercepting Devices

1.5.1 Beam Intercepting Devices and Beam Stored Energy

As it was shown in the two previous sections, with the HL-LHC and the LIU projects the proton beams that will circulate in the CERN accelerator complex will have a double intensity and a double total stored energy if compared with the beams that were running in the previous CERN operational period.

This situation could have harmful consequences [22] for some of the devices installed into the machines, in particular for the beam intercepting devices (BID).

BIDs are mechanical devices designed to be directly impacted by the beam or by a part of the beam. There are several types of BID and each of them has a different purpose. A non exhaustive list of BIDs is:

- **Dumps**. Beam dumps are used for the beam disposal whenever this action is triggered. They are composed by several blocks made by the same or different materials. When a dump is triggered the beam is deviated to impact against the dump absorbing blocks, or the absorbing blocks are inserted in the beam trajectory to absorb and stop the beam.

Figure 1.3. The SPS beam dump. In the picture, an absorbing graphite block is visible in dark grey. Image courtesy of Maximilien Brice.

- **Collimation System Devices** [23]. A collimation system is required in particle accelerators for protection and cleaning reasons [23]. Different kind of devices are part of the collimation system: collimators, absorbers, scrapers, masks and others. At the writing time there is no well defined nomenclature in the literature for these devices [24]. They have in common their main task: they have to absorb the peripheral beam unstable particles (or the results of the interaction of these particles with matters, see for instance the secondary or tertiary collimators in the LHC [23]) in controlled areas avoiding them to irradiate and damage other components. With respect to a dump, usually, these devices cannot absorb completely an operational beam. An example of an LHC collimator is reported in Fig. 1.4, while in Fig. 1.5 the absorber/scraper of the SPS is shown.

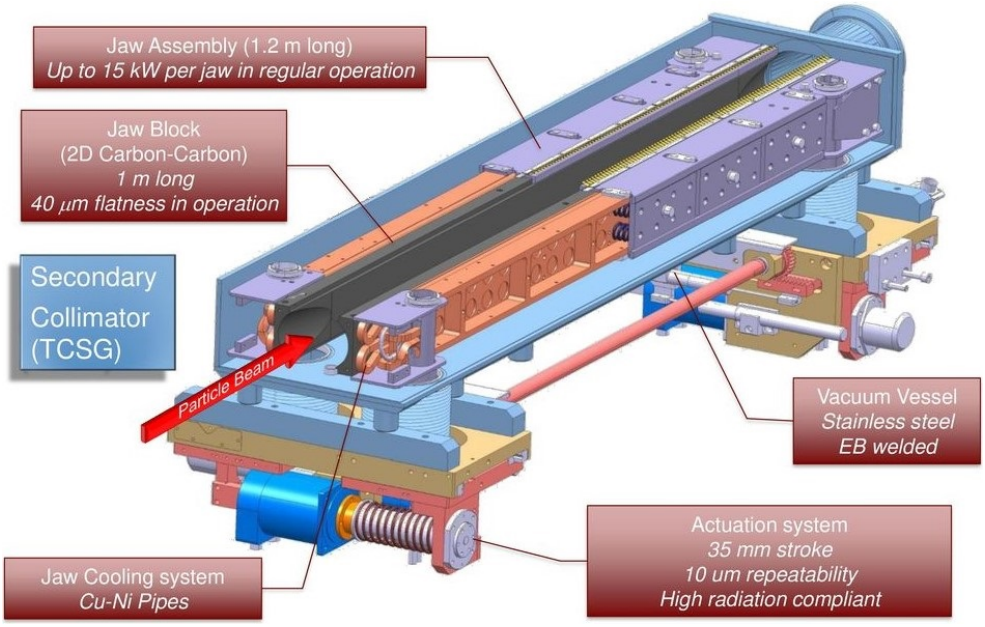

Figure 1.4. Example of an LHC collimator. Image courtesy of Aberle [25].

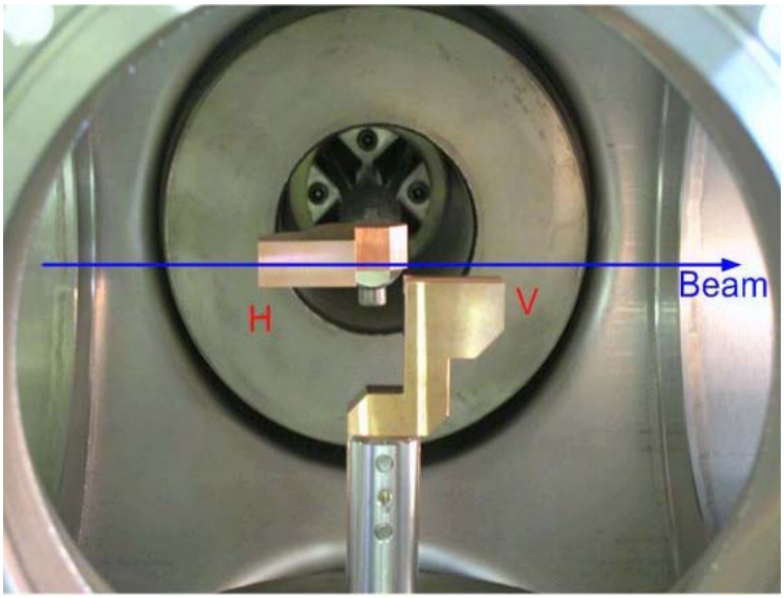

Figure 1.5. Example of an horizontal (H) and vertical (V) SPS movable absorber/scraper. Image courtesy of Burkhardt et al. [26].

- **Strippers** [27]. These devices are used with ion beams. Their scope is to strip electrons from beam ions to increase the positive charge of an ion or to transform a negatively charged ion to a positively charged one. This result is achieved forcing the ions to pass trough a thin foil of matter. The foils have to be very thin to leave the beam energy unchanged.

Figure 1.6. Example of a carbon foil stripper. Image courtesy of Forte [28].

- **Targets**. A target is a device that intercept particle beams to produce secondary particles useful for scientific experiment. The target material depends on the particles needed for the specific experiment.

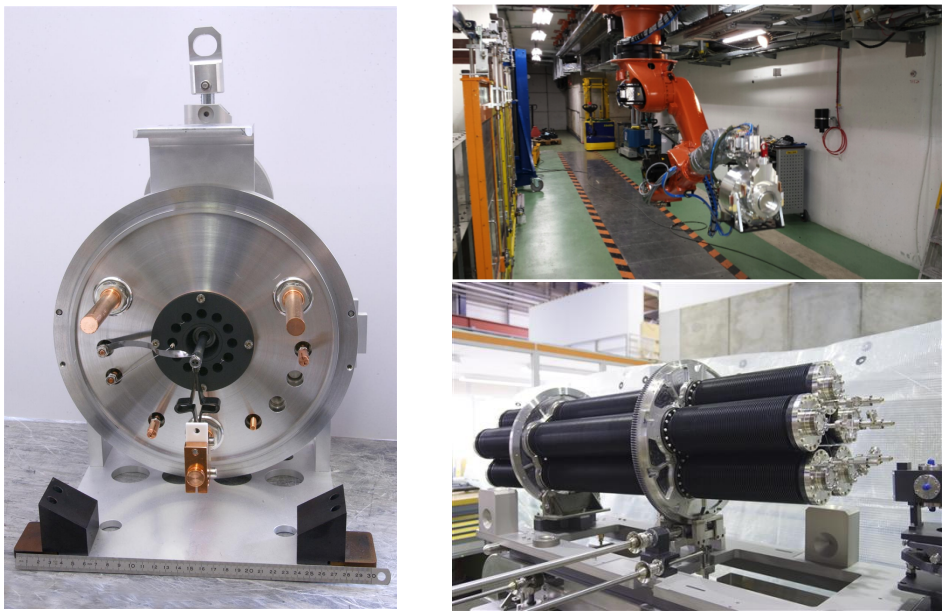

Figure 1.7. Example of Targets. Left, isolde targets, image courtesy Maximilien Brice. Top right, robotics harm moving the radioactive isolde target, image courtesy of the isolde experiment [29]. Bottom right, CERN Neutrino to Gran Sasso (CNGS) targetm image courtesy Maximilien Brice.

The BIDs currently installed in the LHC accelerator chain were designed to work with the LHC beams. It was proved that most of these BIDs cannot perform their task reliably with the new beam stored energy and beam intensity requested by the LIU and HL-LHC upgrades. Thus, most of them have to be redesigned and substituted by a new upgraded version.

1.5.2 Beam Intercepting Devices and Beam Coupling Impedance

With the doubled beam intensity, the total beam charge doubles as well. This increases the electromagnetic fields generated by the beam and consequently, the electromagnetic interaction between beams and devices. The device coupling impedance Z quantifies how much a device is likely to couple electromagnetically with the beam. The impedance depends on the geometry of the device, on its materials, on the trajectory of the beam into the device and on the energy of the beam particles.

The device impedance is among the main responsible for beam instabilities and RF-heating.

- There is a beam instability when one of the beam or of the bunch properties increases exponentially, for instance, the transverse bunch barycenter position or the transverse bunch dimensions. An example of a transverse beam instabilities measured in the LHC, in which the bunch barycenter position increases sharply, is shown in Fig. 1.8, image courtesy of Amorim [30]. In the figure, the barycenter transverse position oscillates around the beam axis ($x = 0$) with an amplitude that increases exponentially.

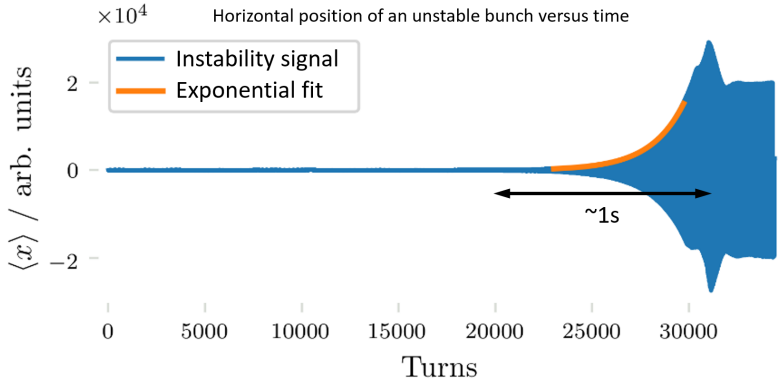

Figure 1.8. Measured horizontal position of unstable bunch barycenter in the LHC as a function of the number of turns. Around 25000 turns the instability develops, i.e. the barycentre transverse position starts to oscillate around the beam axis ($x = 0$) with an amplitude that increases exponentially. The instability takes 1 s to fully develop. If the amplitude of the oscillation is too big, the bunch could impact the wall of the device that is traversing, being lost and causing damages. Image courtesy of Amorim [30].

- When the beam couples electromagnetically with the device in which is passing, energy is deposited on the device. This energy is usually dissipated on the device wall as heat, i.e. RF-heating. As shown by Giordano in his work [31] doubling the total beam intensity, the power deposited on devices may be a factor four higher, depending on the number of bunches and the distance

between them. Further, the energy deposition in the device may not be uniform, it could be extremely uneven and localised in a small area of the device. These facts have to be carefully considered to avoid problems due to accelerator component overheating. An example of the consequences of impedance overheating is reported in Fig. 1.9.

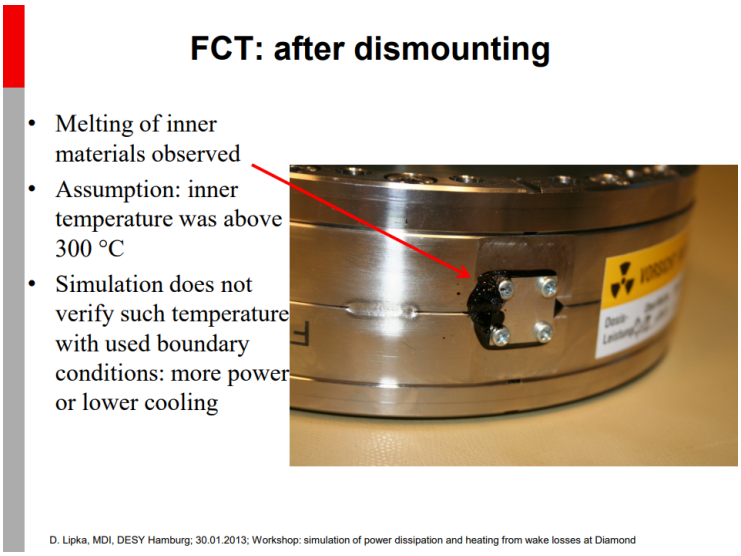

Figure 1.9. Effects of the impedance induced heating on a fast current transformer (FCT) in PETRA III at DESY. Image courtesy of Lipka [32].

In order to perform their main tasks, BIDs operates in close proximity with respect to the beam, they have complex geometries (since often have movable parts) and they are made of not good electric conductor materials[1]. All these characteristics lead, generally, BIDs to have high impedances and often they are among the highest impedance sources in particle accelerators. For example, collimators are among the major impedance sources for the LHC [33].

1.6 Motivations and Goals of the Work

As said in the previous sections, in the context of the HL-LHC and LIU projects most BIDs have to be redesigned and rebuilt, and device impedance minimization is among the design drivers. Thus, a campaign of BID impedance analysis and minimization was launched at CERN and this thesis reports the results of the studies of the campaign. The work done has focused on BIDs installed in circular machines as the LHC collimators, the internal PS dump, the PS Ralentisseur, the PSB absorber/scraper.

The main goals of this thesis work are:

1. Study, development and application of general principles for the mechanical design of low impedance devices. Impedance simulations of the developed

[1]Materials that well withstand thermo-mechanically a beam impact or scraping are usually not good electric conductors, graphite is an example.

designs. Prototype Construction. Test of the principles, benchmark of the simulations against measurements taken on device prototypes.

2. Development of physical models, methodologies and tools to analyse and quantify the RF-heating on components and the induced local thermo-mechanical effects.

Furthermore, the study of the RF-heating mechanism has brought to new developments in the interesting field of research of the electromagnetic beam interaction of two counter-rotating beams circulating simultaneously in the same component. These developments are also reported in this thesis.

1.7 Thesis Overview

According to the stated goals the structure of the thesis is the following:

Chapter 1 has introduced the CERN environment and the scopes and motivation of this work.

Chapter 2 is both a results and background chapter. It defines the wakefield in the classic way. Further, it introduces the new concept of counter-rotating wakefield and shows examples of its applications. The chapter discusses also the problem of two counter-rotating beams passing in the same vacuum chamber.

Chapter 3 is both a results and background chapter. It introduces the concept of longitudinal and transverse coupling impedance and the new concept of counter-rotating impedance and discusses the RF-heating due to two counter-rotating beams passing in the same vacuum chamber.

Chapter 4 is a result chapter. It presents a method to simulate the local thermo-mechanical impedance RF-heating induced effects. In the chapter the results of the method are successfully benchmarked against experimental temperature data taken from an LHC device during the beam run.

Chapter 5 is a background chapter. It reviews the techniques for impedance bench measurements on devices.

Chapter 6 is a result chapter. The main scope of this chapter is to show a way to go through the process of minimising the device impedance dealing with the device functional requirements. The chapter reviews the high impedance features commonly encountered in BID designs and exposes the guidelines to cure them. Subsequently, it shows example of applications of this guidelines on real LIU devices, (the internal PS dump, the PS Ralentisseur, the PSB absorber/scraper).

Chapter 7 is a result chapter. This chapter presents the results of the electromagnetic simulations performed to characterise the impedance of two HL-LHC devices: the LHC injection dump (TDIS) and the Low Dispersion Collimator (TCLD). Also, the results of the impedance measurements performed on the TCLD are reported and compared with the simulation results. Furthermore, the chapter discusses the analysis made to characterise the thermo-mechanical response of the TDIS in a failure scenario.

Finally, Chapter 8 concludes and summarises the work.

1.8 Summary

In this chapter the CERN complex was introduced. It was shown that in order to produce new and more results for physics, the accelerator complex needs an upgrade to increase the instantaneous luminosity. This can be achieved increasing beam intensity and beam brightness, and, as a direct consequence, also the beam stored energy increases. Two main projects were started to reach the high luminosity goal: HL-LHC and LIU. It was shown that, in the framework of these two projects, several machine components have to be redesigned and rebuilt since they will not be able to perform their tasks with the new more intense and more energetic beam. It was also shown that a category of devices that is particularly sensitive to changes in beam stored energy is the BID one. Most BIDs have to be redesigned to face the new challenging scenario. Further, it was said that the BIDs are among the machine components with the highest impedance. In the new design of the BIDs, impedance is one of the key aspect to be considered, since high impedance components may lead to beams instabilities and RF-heating. According to this, the motivations and goals of the thesis were stated: the study and the impedance optimization of the new BIDs design in the framework of the LIU and HL-LHC projects. Finally, an overview of the thesis has been presented.

Chapter 2

Wakefield Theory

2.1 Introduction

2.1.1 Beam Self-induced Fields

Particle beams can be created, accelerated, finely tuned and used in particle accelerators thanks to electromagnetic fields generated externally. Electric fields aligned with the beam propagation directions, created in the RF-cavities, allow for beam acceleration, magnetic fields shape the beam trajectory making the beam turn (dipole fields). Further, they compact and control the particle envelope (quadrupoles and higher order fields).

When the beam particles travel in a region of space where electromagnetic fields are present, they react to the fields being subjected to the Lorentz force [34]:

$$\mathbf{F_e} = q\ (\mathbf{E_e} + \mathbf{v} \times \mathbf{B_e}). \tag{2.1}$$

In Eq. 2.1, $\mathbf{E_e}$ and $\mathbf{B_e}$ are the external electric and magnetic field, q is the particle charge and $\mathbf{v}$ is the particle velocity. $\mathbf{E_e}$ and $\mathbf{B_e}$ are called external because they are externally imposed to guide the particle. Using them as control variables the charged particles can be forced to perform the desired trajectory. This has to be done according with the technological constraints that limit the maximum achievable value of $\mathbf{E_e}$ and $\mathbf{B_e}$.

However, the particles themselves, being charged, are a source of electromagnetic fields, $\mathbf{E_i}$ and $\mathbf{B_i}$, the self-induced electric and magnetic fields respectively. With $\mathbf{E_i}$ and $\mathbf{B_i}$ one is addressing not only the electromagnetic fields radiated directly by the particles but also the fields that result from the interaction between the particles and the vacuum chambers of the accelerator components in which the particles are moving. The self-induced fields add up to the external ones perturbing the particles motion. Calling $\mathbf{F}$ the total electromagnetic force acting on a particle and $\mathbf{F_i}$ the one due to the self-induced fields one obtains:

$$\mathbf{F} = \mathbf{F_e} + \mathbf{F_i} = q\ \left[(\mathbf{E_e} + \mathbf{E_i}) + \mathbf{v} \times (\mathbf{B_e} + \mathbf{B_i})\right], \tag{2.2}$$

The self-induced fields can be seen as a perturbation of the external controlling ones. This means that the actual trajectory that a generic particle is following

can be different from the desired one. If the perturbation is weak, the difference is small, if the perturbation is strong, the particle can critically deviate from the desired trajectory, with the risk of impacting on machine components that could be damaged [35].

The maximum achievable value of the controlling fields $\mathbf{E}_e$ and $\mathbf{B}_e$ is imposed by technological constraints (mainly electric field breakdown and magnetic field limit [36]), while the magnitude of the self-induced fields is linked, among other factors, to the beam intensity, i.e. to the total beam charge. Thus, once a particle accelerator is built, the controlling fields upper limit is fixed while the self-induced fields magnitude increases with the beam intensity. This means that the beam intensity in a given particle accelerator can be increased up to a well defined threshold, after which the perturbing effects of the self-induced fields became so strong that the particle beam cannot be controlled any more, i.e. it cannot be kept in the wanted trajectory, or, the bunches shape strongly deforms.

Since with the LIU and HL-LHC the increased luminosity requires a higher beam intensity, the self-induced fields are of main concern [16, 17]. Each component to be installed in the accelerator (in which the beam passes) has to be characterized under this point of view, and its interaction with the beam has to be minimized by design.

Examples of self-induced fields are:

- Space Charge [37]. When particles of the same charge are grouped together to form a bunch, the Coulomb forces tend to defocus them. This effects plays a key role if the beam is moving at low energy while it is less and less important as the beam energy increases.

- Wakefields [38, 39, 40, 35, 41]. A charged particle moving with arbitrary speed is a source of electromagnetic fields. If this particle (source) transits inside a vacuum chamber and if the walls of the vacuum chamber are made by an electrical conductor, the free charges in the conductor react to the transit of the source following or escaping it, depending on the source charge sign. These free charges move into the vacuum chamber wall and have to follow their geometry, thus generating electromagnetic fields that add up to the ones radiated by the source charge. When, another particle (test) transits in the same vacuum chamber, it experiences these fields and modifies its trajectory consequently. These are called wakefields, with reference to the case in which, if the source is moving at the speed of light, they can exists only behind it.

- Beam-Beam effects [42]. With Beam-Beam effects all the perturbations acting on one beam crossing another beam at and around the interaction point of a particle collider are adressed.

- Electron-cloud [43]. A free electron in a vacuum chamber may be forced to impact on the chamber walls after an interaction with the particle beam. This impact can lead to the release of more electrons by the vacuum chamber walls. If these electrons are forced again to impact the vacuum chamber walls by the beam, so freeing other electrons, an avalanche effects can be triggered. Because of this, more and more electrons can pass from the vacuum chamber walls into the vacuum chamber, forming the so-called electron-cloud. The electron

cloud, interacting electromagnetically with the beam can induce instabilities and RF-heating.

2.1.2 Scope and Structure of the Chapter

This chapter discusses the wakefield concepts, presenting also original research contributions, that will be indicated to the reader in the following. This thesis work focuses on wakefields, other kinds of self-induced fields are not discussed in details in this work.

Furthermore, this thesis distinguishes a co-moving wakefield from a counter-moving wakefield. Both of them describe the effects of the electromagnetic field generated by a source charge acting on a test charge when they travel into a vacuum chamber. The trajectories of the source and the test are considered straight and parallel one with each other. In the co-moving wakefield case, the test particle moves following the source (the velocities of the particles are co-moving, that is they point towards the same direction). In the counter-moving wakefield case the test and source particles move in opposite directions. A cartoon showing the two cases is reported in Fig. 2.1, for a detailed discussion the reader can refer to to section 2.3 and 2.4. The co-moving and counter-moving terms were introduced by Wang, who was among the first researchers to study beam instabilities due to two counter-rotating beams in his work [44].

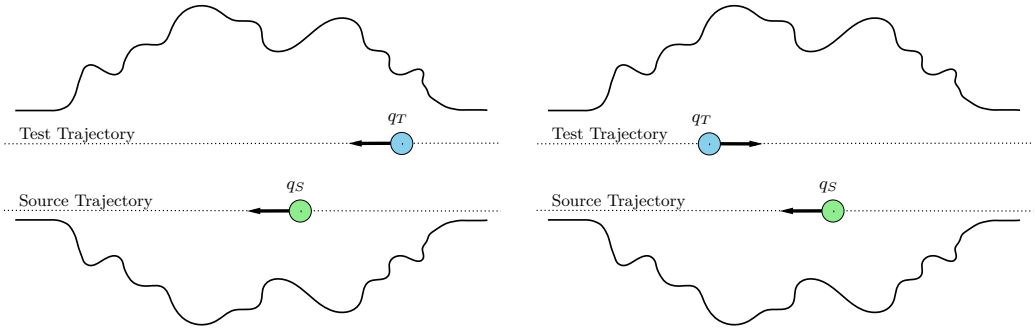

(a) Qualitative representation of the co-moving wakefield case. The test particle moves in the same direction with respect to the source particle.

(b) Qualitative representation of the counter-moving wakefield case. The test particle moves in opposite direction with respect to the source particle.

Figure 2.1. Qualitative representation of the co-moving and counter-moving wakefield cases. The test particle moves on a straight trajectory parallel to the source particle one. The direction of motion of the test and the source charges (q_T and q_S respectively) is indicated by the depicted arrows.

The chapter has the following structure:

Section 2.2 reviews the wakefield concept and the hypotheses under which it can be used, i.e. rigid beam hypothesis and kick approximation. This step is needed to understand how to formally handle the counter-moving wakefield.

Section 2.3 reviews the well known co-moving wakefield (called simply wakefield in the licterature). The longitudinal and transverse wakefunction are defined, the concepts of wakepotential and beam dissipated energy are introduced.

Section 2.4 reports an original contribution on the counter-moving wakefield. Initially, it reviews the previous works on this topic. Then, it defines a counter-moving longitudinal and transverse wakefunction. Further, it formally introduces the concept of counter-moving wakepotential deriving the counter-moving beam energy dissipation.

Subsequently, section 2.5 presents two examples of counter-moving wakefunction and wakepotential: the case of a resistive wall pipe of finite length and the case of a pillbox cavity. For each example the counter-moving wakepotential is obtained by two independent approach, i.e. simulations with a commercial code and a semi-analytical approach. The results of the two approaches agree very well.

Section 2.6 discusses the energy deposited on a device crossed by two counter-moving beams, presenting the case study of a pillbox cavity crossed by two gaussian bunches.

Finally, section 2.7 concludes the chapter recalling the main points.

2.2 The Wakefield Concept

The material discussed in this section and in the next one is mainly based on the books and courses of Ng [35], Palumbo et al. [38], Niedermayer [45], Chao [46], Weiland and Wanzenberg [39], Wilson [40] and Rumolo [47]. This section gives a phenomenological description of the wakefield concept and the hypothesis under which it can be used.

2.2.1 A Phenomenological Description

Let us consider two charged particles: a particle S, with charge q_S, that is the source of the electromagnetic field and a test particle T, of charge q_T, that can feel but does not perturb the electromagnetic field generated by S. With reference to Fig. 2.2, let us suppose that S moves inside a vacuum chamber with arbitrary geometry, made by materials characterized by electrical conductivities σ, electrical permittivities ε and magnetic permeabilities μ. The vacuum chamber is free of electromagnetic fields before the entrance of S, i.e. it is not a cavity or a magnet[1].

The charge S radiates electromagnetic fields, which interact with T and with the vacuum chamber. Usually, a vacuum chamber is made mainly of metals, where electrons can freely move in. The fields generated by the source charge oblige the metal electrons in the vacuum chamber wall to move along the wall itself, following or escaping S, according to the sign of q_S. These electron currents are called also image currents. Let us consider the case in which the vacuum chamber walls are made by an ideal perfect electric conductor (PEC) that has infinite conductivity ($\sigma = \infty$ S/m). The image currents have to move inside the vacuum chamber walls, thus, they have to follow the vacuum chamber walls geometry. In the majority of cases, the image currents path is not straight and it is well known that a charge moving on a curved trajectory radiates electromagnetic fields [34]. The geometry of these electromagnetic fields depends mainly on the vacuum chamber wall geometry,

[1] In case the vacuum chamber is a cavity or another active device, one has to consider also the external imposed electromagnetic fields, not only the self-induced ones.

thus, these fields can be labeled as geometric fields. In case the vacuum chamber walls are not made by PEC material but by a conductor with finite conductivity, i.e. $\sigma \gg 1$ and $\sigma < \infty$, the image currents radiate further fields that could be labeled resistive wall field, [35, 41, 40]. The resistive wall field is radiated also if the vacuum chamber walls are straight, as the ones of a cylindrical pipe. To sum up, when S transits inside the vacuum chamber, three kinds of fields can be found [40]:

1. Electromagnetic fields radiated by S. They depends only on the S charge and on the S motion. They are independent on the vacuum chamber.

2. Electromagnetic fields radiated by the image currents because of geometric variation of the vacuum chamber section. They depend mainly on the geometry of the vacuum chamber walls.

3. Electromagnetic fields of resistive wall type. They depend mainly on the electric conductivities of the vacuum chamber walls.

The electromagnetic fields generated by the interaction between the beam and the vacuum chamber [40], that is points two and three in the list above, are called wakefields. The term wakefield is due to the fact that, if S is an ultra-relativistic charge, due to the causality principle, these electromagnetic fields exist only behind S. The electromagnetic fields directly generated by S are labeled as space charge fields. They can also be a part of the beam-beam fields, depending on the studied problem. Separating between vacuum chamber related fields and non vacuum chamber related fields allows to study independently the two kinds of fields and their effects.

Consider now the particle T. It enters into the vacuum chamber with a delay Δt_{ST} with respect to S. The delay Δt_{ST} can also be a negative number, with the physical meaning that the particle T has entered into the vacuum chamber before the particle S. Once the particle T is in the vacuum chamber, during its motion, it experiences the wakefields generated by S. Thus, on T acts an instantaneous force $\mathbf{F}$, that influences the motion of the test particle changing its trajectory and energy. The force is dependent on the instantaneous position of T, on its trajectory, on the entrance delay between the two charges Δt_{ST}, on the geometry of the vacuum chamber, on the material of its wall and on the trajectory of S. Thus, this force $\mathbf{F}$ represents the effects that a vacuum chamber excited by the transit of a source charge S has on a test charge T that enters the vacuum chamber with a delay Δt_{ST} with respect to the source.

2.2.2 Hypotheses

In order to introduce a quantitative model to describe the wakefields effects on T the following approximations are done [45] [35]:

- **Rigid beam approximation**. The trajectories of S and T are given, they are straight and parallel with each other. Furthermore, the speed modulus of T and S is equal and constant $v_{qS} = \beta_{qS} c = v_{qT} = \beta_{qT} c = v$ while the two particles traverse the vacuum chamber.

- **Kick approximation**. The effects of the electromagnetic force, continuously acting on S and T all along the vacuum chamber, are represented as a lumped single change in particle properties acting after the particles passage. This means that the vacuum chamber is not seen any more as a finite length element in the accelerator but as a point. When a particle passes in that point its energy and its momentum change.

The first hypothesis states that despite of the electromagnetic fields acting on the particles S and T, the modulus of their speed is not affected, thus, $v_{q_S} = v_{q_T} = v$ remains constant all along the motion in the vacuum chamber. This is a really good approximation for ultra-relativistic beams, for which variations in energy hardly reflect in variations in speeds.

It is important to stress that if source and test particles are moving towards the same direction (co-moving wakefield scenario) a consequence of the rigid beam approximation is the fact that the distance between test and source remains constant. This is not the rigid beam approximation but only one of its consequences. In principle, the rigid beam approximation, as stated in this work, remains valid also if the distance between the particles is changing inside the vacuum chamber, as it is the case for the counter-moving wakefield scenario (refer to sec. 2.3).

The rigid beam approximation decouples the mechanical problem, that is the determination of the particle motion, from the electromagnetic one, the determination of the local time dependent electromagnetic field in the vacuum chamber generated by the particles [45]. Indeed, the particle motion is given a priori, and both S and T have a uniform linear motion. Therefore, one has only to solve the electromagnetic problem. However, for non ultra relativistic beams, energy variations mean speed changes of the particles S and T. In this case, the mechanical and the electromagnetic problem cannot be considered decoupled, and the rigid beam hypotesis cannot be justified any more. However, the rigid beam approximation remains valid also for non ultra relativistic beams in the case in which the energy variations due to the electromagnetic fields on the beams are so small that the corresponding particles speed variation is negligible [38].

The second hypothesis states that there is no interest in what happens inside the vacuum chamber, but the only interest is in the total effects of wakefields on T after its transit in the vacuum chamber. This approximation is very well justified in synchrotrons due to the different time scales of the particle passage in the vacuum chamber and the evolution of the wakefield effects, instabilities and heating, that usually build up over several turns.

2.3 Co-moving Wakefield

2.3.1 Basic Quantities

In this subsection the quantities needed for the formal definition of co-moving longitudinal and co-moving transverse wakefunction are given. The previous section, sec. 2.2, defined the particle S, with charge q_S, as the source of the electromagnetic field and the test particle T, of charge q_T, as the one that can feel but does not perturb the electromagnetic field generated by S. They move on two different trajectories that

are straight and parallel between them, as stated by the first hypothesis presented in section 2.2.2. A cartoon that shows the two moving particles and the vacuum chamber is displayed in Fig. 2.2.

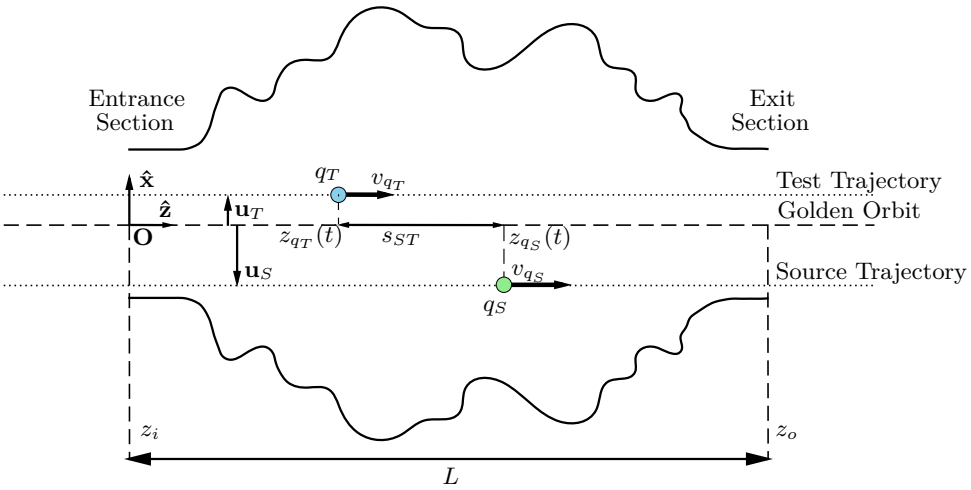

Figure 2.2. co-moving wakefield scenarios, source (q_S) and test (q_T) charge transiting inside a vacuum chamber. The cartoon underlines the instantaneous z positions of the two charges $z_{q_S}(t)$ and $z_{q_T}(t)$, their speeds (v_{q_S}) and test (v_{q_T}), their distance s_{ST} and the transverse position of their trajectories, $\mathbf{u}_T$ and $\mathbf{u}_S$.

Section 2.2 introduced also the vacuum chamber of arbitrary geometry, made by materials characterised by electric conductivities σ, electrical permittivities ε and magnetic permeabilities μ, inside which S moves with velocity $v_{q_S} = \beta_{q_S} c$ and T with velocity $v_{q_T} = \beta_{q_T} c$. Because of the rigid beam hypotesis one has $v = v_{q_S} = v_{q_T}$. Let us define now a reference frame **O** with the origin at the entrance of the vacuum chamber and the $\hat{\mathbf{z}}$ axis lying on the golden orbit, oriented in the direction in which the test charge T is moving. The axes $\hat{\mathbf{x}}$ and $\hat{\mathbf{y}}$ are perpendicular to $\hat{\mathbf{z}}$, they can have an arbitrary orientation but the frame has to be orthonormal. The $\hat{\mathbf{z}}$ axis is also called longitudinal axis, while $\hat{\mathbf{x}}$ and $\hat{\mathbf{y}}$ are also called transverse axes. The length of the vacuum chamber L is defined as the difference between the longitudinal coordinates of the exit of the vacuum chamber z_o and the entrance of the vacuum chamber z_i:

$$L = z_o - z_i, \tag{2.3}$$

that is $L = z_o$ in the current reference frame for which $z_i = 0$.

Furthermore, in this reference frame the instantaneous position of S and T are identified by the vectors:

$$\begin{gathered}\text{instantaneous position of S } (x_{q_S}, y_{q_S}, z_{q_S}(t)) \\ \text{instantaneous position of T } (x_{q_T}, y_{q_T}, z_{q_T}(t))\end{gathered}$$

where t is an arbitrary time. The transverse position of S can be defined as $\mathbf{u}_S = (x_{q_S}, y_{q_S})$ and the transverse position of T as $\mathbf{u}_T = (x_{q_T}, y_{q_T})$. The longitudinal

positions of S is $z_{q_S}(t)$ and of T is $z_{q_T}(t)$. From the hypotheses on the motion of S and T (rigid beam approximation defined in section 2.2.2) it follows that:

$$z_{q_S}(t) = vt + z_{q_S 0} \tag{2.4}$$

$$z_{q_T}(t) = vt + z_{q_T 0}. \tag{2.5}$$

Where $z_{q_S 0}$ and $z_{q_T 0}$ are the positions of S and T at the time $t = 0$. Another important parameter is the longitudinal particles distance, defined as the difference between the S and T instantaneous position:

$$s_{ST} = z_{q_S}(t) - z_{q_T}(t). \tag{2.6}$$

For the co-moving wakefield case, i.e. the case in which S and T moves in the same direction, a consequence of the rigid beam hypothesis is the fact that the distance between S and T is constant. Substituting Eq. 2.4 and 2.5 into Eq. 2.6 one obtains:

$$s_{ST} = z_{q_S 0} - z_{q_T 0}, \tag{2.7}$$

that is, s_{ST} depends only on the longitudinal position of S and T in a reference configuration $z_{q_S 0}, z_{q_T 0}$. This reference configuration in this work is taken at the time $t = 0$.

Let us introduce t_{Si} and t_{Ti} as the times at which S and T enter into the vacuum chamber, respectively. The time delay in the entrance between T and S is:

$$\Delta t_{ST} = t_{Ti} - t_{Si}. \tag{2.8}$$

Multiplying Eq. 2.8 by v one obtains the space entrance delay between S and T

$$\Delta s_{ST} = v \Delta t_{ST}. \tag{2.9}$$

Physically, this represents the distance that T has to cover in order to enter into the vacuum chamber at the time at which S is entering, refer to Fig. 2.3. Looking at Fig. 2.3, one notices that the space entrance delay is coincident with the distance among the particles, s_{ST}, at the time at which S is entering. It has been just shown that, in the co-moving wakefield problem, one of the consequences of the rigid beam approximation is the time independence of the distance between S and T, s_{ST}, thus, the space entrance delay is equal to the particle distance at whatever time:

$$\Delta s_{ST} = s_{ST} = v \Delta t_{ST}. \tag{2.10}$$

This means that, in the co-moving wakefield problem, the concept of distance between the particles and space entrance delay can be used interchangeably. It is important to distinguish these two concepts because, as will be discussed in sec. 2.4.1, Eq. 2.10 is not longer valid in the case of counter-moving particles.

Section 2.2 phenomenologically described the wakefield introducing the force $\mathbf{F}$ acting on the test charge T, crossing the vacuum chamber, because of the wakefields generated by the transit of the source charge S into the vacuum chamber. This force is dependent on the transverse positions of the T and S trajectories, $\mathbf{u}_S$ and $\mathbf{u}_T$, on the instantaneous position of T, $z_{q_T}(t)$, and on the delay between the entrance

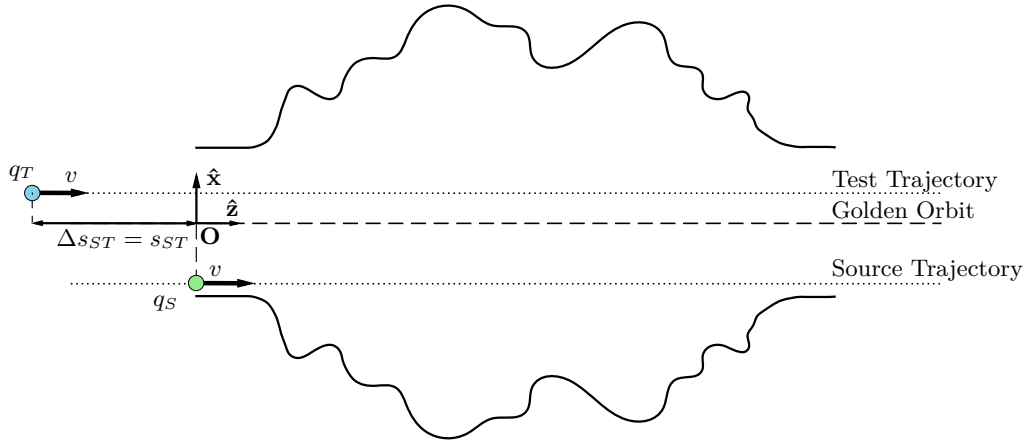

Figure 2.3. co-moving wakefield scenario. The cartoon represents the position of S and T at the time at which the source is entering into the vacuum chamber, t_{Si}. The longitudinal distance between the particles, s_{ST}, represents also the distance that T has to cover to enter into the vacuum chamber once S is entered. Therefore, it can be related to the temporal entrance delay Δt_{ST} considering the rigid beam hypothesis.

of S and T into the vacuum chamber, Δt_{ST}, that is $\mathbf{F}(\mathbf{u}_S, \mathbf{u}_T, \Delta t_{ST}, z_{q_T})$. Thus, $\mathbf{F}$ depends on space variables, in particular z_{q_T} and time variables, in particular Δt_{ST}. However, it is convenient to express $\mathbf{F}$ or just as a function of time variables or just as a function of space variables. This can be done recalling Eq. 2.10 that links Δt_{ST} with s_{ST} and Eq. 2.5 that links z_{q_T} with t. This means that $\mathbf{F}$ can be equivalently expressed as:

$$\mathbf{F}(\mathbf{u}_S, \mathbf{u}_T, \Delta t_{ST}, t) \text{ time variables formulation}$$

or

$$\mathbf{F}(\mathbf{u}_S, \mathbf{u}_T, s_{ST}, z_{q_T}), \quad \mathbf{F}(\mathbf{u}_S, \mathbf{u}_T, \Delta s_{ST}, z_{q_T}) \text{ space variables formulation.}$$

Historically, the space variables formulation expressed in function of s_{ST} is preferred. This subsection derives the main equation of the co-moving wakefield problem following this approach. However, those equations can be rewritten using the time formulation of the force as a function of the time entrance delay, as it is done in section 2.4.3 for the counter-moving wakefield problem.

Finally, the force $\mathbf{F}$ can be decomposed in:

$$\mathbf{F} = (\mathbf{F}_{x,y}, F_z), \tag{2.11}$$

where F_z is the longitudinal component and $\mathbf{F}_{x,y}$ is the transverse one.

2.3.2 Longitudinal Wakefunction

The longitudinal wakefunction w_z is defined as the integral of F_z over the longitudinal path of the particle T inside the vacuum chamber z_{q_T}, normalized with respect to

the product of the S and T charges [46]:

$$w_z(\mathbf{u}_T, \mathbf{u}_S, s_{ST}) = \frac{1}{q_S q_T} \int_0^L F_z(\mathbf{u}_T, \mathbf{u}_S, s_{ST}, z_{q_T}) dz_{q_T}. \tag{2.12}$$

This integral can be transformed into an infinite integral considering two infinitely long circular pipes before and after the vacuum chamber, smooth and perfectly conducting so they do not generate any wakefield and they do not give any contribution to the wakefunction [45]. Since the infinite integral notation is more convenient for manipulating the expressions, this work adopts it from now on except where differently specified. With this notation, Eq. 2.12 becomes:

$$w_z(\mathbf{u}_T, \mathbf{u}_S, s_{ST}) = \frac{1}{q_S q_T} \int_{-\infty}^{\infty} F_z(\mathbf{u}_T, \mathbf{u}_S, s_{ST}, z_{q_T}) dz_{q_T}, \tag{2.13}$$

or, recalling the Lorentz force

$$w_z(\mathbf{u}_T, \mathbf{u}_S, s_{ST}) = \frac{1}{q_S} \int_{-\infty}^{\infty} E_z(\mathbf{u}_T, \mathbf{u}_S, s_{ST}, z_{q_T}) dz_{q_T}. \tag{2.14}$$

Equation 2.13 can be interpreted also in terms of energy. Indeed, by definition, dz_{q_T} represents the elemental displacement of T. This means that $F_z(\mathbf{u}_T, \mathbf{u}_S, s_{ST}, z_{q_T}) dz_{q_T}$ is the elemental work spent by the electric field force $\mathbf{F}$ on T, $dU_{q_S q_T}$:

$$\begin{aligned} w_z(\mathbf{u}_T, \mathbf{u}_S, s_{ST}) =& \frac{1}{q_S q_T} \int_{-\infty}^{\infty} F_z(\mathbf{u}_T, \mathbf{u}_S, s_{ST}, z_{q_T}) dz_{q_T} = ... \\ ... =& \frac{1}{q_S q_T} \int_{-\infty}^{\infty} dU_{q_S q_T} = \frac{\Delta U_{q_T q_S}}{q_S q_T}, \end{aligned} \tag{2.15}$$

where $\Delta U_{q_T q_S}$ is the total energy variation of the particle T induced by the S wakefields after the vacuum chamber crossing.

Equation 2.15 provides the physical meaning of the longitudinal wakefunction: the longitudinal wakefunction represents the total energy variation of the test charge T that enters and travels into a vacuum chamber due to the electromagnetic wakefields excited by the source charge S entered in the chamber a time Δt_{ST} before T.

It is important to note that, while the test particle can gain or lose energy, the source particle S can only lose energy, traversing the vacuum chamber (in the hypothesis that the vacuum chamber is a passive device). Indeed, the lost energy feeds the generation of the electromagnetic fields in the vacuum chamber. It can be only partially recovered from the test charge because there is always a part of this energy that is going to heat the vacuum chamber walls or feed some electromagnetic resonant mode of the structure. It is useful to quantify the total energy lost by the source particle $\Delta U_{q_S q_S}$, since this quantity will be needed later in this work. This is done introducing the loss factor as the energy lost by the source particle normalized to the square of the source particle charge:

$$k = \frac{\Delta U_{q_S q_S}}{q_S^2}. \tag{2.16}$$

Equation 2.16 can be linked with Eq. 2.15 considering S coincident with T, i.e. $\mathbf{u}_T \to \mathbf{u}_S$, $z_{q_T}(t) \to z_{q_S}(t)$ or $s_{ST} \to 0$ and $q_T = q_S$, in this way one has:

$$k = w_z(\mathbf{u}_S, \mathbf{u}_S, s_{ST}) \text{ with } \beta < 1. \tag{2.17}$$

The specification $\beta < 1$ has to be kept in mind, indeed Eq. 2.17 is not valid for relativistic particles, i.e. $\beta \to 1$. In such a case the fundamental theorem of the beam loading states [38]:

$$k = \frac{w_z(\mathbf{u}_S, \mathbf{u}_S, 0)}{2} \text{ with } \beta \to 1. \tag{2.18}$$

2.3.3 Wakepotential and Energy Loss

As explained in section 2.2, the longitudinal wakefunction is intimately linked with the energy lost or gained by the test particle T. This connection is so strong that one can use indifferently Eq. 2.15 as definition of wakefunction instead of Eq. 2.13 or 2.14.

This concept can be extended to the situation in which the excitation source is not a single point charge S with charge q_S but is a bunch, or a beam, of particle with total charge q_S and with a longitudinal shape described by the charge distribution in space $Q_S(z) = q_S\lambda(z)$.

With reference to Fig. 2.4, let us consider the arbitrary charge distribution $Q_S(z)$. As the point charge q_S before, this charge distribution moves in the vacuum chamber on a trajectory parallel to the axis $\hat{\mathbf{z}}$ with a speed $v_S = v_{q_T} = v$. Regarding the test charge, q_T, it can be defined exactly as done in section 2.2.

The source distribution $Q_S(z) = q_S\lambda(z)$, can be represented as the sum of infinitesimal point charges

$$dQ_S(z_{dQ_s}) = q_S\lambda_S(z_{dQ_s})dz_{dQ_s}, \tag{2.19}$$

with $dz_{dQ_s} \to 0$, each one centered at a different coordinate $z_{dQ_s}(t)$ and all moving with the same speed v_S, so that the whole distribution moves rigidly. For each one of these point charges, the distance between the infinitesimal source dQ_S at $z_{dQ_S}(t)$ and the test charge q_T at $z_{q_T}(t)$ can be defined as:

$$s_{ST} = z_{dQ_s}(t) - z_{q_T}(t), \tag{2.20}$$

that is the analogous of Eq. 2.6. Introducing the motion equation of the particle dQ_s:

$$z_{dQ_S}(t) = vt + z_{dQ_S0} \tag{2.21}$$

and recalling the equation of motion of T, Eq. 2.5, one can rewrite Eq. 2.20 as:

$$s_{ST} = z_{dQ_S0} - z_{q_T0}. \tag{2.22}$$

While both $z_{dQ_s}(t)$ and $z_{q_T}(t)$ are in general function of time the hypothesis of rigid beam approximation guarantees that s_{ST} is time-independent. It depends only on the longitudinal position of S and T in the reference configuration z_{dQ_S0}, z_{q_T0}. As already said, this reference configuration is set at $t = 0$.

Let us introduce the concept of distance between the charge q_T and the distribution Q_S. It can be labeled s_{Q_ST} and defined as the distance between a selected point charge dQ_{Sr} of the distribution Q_S (for instance the one with the highest charge or the one in the middle point) and the charge q_T, in the reference configuration.

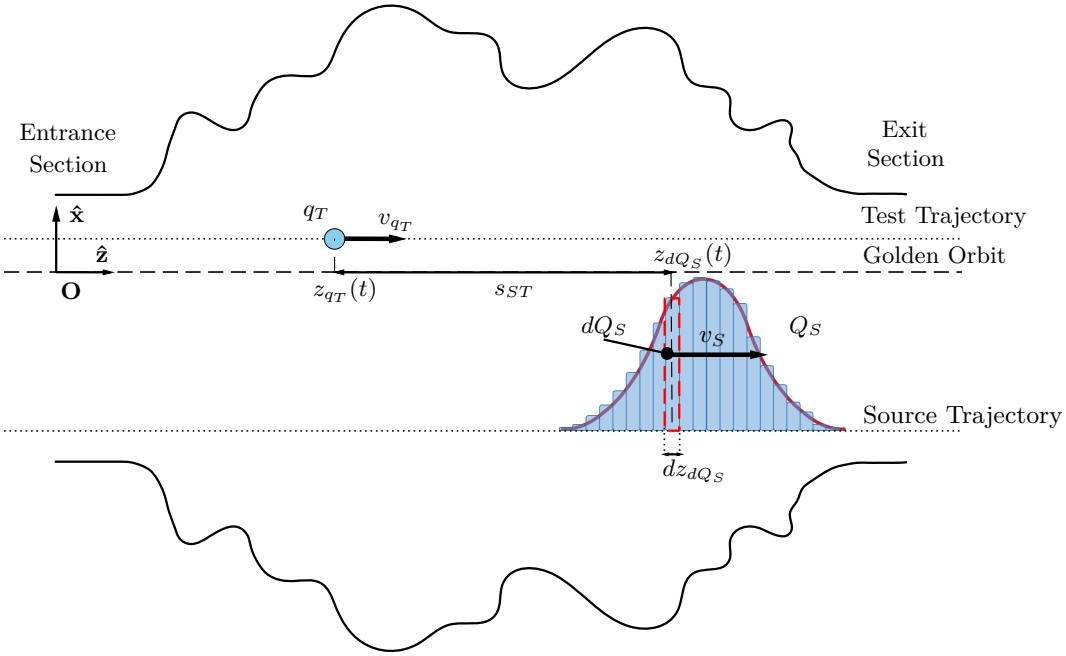

Figure 2.4. Co-moving wakepotential scenarios. Transit of a bunch distribution (Q_S), the source, and the test (q_T) charge inside a vacuum chamber. The source distribution can be imagined as the sum of infinitesimal point charges dQ_S, each one generating its wakefield that acts on the test charge T. The total effects experienced from T is the sum of the wakefield effects of all the infinitesimal charges. The cartoon underlines the charge distribution Q_S, divided into infinitesimal charges dQ_S, the instantaneous longitudinal positions of the charge dQ_S and q_T, $z_{dQ_S}(t)$ and $z_{q_T}(t)$, their speeds v_S and v_{q_T} (with $v_S = v_{q_T}$), their distance s_{ST} and the transverse position of their trajectories with respect to the main reference frame $\mathbf{O}$, $\mathbf{u}_T$ and $\mathbf{u}_S$.

Calling $z_{dQ_{Sr0}}$ the longitudinal coordinate of the selected charge of the distribution in the reference configuration, s_{Q_ST} is:

$$s_{Q_ST} = z_{dQ_{Sr0}} - z_{qT0}. \tag{2.23}$$

In the same way, it is also possible to define the time entrance delay between the the charge q_T and the distribution Q_S:

$$\Delta t_{Q_ST} = t_{Ti} - t_{dQ_{Sr}i}, \tag{2.24}$$

where $t_{dQ_{Sr}i}$ is the entrance time of dQ_{Sr} into the vacuum chamber while t_{Ti} is the entrance time of q_T into the vacuum chamber. From the time entrance delay the space entrance delay is derived as:

$$\Delta s_{Q_ST} = v\Delta t_{Q_ST}, \tag{2.25}$$

A cartoon representing a possible reference configuration and the space and time entrance delay between the distribution Q_S and the charge q_T is shown in Fig. 2.5. These quantities will be useful to plot the wakepotential.

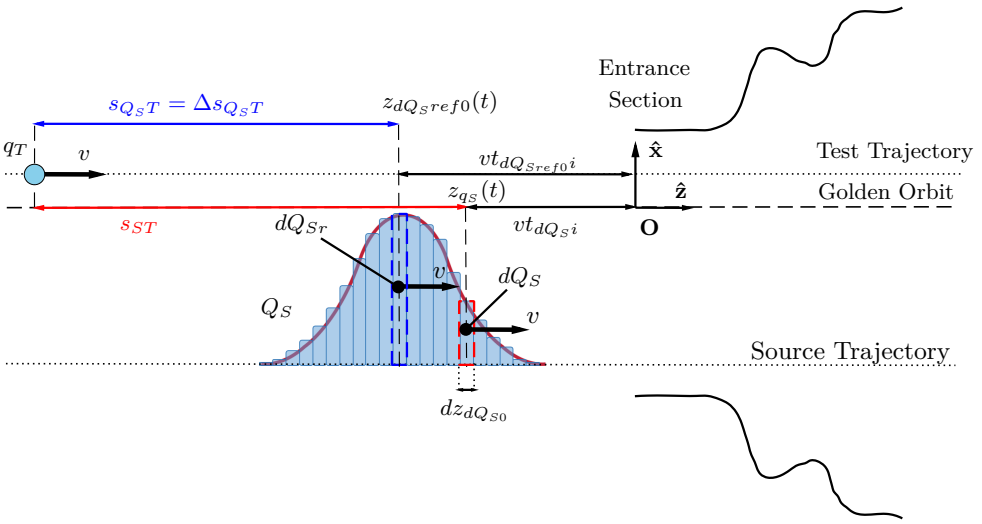

Figure 2.5. Cartoon representing a possible reference configuration. The space and time entrance delay between the distribution Q_S and the charge q_T is shown in blue, as well as the distance between the charge q_T and a generic charge dQ_S of the distribution Q_S, shown in red. Also the entrance time into the vacuum chamber of the charge dQ_{Sr}, $t_{dQ_{Sr}i}$, and of the charge dQ_S, $t_{dQ_S i}$ are shown.

From the wakefunction definition, Eq. 2.15, the energy lost or gained by the test charge T, during the transit into the vacuum chamber because of the infinitesimal source charge $dQ_S(z_{dQ_S0})$ is equal to:

$$\Delta U_{q_T dQ_S} = q_T dQ_S w_z(\mathbf{u}_S, \mathbf{u}_T, s_{ST}) = q_T dQ_S w_z(\mathbf{u}_S, \mathbf{u}_T, z_{dQ_S0} - z_{q_T0}), \qquad (2.26)$$

where Eq. 2.22 was used. To compute the $\Delta U_{q_T Q_S}$, the total energy variation of T, that is the effects of the entire distribution Q_S, one has to sum the energy variation contribution, $\Delta U_{q_T dQ_S}$, of every infinitesimal charge dQ_S that constitues Q_S. This means taking into account all the different distances s_{ST} between the test T and the sources dQ_S. The last point can be accomplished representing the distribution Q_S and the charge test T as a function of z at the reference time $t = 0$, for which $z_{dQ_S} = z_{dQ_S0}$ and $z_{q_T} = z_{q_T0}$, refer to Fig. 2.5. It is clear from this figure that $s_{ST} = z_{dQ_S0} - z_{q_T0}$ changes only because different dQ_S have different z_{dQ_S0}. Rewriting Eq. 2.19 for $t = 0$ one has

$$dQ_S(z_{dQ_S0}) = q_S \lambda_S(z_{dQ_S0}) dz_{dQ_S0}, \qquad (2.27)$$

that substituded into Eq. 2.26 leads to:

$$\Delta U_{q_T dQ_S} = q_T q_S \lambda_S(z_{dQ_S0}) w_z(\mathbf{u}_S, \mathbf{u}_T, z_{dQ_S0} - z_{q_T0}) dz_{dQ_S0}. \qquad (2.28)$$

Integrating Eq. 2.28 over dz_{dQ_S0} allows to sum up the energy variation contribution of the wakefield of every dQ_s on the charge T, so obtaining the total variation of energy $\Delta U_{q_T Q_S}$ due to the whole distribution Q_S:

$$\Delta U_{q_T Q_S} = q_T q_S \int_{-\infty}^{\infty} \lambda_S(z_{dQ_S0}) w_z(\mathbf{u}_S, \mathbf{u}_T, z_{dQ_S0} - z_{q_T0}) dz_{dQ_S0}. \qquad (2.29)$$

Equation 2.29 can be used to define the wakepotential as:

$$W_z(\mathbf{u}_S, \mathbf{u}_T, z_{q_T 0}) = \frac{\Delta U_{q_T Q_S}}{q_T q_S} = \int_{-\infty}^{\infty} \lambda_S(z_{dQ_S 0}) w_z(\mathbf{u}_S, \mathbf{u}_T, z_{dQ_S 0} - z_{q_T 0}) dz_{dQ_S 0}. \tag{2.30}$$

The wakepotential can be defined as the total variation of energy of a point test charge q_T traversing a vacuum chamber a time $\Delta t_{Q_S T}$ after the excitation of a beam of particles described by a charge distribution Q_S, normalized by the product of the total beam charge q_S and the test charge q_T. Please note that, from Eq. 2.30, the wakepotential is the convolution between the wakefunction w_z and the space distribution λ_S. In this sense, the wakefunction is a Green's function of the problem, i.e. knowing the wakefunction one can obtain the wakepotential for every charge distribution λ_S.

The concept of wakepotential can be further expanded to compute the energy variation of a test beam due to the effects of a source beam. The terms test and source have the same meaning of the two charges case, i.e. the source enters the vacuum chamber first, depositing energy into the electromagnetic field. The test enters the vacuum chamber with a defined delay (in time $\Delta t_{Q_S T}$, in space $\Delta s_{Q_S T}$) and interacts with the electromagnetic field excited by the source, gaining or losing energy. In this case, also the test charge is not a point charge any more but it is a charge distribution described by a space profile $Q_T(z) = q_T \lambda_T(z)$. As previously done, the test distribution can be thought as the sum of infinitesimal slices dQ_T, every one of them at a position $z_{dQ_T}(t)$ with thickness dz_{dQ_T} moving with speed $v = v_T = v_S$ on an axis parallel to the $\hat{\mathbf{z}}$ axis, carrying the charge:

$$dQ_T(z_{dQ_T}) = q_T \lambda_T(z_{dQ_T}) dz_{dQ_T}. \tag{2.31}$$

As before, with $dz_{dQ_T} \to 0$, every slice behaves like a point charge of charge $Q_T(z_{dQ_T})$. Let us introduce the equation of motion of the infinitesimal test charge dQ_T as:

$$z_{dQ_T}(t) = vt + z_{dQ_T 0}, \tag{2.32}$$

that for $t = 0$ is $z_{dQ_T}(0) = z_{dQ_T 0}$. This allows to rewrite Eq. 2.31 for $t = 0$ as:

$$dQ_T(z_{dQ_T 0}) = q_T \lambda_T(z_{dQ_T 0}) dz_{dQ_T 0}. \tag{2.33}$$

Therefore, one can compute the energy gained or lost by one of these test slices $\Delta U_{dQ_T Q_S}$ using the definition of wakepotential, Eq. 2.30:

$$\begin{aligned} \Delta U_{dQ_T Q_S} &= q_S dQ_T W_z(\mathbf{u}_S, \mathbf{u}_T, z_{dQ_T 0}) = ... \\ &... = q_S q_T \lambda_T(dz_{dQ_T 0}) W_z(\mathbf{u}_S, \mathbf{u}_T, z_{dQ_T 0}) dz_{dQ_T 0}. \end{aligned} \tag{2.34}$$

To compute the $\Delta U_{Q_T Q_S}$, the total energy variation of the test beam, that is the effect on the entire distribution Q_T of the source Q_S, one has to sum the energy variation contribution, $\Delta U_{dQ_T Q_S}$, of every infinitesimal charge dQ_T that constitutes Q_T. This means integrating Eq. 2.34 over $z_{dQ_T 0}$:

$$\Delta U_{Q_T Q_S} = q_S q_T \int_{-\infty}^{\infty} \lambda_T(z_{dQ_T 0}) W_z(\mathbf{u}_S, \mathbf{u}_T, z_{dQ_T 0}) dz_{dQ_T 0}. \tag{2.35}$$

Equation 2.35 can be rewritten also in terms of wakefunction, considering the wakepotential definition, Eq. 2.30,

$$\Delta U_{Q_T Q_S} = q_S q_T \int_{-\infty}^{\infty} \lambda_T(z_{dQ_T 0}) \int_{-\infty}^{\infty} \lambda_S(z_{dQ_S 0}) w_z(\mathbf{u}_S, \mathbf{u}_T, z_{dQ_S 0} - z_{dQ_T 0}) dz_{dQ_S 0} dz_{dQ_T 0}. \tag{2.36}$$

2.3.4 RF-heating

At this point, it is interesting to consider the energetic effects of the wakefields generated by a beam on itself, i.e. the beam particles act at the same time as sources and tests. Qualitatively speaking, the first particle that enters the vacuum chamber finds it empty. It loses energy, depositing this energy in the vacuum chamber wall, heating it, and exciting electromagnetic resonant modes. Particles that enter later find the electromagnetic fields excited by the previous particle. Thus, these later particles, from one side, behave as the first one, depositing energy into the vacuum chamber as wall heating or modes excitation, from another side, they interact with the electromagnetic fields generated by the previous particles gaining or losing energy. The overall picture is that, the first particle entering always loses energy interacting with the vacuum chamber while the later particles can lose or gain energy. The total energy variation of the beam is the sum of the losses and gains of every single particle, and according to the energy conservation principle, the beam has always to lose energy [2].

In order to quantify this energy loss, Eq.s 2.35 or 2.36 can be used to compute the energy variation of the beam due to itself considering $Q_S = Q_T$. This implies $q_S = q_T = q$, $\mathbf{u}_S = \mathbf{u}_T = \mathbf{u}$ and $\lambda_S = \lambda_T = \lambda$, thus giving:

$$\Delta U_T = q^2 \int_{-\infty}^{\infty} \lambda(z_{dQ_T 0}) \int_{-\infty}^{\infty} \lambda(z_{dQ_S 0}) w_z(\mathbf{u}, z_{dQ_S 0} - z_{dQ_T 0}) dz_{dQ_S 0} dz_{dQ_T 0}. \tag{2.37}$$

According to its definition, Eq. 2.37 is the energy lost by a beam during its transit into the vacuum chamber. Analogously to what has been done for the case of two point charges, one can define the loss factor as the energy lost by the beam traversing the vacuum chamber normalized with respect to the square of the beam charge:

$$k = \frac{\Delta U_T}{q^2} = \int_{-\infty}^{\infty} \lambda(z_{dQ_T 0}) \int_{-\infty}^{\infty} \lambda(z_{dQ_S 0}) w_z(\mathbf{u}, z_{dQ_S 0} - z_{dQ_T 0}) dz_{dQ_S 0} dz_{dQ_T 0}. \tag{2.38}$$

If the vacuum chamber is installed in a circular accelerator, ΔU_T is the energy deposited in the device in one turn of the beam inside the accelerator. Indicating with T_0 the revolution time of the beam into the accelerator, one can define an average power deposited into the device as:

$$P = \frac{\Delta U_T}{T_0} = \Delta U_T f_0, \tag{2.39}$$

[2] This may be not true if there is an externally imposed electric field into the component traversed by the beam, as in the RF-cavities for example. To avoid this case, in section 2.2, we explicitly assumed that the vacuum chamber is empty before the source entrance and that no external fields are imposed later. This is true for all the devices analyzed in this work.

with $f_0 = 1/T_0$ the beam revolution frequency. Substituting Eq. 2.37 into Eq. 2.39 one obtains the well known equation:

$$P = f_0 q^2 \int_{-\infty}^{\infty} \lambda(z_{dQ_{T0}}) \int_{-\infty}^{\infty} \lambda(z_{dQ_{S0}}) w_z(\mathbf{u}, z_{dQ_{S0}} - z_{dQ_{T0}}) dz_{dQ_{S0}} dz_{dQ_{T0}}. \quad (2.40)$$

This power acts as an heating source for the vacuum chamber causing the so called RF-heating.

With in mind the goal of reducing as much as possible the RF-heating, one has to understand the physical mechanisms that regulate it. A possible distinction based on the heat generation mechanisms and the heat distribution in a device is:

- Resistive Losses [34] or transient losses [39]. The resistive losses are due to the resistivity of the vacuum chamber materials. When the beam is passing into the vacuum chamber, it generates image currents in the vacuum chamber walls. These currents, moving in a medium with a finite conductivity dissipates power by joule effect. The magnitude of the power dissipated in the wall depends on the beam-wall distance and on the conductivity of the material. A general rule to reduce resistive losses is to design a device made by good conductors with walls as far as possible from the beam trajectory. However, it has to be borne in mind that this is not always possible, there are devices that by functional specifications have to violate the two principles that have been just stated, as for instance collimators and absorber scrapers (discussed in chapter 1). Further, good conductors reduce the resistive losses but they can generate problems of electron cloud, which is also a source of heating.

- Resonant Mode Losses [48, 39]. The beam transiting inside the structure is a source that excites the electromagnetic resonant modes of the device. These resonant modes are an intrinsic property of the device geometry and material. Each of them resonates at a specific frequency and has a peculiar magnetic and electric field map. In all the points of the vacuum chamber walls in which the magnetic field component of the mode tangential to the wall surface is not null, the phenomenon of the magnetic induction is triggered. Indeed, a magnetic field that changes with time inside a conductor (there is a no null magnetic field inside a conductor in a thickness of some skin depths) induces parasitic currents (eddy currents or foucault's currents) in the conductor. These currents, flowing in the wall material, dissipate the energy of the magnetic field that has generated them because of ohmic losses. This effect is triggered by the beam. However, a resonant mode keeps resonating also after the beam passage. The total resonating time of the mode depends on the time the losses take to dissipate all the energy the beam has deposited in the mode.

- Magnetic Hysteresis Losses [34]. This kind of losses takes place if in the vacuum chamber there are ferromagnetic materials. When this kind of material is immersed in a time varying magnetic field, it absorbs energy from this magnetic field dissipating it as heat. This is due to the magnetic hysteresis cycle. Supposing to have a ferromagnetic material that has not been previously immersed in a magnetic field. Its magnetic domains, the smallest portion of material that has a magnetic field, are randomly oriented and the material

should not generate any magnetic field. If the material is immersed in a steady magnetic field some of its magnetic domains orient their magnetic field as the external one, the strongest the external magnetic field the more magnetic domains align their magnetic field with the external one, up to the saturation. In the case in which the external magnetic field is changing its orientation with time (as in the case of a resonant mode in the device), the material magnetic domains try to follow the changes. However, the process of reorientation of the magnetic domains has to be done against the internal material friction. As a net effect, this transforms the electromagnetic energy of the external field in heating of the ferromagnetic material. Magnetic hysteresis losses can be extremely high, depending on the ferromagnetic material one is considering. This makes ferromagnetic material a possible solution to keep under control unwanted resonant modes in the device structure. Indeed a piece of ferrite, immersed in the magnetic field of a resonant mode, damps the resonant mode very efficiently. As for the resistive losses, the closer the ferromagnetic material to the beam, the stronger the losses. Thus, if ferromagnetic material is used to damp a resonant mode it should be inserted in the resonating mode fields, but as far as possible from the expected beam orbit.

According on the vacuum chamber materials, these losses mechanism can be schematised with: volume losses if they take place in dielectrics and ferromagnetic materials, surface losses if they take place in conductors. The point is better discussed in section 4.2 of this work.

The problem of RF-heating has to be carefully considered since the early design phase of a device [39]. This is because the losses related to electromagnetic resonant modes cannot be taken into account before the component is designed. Indeed, resistive wall heating deposits energy regularly as a function of the electrical conductivity of the vacuum chamber wall and their distance from the beam orbit. Magnetic Hysteresis heats up the ferromagnetic material. However, there is no general rule of thumb to understand where an electromagnetic mode will resonate in a complex device (and thus, where it will heat) and if it will be excited by the beam. The analysis on the electromagnetic resonant modes can be done only once the device design is ready, that is after the conceptual design phase. The cooling system of the device is designed during the conceptual design phase, therefore it is not specifically thought to evacuate the power deposited by the resonant modes. If this deposited power is highly concentrated in unexpected zones, the temperature of such areas increases with the possibility of generating undesired effects as damages, melting, ablation or outgassing [49]. To avoid this, it has to be foreseen an iterative cycle between resonant modes heating studies and design modifications, i.e.: the first tentative design is analyzed, and in case high power deposition of resonant mode is found in unexpected area, the design is modified to eliminate the modes, or the cooling system is adjusted to evacuate the extra heating.

2.3.5 Transverse Wakefunction

Let us recall the case of the two charged particles T and S travelling into the vacuum chamber displayed in Fig. 2.2. The transverse wakefunction $w_{x,y}$ is defined [38] as

the integral of the transverse S induced wakefield force $\mathbf{F}_{x,y}$ acting on T along its path inside the vacuum chamber, normalized with respect to the product of the S and T charges:

$$\mathbf{w}_{x,y}(\mathbf{u}_T, \mathbf{u}_S, s_{ST}) = \frac{1}{q_S q_T} \int_{-\infty}^{\infty} \mathbf{F}_{x,y}(\mathbf{u}_T, \mathbf{u}_S, s_{ST}, z_{q_T}) dz_{q_T}. \tag{2.41}$$

The transverse wakefunction is a vector of two components $\mathbf{w}_{x,y} = [w_x, w_y]$, and it has the same analytic properties as the longitudinal wakefunction since it has the same formal definition. This means that, recalling the expression 2.27 of the source charge distribution Q_S one can define the transverse wakepotential as:

$$\mathbf{W}_{x,y}(\mathbf{u}_T, \mathbf{u}_S, s_{ST}) = \int_{-\infty}^{\infty} \lambda_S(z_{dQ_S 0}) \mathbf{w}_{x,y}(\mathbf{u}_S, \mathbf{u}_T, z_{dQ_S 0} - z_{q_T 0}) dz_{dQ_S 0}. \tag{2.42}$$

Usually, the transverse wakefunction, Eq. 2.41, is expanded into power series in the offset of the trajectory of the source particle and the test particle ($\mathbf{u}_S = (x_{q_S}, y_{q_S)}), \mathbf{u}_T = (x_{q_T}, y_{q_T})$) with respect to the golden orbit or the vacuum chamber axis [50]. Considering only the first order terms and neglecting any coupling between transverse planes one can write:

$$\begin{aligned} w_x &= C_x(s_{ST}) + w_x^{dip}(s_{ST}) x_{q_S} + w_x^{quad}(s_{ST}) x_{q_T}, \\ w_y &= C_y(s_{ST}) + w_y^{dip}(s_{ST}) y_{q_S} + w_x^{quad}(s_{ST}) y_{q_T}. \end{aligned} \tag{2.43}$$

The terms w_x^{dip} and w_y^{dip} [$\mathrm{Vm}^{-1}\mathrm{C}^{-1}$] are called dipolar wakefunction while the terms w_x^{quad} and w_y^{quad} [$\mathrm{Vm}^{-1}\mathrm{C}^{-1}$] are called quadrupolar wakefunction. If x_{q_S}, y_{q_S} and x_{q_T}, y_{q_T} are small with respect to the transverse characteristic dimensions of the vacuum chamber, Eq. 2.43 is a good approximation of the transverse wakefunction [51].

Equation 2.43 gives an operative way to compute its terms :

$$\begin{aligned} C_x &= w_x|_{x_{q_S}=0, x_{q_T}=0}, \\ C_y &= w_y|_{x_{q_S}=0, x_{q_T}=0}, \\ w_x^{dip} &= \frac{w_x|_{x_{q_S}, x_{q_T}=0} - C_x}{x_{q_S}}, \\ w_x^{quad} &= \frac{w_x|_{x_{q_S}=0, x_{q_T}} - C_x}{x_{q_T}}, \\ w_y^{dip} &= \frac{w_y|_{y_{q_S}, y_{q_T}=0} - C_y}{y_{q_S}}, \\ w_y^{quad} &= \frac{w_y|_{y_{q_S}=0, y_{q_T}} - C_y}{y_{q_T}}, \end{aligned} \tag{2.44}$$

Where the various terms may be obtained, for instance, by simulations [51].

2.3.6 Relationship Between Longitudinal and Transverse Wakefunction

Transverse and longitudinal wakefunctions are linked by the Panowsky-Wenzel theorem [52, 39]:

$$\nabla_{x,y}(w_z) = \begin{bmatrix} \frac{\partial w_z}{\partial x} \\ \frac{\partial w_z}{\partial y} \end{bmatrix} = \begin{bmatrix} \frac{\partial w_x}{\partial z} \\ \frac{\partial w_y}{\partial z} \end{bmatrix} = \frac{\partial}{\partial z}(\mathbf{w}_{x,y}). \tag{2.45}$$

As shown in section 5.4.3, Eq. 2.45 is crucial for the estimation of transverse impedance during bench measurements campaign.

2.4 Counter-Moving Wakefield

The material presented in this and in the next sections is original, if not differently specified. In particle colliders, for instance LHC, two counter-moving beams are stored and they collide at the interaction points (IPs). Normally, the two beams do not see each other since they circulate in two separated rings. Of course, this is not true in the colliding chamber. Further, there are also other devices in which the two counter-moving beams circulate in the same vacuum chamber, as for instance the TDIS, discussed in section 7.3.

In this context, it is interesting to understand what are the wakefields consequences of the passage of two counter-moving beams inside the same vacuum chamber. This work especially focuses on the RF-heating effects due two counter-moving beams and does not discuss beam instabilties issues. Previous studies on the RF-heating of two counter-moving beams have been conducted by Zannini et al. [53, 54] and by Grudiev [55].

Thus, in this section, as an extension of those works, an original approach to model the RF-heating of two counter-moving beams is derived. It is based on a generalization of the wakefunction concept applicable also to the case of two counter-moving charges. It will be shown that it is possible to reobtain and extend the results already obtained by Zannini et al. [53, 54] and Grudiev [55].

The section is organized as followed: first the problem of determining the longitudinal wakefunction of two counter-moving charged is addressed; all the quantities needed for the definition of counter-moving wakefunction are introduced, then the definition of wakefunction is given. Subsequently, the formalism presented in section 2.3.3 to compute the wakepotential from the wakefunction is adapted to define the wakepotential and the energy losses for the counter-moving case. Examples, of co-moving and counter-moving wakefunctions are discussed in the next section 2.5.

2.4.1 Basic Quantities

As was done for the definition of the co-moving wakefunction, in this subsection the quantities needed for the formal definition of counter-moving longitudinal and transverse wakefunction are given. With reference to Fig. 2.6, let us consider a vacuum chamber with an arbitrary geometry, made by materials characterized by electric conductivities σ, electrical permittivities ε and magnetic permeabilities μ.

The vacuum chamber is free of external electromagnetic fields before the entrance of the source[3]. Let us consider, as usual, the source charge S, with charge q_S, and the test particle T, of charge q_T. Because of the rigid beam hypothesis (refer to sec. 2.2) both the particles are moving on parallel trajectories. Furthermore, the speeds of the particles are constant during the transit of the two charges in the vacuum chamber and they are equal in modulus $v = v_S = v_T$.

Let us define a reference frame **O** with the origin at the test entrance section of the vacuum chamber and the $\hat{\mathbf{z}}$ axis lying on the golden orbit, oriented in the direction in which the test charge T is moving. The axes $\hat{\mathbf{x}}$ and $\hat{\mathbf{y}}$ are perpendicular to $\hat{\mathbf{z}}$, they can have an arbitrary orientation but the frame has to be orthonormal. As for the co-moving wakefield scenario in the **O** frame the instantaneous position of S and T are identified by the vectors:

$$\text{instantaneous position of S } (x_{q_S}, y_{q_S}, z_{q_S}(t))$$
$$\text{instantaneous position of T } (x_{q_T}, y_{q_T}, z_{q_T}(t))$$

where t is an arbitrary time. The transverse position of S can be defined as $\mathbf{u}_S = (x_{q_S}, y_{q_S})$ and the transverse position of T as $\mathbf{u}_T = (x_{q_T}, y_{q_T})$.

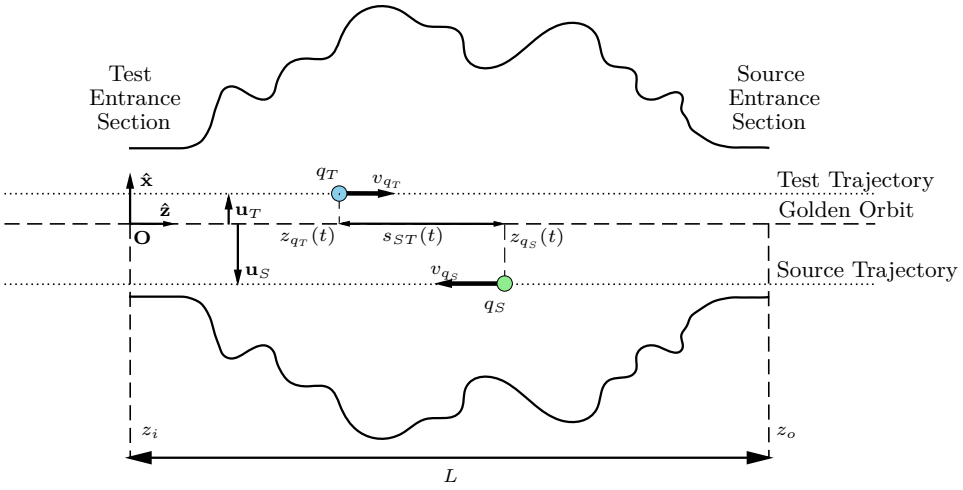

Figure 2.6. counter-moving wakefield scenarios, source (q_S) and test (q_T) charge transiting inside a vacuum chamber. The cartoon underlines the instantaneous z positions of the two charges $z_{q_S}(t)$ and $z_{q_T}(t)$, their speeds v_{q_S} and v_{q_T}, their time-dependent distance $s_{ST}(t)$ and the transverse position of their trajectories with respect to the main reference frame $\mathbf{u}_T$ and $\mathbf{u}_S$. Furthermore, also the reference system **O** and the length of the vacuum chamber L is indicated. In the counter-moving problem, z_i indicates the position of the entrance section through which the test charge enters into the vacuum chamber while z_o indicates the position of the entrance section through which the source enters into the vacuum chamber.

In the counter-moving case test and source particles move in opposite directions inside the structure. This implies that the distance $s_{ST}(t)$ between the charges,

[3]This means that the vacuum chamber is neither an accelerating cavity nor a magnet. In case the vacuum chamber is a cavity or another active device, one has to consider also the external imposed electromagnetic fields, not only the self-induced ones.

defined in Eq. 2.6, is time dependent. Indeed, considering the rigid beam approximation, the longitudinal positions of S, $z_{q_S}(t)$, and of T, $z_{q_T}(t)$, are:

$$z_{q_S}(t) = -vt + z_{q_S 0} \tag{2.46}$$

$$z_{q_T}(t) = vt + z_{q_T 0}. \tag{2.47}$$

Substituting Eq.s 2.46 and 2.47 into Eq. 2.6 one obtains:

$$s_{ST}(t) = z_{q_S}(t) - z_{q_T}(t) = -2vt + z_{q_S 0} - z_{q_T 0}. \tag{2.48}$$

In this case one cannot use the longitudinal and transverse wakefunction definition, Eq.s 2.12 and 2.41. The latter lose their significance being s_{ST} not time independent. However, the counter-moving wakefuncton can be defined recalling the physical meaning of wakefunction: the wakefunction represents the integrated effect (change of energy in the longitudinal direction and change of transverse momentum in the transverse plane) that the electromagnetic field excited by the transit of the source charge S has on the test charge T that enters the vacuum chamber with a time delay Δt_{ST} with respect to the source.

Unlike s_{ST}, Δt_{ST} is well defined also in the counter-moving problem. Indeed recalling the already defined t_{Si}, the time at which S is entering into the vacuum chamber and t_{Ti}, the time at which T is entering into the vacuum chamber, the delay in the entrance between T and S is:

$$\Delta t_{ST} = t_{Ti} - t_{Si}. \tag{2.49}$$

Please note that, S enters into the vacuum chamber when it crosses the source entrance section, while T enters into the vacuum chamber when it crosses the test entrance section. These sections are indicated in Fig. 2.7. The space entrance delay is defined as well as time independent:

$$\Delta s_{ST} = \Delta t_{ST} v. \tag{2.50}$$

As for the co-moving wakefield case, the physical meaning of Eq. 2.50 becomes clear looking at Fig. 2.7: Δs_{ST} represents the distance that the test particle has to cover to enter into the vacuum chamber at the time at which the source particle enters into the vacuum chamber (a negative value of Δs_{ST} means that at t_{Si} the test particle is already inside the vacuum chamber).

Thus, for the counter-moving problem, space entrance delay and particle distances cannot be used interchangeably as done for the co-moving wakefield case. However, according with the wakefunction physical meaning, the quantities needed are the time or space entrance delay, Eq. 2.49 or 2.50, and not the distance between the particles, Eq. 2.48. The former are always defined as time independent, and they will be used in the following to formally define the counter-moving wakefunction.

Another important concept for the counter-moving wakefield is the particle meeting time t_m. It can be defined as the time at which the longitudinal distance between S and T is null. It can be found from Eq. 2.48, imposing $s_{ST}(t) = 0$:

$$t_m = \frac{z_{q_S 0} - z_{q_T 0}}{2v}. \tag{2.51}$$

This quantity is especially important if S and T are counter-moving ultra-relativistic particles. In this case, because of the causality principle, T starts to feel the effects of S only after t_m and not before. This time has to be compared with the entrance and the exit time of T in and from the vacuum chamber, t_{Ti} and t_{To}:

- $t_{Ti} < t_m < t_{To}$, the particles meet inside the vacuum chamber.
- $t_m < t_{Ti}$, the particle does not meet inside the vacuum chamber: when T enters, S is already passed and it is out of the vacuum chamber that is already excited.
- $t_m > t_{To}$, the particles do not meet inside the vacuum chamber: when T leaves the vacuum chamber S is still not entered. For ultra-relativistic particles this case is trivial, the vacuum chamber is not excited when T is passing and the wakefunction is null.

Finally, one has to recall that, in virtue of Eq.s 2.50 and 2.47, $\mathbf{F}$ (the force acting on T because of the wakefield generated by S in the vacuum chamber) can be equivalently expressed as:

$$\mathbf{F}(\mathbf{u}_S, \mathbf{u}_T, \Delta t_{ST}, t) \text{ time variables dependency}$$

or

$$\mathbf{F}(\mathbf{u}_S, \mathbf{u}_T, \Delta s_{ST}, z_{q_T}) \text{ space variables dependency.}$$

and that the force $\mathbf{F}$ can be decomposed in:

$$\mathbf{F} = (\mathbf{F}_{x,y}, F_z), \tag{2.52}$$

where F_z is the longitudinal component and $\mathbf{F}_{x,y}$ is the transverse one.

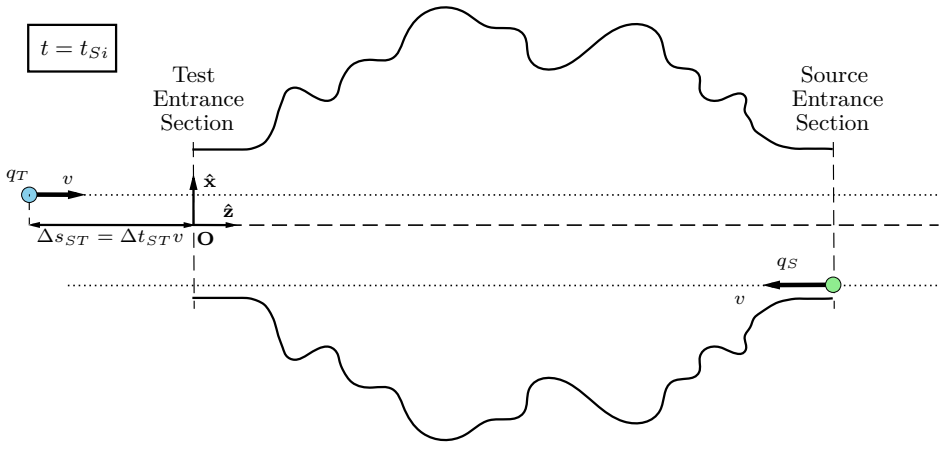

Figure 2.7. counter-moving Wakefield scenario. The cartoon represents the position of S and T at the time at which the source is entering into the vacuum chamber, t_{Si}. The space entrance delay Δs_{ST} is also represented, it is the distance that T has to cover to enter into the vacuum chamber at the time at which S is entering.

2.4.2 Longitudinal counter-moving Wakefunction

As done in section 2.3.2 for the co-moving wakefield, one defines the counter-moving longitudinal wakefunction w_z as the integral of F_z over the instantaneous longitudinal position of the particle T inside the vacuum chamber z_{q_T}, normalized with respect to the product of the S and T charges:

$$w_z(\mathbf{u}_T, \mathbf{u}_S, \Delta s_{ST}) = \frac{1}{q_S q_T} \int_0^L F_z(\mathbf{u}_T, \mathbf{u}_S, \Delta s_{ST}, z_{q_T}) dz_{q_T}, \tag{2.53}$$

where the definition of Δs_{ST} is given in Eq. 2.50. However, in the counter-moving problem it is more intuitive to operate with time variables instead of space variables. Thus, it is more convenient to introduce the wakefunction as:

$$w_z(\mathbf{u}_T, \mathbf{u}_S, \Delta t_{ST}) = \frac{1}{q_S q_T} \int_{t_{Ti}}^{t_{To}} F_z(\mathbf{u}_T, \mathbf{u}_S, \Delta t_{ST}, t) v dt, \tag{2.54}$$

that is Eq. 2.53 with the force expressed in time variables and the substitution $dz_{q_T} = vdt$, obtained from Eq. 2.47. The times t_{Ti} and t_{To} have been already introduced as the entrance and the exit times in the vacuum chamber of the test charge T respectively.

Equation 2.54 can be rewritten as an infinite integral if for $t \leq t_{Ti}$ and $t > t_{To}$ the particle T does not experience any wakefield [45]:

$$w_z(\mathbf{u}_T, \mathbf{u}_S, \Delta t_{ST}) = \frac{1}{q_S q_T} \int_{-\infty}^{\infty} F_z(\mathbf{u}_T, \mathbf{u}_S, \Delta t_{ST}, t) v dt. \tag{2.55}$$

The physical meaning of the wakefunction (the energy variation of the test particle because of the wakefield of a source particle, $\Delta U_{q_T q_S}$, normalized with respect to the product of the two particle charges) remains unchanged. Thus, one can write:

$$\begin{aligned} w_z(\mathbf{u}_T, \mathbf{u}_S, \Delta t_{ST}) =& \frac{1}{q_S q_T} \int_{-\infty}^{\infty} F_z(\mathbf{u}_T, \mathbf{u}_S, \Delta t_{ST}, t) v dt = ... \\ ... =& \frac{1}{q_S q_T} \int_{-\infty}^{\infty} dU_{q_S q_T} = \frac{\Delta U_{q_T q_S}}{q_S q_T}, \end{aligned} \tag{2.56}$$

Furthermore, as for the co-moving wakefield, the loss factor is introduced as the energy lost by the source particle because of its own wakefield ($\Delta U_{q_S q_S}$) normalized with respect to the square of the source particle charge by Eq. 2.16.

2.4.3 Wakepotential and Energy Losses

To define the wakepotential one has to compute the variation of energy induced by the wakefields generated by a charge distribution $Q_S(t)$ on a particle test charge q_T during their transit into a vacuum chamber. To do this let us suppose S to be a charge distribution $Q_S(t) = q_S \lambda_S(t)$, while T remains a particle charge q_T, both moving with speed v on parallel trajectories in opposite directions inside the vacuum chamber. The time charge distribution Q_S can be imagined as the sum of infinitesimal point charges dQ_S each one centered at its entrance time in the vacuum chamber $t_{dQ_S i}$, with width $dt_{dQ_S i}$, refer to Fig. 2.8. The time entrance delay

between the source distribution Q_S and the test charge T can be defined as the time entrance delay between T and a reference point charge dQ_S of the distribution Q_S, as done for the co-moving wakefield case. This reference point charge can be the one in the middle point of the distribution. Thus, indicating with t_{dQ_Sri} the entrance time of the reference point charge, Δt_{Q_ST}, the time entrance delay between Q_S and T, is given again by Eq. 2.24 and the space entrance delay Δs_{Q_ST} by Eq. 2.25. As in the co-moving wakefield case these quantities are usefull to determine the wakepotential.

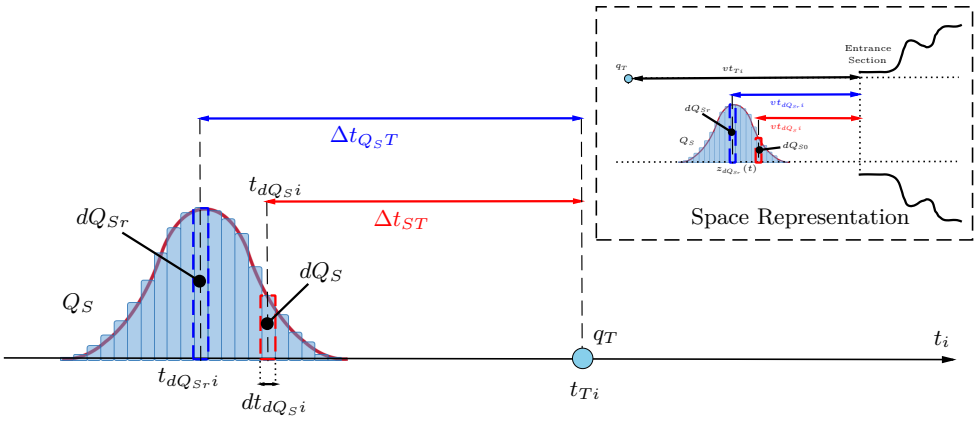

Figure 2.8. Representation of the charge distribution Q_S and of the test charge q_T as a function of their entrance time into the vacuum chamber t_i. In the picture are represented t_{dQ_Si} the entrance time of dQ_S, the generic infinitesimal charge composing the distribution Q_S, t_{dQ_Sri} the entrance time of dQ_{Sr}, the reference infinitesimal charge of the distribution Q_S. The entrance time delay of the test charge q_T with respect with this two charges, Δt_{ST} and Δt_{Q_ST} is also shown. On the top right is shown the space representation of the entrance delay.

The infinitesimal charge $dQ_S(t_{dQ_Si})$ can be expressed as:

$$dQ_S(t_{dQ_Si}) = q_S\lambda_S(t_{dQ_Si})dt_{dQ_Si}. \tag{2.57}$$

The energy change induced on T by one of the dQ_S constituting Q_S is, from the definition of counter-moving wakefunction, Eq. 2.56:

$$\Delta U_{q_TdQ_S} = q_T dQ_S w_z(\mathbf{u}_T, \mathbf{u}_S, \Delta t_{ST}) = q_T q_S \lambda_S(t_{dQ_Si}) w_z(\mathbf{u}_T, \mathbf{u}_S, t_{Ti} - t_{dQ_Si}) dt_{dQ_Si}, \tag{2.58}$$

where Eq. 2.49 was used. To compute $\Delta U_{q_TQ_S}$, the variation of energy induced by the whole charge distribution $Q_S(t)$ on T, one has to sum up the contribution of all the particles dQ_S on t, considering all the different delay Δt_{ST}. Figure 2.8 shows that the Δt_{ST} changes because every dQ_S enters into the vacuum chamber at a different t_{dQ_Si}. Thus, integrating Eq. 2.58 over dt_{dQ_Si} gives $\Delta U_{q_TQ_S}$:

$$\Delta U_{q_TQ_S} = q_T q_S \int_{-\infty}^{\infty} \lambda_S(t_{dQ_Si}) w_z(\mathbf{u}_T, \mathbf{u}_S, t_{Ti} - t_{dQ_Si}) dt_{dQ_Si}. \tag{2.59}$$

The wakepotential is so defined as:

$$W_z(\mathbf{u}_S, \mathbf{u}_T, t_{Ti}) = \frac{\Delta U_{q_T Q_S}}{q_T q_S} = \int_{-\infty}^{\infty} \lambda_S(t_{dQ_S i}) w_z(\mathbf{u}_T, \mathbf{u}_S, t_{Ti} - t_{dQ_S i}) dt_{dQ_S i}. \quad (2.60)$$

One can recognize in Eq. 2.60, that the wakepotential is the convolution between the wakefunction w_z and the time distribution λ_S.

If also the test charge is a distribution $Q_T(t)$, as Q_S, it can be imagined as the sum of infinitesimal point charges dQ_T, each one centered at its entrance time in the vacuum chamber $t_{dQ_T i}$ with width $dt_{dQ_T i}$ and charge:

$$dQ_T(t_{dQ_T i}) = q_T \lambda_T(t_{dQ_T i}) dt_{dQ_T i}. \quad (2.61)$$

From the wakepotential definition, Eq. 2.60, one computes the energy variation of the infinitesimal point charge that constitutes the test distribution as:

$$\begin{aligned} \Delta U_{dQ_T Q_S} &= q_S dQ_T W_z(\mathbf{u}_T, \mathbf{u}_S, t_{dQ_T i}) = ... \\ &... = q_S q_T \lambda_T(t_{dQ_T i}) W_z(\mathbf{u}_T, \mathbf{u}_S, t_{dQ_T i}) dt_{dQ_T i}, \end{aligned} \quad (2.62)$$

summing the energy variation of every dQ_T, i.e. integrating Eq. 2.62 over $dt_{dQ_T i}$, gives $\Delta U_{Q_T Q_S}$ the energy variation of the whole charge distribution Q_T induced by the wakefields generated by Q_S:

$$\Delta U_{Q_T Q_S} = q_S q_T \int_{-\infty}^{\infty} \lambda_T(t_{dQ_T i}) W_z(\mathbf{u}_T, \mathbf{u}_S, t_{dQ_T i}) dt_{dQ_T i}, \quad (2.63)$$

or, in terms of wakefunction

$$\Delta U_{Q_T Q_S} = q_S q_T \int_{-\infty}^{\infty} \lambda_T(t_{dQ_T i}) \int_{-\infty}^{\infty} \lambda_S(t_{dQ_S i}) w_z(\mathbf{u}_T, \mathbf{u}_S, t_{dQ_T i} - t_{dQ_S i}) dt_{dQ_S i} dt_{dQ_T i}. \quad (2.64)$$

In the present and the previous subsections the concept of wakefunction for counter-moving beams was introduced, and it was shown that, considering the definition of the wakefield force $\mathbf{F}$ expressed in time variables, one can obtain an unequivocal wakefunction definition. This definition was used to compute the counter-moving wakepotential, who was found to be the convolution between the counter-moving wakefunction and the beam distribution. The counter-moving wakepotential was used to compute the energy variation of a test bunch passing inside a vacuum chamber excited by the previous passage of a source bunch. Furthermore, it is useful to stress that the formalism developed in the two previous subsection does not apply only to the case of counter-moving wakefield but also to the case of co-moving wakefield. In this sense it can be thought as a generalization of the usual formalism [46].

2.4.4 Transverse counter-moving Wakefunction

As already specified in the introduction of this section, this work especially focuses on the RF-heating problem of two counter-moving beams and so on the longitudinal counter-moving wakefunction. However, using the concepts introduced in the

previous section it is straightforward to obtain also the transverse counter-moving wakefunction and from it the wakepotential. This is shown briefly in this subsection.

Let us recall the case of the two charged particles T and S travelling into the vacuum chamber displayed in Fig. 2.6. The transverse wakefunction $w_{x,y}$ is defined as the integral of the transverse S induced wakefield force $\mathbf{F}_{x,y}$ acting on T (expressed in time variables) along its longitudinal path inside the vacuum chamber, normalized with respect to the product of the S and T charges:

$$\mathbf{w}_{x,y}(\mathbf{u}_T, \mathbf{u}_S, \Delta t_{ST}) = \frac{1}{q_S q_T} \int_{-\infty}^{\infty} \mathbf{F}_{x,y}(\mathbf{u}_T, \mathbf{u}_S, \Delta t_{ST}, t) v dt. \tag{2.65}$$

The transverse wakefunction is a vector of two components $\mathbf{w}_{x,y} = [w_x, w_y]$. It has the same properties of the longitudinal wakefunction since it has the same formal definition. This means that, recalling the expression 2.57 of the source charge distribution Q_S and the definition of Δt_{ST} Eq. 2.49, one can define the transverse wakepotential as:

$$\mathbf{W}_{x,y}(\mathbf{u}_T, \mathbf{u}_S, t_{Ti}) = \int_{-\infty}^{\infty} \lambda_S(z_{dQ_S 0}) \mathbf{w}_{x,y}(\mathbf{u}_S, \mathbf{u}_T, t_{Ti} - t_{dQ_S i}) dt_{dQ_S i}. \tag{2.66}$$

2.5 Examples of Co-moving and Counter-moving Longitudinal Wakepotentials, Theory and Simulations

In this section two examples of co-moving and counter-moving longitudinal wakepotential are given: the wakepotentials of a resisitve wall pipe and the wakepotentials of a pillbox cavity. The general wakefield formalism developed in the previous section is applied, first to obtain again the well know results for the co-moving wakepotential, then to obtain a counter-moving wakepotential.

The wakepotentials are computed semi-analytically starting from the expression of the longitudinal electric field in the studied structures, then they are benchmarked against the results of the CST studio suite commercial software [56], a well tested tool used at CERN [57] and in other research institutions. In the counter-moving wakefield case, this benchmark wants to validate the capabilities of describing the effects of two counter-moving beams in one vacuum chamber both for the proposed formalism and for the CST software. When possible, the semi-analytic approach and the numerical one are compared also with other analytic expressions of the wakepotential available in the literature.

2.5.1 Resistive Wall Pipe

This subsection gives an example of longitudinal wakepotential for the case of a cylindrical pipe made by resistive material. The subsection is organized as followed: first the co-moving wakefunction and wakepotential are computed, subsequently the same is done for the counter-moving wakefunction and wakepotential. Finally, the results are discussed.

The wakefunction (co-moving and counter-moving) is obtained semi-analytically integrating the expression of the longitudinal electric field generated by a point charge travelling inside the resistive pipe. It is subsequently convolved with a Gaussian

bunch distribution to obtain the wakepotential. This wakepotential is benchmarked against the results of the solvers of the CST studio suite commercial software and against other literature results.

The resistive cylindrical pipe problem is extensively discussed by Chao [46], where the longitudinal electric field induced by an ultra-relativistic disk charge traversing an infinitely long pipe is derived as (for the classic thick wall regime):

$$E_z(z_{q_T}(t), z_{q_S}(t)) = -\frac{4q_S}{\pi\epsilon_0 b^2}\left[\frac{1}{3}e^u\cos(\sqrt{3}u) - \frac{\sqrt{2}}{\pi}\int_0^\infty dx\frac{x^2 e^{ux^2}}{x^6+8}\right], \tag{2.67}$$

where, b is the radius of the pipe and

$$u = -\psi\frac{s_{ST}(t)}{b(2\chi)^{\frac{1}{3}}} = -\psi\frac{z_{q_S}(t) - z_{q_T}(t)}{b(2\chi)^{\frac{1}{3}}} \tag{2.68}$$

$$\chi = \frac{c\varepsilon_0}{\sigma b}, \tag{2.69}$$

are two adimentional coefficients. In Eq. 2.68, s_{ST} is the distance between S and T, $z_{q_S}(t)$ is the position of the source particle and $z_{q_T}(t)$ is the position of the test particle at the time t, while σ in Eq. 2.69 is the conductivity of the pipe material and ε_0 is the dielectric vacuum constant. The term ψ is not present in the work of Chao [46], it is needed to extend the validity of Eq. 2.67 also to the counter-moving case. Its value is 1 for the direct case scenario, while is -1 in the counter-moving case scenario[4]. Furthermore, this work defines u with a minus sign with respect to the Chao work [46] because of the different definition of distance between S and T in the two works.

Finally, equations 2.67, 2.68 and 2.69 are expressed in the international unit system SI, while in the work of Chao [46] they are expressed in the CGS unit system. Equation 2.67 holds for an infinitely long pipe, however, one can consider a pipe with finite length as a segment of this infinitely long pipe and compute the wakefunction on that part of the pipe. Using this approach, one has to be particularly careful on what happens at the boundaries, i.e. at the entrance and at the exit of the pipe. This problem is discussed later on in this section. Figure 2.9 helps understanding how the wakefunction is computed showing the time evolution of the electric field on the axis of a resistive pipe and some test charge example trajectories.

Co-moving Wakefield

The geometry of the problem is drawn in Fig. 2.10 top. The source and the test particles are moving at the speed of light along the beam pipe axis in the same direction. If $t = 0$ is chosen as the time at which the source particle enters into the interested pipe region, one can rewrite the equation of motion of the two particles, Eq. 2.4 and Eq. 2.5, as:

$$z_{q_S}(t) = vt \tag{2.70}$$

$$z_{q_T}(t) = vt - \Delta s_{ST}. \tag{2.71}$$

[4]This term represents mathematically the condition that, if the particles are ultra relativistic, the test can feel the electromagnetic field only when is downstream of the source (downstream is defined with respect to the direction of motion of the source).

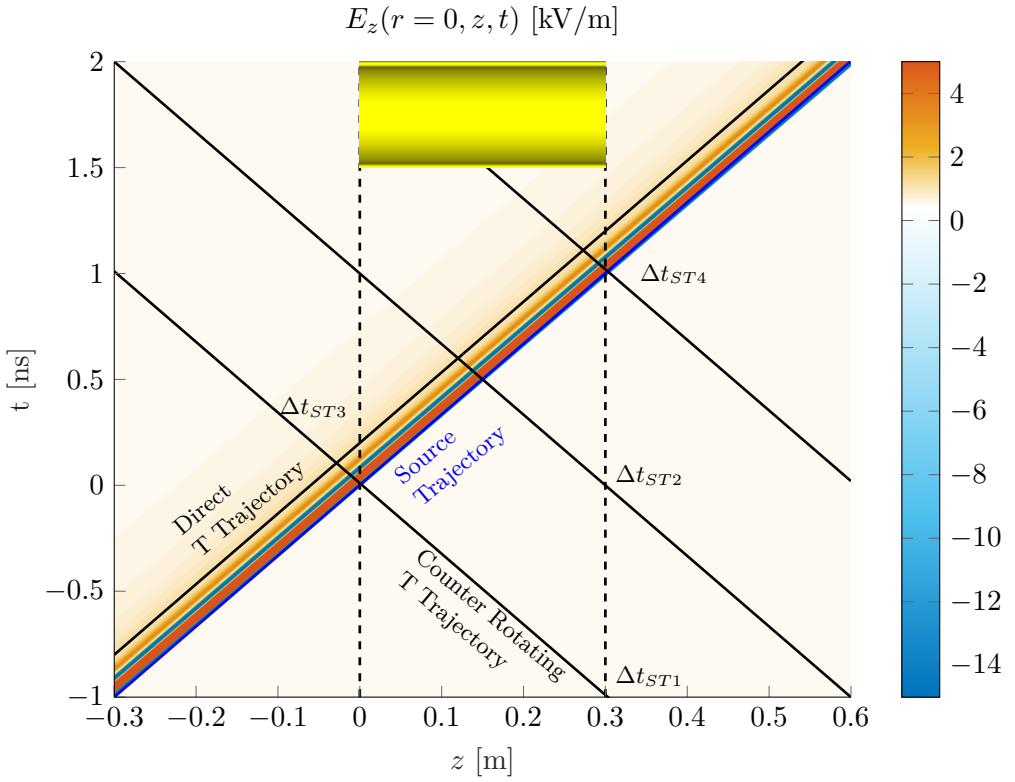

Figure 2.9. Colormap of the time evolution of the longitudinal electric field on the axis of an indefinitely long pipe with resistive wall, excited by a source relativistic charge disc ($q_T = 1$ nC). In the picture the considered pipe segment is highlighted (length $L = 0.3$ m, between $z = 0$ and $z = 0.3$ m and radius $b = 0.05$ m). The trajectory of the source charge is highlighted in blue. Note that the electric field is null before the source passage in every point of the pipe. The trajectories of some example test charges are represented in black with their time entrance delay Δt_{STn}, highlighted. Since the source enters into the pipe at $t = 0$ ns, the time entrance delay can be read on the y axis as the time at which the particles enter into the pipe segment. The trajectory of the sample particles always evolves in the sense of the growing time, thus, the counter-moving particles trajectories have a negative gradient while the direct particle trajectories have a positive one. By computing the electric field experienced by the test particles for each z coordinate in the pipe and integrating it, one can evaluate the wakefunction for an entrance delay value Δt_{ST}. Repeating this operation for different entrance delays gives the whole wakefunction, both the co-moving and the counter-moving ones. From the figure, the first test particle that sees the source is the one with z coordinate 0 at the time at which the source is entering $t = 0$, the space entrance delay of this particle is $\Delta s_{ST} = -L$ and its time entrance delay $\Delta t_{ST} = -L/v$. While the last test particle that sees the source charge is the one with z coordinate L at the exit time of the source, the space entrance delay of this particle is $\Delta s_{ST} = L$ and its time entrance delay $\Delta t_{ST} = L/v$. In Fig. 2.15 the electric field experienced by the sample particles for which the trajectory is drawn in this figure are shown.

Substituting Eq.s 2.70 and 2.71 into Eq. 2.68 (with $\psi = 1$, co-moving wakefield case) one obtains:

$$u = -\frac{s_{ST}}{b(2\chi)^{\frac{1}{3}}} = -\frac{\Delta s_{ST}}{b(2\chi)^{\frac{1}{3}}}, \tag{2.72}$$

Equation 2.72 shows that, as expected (refer to section 2.3.1), in the co-moving wakefield scenario the concept of space entrance delay and distance between the particles are interchangeable. Finally, considering the definition of space entrance delay Eq. 2.50, Eq. 2.72 can be also rewritten as:

$$u = -\frac{v\Delta t_{ST}}{b(2\chi)^{\frac{1}{3}}} = -\frac{v(t_{Ti} - t_{Si})}{b(2\chi)^{\frac{1}{3}}}. \tag{2.73}$$

A plot of the normalized longitudinal wakefield of a source charge in a resistive pipe, Eq. 2.67, as a function of the space entrance delay (or the distance) between S and T is reported in Fig. 2.10, bottom. Since the source particle is moving at the speed of light, there is no electric field in front of it, i.e. $E_z = 0$ for $z_{q_T} > z_{q_S}(t)$ (or $\Delta s_{ST} < 0$). The normalized wakefield has a global negative minimum at null delay from the generating particle. The field increases with delay from the generating particle up to a global positive maximum. With further entrance delay from the generating particle, the wakefield approaches to zero with one small oscillation. Thus, a charged particle travelling in the same direction and at the same speed as the trailing charge, entering immediately after the source charge, loses energy because of the negative electric field, while a charged particle with a slightly higher delay gains energy thanks to a positive longitudinal electric field. Note also that, from Eq. 2.72, in the co-moving wakefield scenarios, the longitudinal electric field experienced by the particle T depends only on the entrance relative distance between T and S, and not on their time dependent positions $z_{q_S}(t)$ and $z_{q_T}(t)$. This is true because the longitudinal electric field pattern moves integrally with the source charge. Thus, a test particle following the source charge at the same speed on a parallel trajectory experiences a constant electric field, refer to Fig. 2.15 top. Applying the definition of wakefunction, Eq. 2.53, for a resistive pipe of length L one obtains:

$$w_z(\Delta t_{ST}) = \frac{L}{q_S} E_z(\Delta t_{ST}) = -\frac{4L}{\pi\epsilon_0 b^2}\left[\frac{1}{3}e^u \cos(\sqrt{3}u) - \frac{\sqrt{2}}{\pi}\int_0^\infty dx \frac{x^2 e^{ux^2}}{x^6+8}\right]. \tag{2.74}$$

Equation 2.74 can be expressed interchangeably as a function of s_{ST}, Δs_{ST} or Δt_{ST} choosing the different expression of u, Eq. 2.72 or 2.73.

Equation 2.74 has been numerically evaluated for a pipe with $L = 0.3$ m, $b = 0.05$ m and $\sigma = 3.5 \cdot 10^3$ [S/m][5]. Subsequently, to obtain the wakepotential as defined in Eq. 2.60, the wakefunction of Eq. 2.74 was numerically convolved with a beam distribution λ_S. To perform this operation it is necessary to recall the link between time and space entrance delay, Eq. 2.50:

$$W_z(t_{Ti}) = \int_{-\infty}^{\infty} \lambda_S(t_{dQ_Si}) w_z(\Delta t_{ST}) dt_{dQ_Si} = \int_{-\infty}^{\infty} \lambda_S(t_{dQ_Si}) w_z(t_{Ti} - t_{dQ_Si}) dt_{dQ_Si} \tag{2.75}$$

[5] This value of the conductivity was chosen to simplify the comparison between the results of the semi-analytic and the numerical approach. The low value of the conductivity drastically reduces the effect of the numerical integration noise on the results obtained by simulations.

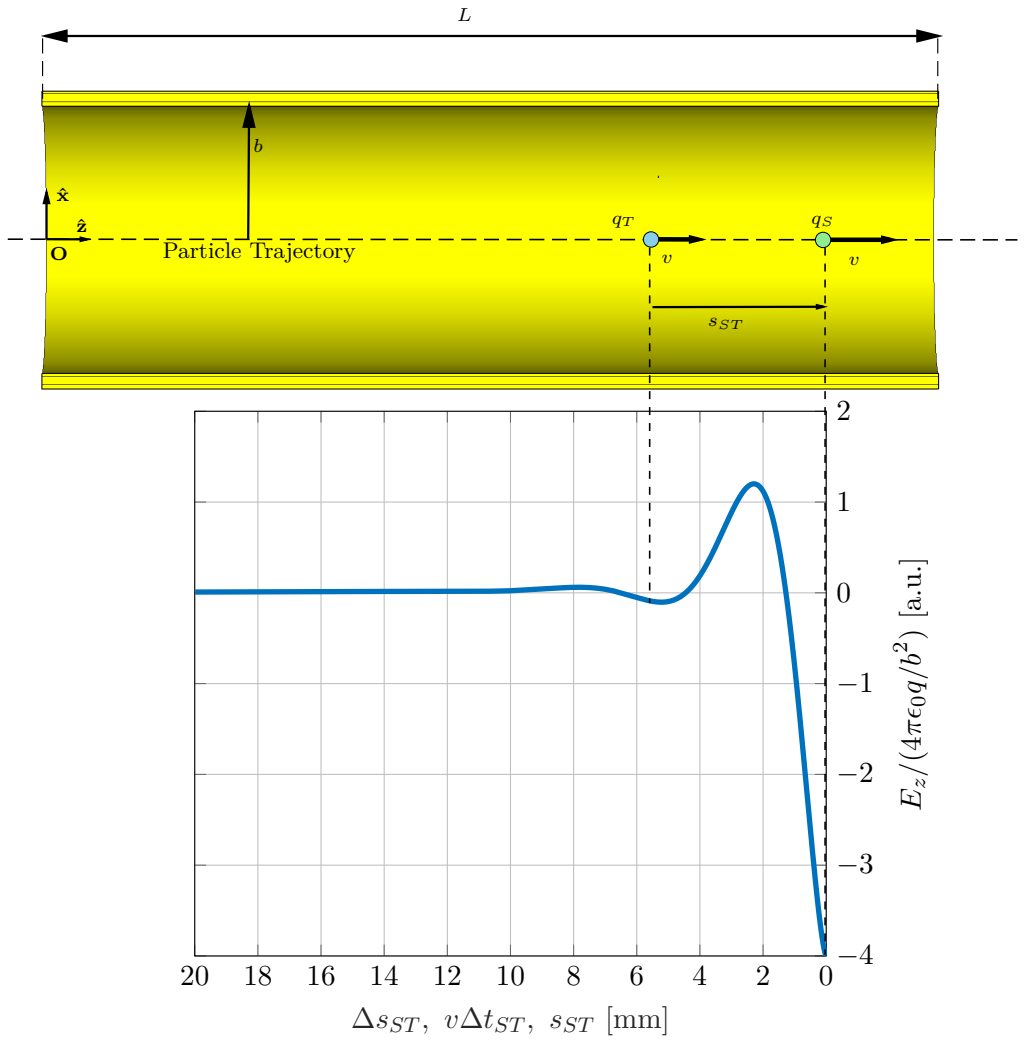

Figure 2.10. Top: Co-moving Wakefield case, test and source charges traversing the resisitive wall pipe at constant speed v. The trajectory of both charges is coincident with the pipe axis, the length of the pipe is L, its radius b and the distance between the charges is s_{ST}. Bottom: Normalized longitudinal electric field generated by a point charge moving at the center of a resistive pipe, pipe radius $b = 0.05$ [m], electric conductivity $\sigma = 3.5 \cdot 10^3$ [S/m], ($\sigma = 3.2 \cdot 10^{13}$ [s^{-1}] in CGS units). Since the test charge q_T is moving at the same speed of the source charge q_S on a parallel trajectory, the same of q_S in the displayed case, and since the electric field generated by q_S moves rigidly with q_S, the charge q_T experience always the same electric field. In the particular case showed in the cartoon the test particle would lose energy experiencing a negative electric field. The electric field plot is not in scale with respect to the pipe image.

The beam distribution λ_S was chosen composed by one bunch with a Gaussian shape since this is the default excitation signal for CST and it makes the benchmark between the semi-analytic and numerical results easier. Furthermore, Bane [58, 59] provided the analytical expression of the wakepotential of a Gaussian bunch passing inside a resistive pipe:

$$\begin{aligned} W_z =& \frac{cL}{4\pi b \sigma_b^{\frac{3}{2}}} \sqrt{\frac{Z_0}{\sigma}} |\Delta s_{Q_S T}|^{\frac{3}{4}} e^{-x'} \Big[I_{\frac{1}{4}}(x') - I_{-\frac{3}{4}}(x') - \mathrm{sgn}(\Delta s_{Q_S T}) I_{\frac{3}{4}}(x') + ... \\ & ... + \mathrm{sgn}(\Delta s_{Q_S T}) I_{-\frac{1}{4}}(x') \Big], \end{aligned} \tag{2.76}$$

where, I is the modified Bessel function of fractional order, $Z_0 = 376.730\Omega$ is the free space impedance, L is the pipe length, σ_b is the Gaussian root mean square and

$$x' = \frac{{\Delta s_{Q_S T}}^2}{4\sigma_b^2}. \tag{2.77}$$

In Fig. 2.11 the wakepotential obtained from the semi-analytical approach (Chao theory), from CST and from the analytic formula 2.76 are evaluated as a function of the entrance delay between the test charge and the source distribution and compared. The agreement among the numerical (CST) the semi-analytic (derived from the formulae reported in Chao [46]) and the analytical approach (from Bane [58, 59]) is excellent being the maximum relative error less than 5%. This result validates the proposed semi-analytic approach to compute the wakepotential.

Counter-moving wakefield

The counter-moving case geometry is displayed in Fig. 2.12. The source and the test particles are moving at the speed of light along the beam pipe axis in opposite directions. As for the co-moving wakefield case, $t = 0$ is chosen as the time at which the source particle enters into the pipe, thus, one can rewrite the equation of motion of the two particles, Eq. 2.46 and Eq. 2.47 as:

$$z_{q_S}(t) = -vt + L, \tag{2.78}$$

$$z_{q_T}(t) = vt - \Delta s_{ST}. \tag{2.79}$$

Substituting Eq. 2.78 and 2.79 into Eq. 2.68 (with $\psi = -1$, counter-moving case) one obtains:

$$u = \frac{\Delta s_{ST} - 2vt + L}{b(2\chi)^{\frac{1}{3}}}, \tag{2.80}$$

or recalling Eq. 2.50

$$u = \frac{v(\Delta t_{ST} - 2t) + L}{b(2\chi)^{\frac{1}{3}}}. \tag{2.81}$$

Equations 2.80 and 2.81 clearly show that in the counter-moving case the electric field that T experiences does not only depends on the entrance delay (Δs_{ST} or Δt_{ST})

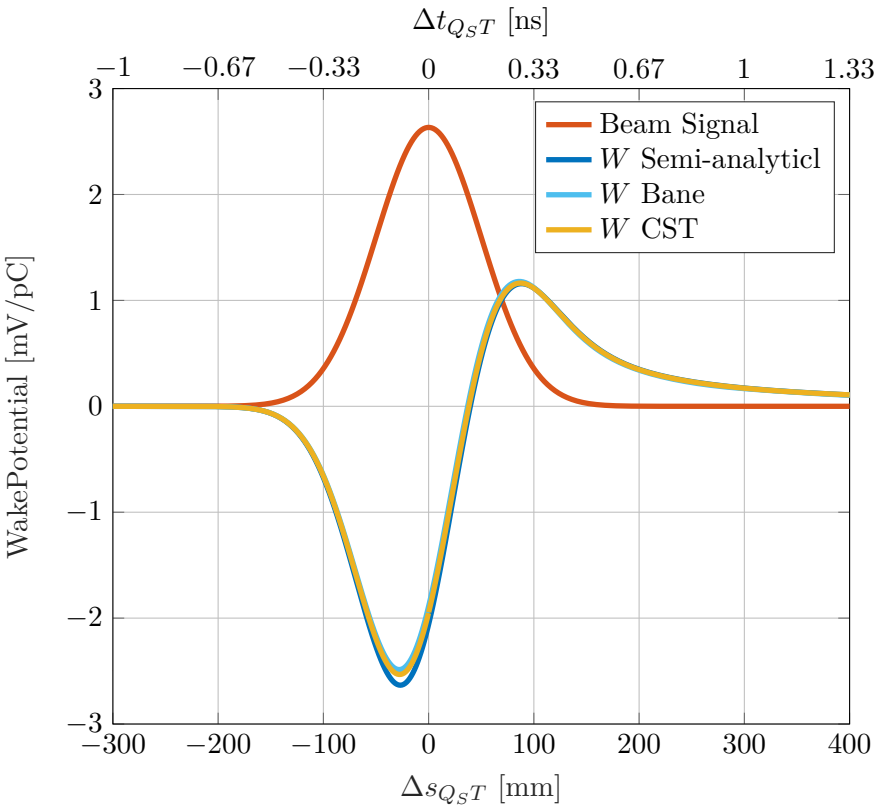

Figure 2.11. wakepotential of a Gaussian bunch profile traversing a beam pipe, comparison between the exposed semi-analytical method, Bane and CST. Pipe's parameters: $b = 0.05$ [m], $\sigma = 3.5 \cdot 10^3 [\Omega^{-1}\mathrm{s}^{-1}]$, $L = 0.3$ [m]. Bunch parameters: $\sigma_b = 0.05$ [m], $v = c$. The beam signal is in arbitrary units for representation purposes.

but also directly on time. The wakefunction in this case can be computed using its definition, Eq. 2.54:

$$w_z(\Delta t_{ST}) = \frac{v}{q_S}\int_{t_{Ti}}^{t_{To}} E_z(\Delta t_{ST}, t)dt = \begin{cases} \frac{v}{q_S}\int_{t_{Ti}}^{t_{To}} E_z(\Delta t_{ST}, t)dt \text{ if } t_{Ti} \geq t_m \\ \frac{v}{q_S}\int_{t_m}^{t_{To}} E_z(\Delta t_{ST}, t)dt \text{ if } t_{Ti} < t_m \end{cases} \tag{2.82}$$

where $E_z(\Delta t_{ST}, t)$ is given by Eq. 2.67 with u defined by Eq. 2.81. The terms on the right of Eq. 2.82 is written to emphasize that, since in this example S and T are both ultrarelativistic, the longitudinal electric field can be integrated from the particle meeting time t_m, defined in Eq. 2.51, up to the test exit time t_{To} if $t_{Ti} < t_m < t_{To}$, i.e. if the two particles meet inside the vacuum chamber. Indeed before the meeting time, because of causality, T cannot experience any wakefield from S, i.e. $E_z(\Delta t_{ST}, t) = 0$ for $t < t_m$. If $t_m \leq t_{Ti}$, thus, the integral must be done from the test entrance time t_{Ti} up to the test exit time t_{To}. The expressions of t_{Ti}, t_{To} and t_m as a function of the entrance delay can be obtained considering the equation of motion of source and test Eq. 2.78 and Eq. 2.79 and the definition of meeting time given by Eq. 2.51:

$$t_m = \frac{L + \Delta s_{ST}}{2v} = \frac{L + v\Delta t_{ST}}{2v}, \tag{2.83}$$

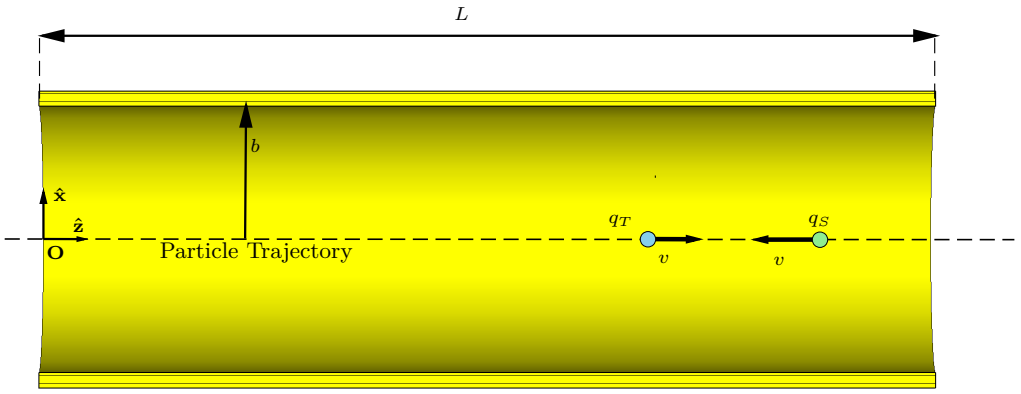

Figure 2.12. counter-moving particle travelling into a resistive pipe.

$$t_{Ti} = \frac{\Delta s_{ST}}{v} = \Delta t_{ST}, \tag{2.84}$$

and

$$t_{To} = \frac{L + \Delta s_{ST}}{v} = \frac{L + v\Delta t_{ST}}{v}. \tag{2.85}$$

Taking into account Eq.s 2.83, 2.84 and 2.85, equation 2.82 was evaluated numerically for a pipe with $L = 0.3$ m, $b = 0.05$ m and $\sigma = 3.5 \cdot 10^3$ [S/m]. The counter-moving wakefunction as a function of the entrance delay is reported in Fig. 2.13. The wakefunction has two sharp peaks, a positive and a negative one. The positive peak is at an entrance delay of -1 ns or -300 mm, that is the length of the pipe. After the positive peak the wakefunction decreases rapidly, remaining positive, until an entrance delay value of 1 ns or 300 mm. At this value there is the negative sharp peak. After it, increasing the entrance delay, the wakefunction approaches to zero. A discussion on this shape is given in later in this subsection.

To compute the counter-moving wakepotential from the wakefunction, the same equation used for the direct case, Eq. 2.75, can be used. Also Eq. 2.75 was evaluated numerically.

Further, two relativistic counter-moving beams, made by one Gaussian bunch ($\sigma_b = 50$ mm) each, traversing a beam pipe, were simulated using the commercial solver Wakefield [60] of the CST software package. The charge of one beam, from now on test beam, was set six order of magnitude lower with respect to the charge of the other beam, the source beam. In this way one can reasonably assume that the electromagnetic field in the pipe was given all by the source beam and the contribution of the test beam was negligible. Thus, the integration line of the test beam experienced only the electric field of the source beam, and test and source beam were moving in opposite directions. Thus, the wakepotential experienced by the test beam was the counter-moving wakepotential generated by the source beam.

The counter-moving wakepotentials as a function of the entrance delay between Q_S and T ($\Delta s_{Q_S T}$ and $\Delta t_{Q_S T}$) obtained from the semi-analytic method and from the CST wakefield solver are reported and compared in Fig. 2.14. The agreement among the numerical (CST) and the semi-analytic approach is excellent being the maximum relative error less than 5%.

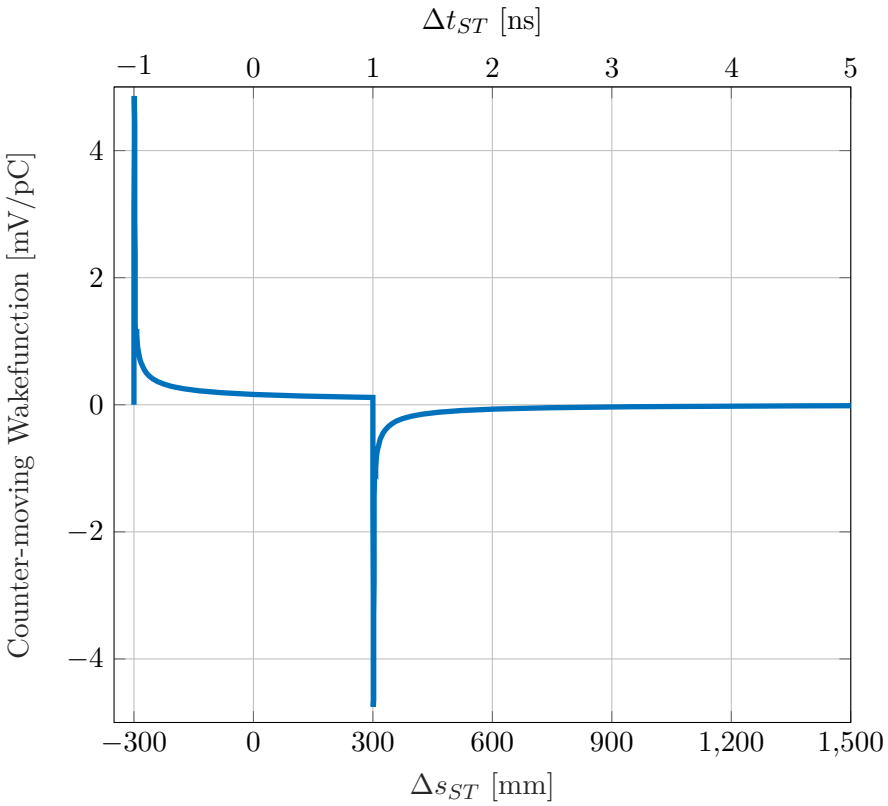

Figure 2.13. Semi-analytic counter-moving wakefunction of a point charge traversing a beam pipe. Pipe's parameters: $b = 0.05$ m, $\sigma = 3.5 \cdot 10^3\ \Omega^{-1}\mathrm{s}^{-1}$, $L = 0.3$ m. Bunch parameters: $\sigma_b = 0.05$ m, $v = c$.

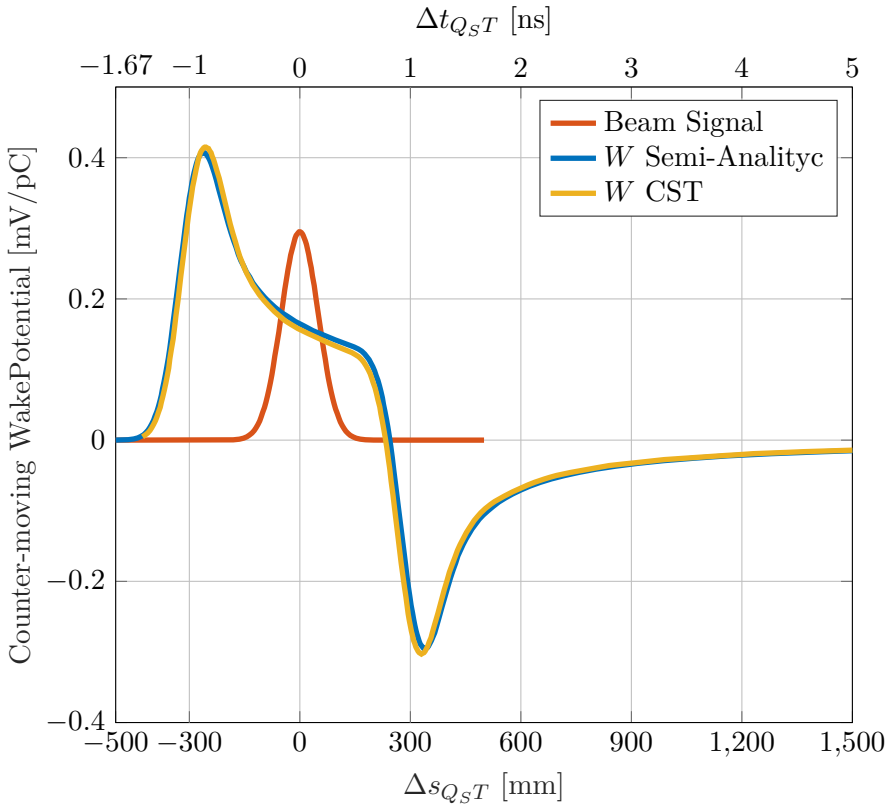

Figure 2.14. Counter-moving wakepotential of a Gaussian bunch profile traversing a beam pipe, comparison between semi-analytical method and CST Wakefield solver. Pipe's parameters: $b = 0.05$ m, $\sigma = 3.5 \cdot 10^3\ \Omega^{-1}\text{s}^{-1}$, $L = 0.3$ m. Bunch parameters: $\sigma_b = 0.05$ m, $v = c$. The beam signal is in arbitrary units for rapresentation purposes.

Discussion on the Results

Previously, the shape of the resistive pipe counter-moving wakefunction, reported in Fig. 2.13, has been described. Remarkably, the wakefunction is characterized by two peaks, one positive and one negative, symmetrically disposed with respect to the axis origin with space entrance delay equal to the length of the pipe (other CST simulations, not shown in this thesis, were performed confirming such a result for different pipe lengths). These peaks are due to the fact that Eq. 2.67, that holds for an indefinitely long pipe, has been used to compute the wakefunction of a finite length pipe, considered as a segment of this infinitely long pipe. In the wakefunction definition 2.54, it is assumed that outside the structure the electric fields are neglected. Indeed, by integrating the electric field experienced by the particle T, E_z, from the test entrance time t_{Ti} up to test exit time t_{To}, i.e. from $z_{q_T} = L$ up to $z_{q_T} = 0$ (counter-moving particles), one cuts the electric field before $z_{q_T} = L$ and after $z_{q_T} = 0$. Figure 2.15 gives a visual explanation of this concept. This cut is also performed by the CST software when a pipe of length L is simulated. Indeed the software is able to compute only the fields inside the structure and it assumes null the field outside. This explains the agreement in the counter-moving wakepotentials shown in Fig. 2.14.

2.5.2 Pillbox Cavity

This subsection gives another example of longitudinal wakepotential for the case of a lossless pillbox cavity. The wakefunction is obtained semi-analytically integrating the expression of the longitudinal electric field generated by a short burst disk of electrons emitted from one side of the cavity that travels towards the other side at a speed v_S, refer to Fig. 2.17 or 2.19. The wakefunction is subsequently convolved with a Gaussian bunch distribution to obtain the wakepotential. This wakepotential is benchmarked against the results of the PIC solver [60] of the CST studio suite commercial software.

The analytic expression of transient longitudinal electric field generated by a disc of electrons moving from one side of a pillbox cavity of radius a and length L, and that travels towards the other side at a speed $v_S = \beta_S c$, was found by Faust [61] as:

$$
\begin{aligned}
E'_z(r'_{q_T}, z'_{q_T}, t) = &-\frac{eN}{\epsilon_0}\Bigg\{\frac{\beta_S}{L}\left[ctU(ct) - \left(ct - \frac{L}{\beta_S}\right)U\left(ct - \frac{L}{\beta_S}\right)\right] - U\left(ct - \frac{z'_{q_T}}{\beta_S}\right) - \dots \\
&- \frac{2a\beta_S}{L}\sum_{m=1}^{m=\infty}\frac{J_0(r'_{q_T}\rho_m/a)}{J_1(\rho_m)\rho_m^2}\left[\sin\left(\rho_m\frac{ct}{a}\right) - \sin\left(\rho_m\frac{ct - L/\beta_S}{a}\right)U\left(ct - \frac{L}{\beta_S}\right)\right] - \dots \\
&- \frac{4a\beta_S}{L}\sum_{m=1}^{m=\infty}\sum_{n=1}^{n=\infty}\frac{J_0(r'_{q_T}\rho_m/a)}{J_1(\rho_m)}\rho_m\frac{\sin(\gamma_1 ct/a) - (-1)^n\sin(\gamma_1\frac{ct-L/\beta_S}{a})U\left(ct - \frac{L}{\beta_S}\right)}{\gamma_1\gamma_2^2}\cos\left(\frac{n\pi z'_{q_T}}{L}\right) + \dots \\
&+ \frac{2}{\pi}\sum_{n=1}^{n=\infty}\frac{I_0(r'_{q_T}n\pi\gamma_S/L)}{nI_0(an\pi\gamma_S/L)}\left[\sin\left(n\pi\beta_S\frac{ct}{L}\right) - (-1)^n\sin\left(n\pi\beta_S\frac{ct - L/\beta_S}{L}\right)U\left(ct - \frac{L}{\beta_S}\right)\right]\cos\left(\frac{n\pi z'_{q_T}}{L}\right)\Bigg\},
\end{aligned}
\tag{2.86}
$$

where, N is the number of electrons per square meter, $J_0(x)$ is the Bessel function of order zero, ρ_m are the roots of the Bessel function J_0, $I_0(x)$ is the modified Bessel function of order zero, $U(t)$ is the unit function, $\gamma_S = 1 - \beta_S^2$, $\gamma_1^2 = \rho_m^2 + (n\pi a/L)^2$ and $\gamma_2^2 = \rho_m^2 + (n\pi a)^2(1 - \beta_S^2)/L^2$. Furthermore, $r_{q_T}(t)'$ and $z_{q_T}(t)'$ are the generic

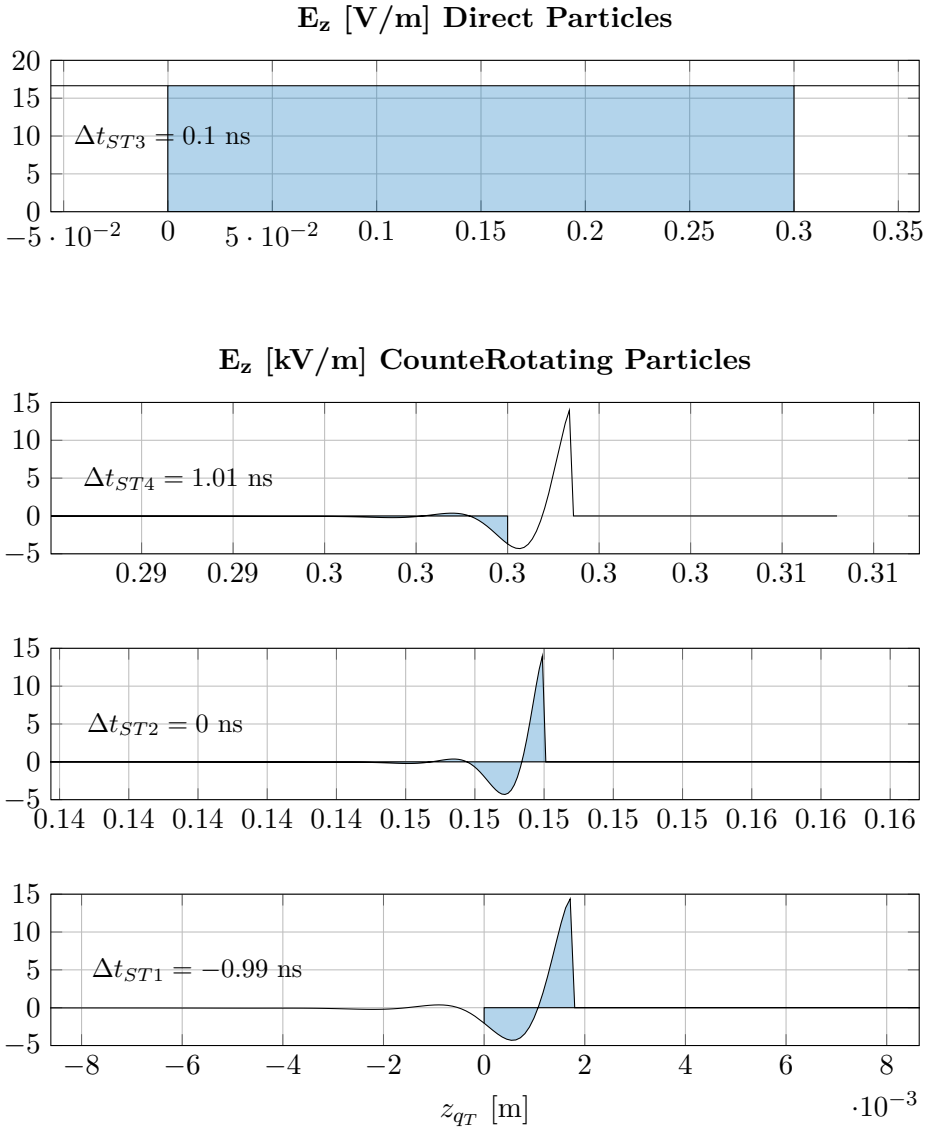

Figure 2.15. The electric field experienced by the example test particles shown in Fig. 2.9, as a function of the position of the test particle in the vacuum chamber. The value of the wakefunction associated to the entrance delay Δt_{STn} is proportional to the highlighted blue areas. As shown, the counter-moving test particle is experiencing wakefields also outside the pipe that is cut by the definition of wakefunction. The cut fields has been reported as the simple black solid line.

radial and longitudinal position of a test particle T in a reference frame $\mathbf{O}'$ with origin in the electron emission face and $\hat{\mathbf{z}}'$ axis oriented in the direction of motion of the electrons. The electric field E'_z given by Eq. 2.86 is also expressed in the $\mathbf{O}'$ reference frame. Finally, t is the generic time. Please note that Eq. 2.86 makes sense only if $t \geq 0$, with if $t = 0$ the time at which the electron disk leaves the emitting face [61]. As done for the resistive pipe, considering the expression of the electric field in the device as a function of time, it is possible to compute both co-moving and counter-moving wakefunction. A visual representation of how the wakefunction is computed is given in Fig. 2.16.

Co-moving Wakefield

The geometry of the problem is drawn in Fig. 2.17. In the co-moving wakefield case the reference frame in which the wakefunction is defined, $\mathbf{O}$, and the one in which the electric field of the electron burst is given, $\mathbf{O}'$, are coincident, thus:

$$\begin{aligned} r'_{q_T} &= r_{q_T} \\ z'_{q_T} &= z_{q_T} \\ E'_z &= E_z \end{aligned} \tag{2.87}$$

where $r_{q_T}(t)$, $z_{q_T}(t)$ are the transverse and the longitudinal positions of the test particle expressed in the $\mathbf{O}$ reference frame and E_z is the electric field acting on the test particle expressed in the $\mathbf{O}$ frame.

As said previously, $t = 0$ is chosen as the time at which the electron burst leaves the emitting face. Recalling the rigid beam hypotesis, the equation of motion of T is:

$$\begin{aligned} r_{q_T}(t) &= k, \\ z_{q_T}(t) &= vt - \Delta s_{ST} = vt - v\Delta t_{ST}, \end{aligned} \tag{2.88}$$

where, $v = v_S = v_T$ because of the rigid beam approximation, k is a constant and Δs_{ST} or Δt_{ST} are the space and time entrance delay. Substituting the T trajectory laws, Eq.s 2.88, into the longitudinal electric field, Eq. 2.86, and recalling Eq.s 2.87, one gets:

$$\begin{aligned} E_z(\Delta t_{ST}, t) = &-\frac{eN}{\epsilon_0}\Bigg\{\frac{\beta_S}{L}\left[ctU(ct) - \left(ct - \frac{L}{\beta_S}\right)U\left(ct - \frac{L}{\beta_S}\right)\right] - U\left(ct - \frac{vt - v\Delta t_{ST}}{\beta_S}\right) - \dots \\ &- \frac{2a\beta_S}{L}\sum_{m=1}^{m=\infty}\frac{J_0(k\rho_m/a)}{J_1(\rho_m)\rho_m^2}\left[\sin\left(\rho_m\frac{ct}{a}\right) - \sin\left(\rho_m\frac{ct - L/\beta_S}{a}\right)U\left(ct - \frac{L}{\beta_S}\right)\right] - \dots \\ &- \frac{4a\beta_S}{L}\sum_{m=1}^{m=\infty}\sum_{n=1}^{n=\infty}\frac{J_0(k\rho_m/a)}{J_1(\rho_m)}\rho_m\frac{\sin(\gamma_1 ct/a) - (-1)^n\sin(\gamma_1\frac{ct-L/\beta_S}{a})U\left(ct - \frac{L}{\beta_S}\right)}{\gamma_1\gamma_2^2}\cos\left(\frac{n\pi(vt - v\Delta t_{ST})}{L}\right) + \dots \\ &+ \frac{2}{\pi}\sum_{n=1}^{n=\infty}\frac{I_0(kn\pi\gamma_S/L)}{nI_0(an\pi\gamma_S/L)}\left[\sin\left(n\pi\beta_S\frac{ct}{L}\right) - (-1)^n\sin\left(n\pi\beta_S\frac{ct - L/\beta_S}{L}\right)U\left(ct - \frac{L}{\beta_S}\right)\right]\cos\left(\frac{n\pi(vt - v\Delta t_{ST})}{L}\right)\Bigg\}. \end{aligned} \tag{2.89}$$

Equation 2.89 can be used to compute the wakefunction. Recalling the wakefunction definition in time variables, Eq. 2.54, one has to integrate the longitudinal

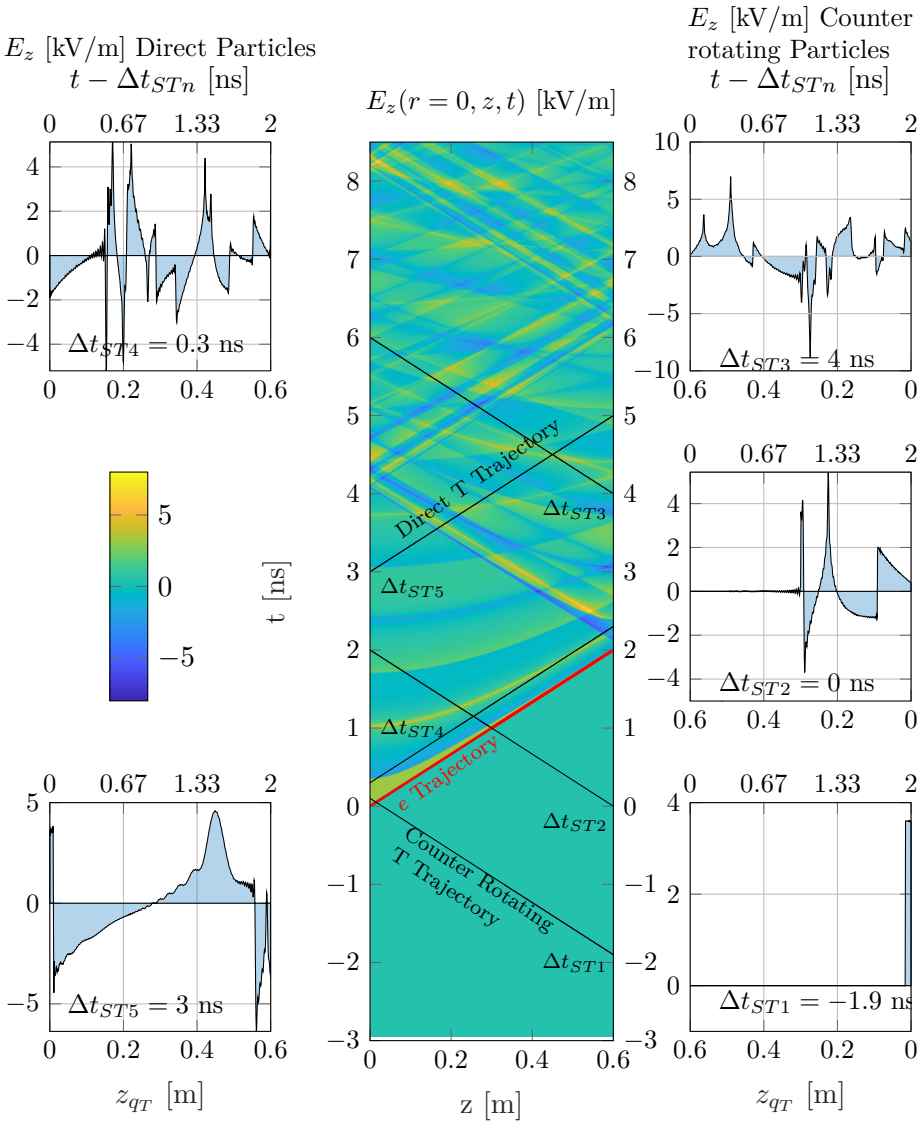

Figure 2.16. Center: Colormap of the time evolution of the longitudinal electric field on the axis of one pillbox cavity (length $L = 0.6$ m and radius $a = 0.1$ m) excited by the a relativistic electron burst emitted from the face at $z = 0$ ($N = 1.9867 \cdot 10^{11}$ electrons/m^2) obtained with the Faust theory [61]. In the picture, the trajectory of the electron burst is highlighted in red. Note that the electric field is null before the electron burst passage in every point of the cavity axis. The trajectories of some example test charges are highlighted in black with their time entrance delay. Right and Left: the electric field experienced by the example test particles (on the right the counter-moving particles on the left the direct ones), as a function of time or the position of the test particle in the vacuum chamber, is reported. The value of the wakefunction associated to the entrance delay Δt_{STn} is proportional to the highlighted areas.

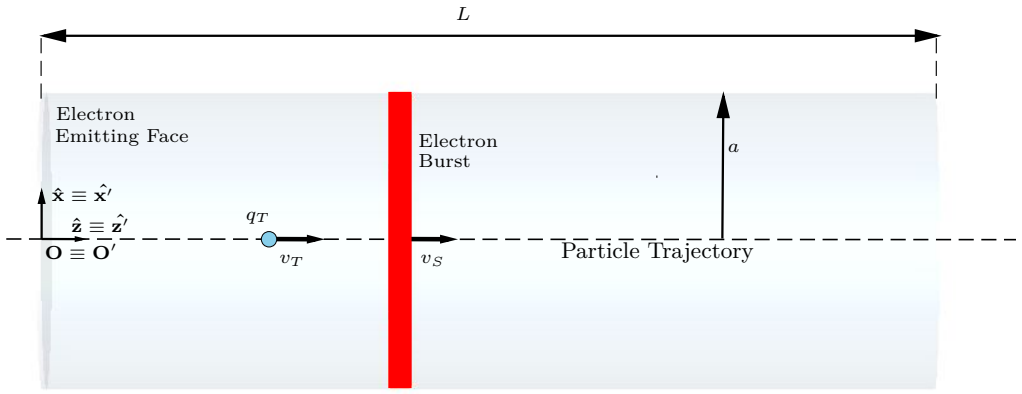

Figure 2.17. Pillbox cavity of length L excited by an electron burst emitted from one of the circular faces, direct case scenario. Please note that in this case the reference frame in which the wakefunction is desired **O** and the reference frame in which Eq. 2.89 gives the electric field are coincident.

electric field $E_z(\Delta t_{ST}, t)$, Eq. 2.89, in time from t_{Ti}, entrance time of the test charge, to t_{To} exit time of the test charge:

$$w_z(\Delta t_{ST}) = \frac{v}{q_S} \int_{t_{Ti}}^{t_{To}} E_z(\Delta t_{ST}, t) dt \tag{2.90}$$

Since $t = 0$ has been chosen as the time at which the source electron burst is emitted from the cavity surface, Δt_{ST} represents also the time at which T enters into the pillbox cavity, thus:

$$t_{Ti} = \Delta t_{ST}, \tag{2.91}$$

while the exit time is the entrance time in the cavity plus the time that T takes to transit into the cavity:

$$t_{To} = t_{Ti} + \frac{L}{v}. \tag{2.92}$$

It is useful to recall that Eq.s 2.89 - 2.92 can be rewritten as a function of the space entrance delay Δs_{ST} simply referring to Eq. 2.50 that links time and space entrance delays.

The wakefunction of Eq. 2.90 was numerically evaluated for the case in which both the electrons and the test particle are ultra-relativistic, i.e. $\beta_S = 1$ and $v = c$. To obtain the wakepotential, the wakefunction Eq. 2.90 was numerically convolved with a beam distribution λ_S. The beam was chosen composed by one bunch with a Gaussian distribution since this is the default excitation signal for CST and it makes the benchmark between the semi-analytic and numerical results easier.

Using the Particle in Cell (PIC) solver of CST, the excitation of a loss free pillbox (length $L = 0.6$ m and radius $a = 0.1$ m) by a burst of electrons emitted by one of the circular face was simulated. The cavity material was set to be perfect electric

conductor (PEC), so that the cavity was loss free. The electrons were emitted uniformly from the face with a Gaussian longitudinal distribution ($\sigma_b = 0.07$ m). One bunch of electrons with a total charge of 1 nC ($1.1 \cdot 10^{21}$ electrons) was emitted. The kinetic energy of the electrons was set to an ultra-relativistic value ($\gamma = 5 \cdot 10^{10}$) to avoid space charge effects. The total simulation time was set to 20 ns, electric field monitors were set to register and store the value of the longitudinal electric field every 1.5 mm along the whole cavity axis, that is every $5 \cdot 10^{-3}$ ns. The position of the test particle T is known at every time t as a function of the entrance delay, Eq. 2.88, i.e. fixing an entrance delay Δs_{ST} or Δt_{ST}, one knows the T longitudinal position z_{q_T} at the time t. If z_{q_T} at the time t is known, one can obtain the value of the longitudinal electric field acting on T at the time t from the fields monitors. If this operation is repeated for every t one obtains the longitudinal electric field experienced by T traversing the cavity as a function of time (or equivalently as a function of its longitudinal position). Integrating this longitudinal electric field one has the wakepotential value for the set entrance delay, repeating the integration for different entrance delays gives the whole wakepotential.

The co-moving wakepotentials as a function of the entrance delay between Q_S and T ($\Delta s_{Q_S T}$ and $\Delta t_{Q_S T}$) obtained from the semi-analytic method and from the CST PIC solver are reported and compared in Fig. 2.18. The agreement between the two methods is really good in general. However, there is a region around null entrance delay in which there are discrepancies between the two wakepotentials of around 15%. This discrepancy is unexplained. As it will be shown in the next subsection, in the counter-moving case such a discrepancy does not appear and the same methodology is applied to compute the wakepotentials. This suggests that it may be due to numerical issues in the semi-analytic method during the integration of the longitudinal electric field to obtain the wakefunction or during the wakefunction convolution with the beam distribution.

Counter-moving Wakefield

The geometry of the problem is drawn in Fig. 2.19. In the counter-moving wakefield case the reference frame in which the wakefunction is defined, $\mathbf{O}$, is not the same one in which the longitudinal electric field of the electron disk is given $\mathbf{O'}$ by Eq. 2.86. Indeed $\mathbf{O}$ has its origin in the test entrance section and its $\mathbf{z'}$ axis points in the direction of motion of T while $\mathbf{O'}$ has its origin in the source entrance section and its $\hat{\mathbf{z}}'$ axis points in the direction of motion of the electron burst, that is opposite to the one in which T is moving in the counter-moving case, refer to Fig. 2.19. The quantities in $\mathbf{O'}$ are linked to the quantities in the $\mathbf{O}$ by the following equations:

$$\begin{aligned} r'_{q_T} &= r_{q_T} \\ z'_{q_T} &= L - z_{q_T} \\ E'_z &= -E_z. \end{aligned} \tag{2.93}$$

Considering Eq.s 2.93, the first two equations can be intuitively derived looking at Fig. 2.19, where both reference frame $\mathbf{O}$ and $\mathbf{O'}$ are represented. The third relation is true because the z axes of the two frames point in opposite directions. Thus, if E_z is positive in one of the frames, $\mathbf{O'}$ for example, i.e. E_z is directed as $\hat{\mathbf{z}}'$, it is naturally negative in the other, $\mathbf{O}$, i.e. E_z is directed against $\hat{\mathbf{z}}$.

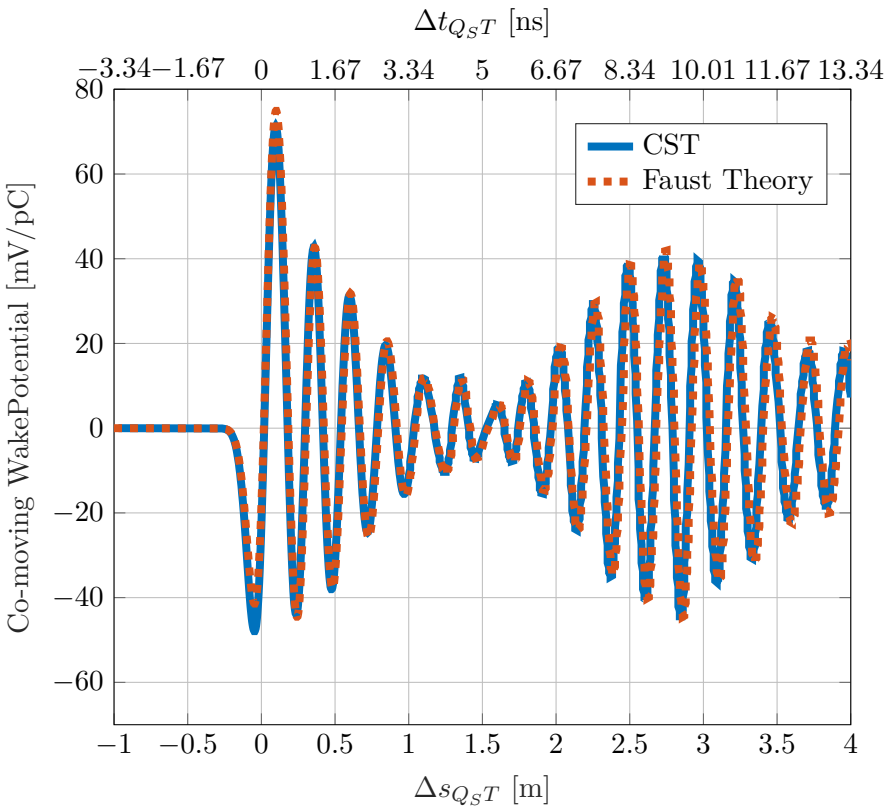

Figure 2.18. Comparison between the co-moving wakepotentials of a burst of ultra-relativistic electrons (1 nC or $1.1 \cdot 10^{21}$ electrons and $\beta_S \to 1$ or $\gamma_S = 5 \cdot 10^{10}$) traversing a pillbox cavity (length $L = 0.6$ m and radius $a = 0.1$ m) computed by the semi-analytic method (Faust Theory [61]) and the CST PIC solver [60]. The electrons are emitted uniformly from one of the circular faces of the cavity. They are longitudinally distributed as a Gaussian bunch ($\sigma_b = 0.07$ m). The cavity material is perfect electric conductor (PEC), loss free. Test particle speed is $v = c$.

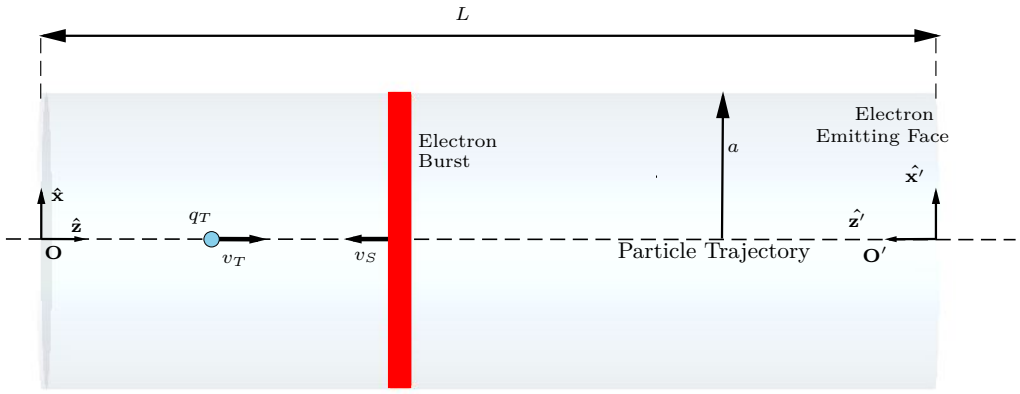

Figure 2.19. Pillbox cavity excited by an electron burst emitted from one of the circular faces, counter-moving case scenario. Note that in this case the reference frame in which the wakefunction is wanted, **O**, and the reference frame in which Eq. 2.89 gives the electric field, **O′**, are not coincident.

As said previously, $t = 0$ is chosen as the time at which the electron disk leaves the emitting face, thus, the Eq.s 2.88 holds as equations of motion of T. Substituing Eq.s 2.88 into Eq.s 2.93 one has:

$$\begin{aligned} r'_{q_T} &= k \\ z'_{q_T} &= L - vt + \Delta s_{ST} = L - vt + v\Delta t_{ST} \\ E'_z &= -E_z, \end{aligned} \tag{2.94}$$

where, $v = v_S = v_T$ was used.

As will be clear in the following, it is more convenient to compute the wakefunction in the **O** frame. Thus, using Eq.s 2.94 into the expression of the longitudinal electric field 2.86, the electric field can be rewritten in the wanted frame (**O**) as a function of time and entrance delay:

$$\begin{aligned} E_z(\Delta t_{ST}, t) = \frac{eN}{\epsilon_0}\Bigg\{ & \frac{\beta_S}{L}\left[ctU(ct) - \left(ct - \frac{L}{\beta_S}\right)U\left(ct - \frac{L}{\beta_S}\right)\right] - U\left(ct - \frac{(L - vt - v\Delta t_{ST})}{\beta_S}\right) - \dots \\ & - \frac{2a\beta_S}{L}\sum_{m=1}^{m=\infty}\frac{J_0(k\rho_m/a)}{J_1(\rho_m)\rho_m^2}\left[\sin\left(\rho_m\frac{ct}{a}\right) - \sin\left(\rho_m\frac{ct - L/\beta_S}{a}\right)U\left(ct - \frac{L}{\beta_S}\right)\right] - \dots \\ & - \frac{4a\beta_S}{L}\sum_{m=1}^{m=\infty}\sum_{n=1}^{n=\infty}\frac{J_0(k\rho_m/a)}{J_1(\rho_m)}\rho_m\frac{\sin(\gamma_1 ct/a) - (-1)^n\sin(\gamma_1\frac{ct - L/\beta_S}{a})U\left(ct - \frac{L}{\beta_S}\right)}{\gamma_1\gamma_2^2}\cos\left(\frac{n\pi(L - vt - v\Delta t_{ST})}{L}\right) + \dots \\ & + \frac{2}{\pi}\sum_{n=1}^{n=\infty}\frac{I_0(kn\pi\gamma_S/L)}{nI_0(an\pi\gamma_S/L)}\left[\sin\left(n\pi\beta_S\frac{ct}{L}\right) - (-1)^n\sin\left(n\pi\beta_S\frac{ct - L/\beta_S}{L}\right)U\left(ct - \frac{L}{\beta_S}\right)\right]\cos\left(\frac{n\pi(L - vt - v\Delta t_{ST})}{L}\right)\Bigg\}. \end{aligned} \tag{2.95}$$

Equation 2.95 can be used to compute the counter-moving wakefunction using its definition, Eq. 2.90.

The wakefunction was numerically evaluated for the case in which both the electrons and the test particle are ultra relativistic, i.e. $\beta_S = 1$ and $v = c$. As for

the co-moving case, to obtain the wakepotential, the wakefunction was numerically convolved with a beam distribution λ_S. The beam had a Gaussian distribution.

The counter-moving wakepotential was obtained also numerically by post processing the PIC solver simulation results as explained in the previous section (co-moving wakefield), considering a test particle moving in opposite direction with respect to the burst of electrons.

The counter-moving wakepotentials as a function of the entrance delay between Q_S and T ($\Delta s_{Q_S T}$ and $\Delta t_{Q_S T}$) obtained from the semi-analytic method and the CST PIC solver are reported and compared in Fig. 2.20. The agreement between the two methods is excellent.

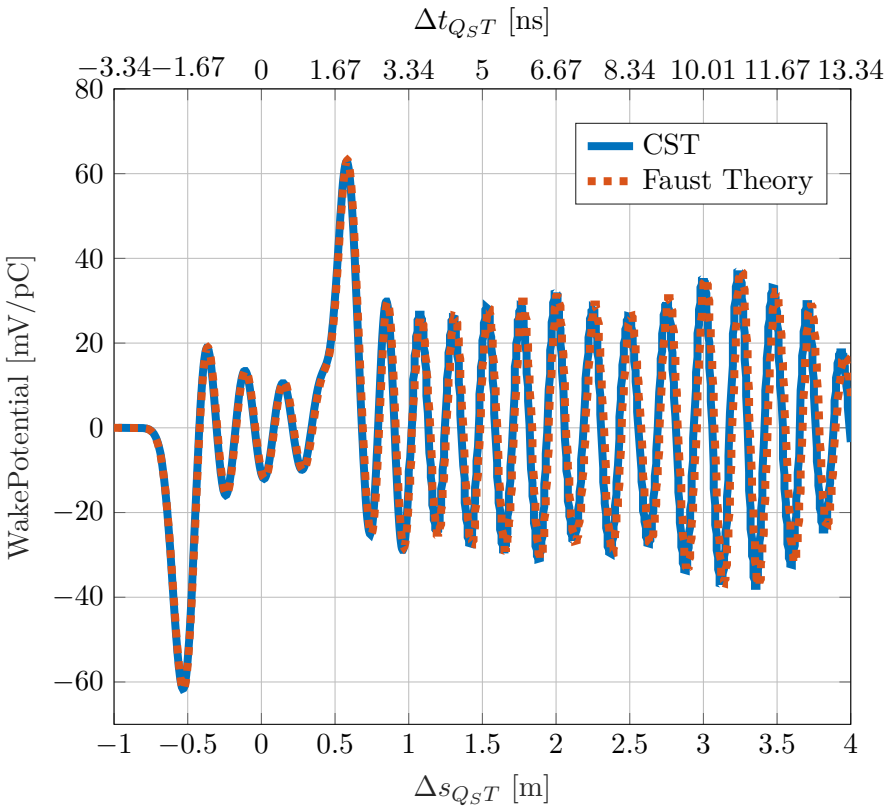

Figure 2.20. Comparison between the counter-moving wakepotentials of a burst of ultra-relativistic electrons (1 nC or $1.1 \cdot 10^{21}$ electrons and $\beta_S \to 1$ or $\gamma_S = 5 \cdot 10^{10}$) traversing a pillbox cavity (length $L = 0.6$ m and radius $a = 0.1$ m) computed by the semi-analytic method (Faust Theory [61]) and the CST PIC solver [60]. The electrons are emitted uniformly from one of the circular face of the cavity. Their longitudinal distribution is a Gaussian bunch ($\sigma_b = 0.07$ m). The cavity material is perfect electric conductor (PEC), loss free. Test particle speed is $v = c$.

Discussion on the Results

Previously, the co-moving and counter-moving wakepotentials for a pillbox cavity excited by a burst of electrons were presented. In this subsection the co-moving and counter-moving wakefunction are reported in Fig. 2.21 with the scope of comparing

them. Further, in Fig. 2.22, the co-moving and counter-moving longitudinal

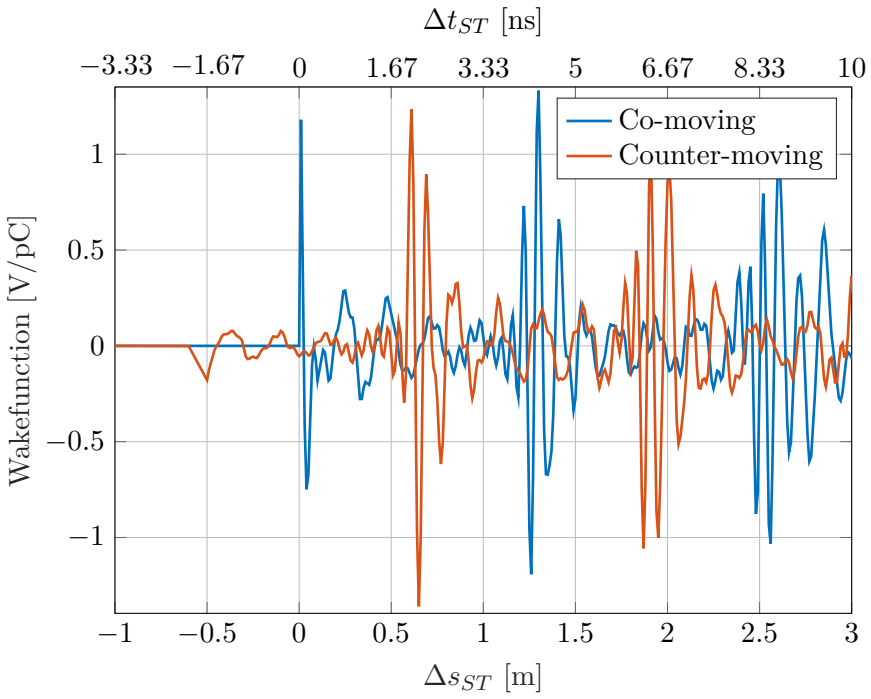

Figure 2.21. Comparison between the co-moving and the counter-moving wake function of a pillbox cavity excited by a burst of electrons emitted by one face. The wakefunctions have been obtained with the Faust theory.

impedance, the fourier tranform of the wakefunctions (refere to chapter 3) are reported. Let us label as transient the interval of time for which the source particle is inside the cavity, ($\Delta s_{ST} < 0.6$ m for the discussed example), and as long range interval the period of time after the transient, i.e. $\Delta s_{ST} > 0.6$ m. With reference to Fig. 2.21, co-moving and counter-moving wakefunctions are very different in the transient region, around null entrance delay between T and S, while for further entrance delay they seem to be similar but translated. This may indicate that the effects of the transient wakefield generated by S is experienced in a very different way if T moves in the same (co-moving wake) or in opposite (counter-moving) direction with respect to S. However, it appears that the effects of the long range wakefield generated by S are quite similar in both the co-moving and the counter-moving case. This makes sense since the long range interval is dominated by the resonant electromagnetic modes trapped in the pillbox, and the geometry of the mode fields and the mode resonant frequency is invariant with respect to the direction of the test particle. This last observation is backed up by the fact that, co-moving and counter-moving impedance modulus compare very well, refer to Fig. 2.22, i.e. the resonant modes have the same effects on the test charge T independently from its propagation direction.

The real and imaginary parts of the co-moving and counter-moving impedance were affected by high noise, thus, in this manuscript, a comparison of the real and imaginary part of the co-moving and counter-moving impedance is not reported and

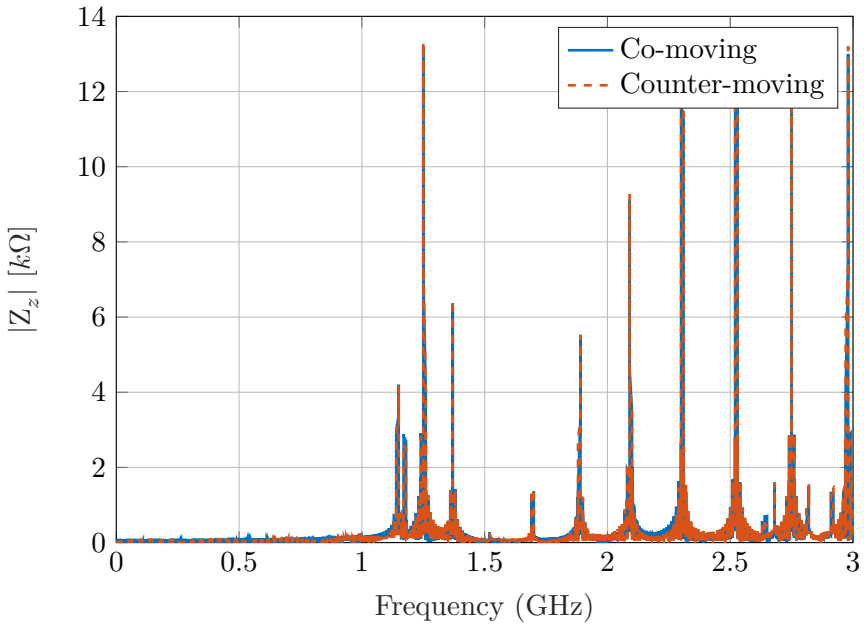

Figure 2.22. Comparison between the absolute values of co-moving and counter-moving impedance of a pillbox cavity excite by a burst of electrons emitted by one face.

this comparison is left for future work.

2.6 The Effective Counter-moving Problem

In the previous sections the concept of co-moving and counter-moving wakefield and wakepotential were introduced and two examples were presented. For the introduction of these concepts only one source and one test distribution are needed. However, when two beams pass into a vacuum chamber they act as two wakefield sources, their wakefields act back on the beams that behave also as tests, thus, the effective counter-moving problem has to take into account two source distributions and two test distributions. This section deals with the effective counter-moving problem, i.e. it investigates the wakefield effects of two counter-moving source charge distributions traversing a vacuum chamber on themselves. In particular, this work focuses on the energy lost by the two beams system.

The section is organized as followed: first all the basic quantities needed for the formal definition of the problem are introduced. Subsequently, recalling the concepts of co-moving and counter-moving wakefield and wakepotential, the energy lost by the two beams system, which could produce the heating of the vacuum chamber, is computed.

2.6.1 Basic Quantities

The majority of the quantities needed for the formal definition of the effective counter-moving problem have been already defined in sec. 2.3.1 and 2.4.1. In this section only the new concepts are discussed. With reference to Fig. 2.23, let us consider

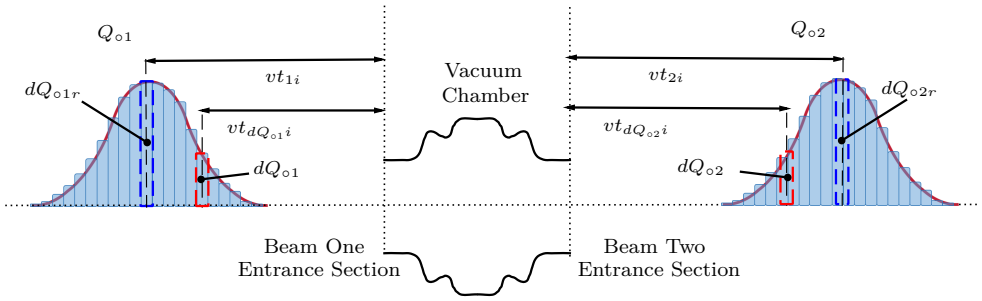

Figure 2.23. The two beam distributions $Q_{\circ 1}$ and $Q_{\circ 2}$, represented as two Gaussian bunches, are shown divided in the infinitesimal charges $dQ_{\circ 1}$ and $dQ_{\circ 2}$. Also the beam entrance times in the vacuum chamber t_{1i} and t_{2i}, as distance concept, are shown as well as the generic entrance time of the generic infinitesimal charge, $t_{dQ_{\circ 1}i}$ and $t_{dQ_{\circ 2}i}$.

two beams: beam one described by a time charge distribution $Q_{\circ 1}(t) = q_{\circ 1}\lambda_{\circ 1}(t)$ and beam two described by a time charge distribution $Q_{\circ 2}(t) = q_{\circ 2}\lambda_{\circ 2}(t)$.

When $Q_{\circ 1}(t)$ enters into the cavity it generates wakefields. In this sense it behaves as a source distribution. The wakefield generated by $Q_{\circ 1}(t)$ is experienced by $Q_{\circ 2}(t)$. However, this wakefield acts also back on the $Q_{\circ 1}(t)$ distribution itself. In this sense $Q_{\circ 1}(t)$ plays the role of a test distribution. The same is true for $Q_{\circ 2}(t)$. Thus, both the distributions act as sources and tests. One needs to distinguish the source behaviour from the test behaviour of the same distribution, to this scope the following notation is adopted: if the distribution is thought as source the linked quantities have the subscript S instead of $\circ$, as example $Q_{S1}(t)$ instead of $Q_{\circ 1}(t)$, if the distribution is thought as test the linked quantities have the subscript T instead of $\circ$, as example $Q_{T1}(t)$ instead of $Q_{\circ 1}(t)$.

Let us label trajectory one the trajectory in which $Q_{\circ 1}(t)$ is moving. Analogously, let us label trajectory two the trajectory in which $Q_{\circ 2}(t)$ is moving. Let us assume that the two trajectories are straight and parallel, that the beams move in opposite directions one with respect to the other and that they have the same speed in modulus, $v_1 = v_2 = v$, a reasonable hypothesis for a collider.

Let us define t_{1i} as the time at which beam one enters in the vacuum chamber, i.e. the time at which the center of the distribution $Q_{\circ 1}$ crosses the beam one entrance section. Let us define t_{2i} as the time at which beam two enters in the vacuum chamber, i.e. the time at which the center of the distribution $Q_{\circ 1}$ crosses the beam two entrance section.

Thus, the time entrance delay between the beams can be defined as:

$$\Delta t_{b_1 b_2} = t_{2i} - t_{1i}, \tag{2.96}$$

for positive value of $\Delta t_{b_1 b_2}$ beam two is delayed with respect to beam one, viceversa for negative value.

As already seen in the previous sections, 2.3.3 and 2.4.3, the time charge distributions $Q_{\circ 1}(t)$ and $Q_{\circ 2}(t)$ can be imagined as the sum of infinitesimal point charges $dQ_{\circ 1}$, $dQ_{\circ 2}$. The particle $dQ_{\circ 1}$ enters into the vacuum chamber when it crosses the beam one entrance section, and the particle $dQ_{\circ 2}$ enters into the vacuum chamber when it crosses the beam two entrance section, refer to Fig. 2.23.

Considering all the concepts introduced, the infinitesimal point charges $dQ_{\circ 1}$ and $dQ_{\circ 2}$ can be written as:

$$dQ_{\circ 1}(t_{dQ_{\circ 1}i}) = q_{\circ 1}\lambda_{\circ 1}(t_{dQ_{\circ 1}i})dt_{dQ_{\circ 1}i}, \tag{2.97}$$
$$dQ_{\circ 2}(t_{dQ_{\circ 2}i}) = q_{\circ 2}\lambda_{\circ 2}(t_{dQ_{\circ 2}i})dt_{dQ_{\circ 2}i}. \tag{2.98}$$

2.6.2 Beam Losses

Both the beams variate their energy in traversing the vacuum chamber. The total energy variation, ΔU, is the sum of the energy lost or gained by beam one, ΔU_1, plus the energy lost or gained by beam two, ΔU_2. Thus, one can write:

$$\Delta U = \Delta U_1 + \Delta U_2. \tag{2.99}$$

The energy variation of beam one is due to the effects of its own wakefield plus the effect of the wakefield generated by the beam two. Also beam two experiences the wakefield generated by the beam one plus its own wakefield, thus, one can further split the terms in Eq. 2.99 as:

$$\Delta U_1 = \Delta U_{Q_{S1}Q_{T1}} + \Delta U_{Q_{S2}Q_{T1}}, \tag{2.100}$$
$$\Delta U_2 = \Delta U_{Q_{S1}Q_{T2}} + \Delta U_{Q_{S2}Q_{T2}}. \tag{2.101}$$

In Eq.s 2.100 and 2.101, $\Delta U_{Q_{S1}Q_{T1}}$, is the energy variation of beam one because of its own wakefield, i.e. this is a co-moving wakefield scenario. The term $\Delta U_{Q_{S2}Q_{T1}}$ is the energy variation of beam one because of the beam two wakefield i.e. this is a counter-moving wakefield scenario. The term $\Delta U_{Q_{S1}Q_{T2}}$, is the energy variation of beam two because of the beam one wakefield, i.e. this is a counter-moving wakefield scenario. Finally, the term $\Delta U_{Q_{S2}Q_{T2}}$ is the energy variation of beam two because of the beam two wakefield i.e. this is a co-moving wakefield scenario.

In section 2.4 a formalism capable of computing the energy lost both in the co-moving and in the counter-moving case was presented. With reference to the Eq.s 2.60 and 2.63 and considering the expressions 2.97 and 2.98 of infinitesimal point charges $dQ_{\circ 1}$ and $dQ_{\circ 2}$, all the terms appearing in Eq.s 2.100 and 2.101 can be rewritten in function of the wakefunction of the vacuum chamber as:

$$\Delta U_{Q_{S1}Q_{T1}} = q_{S1}q_{T1}\int_{-\infty}^{\infty}\lambda_{T1}(t_{dQ_{T1}i})\int_{-\infty}^{\infty}\lambda_{S1}(t_{dQ_{S1}i})w_{z11}(t_{dQ_{T1}i} - t_{dQ_{S1}i})dt_{dQ_{S1}i}dt_{dQ_{T1}i}, \tag{2.102}$$

$$\Delta U_{Q_{S2}Q_{T1}} = q_{S2}q_{T1}\int_{-\infty}^{\infty}\lambda_{T1}(t_{dQ_{T1}i})\int_{-\infty}^{\infty}\lambda_{S2}(t_{dQ_{S2}i})w_{z21}(t_{dQ_{T1}i} - t_{dQ_{S2}i})dt_{dQ_{S2}i}dt_{dQ_{T1}i}, \tag{2.103}$$

$$\Delta U_{Q_{S1}Q_{T2}} = q_{S1}q_{T2}\int_{-\infty}^{\infty}\lambda_{T2}(t_{dQ_{T2}i})\int_{-\infty}^{\infty}\lambda_{S1}(t_{dQ_{S1}i})w_{z12}(t_{dQ_{T2}i} - t_{dQ_{S1}i})dt_{dQ_{S1}i}dt_{dQ_{T2}i}, \tag{2.104}$$

$$\Delta U_{Q_{S2}Q_{T2}} = q_{S2}q_{T2}\int_{-\infty}^{\infty}\lambda_{T2}(t_{dQ_{T2}i})\int_{-\infty}^{\infty}\lambda_{S2}(t_{dQ_{S2}i})w_{z22}(t_{dQ_{T2}i}-t_{dQ_{S2}i})dt_{dQ_{S2}i}dt_{dQ_{T2}i}. \tag{2.105}$$

In Eq.s 2.102-2.105, the terms w_{znm} represent the longitudinal wakefunction of the beam n seen as a source on the beam m seen as a test.

A case of interest is the one of the two counter-moving beams having the same structure, i.e. they are described by the same distribution λ, but with a different total charge, i.e. $q_{\circ 1} \neq q_{\circ 2}$. With this hypothesis, let us consider a time reference frame in which the origin is set such that $t_{1i} = 0$, i.e. the time origin is set at the moment in which beam one is entering into the vacuum chamber. Since there is a delay $\Delta t_{b_1b_2}$ between the two beams, Eq. 2.96, in the just defined time reference frame the following Eq.s hold:

$$\begin{aligned}
\lambda_{T1}(t_{dQ_{T1}i}) &= \lambda(t_{dQ_{T1}i}),\\
\lambda_{S1}(t_{dQ_{S1}i}) &= \lambda(t_{dQ_{S1}i}),\\
\lambda_{S2}(t_{dQ_{S2}i}) &= \lambda(t_{dQ_{S2}i}-\Delta t_{b_1b_2}).
\end{aligned} \tag{2.106}$$

Substituting Eq.s 2.106 into the energy variation expressions 2.102 and 2.103, one obtains:

$$\Delta U_{Q_{S1}Q_{T1}} = q_{S1}q_{T1}\int_{-\infty}^{\infty}\lambda(t_{dQ_{T1}i})\int_{-\infty}^{\infty}\lambda(t_{dQ_{S1}i})w_{z11}(t_{dQ_{T1}i}-t_{dQ_{S1}i})dt_{dQ_{S1}i}dt_{dQ_{T1}i}, \tag{2.107}$$

$$\Delta U_{Q_{S2}Q_{T1}} = q_{S2}q_{T1}\int_{-\infty}^{\infty}\lambda(t_{dQ_{T1}i})\int_{-\infty}^{\infty}\lambda(t_{dQ_{S2}i}-\Delta t_{b_1b_2})w_{z21}(t_{dQ_{T1}i}-t_{dQ_{S2}i})dt_{dQ_{S2}i}dt_{dQ_{T1}i}. \tag{2.108}$$

Equations 2.107 and 2.108 allow to rewrite the energy lost by beam one during its transit inside the vacuum chamber as:

$$\begin{aligned}
\Delta U_1 = q_{T1}q_{S1}\int_{-\infty}^{\infty}\lambda(t_{dQ_{T1}i})\Bigg[\int_{-\infty}^{\infty}\lambda(t_{dQ_{S1}i})w_{z11}(t_{dQ_{T1}i}-t_{dQ_{S1}i})dt_{dQ_{S1}i} + ...\\
\frac{q_{S2}}{q_{S1}}\int_{-\infty}^{\infty}\lambda(t_{dQ_{S2}i}-\Delta t_{b_1b_2})w_{z21}(t_{dQ_{T1}i}-t_{dQ_{S2}i})dt_{dQ_{S2}i}\Bigg]dt_{dQ_{T1}i}.
\end{aligned} \tag{2.109}$$

The same can be done for the beam two. However, to compute the energy losses of this beam it is more convenient to consider a time reference frame which origin is set such that $t_{S2i} = 0$, i.e. the time origin is set at the moment in which beam two is entering into the vacuum chamber. In this time frame the following equations hold:

$$\begin{aligned}
\lambda_{T2}(t_{dQ_{T2}i}) &= \lambda(t_{dQ_{T2}i}),\\
\lambda_{S2}(t_{dQ_{S2}i}) &= \lambda(t_{dQ_{S2}i}),\\
\lambda_{S1}(t_{dQ_{S1}i}) &= \lambda(t_{dQ_{S1}i}+\Delta t_{b_1b_2}).
\end{aligned} \tag{2.110}$$

Substituting Eq.s 2.110 into the energy variation expressions 2.104 and 2.105 and then inserting them into the expression of the beam two energy losses ΔU_2, Eq.

2.101, one obtains:

$$\Delta U_{Q_{S2}Q_{T2}} = q_{S2}q_{T2}\int_{-\infty}^{\infty}\lambda(t_{dQ_{T2}i})\int_{-\infty}^{\infty}\lambda(t_{dQ_{S2}i})w_{z22}(t_{dQ_{T2}i}-t_{dQ_{S2}i})dt_{dQ_{S2}i}dt_{dQ_{T2}i}, \tag{2.111}$$

$$\Delta U_{Q_{S1}Q_{T2}} = q_{S1}q_{T2}\int_{-\infty}^{\infty}\lambda(t_{dQ_{T2}i})\int_{-\infty}^{\infty}\lambda(t_{dQ_{S1}i}+\Delta t_{b_1b_2})w_{z12}(t_{dQ_{T2}i}-t_{dQ_{S1}i})dt_{dQ_{S1}i}dt_{dQ_{T2}i}, \tag{2.112}$$

and

$$\begin{aligned}\Delta U_2 = q_{T2}q_{S2}\int_{-\infty}^{\infty}\lambda(t_{dQ_{T2}i})\Bigg[\int_{-\infty}^{\infty}\lambda(t_{dQ_{S2}i})w_{z22}(t_{dQ_{T2}i}-t_{dQ_{S2}i})dt_{dQ_{S2}i}+...\\ \frac{q_{S1}}{q_{S2}}\int_{-\infty}^{\infty}\lambda(t_{dQ_{S1}i}+\Delta t_{b_1b_2})w_{z12}(t_{dQ_{T2}i}-t_{dQ_{S1}i})dt_{dQ_{S1}i}\Bigg]dt_{dQ_{T2}i}.\end{aligned} \tag{2.113}$$

Equations 2.109 and 2.113 are formally identical to the one obtained by Zannini et al. [53] using a different model.

Considering Eq. 2.99, to get the total energy loss by the two beams ΔU, one has to sum the contributions of beam one and beam two, ΔU_1 and ΔU_2. It is important to stress that this energy variation is independent from the origin of the time reference frame. Indeed, it represents the work done by the electric field in the vacuum chamber (the wakefield) on the beams. Thus, even if ΔU_1 has been computed in a different time frame than ΔU_2, this two quantities are still summable.

Finally, let us define the loss factor of beam one and beam two as:

$$k_1 = \frac{\Delta U_1}{q_{S1}q_{T1}}, \tag{2.114}$$

$$k_2 = \frac{\Delta U_2}{q_{S2}q_{T2}}, \tag{2.115}$$

and naturally, the total loss factor k is given by

$$k = k_1 + k_2. \tag{2.116}$$

2.6.3 Wakepotentials

Considering Eq. 2.109, in analogy with Eq. 2.63, one could define W_1 as the wakepotential experienced by an arbitrary charge in the beam one because of the electric fields of the beam one itself and because of the electric field of beam two:

$$\begin{aligned}W_1(t_{T1i}) = \int_{-\infty}^{\infty}\lambda(t_{dQ_{S1i}})w_{z11}(t_{T1i}-t_{dQ_{S1}i})dt_{dQ_{S1}i}+...\\ \frac{q_{S2}}{q_{S1}}\int_{-\infty}^{\infty}\lambda(t_{dQ_{S2}i}-\Delta t_{b_1b_2})w_{z21}(t_{T1i}-t_{dQ_{S2}i})dt_{dQ_{S2}i},\end{aligned} \tag{2.117}$$

where t_{T1i} is the generic entrance time in the vacuum chamber of the arbitrary infinitesimal beam one charge. Equation 2.117 may be rewritten as:

$$W_1(t_{T1i},\Delta t_{b_1b_2}) = W_{11}(t_{T1i}) + \frac{q_{S2}}{q_{S1}}W_{12}(t_{T1i},\Delta t_{b_1b_2}), \tag{2.118}$$

where the terms W_{nm} represent the wakepotential generated from the beam m on a test charge that is part of the beam n. And analogously for the beam two

$$\begin{aligned} W_2(t_{T2i}) = &\int_{-\infty}^{\infty} \lambda(t_{dQ_{S2}i}) w_{z22}(t_{T2i} - t_{dQ_{S2}i}) dt_{dQ_{S2}i} + ... \\ &\frac{q_{S1}}{q_{S2}} \int_{-\infty}^{\infty} \lambda(t_{dQ_{S1}i} + \Delta t_{b_1 b_2}) w_{z12}(t_{T2i} - t_{dQ_{S1}i}) dt_{dQ_{S1}i}, \end{aligned} \tag{2.119}$$

where t_{T2i} is the generic entrance time in the vacuum chamber of the arbitrary beam two charge. Further,

$$W_2(t_{T2i}, \Delta t_{b_1 b_2}) = \frac{q_{S1}}{q_{S2}} W_{21}(t_{T2i}, \Delta t_{b_1 b_2}) + W_{22}(t_{T2i}). \tag{2.120}$$

Thus, the wakepotential experienced by a charge of one of the beams, beam one for instance, is the sum of the wakepotential due to beam one, plus the wakepotential due to beam two, shifted in time with a delay $\Delta t_{b_1 b_2}$ and weighted by the ratio of the beams charges.

2.6.4 Example: Simulations of energy dissipated in a resonant cavity by two counter-moving beams

In this subsection the study of the energy dissipated by two counter-moving beams on a pillbox cavity is discussed.

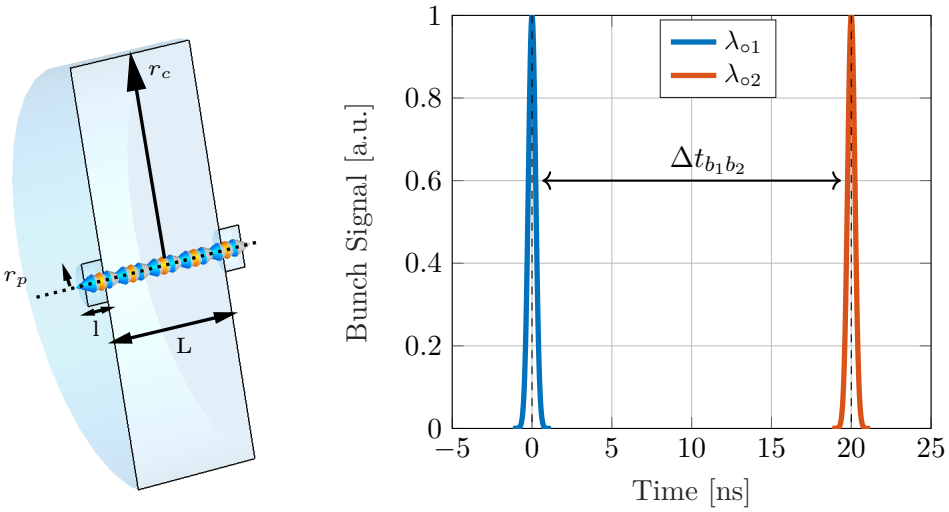

(a) **(b)**

Figure 2.24. (a) Simulated cavity model with geometrical quantities: $r_c = 100$ mm, $r_p = 10$ mm, $L = 60$ mm, $l = 10$ mm. (b) Gaussian bunch signal, the time delay $\Delta t_{b_1 b_2}$ is indicated.

Using the CST Wakefield solver [60] the passage of two counter-moving beams, both positioned exactly at the center of the structure, was modelled for the pillbox cavity shown in Fig. 2.24a. Both beams were composed of only one Gaussian bunch with a charge $q = 4.5\ 10^{-8}$ C and a root mean square $\sigma_b = 70$ mm. The first

beam entered the structure at time $t_{1i} = 0$ s, while the second one entered with an arbitrary delay $\Delta t_{b_1 b_2}$ (see Fig. 2.24b). The pillbox cavity was geometrically built such that the described beams were able to excite only the first resonant mode, (with reference to Fig. 2.24a, $r_c = 100$ mm, $r_p = 10$ mm, $L = 60$ mm, $l = 10$ mm). Further, the electrical conductivity of the cavity wall was set to $\sigma = 10^3$ S/m in order to have a quick dumping of the excited mode.

Wakepotentials

The wakepotentials W_1 and W_2 are shown in Fig. 2.25 as a function of the entrance delay between the excitation pulse ($\lambda_{\circ 1}$ and $\lambda_{\circ 2}$, also shown) and the generic test particle. The wakepotential of the first beam W_1 starts to oscillate at the entrance of the first bunch $\lambda_{\circ 1}$, and the oscillation decreases for further entrance delay. When the second bunch enters into the cavity the oscillation generated by the first bunch can be considered decayed. At the entrance of the second bunch $\lambda_{\circ 2}$, the wakepotential W_1 starts to oscillate again. The two oscillatory behaviours are very similar, they can be recognized as the different terms that compose the W_1 in Eq. 2.118; i.e. W_{11} and W_{12}, indicated in Fig. 2.25 Top.

However, comparing the region around the entrance of the first bunch (around $\Delta t_{Q_S T_1} \approx 0$) and the entrance of the second bunch (and $\Delta t_{Q_S T_1} \approx 100$ ns) it can be noticed that the behaviour of the wakepotentials W_{11} and W_{12} is remarkably different. The same observation can be done for the wakepotential relative to the second beam W_2, that is shown in Fig. 2.25 Bottom, split in its two parts W_{21} and W_{22}. The oscillations in the wakepotentials, W_1 and W_2, represent the excitation of the mode in the cavity. The wall conductivity was set such that at the entrance of the second bunch, the mode excited by the first bunch was damped. This allowed to decouple the single terms composing the wakepotential. Due to the problem symmetry it was expected to have $W_{11} = W_{22}$ and $W_{12} = W_{21}$, relationships that were verified. In Fig. 2.26 both the wakepotentials W_{11} and $-W_{12}$ are represented for comparison. It is clearly visible that the oscillatory behaviour after the transient is the same both for the W_{11}, co-moving wakepotential, and for W_{12}, the counter-moving wakepotential. However, there are differences in the transient. This result agrees with what has been discussed about the counter-moving pillbox cavity example in section 2.5.2.

In order to benchmark the equations given in section 2.6.2 and 2.6.3 and the capabilities of the CST wakefield solver [60] of simulating the counter-moving beams problem, the same pillbox cavity configuration discussed in the previous lines was simulated with a beam delay of $\Delta t_{b_1 b_2} = 20$ ns. The wakepotential W_1 is reported in Fig. 2.27 Top. For this value of $\Delta t_{b_1 b_2}$ the mode excited by the first bunch that entered the structure is not completely damped at the entrance of the second bunch and W_1 has a more complex shape with respect to the case in which $\Delta t_{b_1 b_2} = 100$ ns (Fig. 2.25). However, W_1 is expected to be a combination of W_{11} and W_{12} according to Eq. 2.118. To verify this point, W_{11} and W_{12} were obtained decomposing W_1, resulting from the simulation performed with $\Delta t_{b1b2} = 100$ ns. Subsequently, the term W_{11} and W_{12} were summed up, considering a translation of $\Delta t_{b1b2} = 20$ ns for W_{12}, refer to Fig. 2.27 Bottom. Then, W_1 obtained directly from the CST simulation and W_1 obtained from the summation of W_{11} and W_{12}, according to Eq. 2.118, were compared.

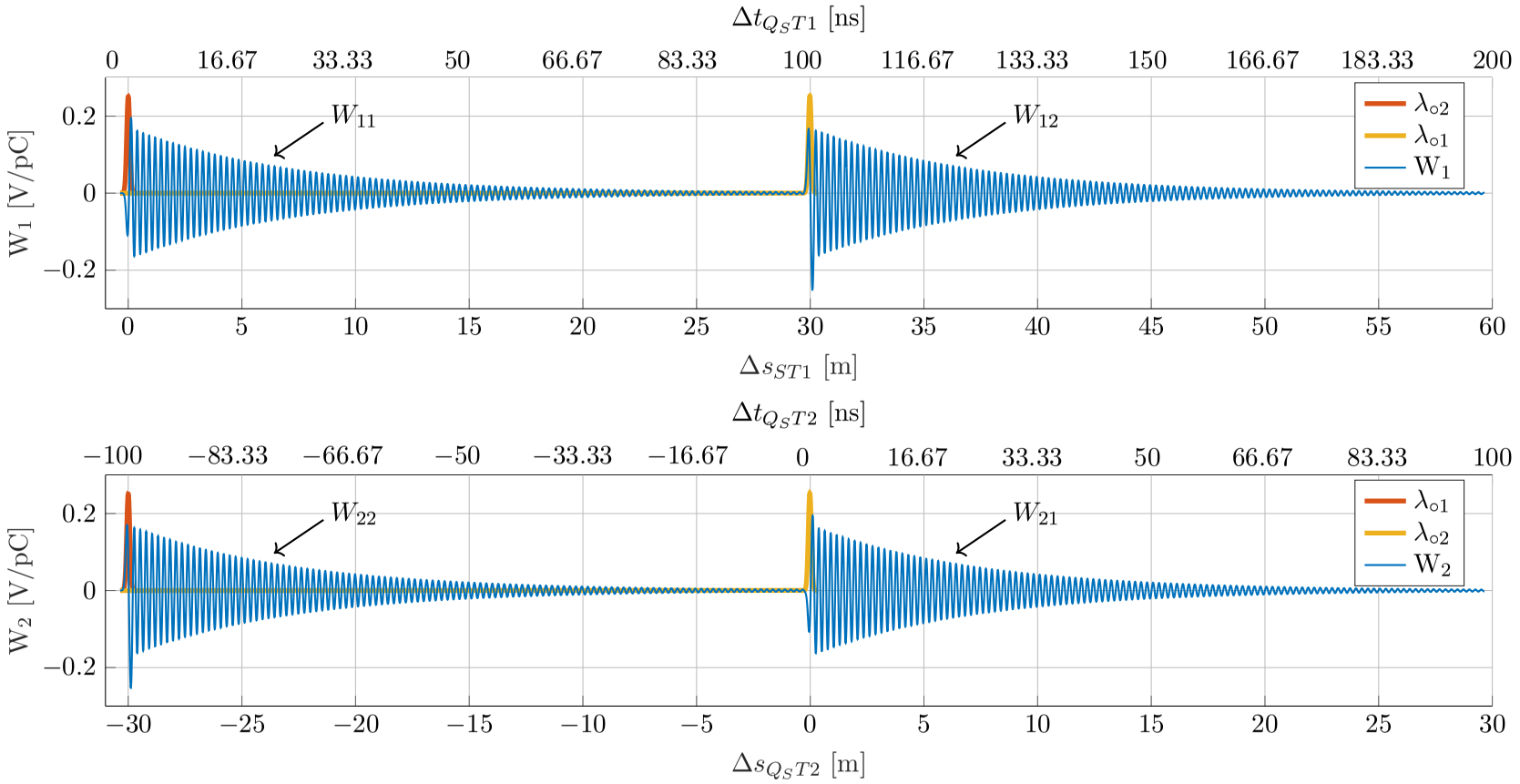

Figure 2.25. Wakepotentials of two counter-moving Gaussian bunch ($\sigma_b = 70$ mm, $q = 4.5 \cdot 10^{-8}$ C) passing through a pillbox cavity ($r_c = 100$ mm, $r_p = 10$ mm, $L = 60$ mm, $l = 10$ mm). Top: wakepotential experienced by a particle moving in the same direction of beam one. Bottom: wakepotential experienced by a particle moving in the same direction of beam two (opposite with respect to beam one). The simulated time delay between the entrance in the cavity of the two bunches ($\Delta t_{b_1 b_2} = 100$ ns), is enough to allow that, when the second bunch enters, the mode excited by the first bunch is decayed. It is so possible to recognise the different contributions to the wakepotentials W_1 and W_2, the W_{nm}, highlighted in the picture. Bunch signals are shown in arbitrary units for representation purposes.

The results of this comparison are shown Fig. 2.27 Bottom, around the region in which the second bunch is entering into the cavity. In the figure also the terms W_{11} and W_{12} translated are reported. The agreement between W_1 obtained directly from the CST simulation and W_1 obtained from the summation of W_{11} and W_{12} is excellent. The same agreement can be obtained considering W_2, W_{22}, W_{21} and Eq. 2.120.

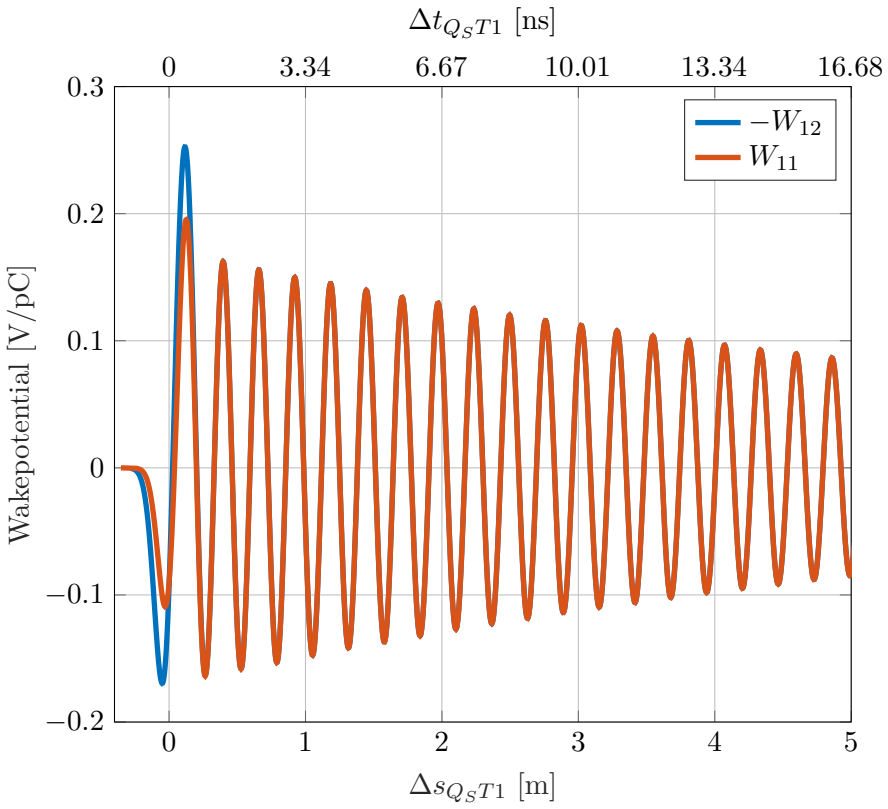

Figure 2.26. Comparison between the terms W_{11} and $-W_{12}$ composing the beam one wakepotential W_1.

Energy losses

For the same pillbox cavity and the same beams described previously in this subsection the beam loss factors in the cavity were computed as a function of the entrance delay between the two beams ($\Delta t_{b_1 b_2}$). Starting from the value of W_{11} and W_{12} (obtained trought the CST simulation with set up $\Delta t_{b_1 b_2} = 100$ ns), W_1 was reconstructed for different values of $\Delta t_{b_1 b_2}$ using Eq. 2.118, the same was done for W_2, considering W_{22}, W_{21} and Eq. 2.120. Thus, using Eq.s 2.109 and 2.113 it was possible to compute the energy lost by beam one ΔU_1 and the energy lost by beam two ΔU_2. Knowing this two quantities it was possible to compute the beams loss factors using Eq.s 2.115 and 2.116. As a benchmark, the beam loss factors of the two counter-moving beams were obtained also by CST simulations for some values

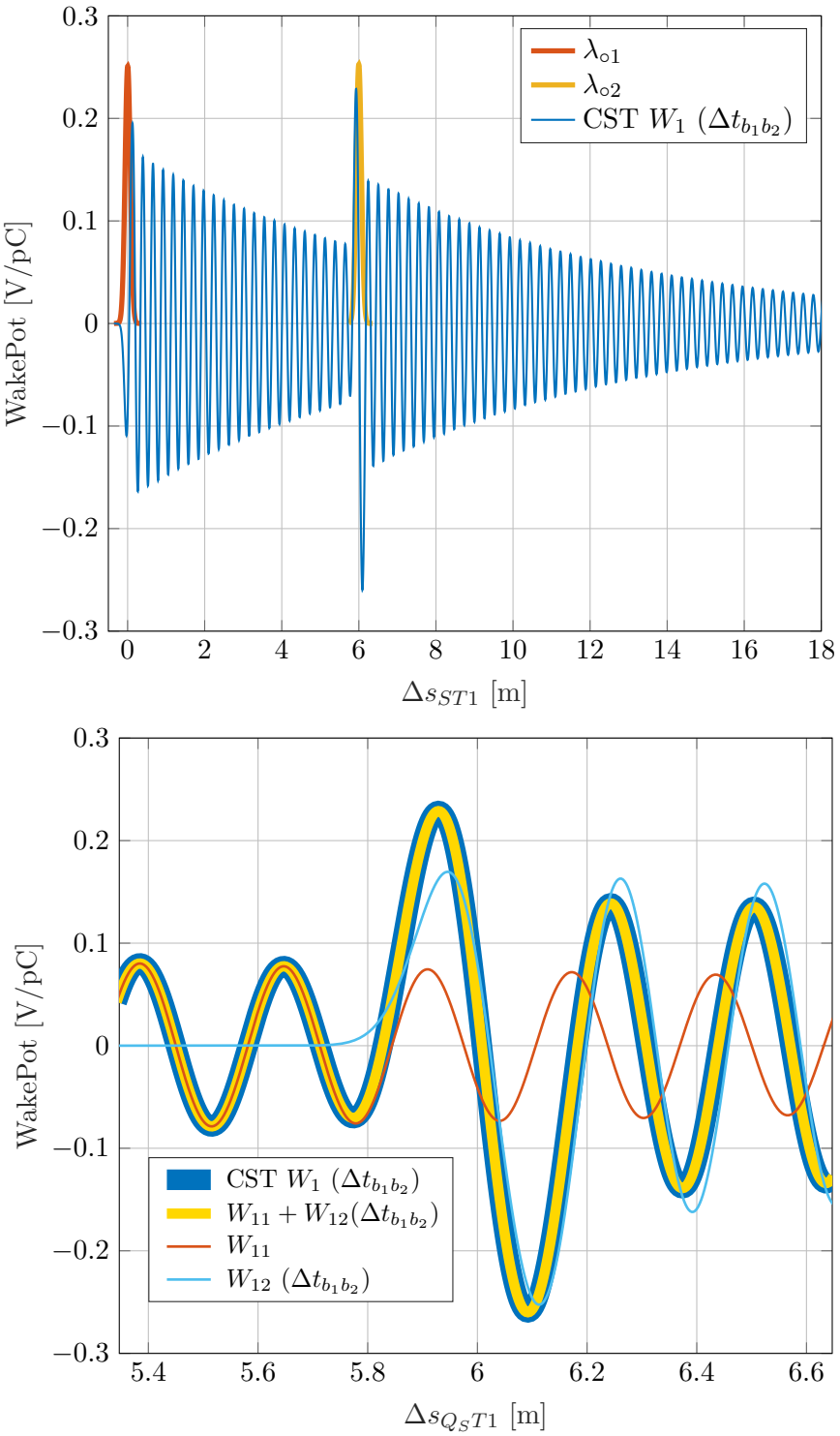

Figure 2.27. Top: CST simulation, wakepotential experienced by the first of two counter-moving Gaussian bunch ($\sigma_b = 70$ mm, $q = 4.5 \cdot 10^{-8}$ C) passing trough a pillbox cavity with $r_c = 100$ mm, $r_p = 10$ mm, $L = 60$ mm, $l = 10$ mm, and delay between the bunches entrance $\Delta t_{b_1 b_2} = 20$ ns. Bunch signals are shown in arbitrary units for representation purposes. Bottom: Comparison between W_1 directly computed by CST and W_1 reconstructed from W_{11} and W_{12} for a $\Delta t_{b_1 b_2} = 20$ ns. The agreement is excellent.

of $\Delta t_{b_1 b_2}$ and compared with what obtained by the Eq.s 2.115 and 2.116 [6] . In Fig. 2.28 the beam loss factors of beam one, beam two and the total one, as a function of the entrance delay between the two beams ($\Delta t_{b_1 b_2}$) are reported. The beam loss factors in the figure are reported normalized with respect to k_r, i.e. the beam loss factor that one of the two beams would have had crossing alone into the vacuum chamber.

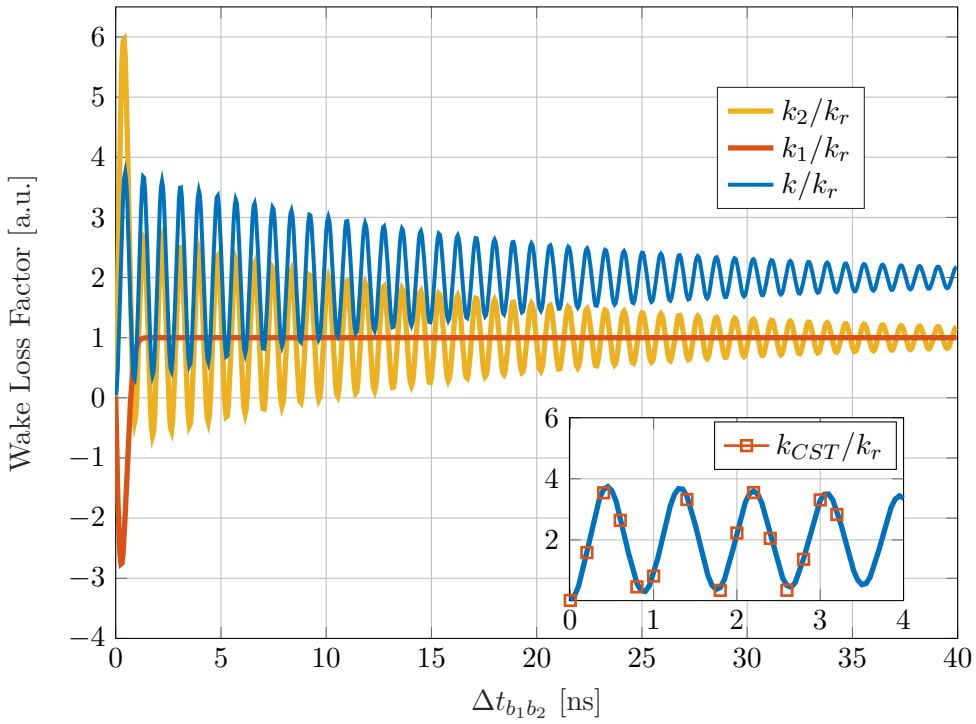

Figure 2.28. Wake loss factors of beam one k_1, beam two k_2 and total wake loss factor k, represented as function of the entrance delay between the two beams $\Delta t_{b_1 b_2}$. They have been reported normalized with respect to k_r ($k_r = 2.5 \cdot 10^{-2}$ [V/pC]), i.e. the wake loss factor of one of the two beams if it would have been entered into the vacuum chamber alone. In the zoom also k_{CST} the total beam loss factor computed directly with CST is shown normalized by k_r.

The loss factor of the first beam, k_1/k_r, is about zero at zero $\Delta t_{b_1 b_2}$, for further $\Delta t_{b_1 b_2}$ it sharply decreases until a negative peak, to increase again sharply until the value of 1 at around 2 ns. For further values of the entrance delay, k_1/k remains constant to 1. The loss factor of the second beam, k_2/k_r, is about zero at zero $\Delta t_{b_1 b_2}$, for further $\Delta t_{b_1 b_2}$ it sharply increases until a positive peak, then it rapidly decreases starting to oscillate around the value of 1 with a decreasing amplitude. The sum of the two loss factors k/k_r, is about zero at zero $\Delta t_{b_1 b_2}$. For further $\Delta t_{b_1 b_2}$, k/k_r performs damped oscillation around the value of 2 with maximum peaks of around

[6] The CST 2018 Wakefield solver [60] computes automatically the loss factor of a beam. However, when two beams are simulated, a problem in the software makes it show, for both beams, the loss factor of the last beam defined in the simulation. Thus, to obtain the correct value of the loss factor for the two beams, two simulations have to be repeated defining the two beams in different order. A ticket with the software house was opened to solve the issue.

4 and minimum of around 0.

In this work positive values of loss factors mean energy lost by the beam and negative values energy gained, one possible explanation for such a behaviour is the following: If the entrance delay between the two beams is null, they both excite the mode inside the pillbox cavity but with an opposite phase, since the geometry of the problem is symmetric. The net results is that the mode inside the cavity is not excited and so the only dissipated power is due to the resistive wall effects. If the delay between the beam is different from zero but such that the two beams meet each others inside the pillbox cavity (transient time interval) there is a more complex scenario. The first beam entered (beam one in this example) gains energy while the delayed beam loses energy. The energy lost by beam two is higher than the energy gained by beam one, the extra energy is going in the vacuum chamber as heat. After the transient, beam one does not meet any more beam two inside the pillbox cavity because the delay is such that beam one is out before beam two enters. This explains the fact that after about 1.5 ns k_1/k_r stabilizes around the value of 1, i.e. the value of the wake loss factor that one beam would have if it had crossed the vacuum chamber alone. After the transient, beam two enters in the cavity where a resonant mode has already been excited by the previous passage of beam one. Beam two interacts with the resonating mode, depending on the entrance delay it can absorb energy from the mode or excite it more, as it is visible from the oscillations behaviour of k_2/k_r. The oscillation is damped by the fact that the mode in the cavity dissipates energy heating the cavity walls. Thus, the higher $\Delta t_{b_1 b_2}$ is the lower is the energy available to be exchanged with the beam. As expected the damped oscillations converge towards the value of 1 for $\Delta t_{b_1 b_2} \to \infty$. Indeed, if the beam entrance delay is big enough that the mode excited by the first beam passing is completely decayed when the second beam arrives, then the latter is in the same situation of the first one: it arrives finding an empty cavity and with its passage it excites the mode. The total loss factor k has an oscillating behaviour and it is always positive. Thus, energy is always dissipated in the cavity wall. Its oscillations have a maximum of about 4, this means that in the worst case scenario, two counter-moving beams can dissipate on a resonant mode up to four times the energy that would be dissipated by only one beam. This finding is in agreement with the prediction of the model of Grudiev [55] and with the observation of Giordano [62]. On the other side, for specific values of the beams entrance delay $\Delta t_{b_1 b_2}$, the total energy dissipated on the cavity approaches the zero value. In Fig. 2.27, in the bottom right corner, the value of total loss factor computed directly with the CST solver for same values of $\Delta t_{b_1 b_2}$ are reported. The agreement between the CST computed total beam loss factor and the one computed trough Eq. 2.116 is excellent.

2.7 Conclusions

This chapter has been both a background and a result chapter. It has first reviewed the wakefield concept in general, introducing the hypothesis under which it can be used. Then, it has distinguished between co-moving and counter-moving wakefield and it has reported the already well know co-moving wakefield theory, introducing longitudinal and transverse wakefunction, wakepotentials, beam dissipated energy

and beam induced heating. Subsequently, some original contributions for the counter-moving wakefield have been presented, in particular a definition of counter-moving wakefunction has been given as well as a formalism to compute the counter-moving wakepotential and the related beam induced heating. Some example of counter-moving wakefunction and wakepotential have been discussed. The wakepotential computed by the PIC and the Wakefield solver of the commercial CST software have been benchmarked against the wakepotential obtained semi-analytically for the discussed examples with very good agreement. This has assessed the capacity of the CST software to simulate the counter-moving problem and it is a good indication that the proposed model works. This part has given hints on the fact that the counter-moving wakefunction and the co-moving wakefunction are very different in the short range regime but they are not in the long range one when resonant modes are trapped in the vacuum chamber. Furthermore, the problem of the beam induced heating of two counter-moving beams traversing the same vacuum chamber has been extensively addressed. The formalism in this work was able to explain the results obtained by simulations and by previous studies. It was possible to compute the RF-heating power of the vacuum chamber as a function of the delay between the counter-moving beams entrance. This is a critical point to obtain the worst case scenario that a device could experience and, according to it, design the device cooling system.

Chapter 3

Impedance Theory

3.1 Introduction

Coupling impedance can be simply introduced as the Fourier transform of the wakefunction. This means that, physically, it has the same meaning of the wakefunction. However, switching from time to frequency domain is useful for several reasons: the wakefunction can contain a number of well defined frequencies that are easy to recognise performing the Fourier transform. These frequencies correspond to resonant electromagnetic modes trapped in the device [46]. Furthermore, many electromagnetic properties of materials are frequency dependent. Finally, also the formula of the energy dissipated on a device simplifies if expressed in frequency domain. This allows to better understand the influence of the entrance delay between the two beams on the energy dissipated in the device.

3.1.1 Scope and Structure of the Chapter

This is both a background and a results chapter.

Section 3.2 reviews the definition of the longitudinal and transverse impedance defining also dipolar and quadrupolar impedance. Further, the section describes qualitatively the frequency behaviour of the coupling impedance.

Section 3.3.1 and 3.3.2 formulate the energy deposited in a device as a function of its impedance in case the device is crossed by one beam or by two beams. The main reference used to shape this part are Chao [46], Zannini et al. [54], Rumolo [63] and an unpublished note of Vasileios Vlachodimitropoulos.

Section 3.3.3 reports the original contribution of this chapter: the analysis of the energy dissipated in a device crossed by two beams as a function of the time delay between the two beams entrance in the vacuum chamber. The two beams can be or not counter-rotating, this is taken into account by the wakefunction, and so by the impedance. The section focuses in particular on the identification of the value of the entrance delay between the beams, $\Delta t_{b_1 b_2}$, that maximizes or minimizes the dissipated energy and power in the device.

Finally, section 3.4 concludes the chapter recalling the main points.

3.2 Longitudinal and Transverse Impedance

3.2.1 Longitudinal Impedance

The longitudinal impedance Z_z is defined as the Fourier transform of the longitudinal wakefunction w_z:

$$Z_z(\omega) = \int_{-\infty}^{\infty} w_z(\Delta t_{ST}) e^{-i\omega\Delta t_{ST}} d(\Delta t_{ST}), \tag{3.1}$$

where the time variable formulation of the longitudinal wakefunction, Eq. 2.54, has been used, $\omega = 2\pi f$, with f the frequency and $i = \sqrt{-1}$. The unit of measure of the longitudinal impedance is ohm, Ω. Let's recall that Δt_{ST} is the time entrance delay between the source and the test charge defined in section 2.3.1 for the co-moving wakefield case and in section 2.4.1 for the counter-moving wakefield case. Needless to say, there is no difference in the longitudinal impedance definition between direct and counter-moving wakefield cases. The difference is taken into account by the wakefunction, that, as was shown in the previous chapter, is not the same in the co-moving and in the counter-moving case.

3.2.2 Transverse Impedance

The transverse impedance $\mathbf{Z}_{x,y}$ is defined as the Fourier transform of the transverse wakefunction $\mathbf{w}_{x,y}$ multiplied by the imaginary unit i:

$$\mathbf{Z}_{x,y}(\omega) = i \int_{-\infty}^{\infty} \mathbf{w}_{x,y}(\Delta t_{ST}) e^{-i\omega\Delta t_{ST}} d(\Delta t_{ST}), \tag{3.2}$$

where the time variables formulation of the transverse wakefunction, Eq. 2.65, has been used, $\omega = 2\pi f$, with f the generic frequency and $i = \sqrt{-1}$. The unit of measure of the transverse impedance is ohm per meter, Ω/m. The transverse impedance is a vector of two components, one for each transverse axes, as it is for the transverse wakefunction.

Furthermore, section 2.3.5 has shown that, usually, the transverse wakefunction is expanded in power series (up to the first order terms) in the offset of the trajectory of the source particle and the test particle ($\mathbf{u}_S = (x_{q_S}, y_{q_S})$), $\mathbf{u}_T = (x_{q_T}, y_{q_T})$) with respect to the vacuum chamber axis. The same is done for the impedance leading to:

$$\begin{aligned} Z_x &= C_x(\Delta t_{ST}) + Z_x^{dip}(\Delta t_{ST}) x_{q_S} + Z_x^{quad}(\Delta t_{ST}) x_{q_T}, \\ Z_y &= C_y(\Delta t_{ST}) + Z_y^{dip}(\Delta t_{ST}) y_{q_S} + Z_x^{quad}(\Delta t_{ST}) y_{q_T}. \end{aligned} \tag{3.3}$$

The terms Z_x^{dip} and Z_y^{dip} [Ω/m] are called dipolar impedances while the terms Z_x^{quad} and Z_y^{quad} [Ω/m] are called quadrupolar impedances. If x_{q_S}, y_{q_S} and x_{q_T}, y_{q_T} are small with respect to the transverse characteristic dimensions of the vacuum chamber [1] , Eq. 3.3 is a good approximation of the transverse impedance [51]. If this is true, the disctinction between dipolar and quadrupolar impedance is very important since they result in different effects on the beam [64].

[1] this is usually the case since, as said in section 2.2.2, the beam control system is doing its best to keep the beam on the vacuum chamber axis.

Equation 3.3 gives an operative way to compute its terms :

$$
\begin{aligned}
C_x &= Z_x|_{x_{q_S}=0,x_{q_T}=0}, \\
C_y &= Z_y|_{x_{q_S}=0,x_{q_T}=0}, \\
Z_x^{dip} &= \frac{Z_x|_{x_{q_S},x_{q_T}=0} - C_x}{x_{q_S}}, \\
Z_x^{quad} &= \frac{Z_x|_{x_{q_S}=0,x_{q_T}} - C_x}{x_{q_T}}, \\
Z_y^{dip} &= \frac{Z_y|_{y_{q_S},y_{q_T}=0} - C_y}{y_{q_S}}, \\
Z_y^{quad} &= \frac{Z_y|_{y_{q_S}=0,x_{q_T}} - C_y}{y_{q_T}},
\end{aligned}
\tag{3.4}
$$

The various terms may be obtained by simulations [51]. The first two terms correspond to the impedance obtained if both the source and the test particle paths are on the vacuum chamber axis. The dipolar impedance terms, $Z_{x,y}^{dip}$, can be obtained considering the test charge passing on the vacuum chamber axis and the source charge passing on a trajectory displaced of a fixed amount in x or y, depending if one is studying the transverse dipolar impedance along x or y. The same is done for obtaining the value of the quadrupolar impedance, $Z_{x,y}^{quad}$, however, in this case the source charge moves on the vacuum axis and the test charge is displaced.

3.2.3 Relationship Between Longitudinal and Transverse Impedance

It was already shown that longitudinal and transverse wakefields are linked by the Panowsky-Wenzel theorem, Eq. 2.45. This relation can be rewritten in the frequency domain applying the Fourier transform and the impedance definition. It turns into [46]:

$$
\nabla_{x,y}(Z_z) = \begin{bmatrix} \frac{\partial Z_z}{\partial x} \\ \frac{\partial Z_z}{\partial y} \end{bmatrix} = \begin{bmatrix} \frac{\omega}{c} Z_x \\ \frac{\omega}{c} Z_y \end{bmatrix} = \frac{\omega}{c} \mathbf{Z}_{x,y}. \tag{3.5}
$$

As is shown in section 5.4.3, Eq. 3.5 is crucial for the estimation of transverse impedance during bench measurement campaigns.

3.2.4 Qualitative Description of an Impedance Curve

As a last point of the section it is useful to introduce a qualitative description of the frequency behaviour of an impedance.

In section 2.2.1 it was shown that the wakefield has a component dependent mainly on the geometry of the device and a component dependent mainly on the

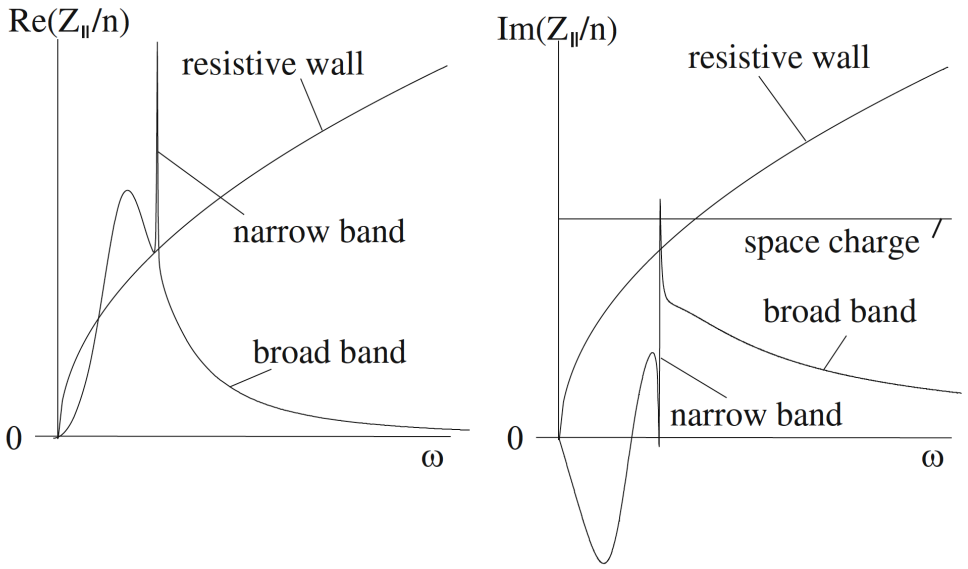

Figure 3.1. Qualitative representation of the real and imaginary part of an impedance curve, courtesy of Wiedemann [65]. The geometric contribution, narrow band and broad band impedance, is separated from the resistive contribution, resistive wall impedance. It is shown also the space charge impedance.

electrical properties (σ, ε and μ) of the device materials. The wakefunction takes into account both these effects. However, it is not trivial to distinguish the contribution of the resistive wall field and geometric fields in the wakefunction. This task becomes easier in the frequency domain, i.e. if instead of the wakefunction one looks at the impedance. An example impedance curve is drawn in Fig. 3.1 (courtesy of Wiedemann [65]), in which the real and imaginary parts of the impedance are represented as a function of $\omega = 2\pi f$. With reference to Fig. 3.1, one can clearly distinguish three different impedance behaviours.

- The resistive wall impedance behaviour, typical of the longitudinal and transverse impedance. Generally, this is the dominant component at low frequencies. This contribution is the one due to the electric conductivities and permittivity and to the magnetic permeability of the materials. In this case both real and imaginary parts of the impedance are smooth curves. In particular, for the case of a cylindric pipe of lenght L, radious b made by a material with resisitivty σ, in the thick wall frequency regime , the longitudinal impedance is [46]:

$$Re[Z_z(\omega)] = Im[Z_z(\omega)] = \frac{L}{b\sqrt{\sigma}}\sqrt{\frac{Z_0|\omega|}{8\pi^2 c}}, \tag{3.6}$$

  where c is the light speed and $Z_0 = 376.73\ \Omega$ is the vacuum characteristic impedance. It is clear that to reduce this kind of impedance one has to increase the material conductivies σ, or, even better, to increase the distance between the beam and the resistive walls.

- Narrow band behaviour, typical of both tranverse and longitudinal impedance. This contribution is mainly geometric, it is due to resonant electromagnetic modes into the device. In this case the real part of the impedance is characterized by a narrow peak at the mode resonant frequency f_r. The imaginary part has a sharp variation at the mode resonant frequency. It is well known that, the narrow band impedance is well represented by a Lorentzian function [38]:

$$Z_{z,x,y}(f) = \frac{R_{z,x,y}}{1 + iQ\left(\frac{f}{f_r} - \frac{f_r}{f}\right)}, \tag{3.7}$$

  where, $R_{z,x,y}$ is called shunt impedance and the subscripts z, y, x refer to the axis in which impedance is computed. The shunt impedance is the maximum value of the impedance peak. The term Q is also called unloaded mode quality factor and defines the width of the peak, the higher the Q the narrower the peak.

- Broad band behaviour, typical of both transverse and longitudinal impedance. This impedance behaviour is both due to device geometry and material properties. It is similar to the narrow band behaviour and can be described using Eq. 3.7. However, it is characterized by low Q values, of the orders of 10 or lower. The effects of the low Q value is a smoother peak in the impedance real part and a smoother transition in the impedance imaginary part. This impedance behaviour appears, for example, if in a device a resonant mode is damped with ferromagnetic material (ferrite).

3.3 Impedance and RF-heating

In this section, the equation of the energy lost by one beam or by a system of two beams crossing a vacuum chamber is rewritten in the frequency domain in terms of impedance. First the case of one single beam crossing a vacuum chamber is considered, subsequently the two beams problem is discussed. Finally, the problem of identifying the time delay between the two beam entrances in the device that maximizes or minimizes the dissipated power in the device is tackled.

Before starting it is useful to introduce the notation that will be used. The Fourier transform operator is labeled by $\mathscr{F}(\cdot)$, the inverse Fourier transform is labeled by $\mathscr{F}^{-1}(\cdot)$. Further, indicating $g(t)$ as a generic function of time and $G(\omega)$ as its Fourier transform, $g(t)$ can be obtained performing inverse Fourier transformation on $G(\omega)$.

3.3.1 Single Beam Case

The following discussion is based on an unpublished note by Vasileios Vlachodimitropoulos.

In case of a single beam passing in a vacuum chamber, in section 2.4.3, it was shown that the energy variation of that beam due to the beam itself, $\Delta U_{Q_T Q_S}$, is described by Eq. 2.64. In Eq. 2.64, $\lambda_T(t_{dQ_T i})$ represents the beam distribution when the beam is considered as test charge, $\lambda_S(t_{dQ_S i})$ represents the beam distribution

when the beam is considered as source charge. In the studied case only one beam is passing into the vacuum chamber, this means that both λ_T and λ_S describe the same distribution. Thus, one can rewrite:

$$\lambda_T(t_{dQ_Ti}) = \lambda(t_{dQ_Ti}), \tag{3.8}$$

$$\lambda_S(t_{dQ_Si}) = \lambda(t_{dQ_Si}). \tag{3.9}$$

and $q_S = q_T = q$.

Further, let's introduce the Fourier transform of λ as Λ:

$$\Lambda(\omega) = \mathscr{F}(\lambda(t)). \tag{3.10}$$

With the aim of expressing $\Delta U_{Q_TQ_S}$, Eq. 2.64, in frequency domain, let's rewrite the entities that compose the equation as a function of their Fourier transforms:

$$\lambda_T(t_{dQ_Ti}) = \mathscr{F}^{-1}[\Lambda(\omega_1)] = \frac{1}{2\pi}\int_{-\infty}^{\infty}\Lambda(\omega_1)\exp(-j\omega_1 t_{dQ_Ti})d\omega_1, \tag{3.11}$$

$$\lambda_S(t_{dQ_Si}) = \mathscr{F}^{-1}[\Lambda(\omega_2)] = \frac{1}{2\pi}\int_{-\infty}^{\infty}\Lambda(\omega_2)\exp(-j\omega_2 t_{dQ_Si})d\omega_2, \tag{3.12}$$

$$w_z(t_{dQ_Ti} - t_{dQ_Si}) = \mathscr{F}^{-1}[Z_z(\omega_3)] = \frac{1}{2\pi}\int_{-\infty}^{\infty}Z_z(\omega_3)\exp(-j\omega_3(t_{dQ_Ti} - t_{dQ_Si}))d\omega_3. \tag{3.13}$$

Where Eq.s 3.8, 3.9 and 3.10 were used.

Substituting Eq.s 3.11 to 3.13 in the $\Delta U_{Q_TQ_S}$ expression, Eq. 2.64, one obtains:

$$\begin{aligned}\Delta U_{Q_TQ_S} =& \frac{q^2}{(2\pi)^3}\int_{-\infty}^{\infty}Z_z(\omega_3)\Lambda(\omega_2)\Lambda(\omega_1)\exp(-j\omega_3(t_{dQ_Ti} - t_{dQ_Si}))... \\ &... \exp(-j\omega_2 t_{dQ_Si})\exp(-j\omega_1 t_{dQ_Ti})d\omega_1 d\omega_2 d\omega_3 dt_{dQ_Ti}dt_{dQ_Si}.\end{aligned} \tag{3.14}$$

Equation 3.14 can be rearranged as:

$$\begin{aligned}\Delta U_{Q_TQ_S} =& \frac{q^2}{(2\pi)^3}\int_{-\infty}^{\infty}Z_z(\omega_3)\Lambda(\omega_2)\Lambda(\omega_1)\exp(-j(\omega_1+\omega_3)t_{dQ_Ti})... \\ &... \exp(-j(\omega_2-\omega_3)t_{dQ_Si})d\omega_1 d\omega_2 d\omega_3 dt_{dQ_Ti}dt_{dQ_Si}.\end{aligned} \tag{3.15}$$

Recalling the identity [66]:

$$\delta(x) = \frac{1}{2\pi}\int_{-\infty}^{\infty}\exp(-jkx)dk \tag{3.16}$$

one can integrate in dt_{dQ_Ti} and dt_{dQ_Si} obtaining two delta functions $\delta(\omega_1+\omega_3)$ and $\delta(\omega_2-\omega_3)$. Thus, Eq. 3.15 turns into:

$$\Delta U_{Q_SQ_T} = \frac{q^2}{2\pi}\int_{-\infty}^{\infty}Z_{11}(\omega_3)\Lambda(\omega_2)\Lambda(\omega_1)\delta(\omega_1+\omega_3)\delta(\omega_2-\omega_3)d\omega_1 d\omega_2 d\omega_3. \tag{3.17}$$

Integrating now on $d\omega_2$ and $d\omega_1$, because of the property of δ [66], one derives the following relations: $\omega_1 = -\omega_3$ and $\omega_2 = \omega_3$. Renaming $\omega_3 = \omega$ one can rewrite Eq. 3.17 as:

$$\Delta U_{Q_SQ_T} = \frac{q^2}{2\pi}\int_{-\infty}^{\infty}Z_z(\omega)\Lambda(\omega)\Lambda(-\omega)d\omega. \tag{3.18}$$

Before proceding, some basic properties of the Fourier transform have to be recalled. The Fourier transform $F(\omega)$ of a real function $f(t)$ has the following properties

$$\begin{gathered} F(-\omega) = F^*(\omega) \\ Re[F(\omega)], |F(\omega)|^2 : even \\ Im[F(\omega)] : odd, \end{gathered} \tag{3.19}$$

where with $(\cdot)^*$ is intended the complex conjugated of $(\cdot)$. Applying relations 3.19 to Eq. 3.18 one obtains:

$$\Delta U_{Q_S Q_T} = \frac{q^2}{2\pi} \int_{-\infty}^{\infty} Z_z(\omega)\Lambda(\omega)\Lambda^*(\omega)d\omega \tag{3.20}$$

$$\Delta U_{Q_S Q_T} = \frac{q^2}{2\pi} \int_{-\infty}^{\infty} Z_z(\omega)|\Lambda(\omega)|^2 d\omega, \tag{3.21}$$

considering that $|\Lambda(\omega)|^2$ is an even function and that the whole integral is taken on a symmetric domain, only the even part of the impedance, the real impedance, plays a role in the integration leading to:

$$\Delta U_{Q_S Q_T} = \frac{q^2}{2\pi} \int_{-\infty}^{\infty} Re[Z_z(\omega)]|\Lambda(\omega)|^2 d\omega. \tag{3.22}$$

Equations 3.22 is the well known expression [63, 46] which quantifies the energy lost by a beam due to the self-induced wakefields.

In a synchrotron, where there are repeated passages of the beam inside the same vacuum chamber, Eq. 3.22 can be rewritten as [63, 67]:

$$\Delta U_{Q_S Q_T} = \frac{q^2 \omega_0}{2\pi} \sum_{p=-\infty}^{p=\infty} Re\left[Z_z(p\omega_0)\right] |\Lambda(p\omega_0)|^2, \tag{3.23}$$

where $\omega_0 = 2\pi f_0$, with f_0 the revolution frequency of the beam inside the synchrotron.

Finally, in section 2.3.4 it was shown how to pass from the energy lost by a beam in a device to the power deposited by the beam in the same device by Eq. 2.39. Using Eq. 2.39, one can define the power in terms of impedance as:

$$\Delta P_{Q_S Q_T} = \frac{f_0 q^2}{2\pi} \int_{-\infty}^{\infty} Re[Z_z(\omega)]|\Lambda(\omega)|^2 d\omega, \tag{3.24}$$

Or, for a synchrotron:

$$\Delta P_{Q_S Q_T} = f_0^2 q^2 \sum_{p=-\infty}^{p=\infty} Re\left[Z_z(p\omega_0)\right] |\Lambda(p\omega_0)|^2, \tag{3.25}$$

Equations 3.24 and 3.25 provide the RF-heating power in the device with impedance Z_z, traversed by the beam with spectrum Λ and with revolution frequency in the accelerator f_0. These equations are extremely powerful since they separate the contribution of the beam (Λ) from the contribution of the vacuum chamber (Z_z). Thus, in case one wants to study the impact on the RF-heating of different solutions for a design, each one of them characterised by an impedance function Z_z, one has to simply replace in the expressions 3.25 the different impedance functions.

3.3.2 Two Beams Case

In the counter-rotating case, or in general in the case in which two beams are passing into the same vacuum chamber, the total energy variation of the two beams system is given in section 2.6.2 by Eq.s 2.99-2.105. As already discussed the total energy variation ΔU is the sum of four terms $\Delta U_{Q_{Sm}Q_{Tn}}$, the energy variation experienced by the beam n because of the wakefield of the beam m. In the previous section 3.3.1, the term that represents the effects of one beam on itself (i.e. $n = m$) has been expressed in frequency domain. This section first works out the terms peculiar to the double beam case, i.e. the terms for which $n \neq m$, $\Delta U_{Q_{S1}Q_{T2}}$ and $\Delta U_{Q_{S1}Q_{T2}}$. Subsequently, the section reports the expression of the total energy variation of the two beams system.

The two beams are assumed with the same structure, i.e. they are described by the same distribution λ according to the Eq.s 2.106 and 2.110. The terms $\Delta U_{Q_{S2}Q_{T1}}$ and $\Delta U_{Q_{S1}Q_{T2}}$ are given by Eq. 2.108 and 2.111. Let's recall that w_{znm} is the longitudinal wakefunction acting on the test charge of the beam n because of the wakefield of the beam m. Thus, the impedance Z_{nm} is the longitudinal impedance felt by the beam n because of the wakefield of the beam m.

Let's express the term $\Delta U_{Q_{S2}Q_{T1}}$, Eq. 2.108, in frequency domain using the same procedure adopted in section 3.3.1. Let's rewrite the entities that compose Eq. 2.107 as a function of their Fourier transform:

$$\lambda_T(t_{dQ_{T1}i}) = \mathscr{F}^{-1}[\Lambda(\omega_1)] = \frac{1}{2\pi}\int_{-\infty}^{\infty}\Lambda(\omega_1)\exp(-j\omega_1 t_{dQ_{T1}i})d\omega_1, \tag{3.26}$$

$$\begin{aligned}\lambda(t_{dQ_{S2}i} - \Delta t_{b_1b_2}) =& \mathscr{F}^{-1}[\Lambda(\omega_2)\exp(-j\omega_2\Delta t_{b_1b_2})] = \\ =& \frac{1}{2\pi}\int_{-\infty}^{\infty}\Lambda(\omega_2)\exp(-j\omega_2 t_{dQ_{S2}i})\exp(-j\omega_2\Delta t_{b_1b_2})d\omega_2,\end{aligned} \tag{3.27}$$

$$w_{z21}(t_{dQ_{T1}i} - t_{dQ_{S2}i}) = \mathscr{F}^{-1}[Z_{21}(\omega_3)] = \frac{1}{2\pi}\int_{-\infty}^{\infty}Z_{21}(\omega_3)\exp(-j\omega_3(t_{dQ_{T1}i} - t_{dQ_{S2}i}))d\omega_3, \tag{3.28}$$

Substituting Eq.s 3.26-3.28 into Eq. 2.108 one obtains:

$$\begin{aligned}\Delta U_{Q_{S2}Q_{T1}} =& \frac{q^2}{(2\pi)^3}\int_{-\infty}^{\infty}Z_{12}(\omega_3)\Lambda(\omega_2)\Lambda(\omega_1)\exp(-j(\omega_1+\omega_3)t_{dQ_{T1}i})... \\ &...\exp(-j(\omega_2-\omega_3)t_{dQ_{S2}i})\exp(-j\omega_2\Delta t_{b_1b_2})d\omega_1 d\omega_2 d\omega_3 dt_{dQ_{T1}i}dt_{dQ_{S2}i}.\end{aligned} \tag{3.29}$$

As before, integrating on $dt_{dQ_{T1}i}$ and $dt_{dQ_{S2}i}$ leads to:

$$\Delta U_{Q_{S2}Q_{T1}} = \frac{q^2}{2\pi}\int_{-\infty}^{\infty}Z_{12}(\omega_3)\Lambda(\omega_2)\Lambda(\omega_1)\delta(\omega_1+\omega_3)\delta(\omega_2-\omega_3)\exp(-j\omega_2\Delta t_{b_1b_2})d\omega_1 d\omega_2 d\omega_3. \tag{3.30}$$

Integrating on ω_1 and ω_2 and renaming $\omega_3 = \omega$, using the properties of δ [66] one gets:

$$\Delta U_{Q_{S2T1}} = \frac{q^2}{2\pi}\int_{-\infty}^{\infty}Z_{12}(\omega)\Lambda(\omega)\Lambda^*(\omega)\exp(-j\omega\Delta t_{b_1b_2})d\omega, \tag{3.31}$$

that turns into:

$$\Delta U_{Q_{S2}Q_{T1}} = \frac{q^2}{2\pi}\int_{-\infty}^{\infty} Z_{12}(\omega)|\Lambda(\omega)|^2 \exp(-j\omega\Delta t_{b_1b_2})d\omega. \tag{3.32}$$

Since the integral is to be done on a symmetric domain, only the even part of the function to be integrated will give a non trivial result. Finding the even part of the function under the integral in Eq. 3.32 is an easy task. Indeed, recalling the 3.19, one can say that $|\Lambda(\omega)|^2$ is even and that the problem is reduced to find the even part of the product $Z_{12}(\omega)\exp(-j\omega\Delta t_{b_1b_2})$:

$$\begin{aligned} Z_{12}(\omega)\exp(-j\omega\Delta t_{b_1b_2}) = &\overbrace{Re[Z_{12}]\cos(\omega\Delta t_{b_1b_2}) + Im[Z_{12}]\sin(\omega\Delta t_{b_1b_2})}^{\text{even}} + ... \\ &... + \underbrace{j\left[Im[Z_{12}]\cos(\omega\Delta t_{b_1b_2}) - Re[Z_{12}]\sin(\omega\Delta t_{b_1b_2})\right]}_{\text{odd}}. \end{aligned} \tag{3.33}$$

Finally,

$$\Delta U_{Q_{S2}Q_{T1}} = \frac{q^2}{2\pi}\int_{-\infty}^{\infty} |\Lambda(\omega)|^2\{Re[Z_{12}]\cos(\omega\Delta t_{b_1b_2}) + Im[Z_{12}]\sin(\omega\Delta t_{b_1b_2})\}d\omega. \tag{3.34}$$

Proceeding in the same way for $\Delta U_{Q_{S1}Q_{T2}}$, $\Delta U_{Q_{S1}Q_{T1}}$ and $\Delta U_{Q_{S2}Q_{T2}}$, Eq. 2.111, 2.107 and 2.111, and considering that an even function is being integrated on a symmetric domain, one ends with:

$$\Delta U_{Q_{S1}Q_{T2}} = \frac{q^2}{\pi}\int_{0}^{\infty} |\Lambda(\omega)|^2\{Re[Z_{21}]\cos(\omega\Delta t_{b_1b_2}) - Im[Z_{21}]\sin(\omega\Delta t_{b_1b_2})\}d\omega. \tag{3.35}$$

$$\Delta U_{Q_{S1}Q_{T1}} = \frac{q^2}{\pi}\int_{0}^{\infty} |\Lambda(\omega)|^2 Re[Z_{11}]d\omega. \tag{3.36}$$

$$\Delta U_{Q_{S2}Q_{T2}} = \frac{q^2}{\pi}\int_{0}^{\infty} |\Lambda(\omega)|^2 Re[Z_{22}]d\omega. \tag{3.37}$$

Finally, one can write the energy lost by two particle beams traversing the same vacuum chamber, recalling Eq.s 2.99, 2.100 and 2.101:

$$\begin{aligned} \Delta U = &\frac{q^2}{\pi}\int_{0}^{\infty} |\Lambda(\omega)|^2\{Re[Z_{11}] + Re[Z_{22}] + Re[Z_{12}]\cos(\omega\Delta t_{b_1b_2}) + ... \\ &... + Re[Z_{21}]\cos(\omega\Delta t_{b_1b_2}) + Im[Z_{12}]\sin(\omega\Delta t_{b_1b_2}) - Im[Z_{21}]\sin(\omega\Delta t_{b_1b_2})\}d\omega. \end{aligned} \tag{3.38}$$

Using the same reasoning that allows to pass from Eq. 3.22 to 3.25, [63], Eq. 3.38 becomes in a synchrotron:

$$\begin{aligned} \Delta U = &\frac{\omega_0 q^2}{2\pi}\sum_{p=-\infty}^{p=\infty} |\Lambda(p\omega_0)|^2\{Re[Z_{11}] + Re[Z_{22}] + Re[Z_{12}]\cos(p\omega_0\Delta t_{b_1b_2}) + ... \\ &... + Re[Z_{21}]\cos(p\omega_0\Delta t_{b_1b_2}) + Im[Z_{12}]\sin(p\omega_0\Delta t_{b_1b_2}) - Im[Z_{21}]\sin(p\omega_0\Delta t_{b_1b_2})\}, \end{aligned} \tag{3.39}$$

Also the energy variation of the single beam can be expressed as a function of impedance. For the general case:

$$\Delta U_1 = \frac{q^2}{\pi}\int_0^\infty |\Lambda(\omega)|^2\{Re[Z_{11}] + Re[Z_{21}]\cos(\omega\Delta t_{b_1b_2}) - Im[Z_{21}]\sin(\omega\Delta t_{b_1b_2})\}d\omega, \tag{3.40}$$

$$\Delta U_2 = \frac{q^2}{\pi}\int_0^\infty |\Lambda(\omega)|^2\{Re[Z_{22}] + Re[Z_{12}]\cos(\omega\Delta t_{b_1b_2}) - Im[Z_{12}]\sin(\omega\Delta t_{b_1b_2}),\}d\omega, \tag{3.41}$$

and for the synchrotron case:

$$\Delta U_1 = \frac{q^2}{2\pi}\sum_{p=-\infty}^{p=\infty} |\Lambda(p\omega_0)|^2\{Re[Z_{11}] + Re[Z_{21}]\cos(p\omega_0\Delta t_{b_1b_2}) - Im[Z_{21}]\sin(p\omega_0\Delta t_{b_1b_2})\}, \tag{3.42}$$

$$\Delta U_2 = \frac{q^2}{2\pi}\sum_{p=-\infty}^{p=\infty} |\Lambda(p\omega_0)|^2\{Re[Z_{22}] + Re[Z_{12}]\cos(p\omega_0\Delta t_{b_1b_2}) + Im[Z_{12}]\sin(p\omega_0\Delta t_{b_1b_2})\}. \tag{3.43}$$

To benchmark these calculations, the energy variation of the two beams system, ΔU_1, the energy variation of beam one, ΔU_2, the energy variation of beam two and ΔU the total energy variation of two beams, were computed both in time and in frequency domain for the pillbox cavity and the beams discussed in section 2.6.4 as a function of $\Delta t_{b_1b_2}$. The beam loss factors, the energy variations divided by the product of the beam charges q^2, are shown in Fig. 3.2, as a function of $\Delta t_{b_1b_2}$, the entrance delay into the pillbox of beam two with respect to beam one. The behaviour of the beam loss factor has been already discussed in section 2.6.4. What is important to note at this point is that there is no difference between the results of the equations in time domain (Eq.s 2.109, 2.113 and 2.99) or in frequency domain (Eq.s 3.40, 3.41 and 3.38), as expected.

Finally, Using Eq. 2.39, one can define the power flux deposited in a device by the two beam system in terms of impedance as:

$$\begin{aligned}\Delta P = &\frac{f_0q^2}{\pi}\int_0^\infty |\Lambda(\omega)|^2\{Re[Z_{11}] + Re[Z_{22}] + Re[Z_{12}]\cos(\omega\Delta t_{b_1b_2}) + ... \\ &... + Re[Z_{21}]\cos(\omega\Delta t_{b_1b_2}) + Im[Z_{12}]\sin(\omega\Delta t_{b_1b_2}) - Im[Z_{21}]\sin(\omega\Delta t_{b_1b_2})\}d\omega,\end{aligned} \tag{3.44}$$

or for a synchrotron:

$$\begin{aligned}\Delta P = &f_0^2q^2\sum_{p=-\infty}^{p=\infty} |\Lambda(p\omega_0)|^2\{Re[Z_{11}] + Re[Z_{22}] + Re[Z_{12}]\cos(p\omega_0\Delta t_{b_1b_2}) + ... \\ &... + Re[Z_{21}]\cos(p\omega_0\Delta t_{b_1b_2}) + Im[Z_{12}]\sin(p\omega_0\Delta t_{b_1b_2}) - Im[Z_{21}]\sin(p\omega_0\Delta t_{b_1b_2})\}.\end{aligned} \tag{3.45}$$

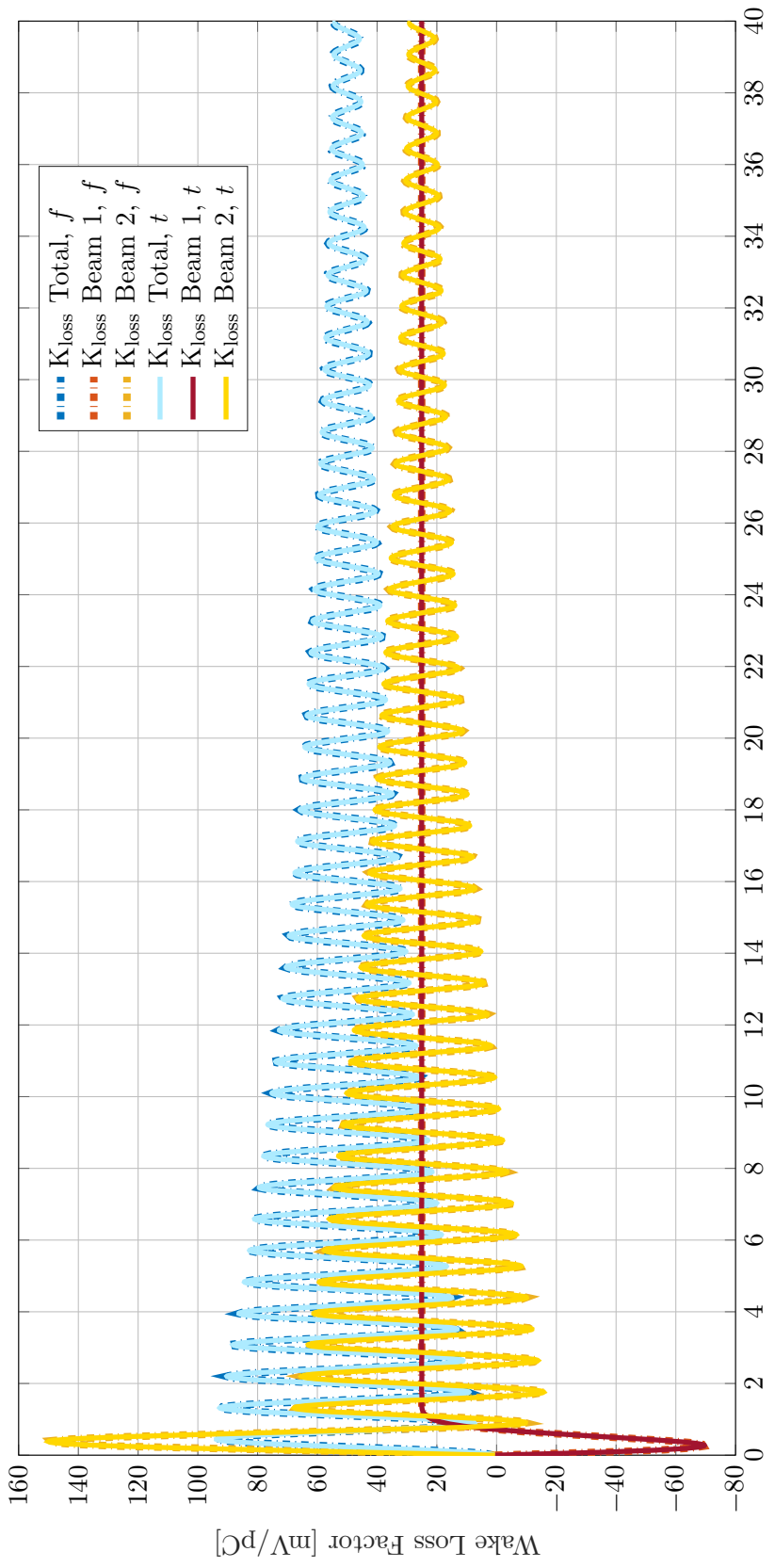

Figure 3.2. Beam Loss factor of two gaussian bunch profiles traversing a cavity with a delay $\Delta t_{b_1 b_2}$. Comparison between dissipated power for formulations in time domain (indicated with t) and frequency domain (indicated with f). Cavity's parameters: $b = 0.05$ m, $\sigma = 3.5 \cdot 10^3\ \Omega^{-1}\mathrm{s}^{-1}$, $L = 0.3$ m. Bunch parameters: $\sigma_b = 0.05$ m.

3.3.3 Maxima and Minima of the RF-heating Power In The Two Beams Case

As discussed in section 2.6.4, the energy dissipated by the two beams in the vacuum chamber is strongly dependent on the entrance delay between beam one and beam two inside the vacuum chamber, $\Delta t_{b_1 b_2}$. It is interesting to understand what are the value of the $\Delta t_{b_1 b_2}$ for which the power dissipated in the device has a maximum or a minimum so that the maxima can be avoided. This is an easy task if one considers the dissipated power equations in the frequency domain 3.44 and 3.45 where the contribution of $\Delta t_{b_1 b_2}$ is isolated with respect to the other contributions. Further, since the dissipated power and the dissipated energy in the device are simply linked by a constant by Eq. 3.38, the problem of finding the extreme points of the power translates in finding those points for the energy. With this aim, let's consider the energy dissipated by a two beams system traversing a device, Eq. 3.38. To find its maxima and minima one can derive the equation with respect to $\Delta t_{b_1 b_2}$, so obtaining:

$$\begin{aligned}\frac{d(\Delta U)}{d(\Delta t_{b_1 b_2})} =& \frac{q^2}{\pi} \int_0^\infty \omega |\Lambda(\omega)|^2 \{ -Re[Z_{12}] \sin(\omega \Delta t_{b_1 b_2}) - Re[Z_{21}] \sin(\omega \Delta t_{b_1 b_2}) + ... \\ & ... + Im[Z_{12}] \cos(\omega \Delta t_{b_1 b_2}) - Im[Z_{21}] \cos(\omega \Delta t_{b_1 b_2}) \} d\omega = 0,\end{aligned} \tag{3.46}$$

working out Eq. 3.46 leads to:

$$\Delta t_{b_1 b_2} = \frac{1}{\omega} \arctan\left(\frac{Im[Z_{21}] - Im[Z_{12}]}{Re[Z_{21}] + Re[Z_{12}]} \right) + \frac{n\pi}{\omega} \tag{3.47}$$

where $n \in \mathbb{N}$ and $n \geq 0$.

It is well known that in the co-moving wakefield scenario $Z_{12} = Z_{21}$ holds because of the reciprocity theorem [68], however, there is no hard proof at the moment that such relations holds also for the counter-moving wakefield scenario. Let's make the hypothesis that this relation always holds. This means that in Eq. 3.47 the first term is always equal to zero. Thus, Eq. 3.47 becomes:

$$\Delta t_{b_1 b_2} = \frac{n}{2f}, \tag{3.48}$$

where $\omega = 2\pi f$ has been used.

The implication of the Eq. 3.48, can be better understood with an example. Let's consider again the case of the pillbox cavity traversed by the two beams discussed in section 2.6.4. The beams are able to excite only the first resonant mode of the cavity that resonates at a frequency $f_r = 1.1418$ GHz. To find the delay between the two beams that gives the maxima and the minima of the dissipated power in the pillbox, one applies Eq. 3.48 with $f = f_r$. The first extreme point is found at $\Delta t_{b_1 b_2} = 0$ and it is a minimum , the second at $\Delta t_{b_1 b_2} = 1/(2f_r)$ and is a maximum, the third at $\Delta t_{b_1 b_2} = 2/(2f_r)$ and is a minimum, the fourth at $\Delta t_{b_1 b_2} = 3/(2f_r)$ is again a maximum and so on. As it was already discussed in section 2.6.4, if the entrance delay between the two beams is null, they both excite the mode inside the pillbox cavity but with opposite phases, since the geometry of the problem is symmetric. The net result is that the mode inside the cavity is not excited. However, if the delay between the entrance of the two beams is such that the second beam enters in phase

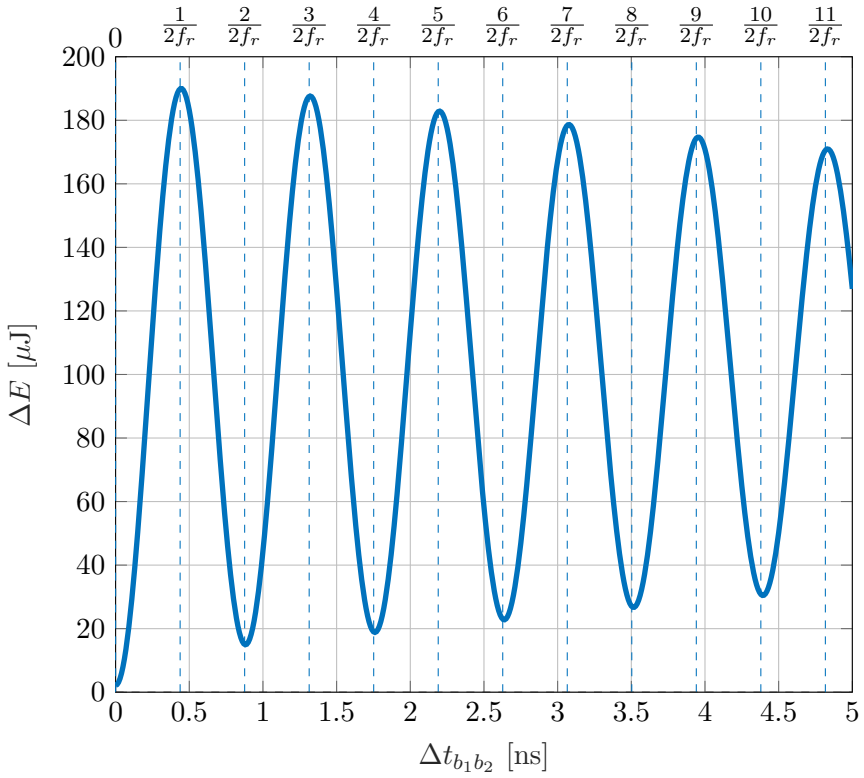

Figure 3.3. The energy dissipated in the pillbox cavity traversed by two beams, discussed in section 2.6.4, as a function of $\Delta t_{b_1 b_2}$ is reported with the coordinate of the maxima and minima obtained by Eq. 3.48 highlighted. The energy dissipated was obtained by simulations.

with the resonating mode excited by the first beam, then, the second beam and the mode interact constructively, i.e. the second beam provide even more energy to the mode. This happens when $\Delta t_{b_1 b_2} = 1/2f_r$, while for $\Delta t_{b_1 b_2} = 2/2f_r$ the beam and the mode are out of phase and the beam takes energy from the mode. The energy dissipated in the pillbox cavity as a function of $\Delta t_{b_1 b_2}$ is reported in Fig. 3.3 where also the coordinate of the maxima and minima obtained by Eq. 3.48 are highlighted. It is possible to see that Eq. 3.48 can individuate all the $\Delta t_{b_1 b_2}$ corresponding to the maxima and minima of the dissipated energy, and so of the dissipated power.

Usually, $\Delta t_{b_1 b_2}$ is fixed and depends on the distance of the studied equipment from the closest beam interaction point, refer to Appendix A. In this context, the method exposed to find maxima and minima of the dissipated power can help in understanding if there are modes in the device that could be intensified constructively because of the passage of the two beams (the modes that have a resonant frequency $f_r \approx n/2\Delta t_{b_1 b_2}$, with n odd), in such a case the frequency of those modes should be shifted with dedicated modification in the design.

Since the energy and the power dissipated in the device are proportional via the revolution frequency (refer to Eq. 2.39), an oscillating behaviour like the one presented in Fig. 3.3 for the dissipated energy is expected also for the dissipated power. This was verified by simulations by Giordano et al. [62].

3.4 Conclusions

This was a background and a results chapter. The definition of longitudinal and transverse impedance has been introduced and the energy and power dissipated in a device by one or two beams has been expressed as a function of impedance in the frequency domain. As original contribution, the chapter has presented the derivation of the entrance delay between two beams into a vacuum chamber that maximizes or a minimizes the dissipated power and energy into the vacuum chamber itself. It was shown that these entrance delays are frequency dependent and an example was discussed for one mode in a pillbox cavity for which the derived equation was able to match the maxima and minima. This tool, if the time entrance delay between the beams is fixed, can be used to easily detect modes in the device that could be intensified constructively because of the passage of the two beam, allowing to take the due modifications on the design.

Chapter 4

Simulations of Impedance Induced Thermal Effects

This chapter contains original material partially published as light peer review proceeding [69].

The project High Luminosity Large Hadron Collider (HL-LHC) calls for the increase of beam intensity and brightness in the LHC machine. In such a scenario, beam-environment electromagnetic interactions are a crucial topic: they could lead to uneven power deposition in machine equipment. This could lead to several problems, for instance: the resulting irregular temperature distribution would generate local thermal gradients, and this would create mechanical stresses which could lead to cracks and premature failure of accelerator devices. Further, the temperature increase can lead to material outgassing. This may be unacceptable for the accelerator performance because of the vacuum pollution.

This chapter presents a method to study this phenomenon by coupled electromagnetic thermo-mechanical simulations. The method is subsequently benchmarked against experimental data taken on an installed device during the LHC run.

4.1 Introduction

Beam induced heating, or RF-heating, on components i.e. the heat load due to electromagnetic interactions between particles beam and equipment, is a crucial issue for high intensity/brightness particle accelerators. Taking as example the LHC, RF-heating imposed severe limitations on its first operational run (2009-2013); some devices were damaged and numerous actions had to be taken to reduce the RF-heating detrimental effects [49].

Previously in this manuscript (section 3.3.1), it was shown that the electromagnetic beam-equipment interaction causes a power deposition proportional to the square of the beam intensity and to the real part of the device impedance according to Eq. 3.25:

$$\Delta P = \left(f_0 e N_{beam}\right)^2 \sum_{p=-\infty}^{p=+\infty} |\, \Lambda(p\omega_0)|^2 \; Re\left[Z_z(p\omega_0)\right] \tag{4.1}$$

Where N_{beam} is the beam intensity, e is the elementary charge, f_0 is the revolution

frequency of the beam and $\omega_0 = 2\pi f_0$, Λ is the normalized beam spectrum and $Re[Z_z]$ is the real part of the longitudinal coupling impedance.

RF-heating can be split in two contributions:

- Resistive wall impedance (RWI) heating. This phenomenon distributes the heat flux regularly on the device walls according to the electric conductivity and permittivity and the magnetic permeability of the material and to the inverse of the beam-wall distance.
- Resonant Modes (RM) heating. Due to the presence of trapped electromagnetic resonant modes in a device, the heat flux is distributed in a highly irregular way dependent on the mode field maps.

As a result, while RWI generates smooth temperature maps, RMs can lead to an uneven temperature distribution. Temperature gradients or power deposition in unexpected areas may induce intense mechanical stresses that can cause failures, or generate other undesired effects as material damage [32] and/or outgassing [70]. With the increase in beam intensity and the decrease in bunch length planned for the next generation of particle accelerators, the RF-heating phenomenon will be intensified. Thus, this problem must be considered in equipment design, particularly, for the Beam Intercepting Devices (BIDs) as collimators or scrapers. They can suffer of severe RM and RWI heating because they work in close proximity to the particle beam, their geometry is complex and they are made by materials that have suboptimal electromagnetic properties (as discussed in chapter 1).

4.1.1 Scope and Structure of the Chapter

In the context just outlined, a method that allows to simulate accurately the local thermo-mechanical effects of the RF-heating would be extremely helpful in BIDs design. However, at present, just few studies deal with this problem [32, 71, 72]. This chapter presents an alternative way to simulate the thermo-mechanical RF-heating induced effects and benchmarks it against experimental temperature data taken from an LHC device during the beam run.

Section 4.2 discusses the methodology to obtain a local 3D map of the RWI and RMs RF-heating that is used to simulate the RF-heating thermal and mechanical effects on accelerator devices. In the same section an example of practical application of the method on a BID, the TDIS, is also reported (for more detail on the device refer to section 7.3).

Subsequently, in section 4.3 the method is benchmarked against experimental temperature data from the TOTEM roman pot in the LHC.

Finally, in section 4.4, the chapter is concluded and the main discussed points are recalled.

4.2 Methodology

The current investigation defines a procedure to interface the two commercial programs CST studio suite® [56] and ANSYS mechanical® [73]. These tools are well known and tested at CERN: CST studio suite® is a standard for device impedance

computations [57, 49], while ANSYS mechanical® is widely used for structural and thermal analysis [74, 75, 76, 77]. The former simulates the RF-heating map that is subsequently imported into the latter to calculate thermal and mechanical effects.

The entire procedure is depicted in Fig. 4.1. There are three main macro-areas: Electromagnetic Simulations (A, B and C blocks for RM heating and F input for RWI heating), CST®, Beam Power Dissipation and Interface (D and E blocks), Thermomechanical Simulations (G block), ANSYS®. Every macro-areas is divided in sub-blocks. Each of them will be explained taking as example the analysis done on the Target Dump Injection Segmented (TDIS) [78]. The TDIS is a BID that will protect LHC downstream equipment during the injection phase, absorbing the injected beam in case of a misfiring injection kicker [79]. This device is treated in depth in section 7.3.

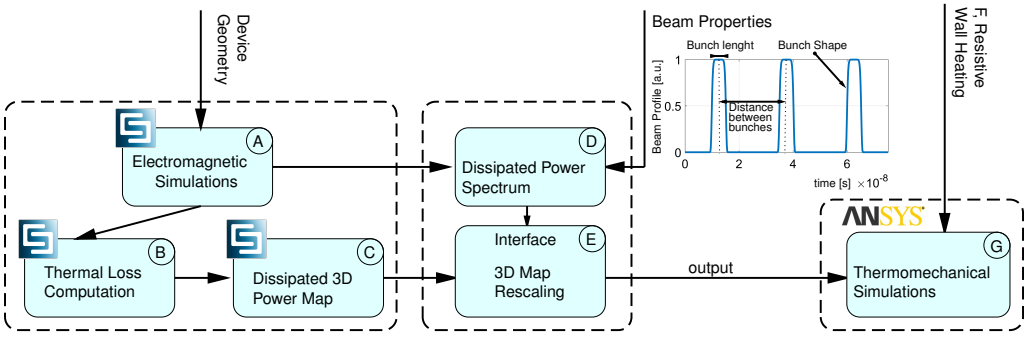

Figure 4.1. Block diagram of the methodology with some of the beam properties.

4.2.1 A, Electromagnetic Simulations

The device CAD model for production is simplified and taken as geometric model for the electromagnetic simulations. Only the electromagnetic important elements should be considered (screws, little grooves, small surfaces should be removed, see Fig. 4.2 for example), in order to obtain the balance between accuracy of the model and simulation speed.

Subsequently, the presence of trapped RM in the device is investigated through the CST Eigenmode solver [60]. The solver provides for each RM the resonating frequency f_m, the quality factor Q, the Shunt impedance R_s, the local value of electric and magnetic fields and the surface currents in the entire geometry [48]. After this is done, a second Wakefield simulation is run. In this simulation electric and magnetic field monitors are set at the resonant frequency of each RM obtained by the Eigenmode solver, plus an electric and magnetic monitor is to be set at low frequency far from any resonant mode frequency. These last monitors are needed for the RWI heating map, discussed later in this section.

As a first benchmark the modes found by the two solvers should well agree in resonating frequency, quality factor, and shunt impedance. If this is the case the procedure can continue, otherwise the disagreement has to be investigated and fixed[1].

[1] A small disagreement between the results of the two solvers is expected due to the fact that, at

Since the beam can excite only a finite number (N) of modes in the device, because of its limited spectrum bandwidth, henceforth, only they should be considered.

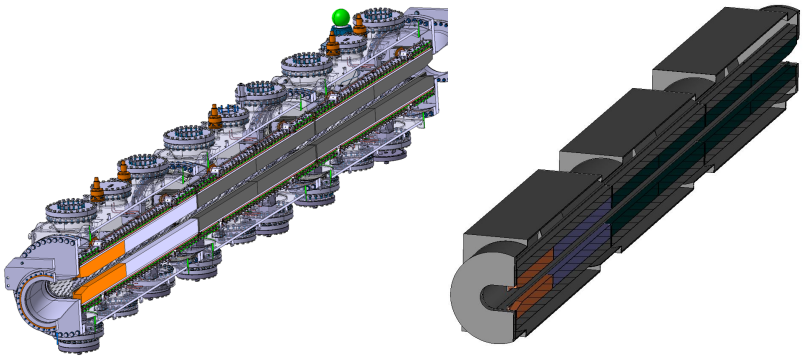

Figure 4.2. TDIS CAD model, left, and simplified TDIS CAD model, right.

4.2.2 B, Thermal Loss Computation

By processing the data from Wakefield or Eigenmode, the local dissipated power map for each mode can be obtained. The power dissipated by the mth mode can be divided in:

- Losses per unit volume $P_{\mathcal{V}m}$ [W/m^3].

  In this category one finds the losses in dielectric, i.e. resistive Joule losses, and in ferromagnetic materials, i.e. eddy current losses and magnetic hysteresis losses. The Joule and eddy currents losses can be computed using the first term on the right of Eq. (4.2) [34]. More involved is the computation of $P_{\mathcal{VH}m}$, the power dissipated by magnetic hysteresis in ferromagnetic material [80].

$$P_{\mathcal{V}m}(x,y,z,f_m) = \sigma E^2_{rms}(x,y,z,f_m) + P_{\mathcal{VH}m}, \tag{4.2}$$

  where σ is the electric conductivity of the material (frequency dependent), E_{rms} is the root mean square value of the local electric field.

- Losses per unit surface $P_{\mathcal{S}m}$ [W/m^2].

  Using the flux of the real part of the Poyinting vector, one can compute the power which flows and is dissipated within the walls of good conductors, Eq. (4.3) [48].

$$P_{\mathcal{S}m}(x,y,z,f_m) = \sqrt{\frac{\pi f_m \mu_0}{4\sigma}} \mid \boldsymbol{H}_t(x,y,z,f_m) \mid^2 . \tag{4.3}$$

  where $\boldsymbol{H}_t$ is the local surface current vector and μ_0 is the vacuum permeability.

The CST® software automatically computes both these local losses ($P_{\mathcal{S}m}(x,y,z,f_m)$ and $P_{\mathcal{V}m}(x,y,z,f_m)$) using the data of the magnetic and electric field monitors.

the writing time, it is not possible to set the same boundary conditions (open, non reflective), in both the solvers.

4.2.3 C, Dissipated 3D Power Map

The results of the previous step can be mapped into the device model geometry using the CST thermal solver® [60]. This generates a 3D map of the power dissipated on the device by each RM[2]. However, the map does not take into account the properties of the real beam that is passing through the device: beam revolution frequency f_0 and intensity N_{beam}, bunch shape, bunch length, distance between bunches and number of bunches. Indeed, the Eigenmode solver calculates the electromagnetic field pattern solving an Eigenmode problem with no excitation applied [81], while in the Wakefield solver the excitation bunch is different with respect to the real beam that passes into the component. This implies that, while the 3D dissipated power distribution on the device is correct, the local absolute value is not. There is a scaling factor between the power dissipated by the actual beam and the one computed by the solvers.

4.2.4 D, Dissipated Power Spectrum

To obtain this scale factor the real beam characteristics are considered to compute the beam spectrum $\Lambda(f)$ and so the deposited power $\Delta P(f)$ by Eq. (4.4) [67]:

$$\Delta P(f) = \left(f_0 e N_{beam}\right)^2 |\, \Lambda(f)|^2 \; Re[Z_z(f)], \tag{4.4}$$

where f is a generic frequency.

Dissipated Power due to Resonant Mode

Since the simulated model is an approximation of the reality, the resonant frequency of the real modes in the device could slightly differ from the resonant frequencies of the simulated modes. This could have a huge impact on their dissipated power. Thus, a sensitivity analysis of this quantity should be performed. Using the Eigenmode results, the device impedance due only to the resonant modes can be obtained. The single mode impedance is found considering Eq. (4.5) [82], (where $i = \sqrt{-1}$) for a given Q factor, shunt impedance and resonating frequency.

$$Z_z(f) = \frac{R_s}{1 + iQ\left(\frac{f_m}{f} - \frac{f}{f_m}\right)} \tag{4.5}$$

Summing the results of Eq. (4.5) for N modes, one determines the impedance contribution due only to the resonant modes, RM impedance. To study the sensitivity of the dissipated power with respect to the frequency of the resonant modes, several RM impedance profiles can be computed moving the resonant frequency of every single mode randomly within an arbitrary frequency range [83]. This analysis should consider a statistically significant number of computed dissipated powers for different resonant frequencies.

Among all the results obtained, two cases should be analysed; the case of maximum induced power loss in the device and the average case. The former is to

[2]At the writing day the CST thermal solver seems not able to import volumetric heating load from the Eigenmode solver while the import of volumetric loads works with the Wakefield solver. No issues have been observed with the surface load import from both solvers.

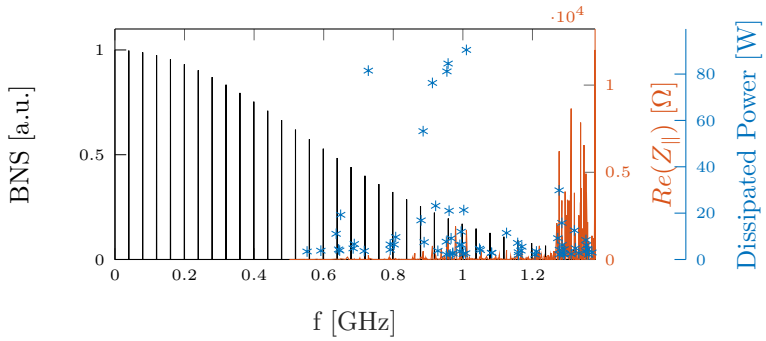

Figure 4.3. Power spectrum, Beam normalized spectrum (BNS) and longitudinal impedance real part, in different scales, refer to colors.

be chosen during the design phase of the device since it better represents a worst case scenario, the latter should represent a more realistic scenario.

The maximum frequency shift can be set considering the geometrical simplifications done to the CAD model. Furthermore, if there are movable parts in the device, the frequency shift should also take into account this point. In real situations, the motion of the movable parts may be slightly different from the expected one because of the not perfect control system accuracy. In simulations, usually, the motion is considered as perfectly coincident with the expected one. Thus, the difference in the real and the simulated configurations may lead to a frequency shift between the real and the simulated mode resonant frequency. As example for the TDIS a frequency shift of ± 10 MHz was used. Figure 4.3 shows the TDIS longitudinal impedance, the HL-LHC beam normalized spectrum (BNS) and the dissipated power spectrum.

Dissipated Power Due to Resistive Wall Impedance

The RF-heating contribution of the RWI has to be separated from the contribution of the RMs. This can be done performing a further wakefield simulations with a modified geometry that eliminates the resonant modes in the frequency range of interest, keeping the RWI contribution. The resulting broad band impedance is used in Eq. 4.1 to compute the RWI Heating. In section 4.3.2 it is shown an example of how this can be done.

4.2.5 E, 3D Map Rescaling

For each mode, the surface and volumetric power distribution, $P_{\mathcal{S}m}(x, y, z, f_m)$ and $P_{\mathcal{V}m}(x, y, z, f_m)$, are rescaled and added to the contributions of the other RMs to obtain the total volumetric power losses $P_{\mathcal{V}}(x, y, z)$ and the total surface power losses, $P_{\mathcal{S}}(x, y, z)$. This is done according to the following relations:

$$P_{\mathcal{S}}(x, y, z) = \sum_{m=1}^{m=N} \Delta P(f_m) K_m P_{\mathcal{S}m}(x, y, z, f_m) \tag{4.6}$$

$$P_{\mathcal{V}}(x, y, z) = \sum_{m=1}^{m=N} \Delta P(f_m) K_m P_{\mathcal{V}m}(x, y, z, f_m) \tag{4.7}$$

where N is the number of RMs considered and

$$K_m = \frac{1}{\iiint_{\mathcal{V}} P_{\mathcal{V}m}(x,y,z,f_m)d\mathcal{V} + \iint_{\mathcal{S}} P_{\mathcal{S}m}(x,y,z,f_m)d\mathcal{S}} \tag{4.8}$$

is the inverse of the total dissipated power computed by the CST solver. It is useful to recall that, in Eq. 4.8, the terms $P_{\mathcal{S}m}(x,y,z,f_m)$ and $P_{\mathcal{V}m}(x,y,z,f_m)$ are provided by CST software.

The term K_m is the normalization factor of the power map. To better explain its meaning, let's consider the case of a device with only surface losses (the device is made just of metals). Thus, in Eq. (4.6), $K_m P_{\mathcal{S}m}(x,y,z,f_m)$ is the unit 3D dissipated power map for the mth mode i.e. its surface integral on the whole device is one. If also volumetric power losses are present, the surface integral on the whole device of $K_m P_{\mathcal{S}m}(x,y,z,f_m)$ it is not one any more but it is a number between zero and one that represents the percentage of surface losses with respect to the total losses (volumetric plus surface losses).

Once the volumetric and surface power map has been normalized by the factor K_m, multiplying by the expected dissipated power for that mode ($\Delta P(f_m)$), the 3D power map with the local correct absolute values of the dissipated power is obtained. Finally, the heating contribution of every RM is summed in order to have the 3D map of the total heating power $P_{\mathcal{S}}(x,y,z,f_m)$ and $P_{\mathcal{V}}(x,y,z,f_m)$.

4.2.6 F, The Resistive Wall Impedance Heating

The RWI power is distributed as a heat flux in the geometry according to the beam-wall distance and the electromagnetic properties of the wall material. A 3D map like this one can be obtained practically in a Wakefield simulations considering a magnetic and electric field monitor at very low frequency far from any resonant modes [84]. The volumetric contribution of the RWI heating are added to the total volumetric power losses $P_{\mathcal{V}}(x,y,z)$ and the surface contribution of the RWI heating are added to the total surface power losses, $P_{\mathcal{S}}(x,y,z)$ as if RWI heating was another resonant mode. An example on how to include the RWI in the simulations is shown in section 4.3.4. Please note that the RWI heating map can be obtained only with the Wakefield solver and not with the Eigenmode one.

4.2.7 G, Output and Thermo-mechanical Simulations

To perform the thermo-mechanical simulations the maps $P_{\mathcal{V}}(x,y,z)$ and $P_{\mathcal{S}}(x,y,z)$ are imported in the ANSYS workbench® and mapped as a surface heat load for good conductors or as volume heat load for dielectric and ferromagnetic materials.

The same geometrical model of the electromagnetic simulations should be used, every modification can lead to an inaccurate import of the impedance heating load. As validation, a steady state thermal simulations is done, the heating source is set as the $P_{\mathcal{V}}$ and $P_{\mathcal{S}}$ maps, the cooling source is a fictitious convection on all the bodies. If the RF heat load is correctly imported the power evacuated by convection must be the one expected from Eq. (4.1). If the evacuated power does not match the expected value of the imported power, it could be due to mesh issues, the mesh of the CST thermal solver and ANSYS should be very similar. An example of imported

power map for the TDIS is shown in Fig. 4.4. In Fig. 4.5 the temperature map induced by the RF-heating in the TDIS is reported and in Fig. 4.6 the related mechanical stresses, due to the thermal differential expansion, are shown.

4.3 The Benchmark Case: The TOTEM Roman Pot

The TOTEM experiment [85, 86] in the LHC has the aim of measuring the total proton-proton cross section and to study elastic and diffractive scattering at the LHC energy.

These measurements are performed on protons at distances as small as 1 mm from the beam center. The experiment uses Roman Pots (RP), to move silicon detectors close to the beam to detect these core[3] particles. An RP is a device with a movable part that allows the positioning of the silicon detector in the beam core without interfering with the primary vacuum.

In the first LHC run, during close insertions with high intensity beams running, impedance heating issues were observed in RPs [49], i.e. ferrite outgassing due to a too high temperature of the material. Since after LS2 the LHC beam intensity is planned to be increased up to twice the current value, these pieces of equipment had to be optimized for the new scenario. A new RP, the so called cylindrical RP, optimized to minimize the electromagnetic beam coupling, was designed [86]. A prototype was built and installed in the LHC. On this prototype in 2015 and 2016, several temperature sensors were installed and the temperature increase of the device during a beam run was recorded [87]. There was not active cooling acting on the RP during this run.

In this section the method to simulate impedance related heating effects is applied to replicate those experimental temperature measurements.

In Section 4.3.1 the geometry and the materials of the TOTEM RP are reported.

Section 4.3.2 shows the electromagnetic simulations performed to estimate the device impedance, and section 4.3.3 reports the RF-heating calculation.

Finally, section 4.3.4 discusses the results of the thermal simulations comparing them with the measurements.

4.3.1 Geometry and Materials of the TOTEM Roman Pot

The geometry of a cylindrical TOTEM RP is reported in Fig. 4.7. In Fig. 4.7a the picture of a spare RP is shown. Figure 4.7b shows an isometric view of the RP CAD model, which was reconstructed according to the mechanical drawing and to measurements taken on the spare RP. In this picture one can distinguish two parts constituting the device, a fixed primary vacuum vessel, to be attached to the LHC pipe, and a secondary vacuum vessel, which can move along the y axis. The bellow deformation allows the motion of the secondary vacuum vessel while the primary vacuum vessel remains fixed. Figure 4.7c displays a section cut of the RP, the x axis is normal to the cut plane. In this figure it is shown the movable cylinder on which the silicon target and the electronics are installed. Neither electronics nor the silicon

[3] A definition of beam halo and beam core can be found in section 7.2.1

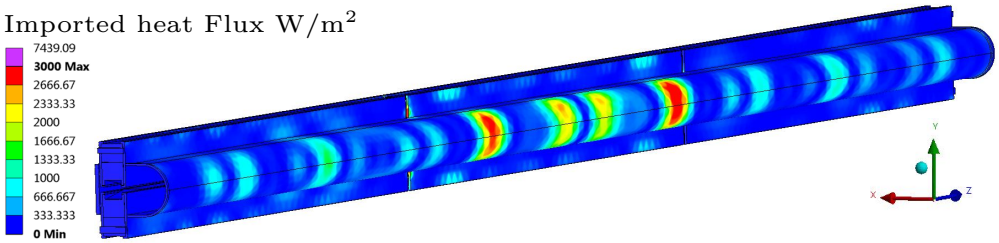

Figure 4.4. Example of a mode RF-heating map imported in ANSYS®, for the TDIS core components.

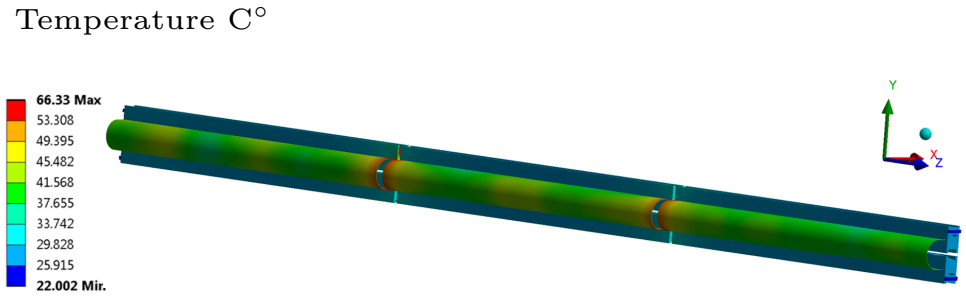

Figure 4.5. Global Temperature distribution of the TDIS.

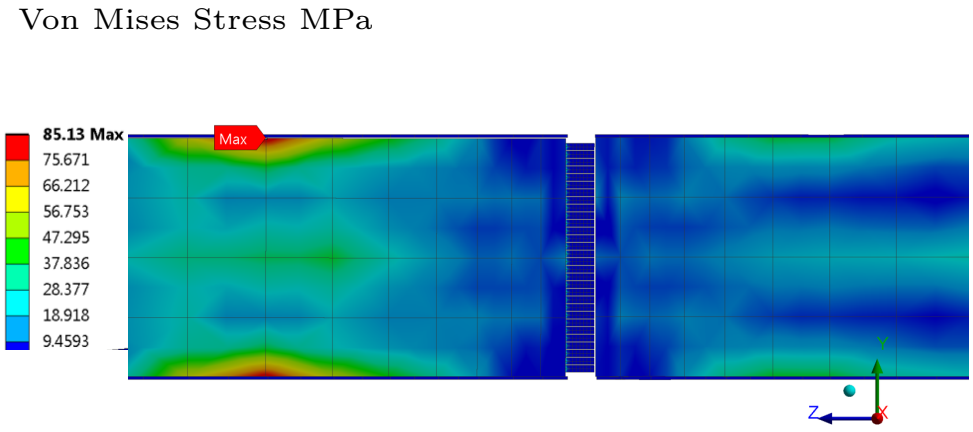

Figure 4.6. Maximum mechanical stresses in the TDIS. These stresses, 85 MPa maximum, are not critical for the device, however, they are not negligible if compared with the yield stress of the material, 250 MPa.

target are shown since they were removed during the temperature data acquisition, thus, they were not modelled.

This cylinder is rigidly attached by flanges to the secondary vacuum vessel and moves with it. The top face of the cylinder can be placed at an arbitrary distance with respect to the beam orbit, also shown in the picture. Between the movable cylinder and the wall of the primary vacuum vessel there is a gap of 2.5 mm, needed for the motion of the cylinder. Previous electromagnetic studies [88], have shown the presence of a strong electromagnetic mode resonating in this gap. To damp it, at the bottom of the cylinder, a ferrite ring was inserted. A system of springs (not represented in the CAD model) is pushing the ferrite ring towards the bottom flange to ensure good thermal contacts to evacuate the heat.

Regarding the materials, the whole TOTEM RP is made of Stainless Steel 316LN (SS316LN) except for the ferrite ring made of Trans-Tech® TT2-111R ferrite. The physical properties of the materials are reported in Table 4.1 and in Fig.s 4.8.

Finally, two last remarks: for the thermal simulations, it is useful to underline that inside both the primary vacuum vessel and the secondary vacuum vessel there is vacuum, thus, there is no convection in there. In this work, the distance of the beam-movable cylinder top surface was considered always equal to 3 mm. Because this was the distance used when the temperature measurements to reconstruct were taken.

Table 4.1. Material physical properties. The ferrite thermal properties were taken from the work of de Jong et al. [89]. Its electromagnetic parameters were measured at CERN [90]. The Stainless Steel 316LN data missing from the table were considered temperature dependent and are reported in Fig.s 4.8.

Material	$\sigma \left[\frac{\mathrm{S}}{\mathrm{m}}\right]$	k $\left[\frac{\mathrm{W}}{\mathrm{Km}}\right]$	C $\left[\frac{\mathrm{kJ}}{\mathrm{Kkg}}\right]$	$\rho \left[\frac{\mathrm{kg}}{\mathrm{m}^3}\right]$
SS316LN	$1.32e6$	·	·	·
Ferrite TT2-111R	·	5.4	0.712	5270

4.3.2 Electromagnetic Simulations

The electromagnetic properties of the TOTEM RP were estimated with CST Wakefield and Eigenmode simulations. First an Eigenmode simulation was run to obtain the resonant frequency f_m, the quality factor Q, and the shunt impedance R_s, for the first 10 modes. The device impedance was reconstruced from the Eigenmode data[4] using Eq. 4.5 for every mode and summing the results. After this was done, a Wakefield simulation was run, with electric and magnetic field monitors set at the resonant frequency of each RM obtained by the Eigenmode solver.

The real part of the impedance (the important part for the RF-heating computation) reconstructed from Eigenmode and the impedance real part obtained directly from Wakefield are reported and compared in Fig. 4.9. The agreement between

[4]Because of different convention between Eigemode and Wakefield, to compare the Wakefield impedance with the Eigenmode reconstructed one the Shunt Impedance obtained from Eigenmode has to be divided by 2 before reconstructing the impedance curve as a function of frequency.

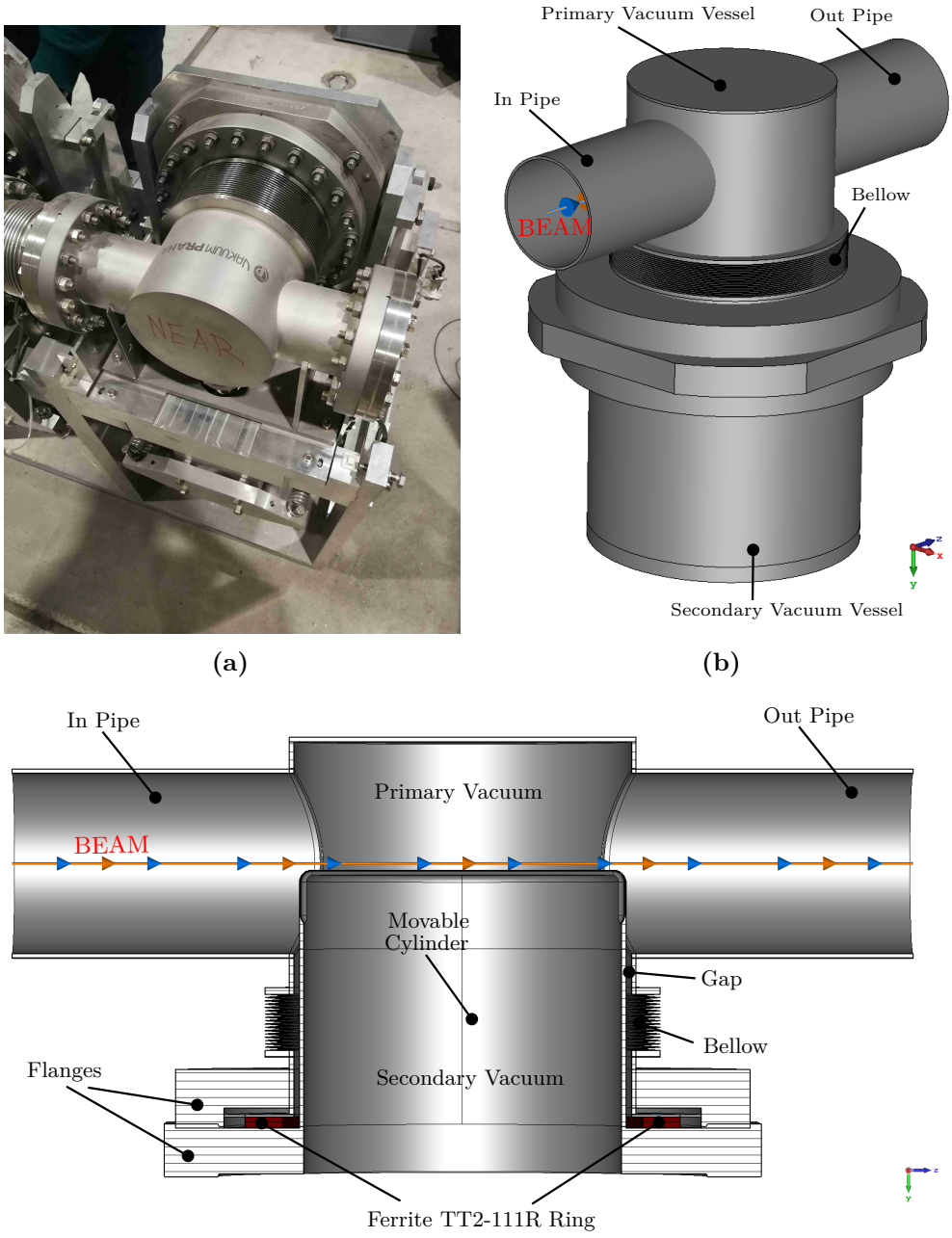

Figure 4.7. Geometry of the TOTEM RP. (a) Photo of a cylidrical TOTEM RP spare. (b) CAD model recontruced from drawing and measurements for electromagnetic and thermal simulations. (c) Section cut of the RP, the x axis is normal to the cut plane.

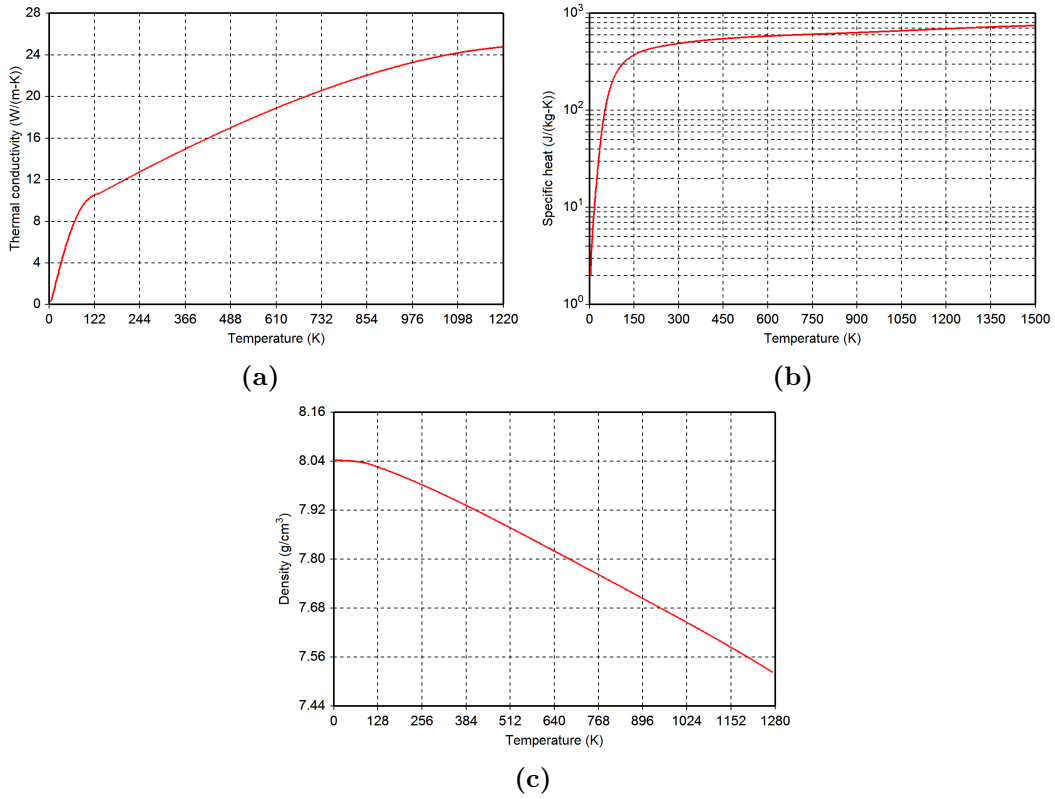

Figure 4.8. SS316LN physical properties as a function of temperature, taken from the CERN Engineering Source Target Interaction group database MPDB. (a) Thermal conductivity. (b) Specific heat. (c) Density.

the two curves is good. Furthemore, these results well agree also with previous investigations [88].

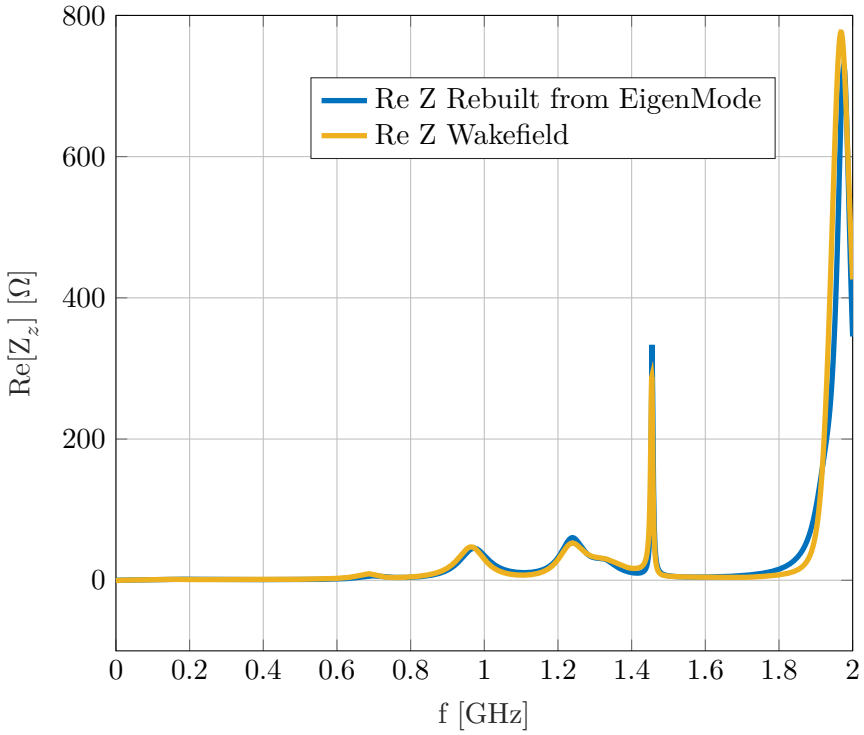

Figure 4.9. Impedance of the TOTEM roman pot. Comparison between the impedance rebuilt from Eigenmode and the impedance computed from Wakefield.

The Wakefield solver can take into account both the RWI and RM impedance while the Eigemode can estimate only RM impedance. However, the Wakefield solver does not separate the impedance contribution of the resistive wall from that of the device modes. Disentangling these two contributions allows to estimate separately the RF-heating due to each one of them and so to scale correctly the 3D heat maps for thermal simulations.

In order to divide the two contributions, the following steps were taken. The impedance due exclusively to the resonant modes was obtained as the impedance reconstructed from eigenmode. Thus, in principle, subtracting from the wakefield impedance the eigenmode reconstructed impedance should have given only the impedance contribution due to the resistive wall impedance. However, this approach could have been prone to numerical errors. Thus, to estimate only the contribution of the resistive wall impedance for the RP, another procedure was used. In the TOTEM RP, the element that is contributing the most to the impedance resistive wall is the movable cylinder top surface because it is the closest element to the beam, 3 mm distance. The impact of all the other components of the RP may be considered negligible due to their distance from the beam, that is 40 mm at least. Thus, a further Wakefield simulation was performed, with a beam passing at a distance of 3 mm from a squared SS316LN plate of dimension equal to the diameter of the cylinder top surface (143.5 mm). The geometry of the beam passing on the plate is

shown in Fig. 4.10a and the real part of the computed impedance is shown in Fig. 4.10b. This impedance was considered as the RP resistive wall impedance.

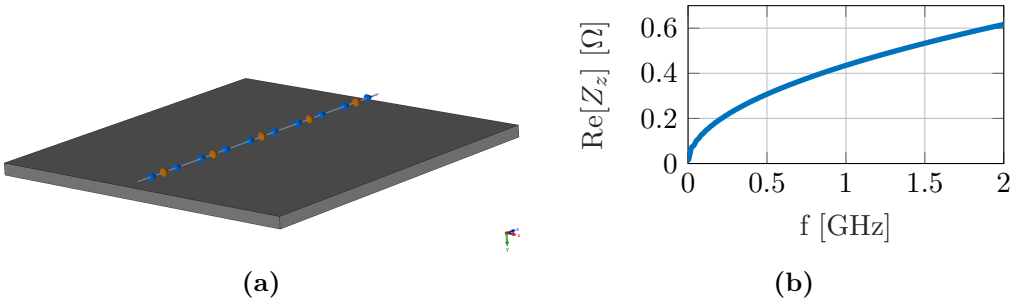

(a) **(b)**

Figure 4.10. Impedance simulations for the RM RWI. (a) Simulated Geometry. (b) Real part of the RWI.

4.3.3 Impedance Induced Heating

The measured temperature data to reproduce were acquired during the LHC fill 4381 (December 2015). In Table 4.2 the beam parameters for that fill are reported. The bunch distribution with respect to time was assumed to be Gaussian. The parameter f_0 is the revolution frequency of a particle in the LHC.

Table 4.2. Bunch parameters of LHC beam fill 4381, for which the temperature data in the RP were taken, ppb stands for protons per bunch, f_0 is the revolution frequency of a particle in the LHC.

Bunch Shape	Length ($4\sigma_{\text{rms}}$)	Interbunch Distance	N Bunches	ppb	f_0
Gaussian	1.229 [ns]	25 [ns]	1033	1.007e11	11.25 [kHz]

Considering the parameters reported in table 4.2, it was possible to compute the beam spectrum Λ and so, with the TOTEM RP impedance computed in the previous subsection, the RF-heating was estimated according to what was discussed in section 4.2.3.

In Fig. 4.11 the RF-heating due to every resonant mode is reported as a function of frequency. Both the average value and the worst case scenario values of the RF-heating are given for every mode. These two scenarios present similar losses values. This is because the modes resonating in the RP at frequencies lower than 1.5 GHz are broad band modes. Thus, a slight change of the mode resonant frequency of ($\pm$20) MHz cannot change dramatically the coupling between the beam and the device. Narrow band modes are present for frequency above 1.5 GHz. However, at that frequency the LHC beam spectrum is practically decayed and the power dissipation is negligible.

In table 4.3 the roman pot RF-heating computed with the Wakefield impedance (refer to Fig.4.9), with the impedance reconstructed from Eigenmode (refer to Fig. 4.9) and with the Wakefield resistive wall impedance shown in Fig. 4.10b is reported.

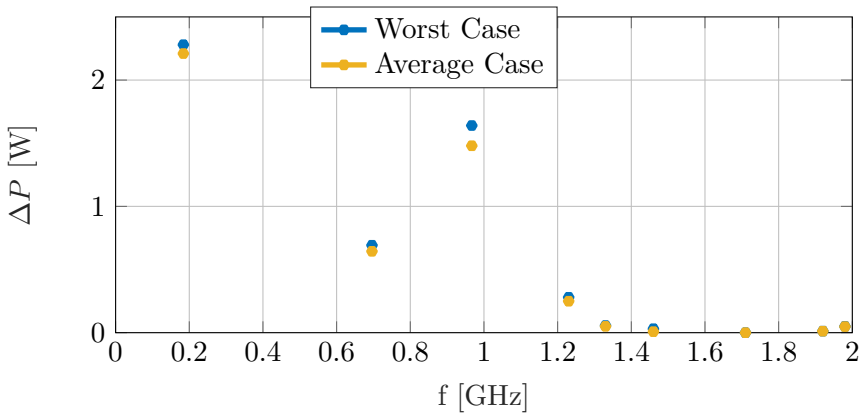

Figure 4.11. RM Impedance induced power spectrum for the TOTEM roman pot.

Looking at the numbers, the RF-heating computed from the RP impedance obtained directly from Wakefield (RWI+RM RF-heating in the table) is higher than the one computed with the impedance reconstructed from the Eigenmode data (RM RF-heating in the table). And the difference between the two losses is of the same order of magnitude of the resistive wall losses (RWI RF-heating in the table). This was expected because, as already said, the Wakefield solver takes into account both the resistive wall and the resonant mode losses, while the Eigenmode solver takes into account only the resonant mode losses. Thus, the losses computed using the eigemode solver impedance should be equal to the losses computed using the Wakefield solver impedance subtracting the losses computed using the resistive wall impedance, and this seems to be the case.

Using the CST thermal solver it was possible to obtain automatically the volumetric and surface power dissipated map for every resonant mode and for the resistive wall losses. As already said, it was found that setting an electric and magnetic field monitor at really low frequency, far from a device resonant mode, gives the resistive wall power distribution. For the TOTEM RP the monitors were set at 10 MHz. In Fig. 4.12 the RWI 3D power dissipated map computed from the CST thermal solver is reported. As expected, virtually the whole heating power (more than 99.9%) is dissipated as a surface load on the movable cylinder top surface right down the beam trajectory.

Another example of 3D power dissipated map is reported in Fig. 4.13 for the mode at 677 MHz. In this case most of the power is dissipated in the ferrite ring volume (about 86%), and a small percentage is dissipated as surface load on the internal walls of the roman pot (about 14%).

Using the developed CST-ANSYS interface introduced in section 4.2, these 3D maps were rescaled according to what exposed in section 4.2.5 and imported from CST into ANSYS. For the rescaling, the RM losses in the average case scenario were considered since this scenario is supposed to be more realistic. The RF-heating of each mode was imported separately. As import validation, a steady state thermal simulation was done, setting the imported map as heating load and the cooling source as a fictitious convection on all the bodies. It was verified for every import that the convection was evacuating the power dissipated in that mode given by Fig.

Table 4.3. Total dissipated power computed with the Wakefield impedance of the TOTEM RP (RWI+RM), with the impedance reconstructed by Eigenmode (RM) and with the Wakefield resistive wall impedance (RWI).

	Average Case Scenario	Worst Case Scenario
RM RF-heating Eigenmode	4.712 W	5.045 W
RWI RF-heating Wakefield	0.612 W	
RWI+RM RF-heating Wakefield	5.613 W	

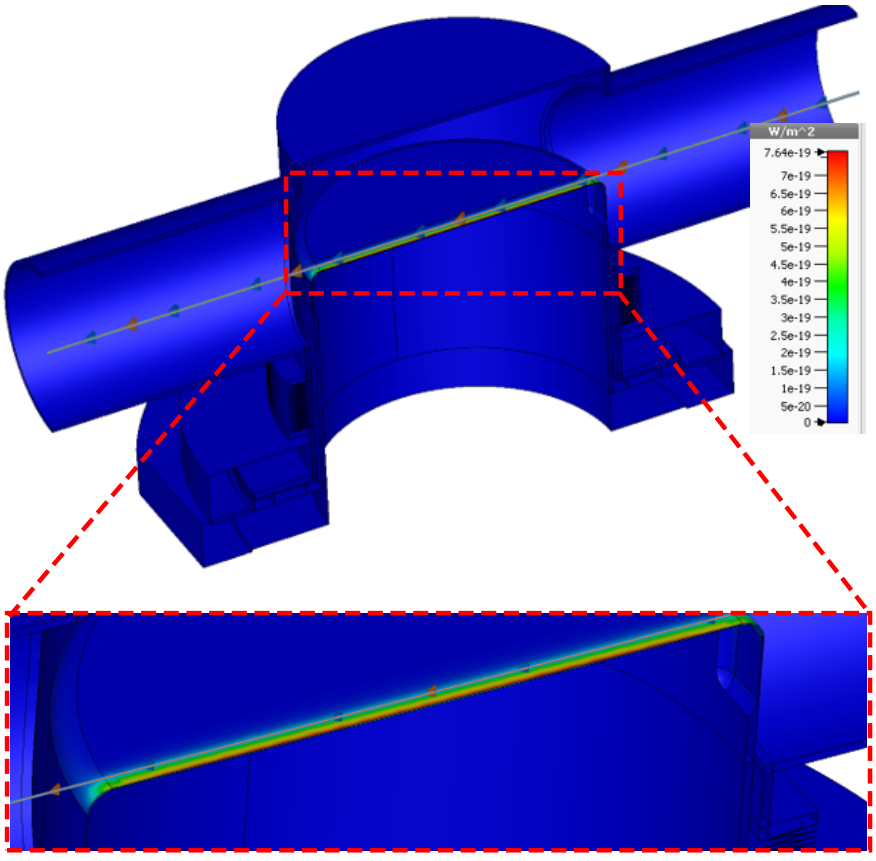

Figure 4.12. Resistive wall impedance RF-heating 3D map from CST thermal solver. As expected, virtually the whole heating power is dissipated on the movable cylinder top surface rigth down the beam trajectory.

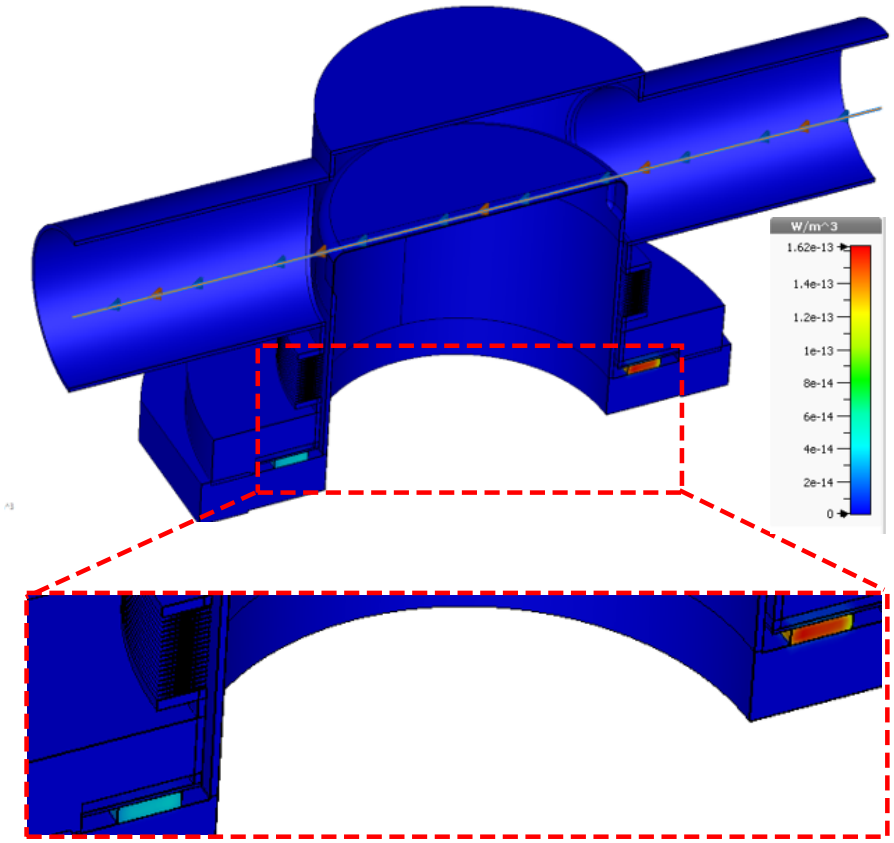

Figure 4.13. Resonant mode at 677 MHz impedance RF-heating 3D map from CST thermal solver. Almost the whole heating power is dissipated in the ferrite ring.

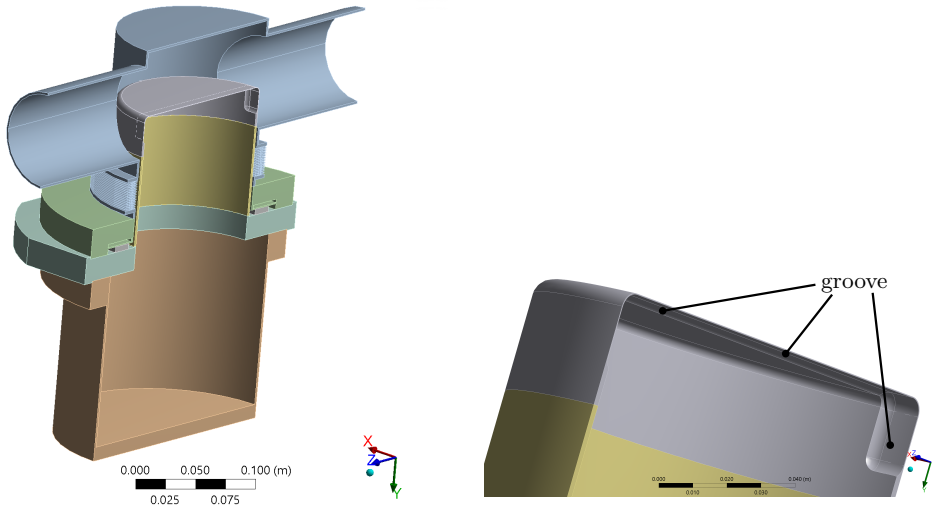

(a) (b)

Figure 4.14. (a) RP model for thermal simulations. (b) RP model, detail of the movable cylinder, groove. At the groove the thickness of the movable cylinder is reduced at 0.3 mm. Since the silicon detector has to be placed in the grove, the small thickness of the cylinder reduces the chances that particles are stopped in the metal of the cylinder before it can reach the detector.

4.11. The same verification was done for the resistive wall RF-heating with the value reported in table 4.3.

4.3.4 Thermal Simulations

Some Other Geometric Detail

For the thermal simulations it was used the same RP CAD model on which the electromagnetic simulations were run to help the thermal load import remapping process. In Fig. 4.14 the ANSYS RP model is shown. In particular, in Fig. 4.14a a global view of the geometry is reported while in Fig. 4.14b a detail of a groove on the movable cylinder top internal surface is shown. At the groove, the thickness of the movable cylinder is reduced to 0.3 mm. This is because inside this groove the silicon detector is supposed to be placed, and the small thickness of the cylinder reduces the chances that a particle is stopped in the metal of the cylinder before it can reach the detector, .

All the internal metal surfaces of the TOTEM RP are polished, i.e. they are machined to decrease their surface roughness, with the exception of the internal groove surface. These details are important for the estimation of the cooling mechanism, as will be clear in the following.

Heating and Cooling Sources

To reproduce the measured temperature data one needs to simulate the heating sources and the cooling sources that were present when the data were taken. In

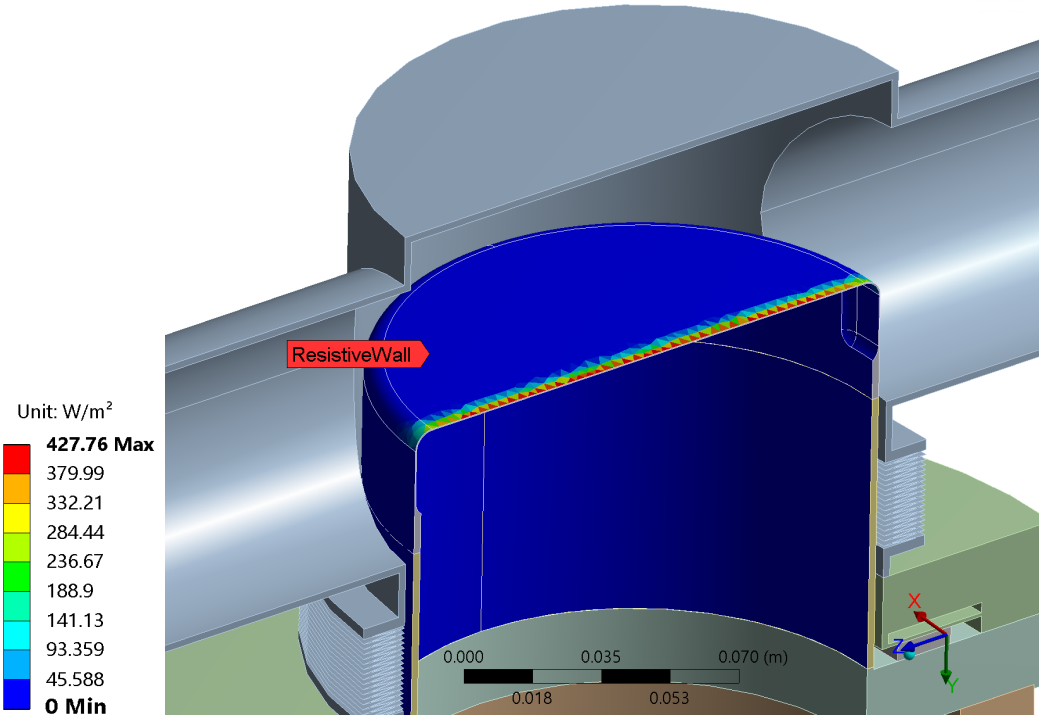

Figure 4.15. Example of rescaled dissipated 3D powermap imported in ANSYS from CST. The resistive wall losses is shown.

general the TOTEM RP can experience heating from three main sources, impedance heating, particle irradiation heating and dissipation due to electronics. During the temperature measurements the detector and all its electronics were removed from the secondary vacuum vessel, thus, there were no electronics dissipation. Furthermore, previous studies revealed that the expected particle irradiation heating in the cylindrical TOTEM RP is of the order of 10 mW [91, 92]. This value is negligible if compared with the about 5 W dissipated by impedance. Thus, one can assume that the only heating source acting on the TOTEM RP is the impedance induced heating. In Fig. 4.15, an example of the rescaled dissipated 3D powermap imported into ANSYS is shown for the resistive wall impedance, and the related power map computed by CST is shown in Fig. 4.12.

Regarding the cooling mechanism, at the measurement time there was no active cooling in the TOTEM RP, the heat was evacuated by conduction, radiation and natural convection. The radiation and conduction are the most important cooling mechanisms for the device internal parts since there is vacuum both in the primary vacuum vessel and in the secondary vacuum vessel, thus, there is no convection. The external surfaces of the device experience convection and radiation. Furthermore, in the simulated model, the long in and out pipes collect heat by conduction and dissipate it by radiation and convection, this is also expected to take place in the real device.

Regarding the radiation, the emissivity parameter ε is strongly dependent on the surface roughness of the RP surfaces. It was set to 0.1 for all the polished

stainless steel surfaces [93], while it was set to 0.35 for the groove internal surface, not polished [94][5].

Regarding the convection, natural convection was considered on the external surface. The convection coefficient was computed as temperature dependent following the paper of Churcill et al. [95]. The TOTEM RP was simplified as an horizontal cylinder in steady air. The convection coefficient as a function of the temperature of the RP external surfaces is reported in Fig. 4.16.

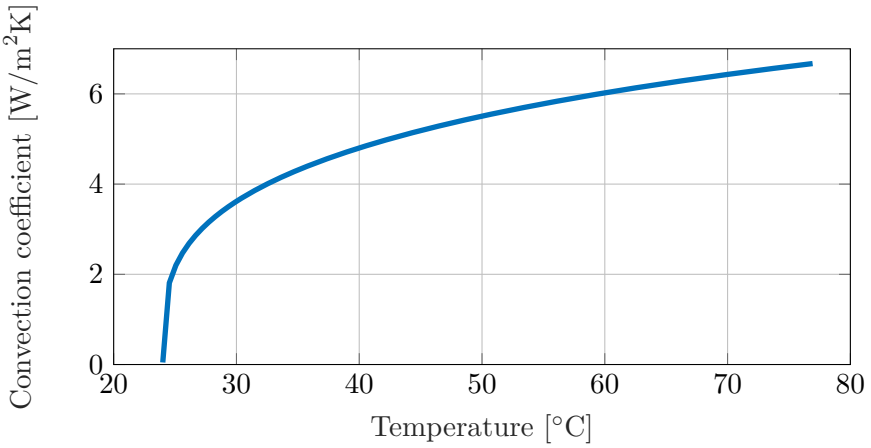

Figure 4.16. Natural convection coefficient as a function of the temperature of the RP external surfaces for an ambient temperature of 24 °C.

The external ambient temperature was considered 24 °C during the beam running and 20 °C during the cooling period, when the beam is not running. These temperatures were estimated from experimental data in the LHC cavern, the highest temperature when the beam is running is due to the running electronics[6] and the working devices dissipation.

The conduction is regulated by the thermal conductivity k, reported in Table 4.1 for the ferrite and in Fig. 4.8 for the stainless steel.

Another important parameter is the thermal contact resistance (TCR) among the different parts of the TOTEM roman pot.

When two bodies at different temperatures are put in contact, they exchange heat to reach the equilibrium. At the interface between these bodies there is a resistivity to the heat circulation because the surface roughness of the bodies does not allow perfect contacts. This resistivity is called thermal contact resistance (TCR) and its inverse is the thermal contact conductance (TCC).

In the roman pot this parameter can be considered critical in two areas: at the contacts among the flanges and at the contacts between the ferrite and the RP vessel flanges, refer to Fig. 4.7c. The TCC at the contacts among the flanges

[5]The two cited references report the value of the emissivity for the stainless steel 304L that is in principle different from the 316LN used for the RP. However, emissivity data of stainless steel 316LN were not found for room temperatures (around 30 °C) and the difference between the two stainless steel should be negligible.

[6]Note that the electronics of the RP has been removed for the temperature measurements but the other equipment in the cavern has its own electronics that dissipate heat to work.

was considered infinite, i.e. perfect contacts. This is because the flanges are fixed together to be vacuum tight, i.e. they are kept together by a very high pressure and the contact between them has to be good to avoid vacuum leak. Regarding the value of the TCC between the ferrite and the RP vessel, this quantity depends by a huge number of parameters (among others, surface roughness, contact pressure and material properties) that were not available at the simulations time. Thus, two steady state simulations considering the heating sources and the cooling mechanism just outlined were performed to investigate the impact of the TCC variation on the simulation results. For the first simulation, an empirical value of 20 $W/(m^2K)$ for the TCC between the ferrite and RP vessel was considered, for the other simulation, perfect contact was assumed, i.e. infinite TCC.

Steady State Simulations

The results of the steady state simulations, i.e. the equilibrium temperature map in the TOTEM RP, are shown in Fig. 4.17a for the infinite TCC and in Fig. 4.17b for the 20 $W/(m^2K)$ TCC. In the figures also the mesh is visible. An accurate analysis of the temperature reveals that the main effects of changing the TCC between the ferrite and the RP vessel is a temperature change in the ferrite, the lower the TCC the higher the temperature reached by the ferrite ring. One conclusion is that extra care has to be taken in the cooling of the ferrite. Indeed its temperature has to remain under the curie temperature, otherwise the material will lose its magnetization losing also the electromagnetic damping properties. On the other side, the TCC between the ferrite and RP vessel has a small effect on the temperatures of the other points of the TOTEM RP. This can be seen comparing the temperature probe points in the two Fig.s 4.17a and 4.17b.

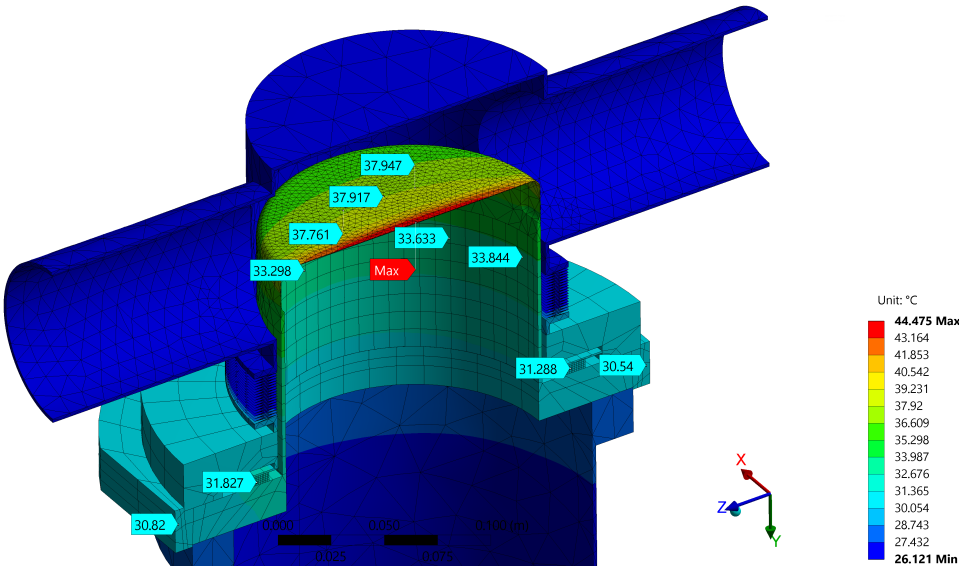

(a)

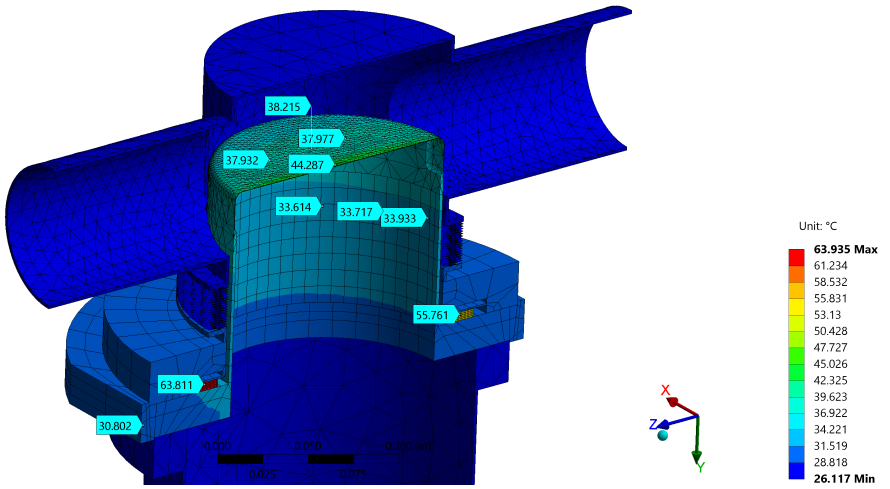

(b)

Figure 4.17. Equilibrium temperature map in the TOTEM RP at the steady state. (a) TCC between ferrite and RP vessel infinite. (b) TCC between ferrite and RP vessel 20 W/(m^{2}K).

Transient Simulations and Experimental Data

As already said, on December 2012, five PT100 temperature sensors were installed on the roman pot. During the beam run the temperature evolution in time in the device was recorded in different points. Two pictures of the PT100 locations are shown in Fig. 4.18a and 4.18b. A sensor is outside vacuum, on the external surface of the cylinder flange (refer to Fig. 4.18a), and the other four sensors were placed on the internal surface of the movable cylinder (refer to Fig. 4.18b). The sensors are indicated as S1, S2, S3, S4, S5. To reproduce the measured temperature trend, transient thermal simulations were run considering the heating and cooling sources previously defined in this section. Virtual sensors, also called pick up points (PK), were defined in the simulations. In Fig. 4.18c the pick up point positions are shown. In particular, PK1 should correspond to S1 or S2, PK3 should correspond to S3 or S4 and PK2 should correspond to S5.

In Fig.s 4.19, 4.20 and 4.21 the time temperature trend measured by the real sensors and the simulated ones is reported. The coloured solid lines represent the measured data, the black lines represent the simulated data. The classic behaviour of the temperature of a body first heated and then cooled can be seen. At the beginning there is a sharp temperature increase, the gradient of the temperature curve decreases with time while the value of the temperature reaches approximately the convergence value, i.e. the equilibrium temperature. Subsequently, when the beam is damped, the temperature drops sharply due to the absence of heating sources.

To study the sensitivity of the simulated time-temperature curve with respect to the simulations parameters (they are reported in the paragraph "Heating and Cooling Sources" and are emissivity, convection coefficient, ambient temperatures etc), a parametric analysis was performed. Several simulations were done changing $\pm 20\%$ the simulations parameters from its nominal value, i.e. the value reported in the paragraph "Heating and Cooling Sources". In Fig.s 4.19, 4.20 and 4.21, the results obtained using the nominal value of the parameters are drawn with a black solid line and the results obtained by the parametric study are drawn with black dashed lines.

Looking at the results of the parametric study, it can be noted that different parameter combinations bring to a simulated temperature time curve that is always close to the experimental data. This indicates that the analysis is robust.

Furthermore, the agreement between experimental and simulated data is good.

In addition, from Fig.s 4.19, 4.20 and 4.21, it can be also noted that after 9 hours of heating, around 15:00, the RP has almost reached the steady state temperature. The value of the steady state temperature measured agrees well both with the transient simulations and with the steady state simulations, refer to Fig.s 4.17.

As for the steady state simulations also the transient simulations were performed for two different values of the TCC between the ferrite and the vacuum vessel, 20 $W/(m^2K)$ and infinite. No changes were found regarding the temperature time trend at the pick up points PK1, PK2 and PK3. In Fig.s 4.19, 4.20 and 4.21, the results for a TCC value of 20 $W/(m^2K)$ are shown.

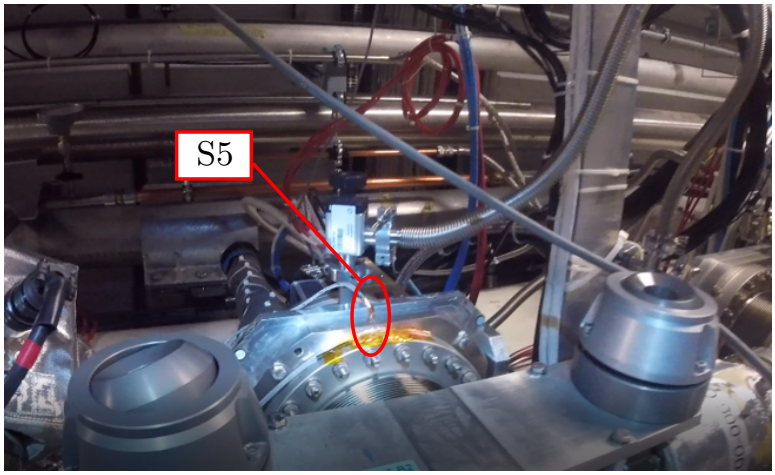

(a) Courtesy of Gueorgui Antchev.

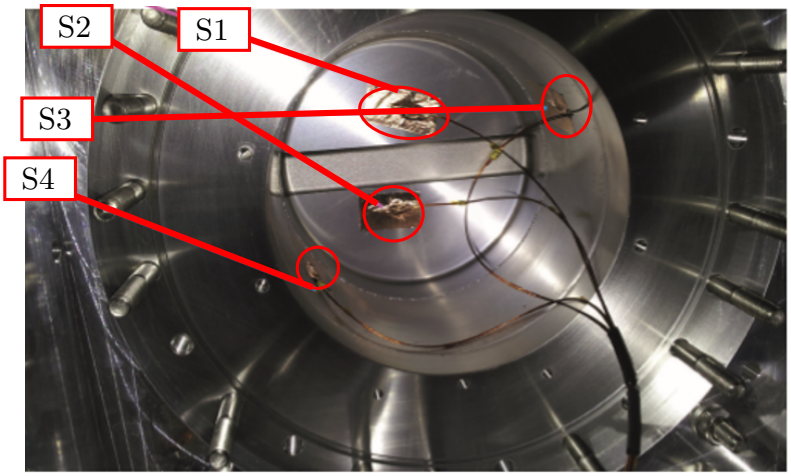

(b) Courtesy of Deile [96].

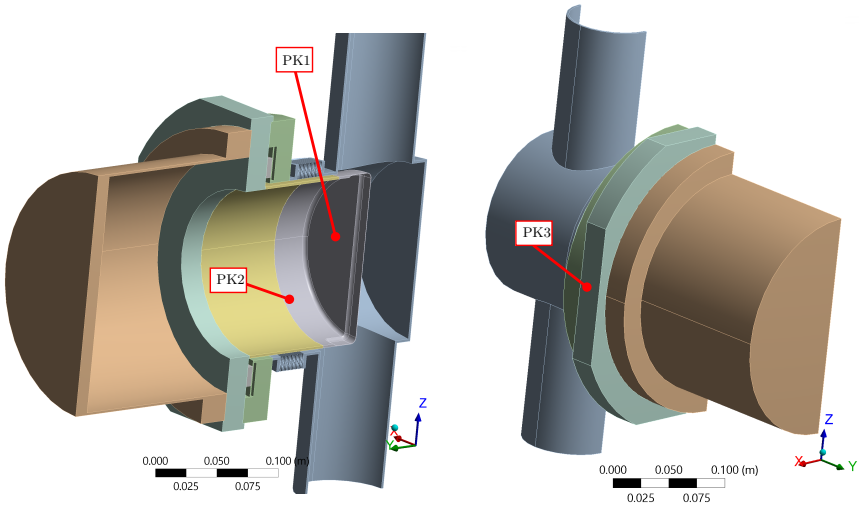

(c)

Figure 4.18. (a), (b) Temperature sensor positions in the RP. (c) Simulated temperature sensor positions in the RP.

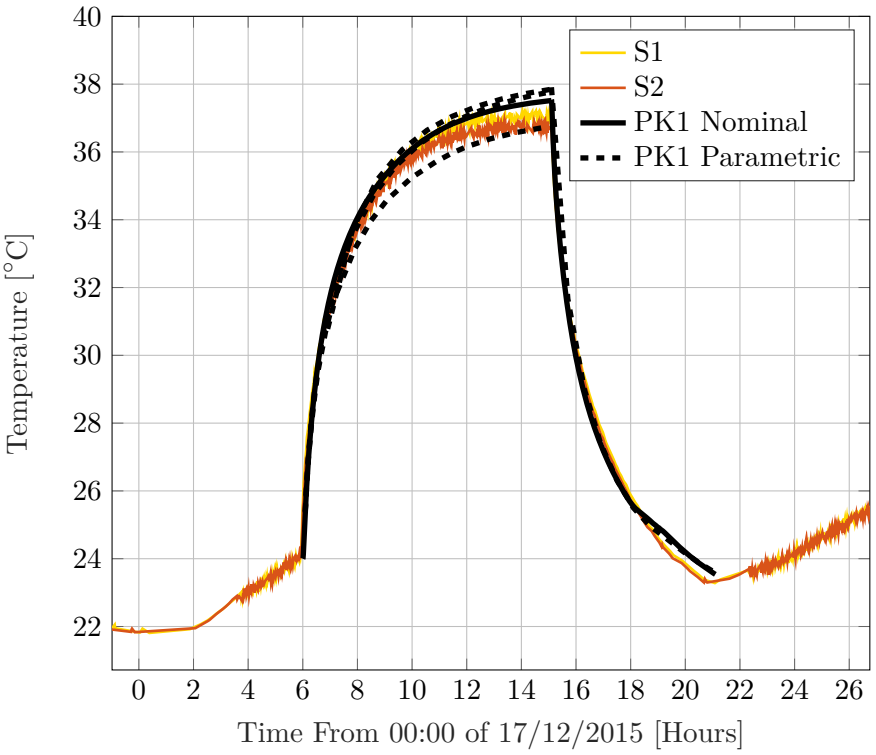

Figure 4.19. Transient temperature measured on the TOTEM roman pot for the sensors S1 and S2 and transient temperature simulated on the virtual sensor PK1. With the black solid line is indicated the simulation result obtained using the nominal value of the simulations parameters, while the black dashed lines are indicated the simulation results from the parametric study.

4.4 Conclusions

This chapter has illustrated an accurate multi-physics approach to simulate the local RF-heating mechanical and thermal effects on accelerator devices. It has explained the method work flow and has showed examples of its use. Furthermore, the method proposed was successfully benchmarked against temperature experimental data taken during the LHC fill 4381 on the cylindrical TOTEM Roman Pot. The thermal transient simulations well reproduced the temperature evolution of the roman pot during the LHC run. The results were found robust against variation of cooling parameters such as surface emissivities, convection coefficients or contact properties. The method could identify a critical point in the design of the Roman Pot, the thermal contact conductance between the ferrite and the roman pot vessel. For low value of this parameters the temperature of ferrite at the steady state was found alarmingly high. It was proposed to use these data to improve the design of the ferrite cooling system. To summarize, the proposed method revealed itself to able to simulate the local thermal effects induced by impedance on a device and it was used to understand the possible design improvements. This method could be a key approach to deal with RF-heating design problems of future high intensity, low emittance particle accelerators.

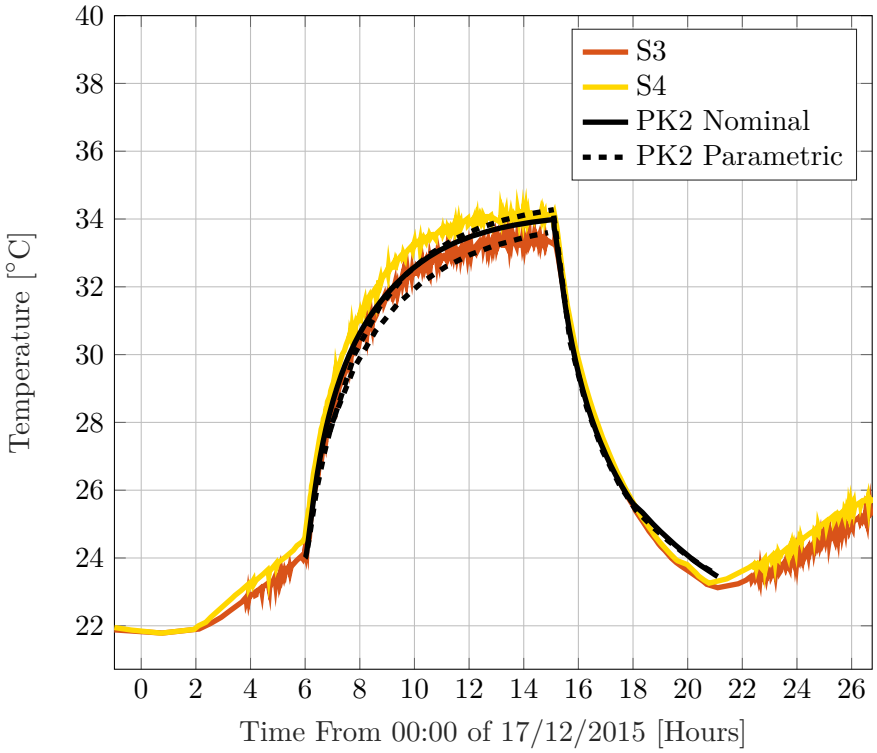

Figure 4.20. Transient temperature measured on the TOTEM roman pot for the sensors S3 and S4 transient temperature simulated on the virtual sensor PK2. With the black solid line is indicated the simulation result obtained using the nominal value of the simulations parameters, while the black dashed lines are indicated the simulation results from the parametric study.

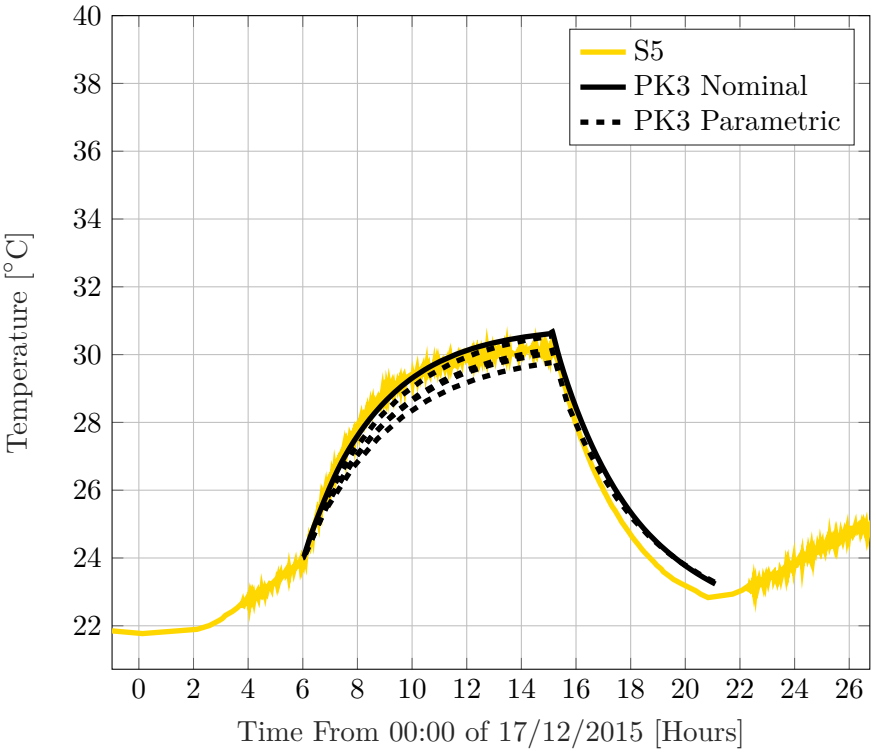

Figure 4.21. Transient temperature measured on the TOTEM roman pot for the sensors S5 transient temperature simulated on the virtual sensor PK3. With the black solid line is indicated the simulation result obtained using the nominal value of the simulations parameters, while the black dashed lines are indicated the simulation results from the parametric study.

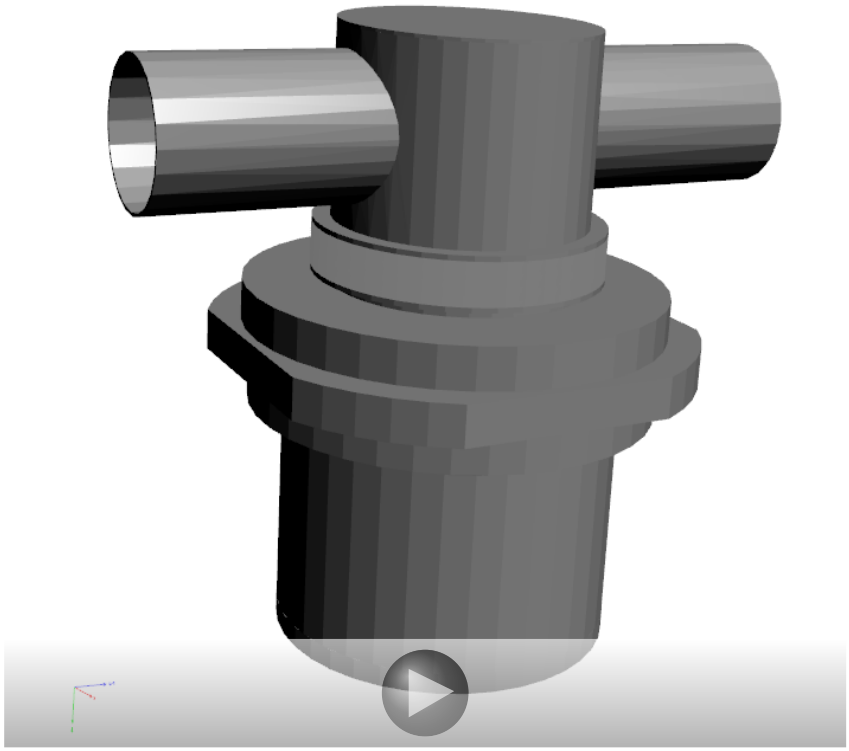

Figure 4.22. A 3D, schematic model of the Totem Roman Pot. If the figure does not appear interactive, please enable this function and click on it or use a recent version of Adobe Reader.

Chapter 5

Impedance Measurements Background

5.1 Introduction

Before an accelerator component is installed in the machine it has to go through a series of tests and measurements to guarantee its quality, i.e. the behaviour of the built unit has to be as similar as possible to the one predicted by simulations during its conceptual design phase. Among these tests, impedance measurements are also done.

In general, they can be divided into beam measurements and bench measurements. The former can be performed after the device is installed in the machine and the beam is running. They consist in evaluating variation in the beam observables sensitive to impedance, for example the tune shift [64, 97, 98]. This kind of measurements gives a good understanding of the machine impedance. However, it is not suitable for the impedance quality check of a single accelerator device. Indeed, beam impedance measurements would require the component to be already installed in the machine, and if it is found faulty it should be removed. This would require a substantial amount of time. Furthermore a bunch of particles moving in an accelerator is subjected to the integrated effects of its electromagnetic interactions with all the traversed machine equipment, thus, impedance beam measurements provide the global picture of the machine impedance. It is possible to localise and extract information for a single component only if the impedance of the device to study is dominant with respect to the other impedance sources. As an example, impedance beam measurements were performed for a single collimator in the CERN LHC machine [30].

Conversely, impedance bench measurements can be used to test the electromagnetic response of a prototype piece of equipment in the laboratory, avoiding the previous issues. What is needed is the device to be measured, i.e. the device under test (DUT), a vector network analyser (VNA) and some other tools (they will be described in detail in the following). In this kind of measurements the device vacuum chamber is electromagnetically excited and its response is measured. The excitation tools may be different depending on the method one wants to apply. Both transverse and longitudinal impedance can be measured.

5.1.1 Scope and Structure of the Chapter

This chapter reviews impedance bench measurements techniques since they best suit the need of checking impedance for a single device. In particular, the techniques used for this work, and presented in this chapter, detect and measure impedance of electromagnetic resonant modes in devices. A resonant mode at an unexpected frequency, not predicted by simulations, could be a sign of a non conformity in a device assembly. Further, also if the mode is found at the frequency expected by simulations, its shunt impedance has to be measured and benchmarked against the results of the simulations performed during the device design phase. This ensures that the device works as expected. Other measurements techniques should be used if the scope is to analyze the resistive wall impedance of the device, as, for instance the resonant wire method [99]. However, they are not treated in this work.

The chapter is organized as follows: Section 5.2 introduces the measurements tools and some basic radio frequency (RF) concepts: the mode resonant frequency, shunt impedance and quality factor, loaded and unloaded.

Probe measurements are described in section 5.3. The measurements set-up, the data post-processing, and the limitations of this method are reported.

Wire measurements are described in section 5.4. The measurements set-up, the data post-processing for obtaining transverse and longitudinal impedance, and the limitations of this method are reported.

Beam Position Monitors (BPM) measurements are described in section 5.5.

Finally, section 5.6 reports the summary and conclusion of this chapter.

The main references to prepare this chapter have been the work of Kroyer et al. [99], Bray et al. [100], Jensen [48] and Kajfez [101]; a procedure to perform impedance measurements on collimators can be found in the CERN report [102].

5.2 Measurements Tools & Basic RF Entities

The main idea of the impedance measurements is to excite the DUT inserting in it excitation sources and analyzing its response. However, when the measurements tools are inserted into the DUT, they perturb the system. Thus, the measurements that one is reading is the perturbed response of the DUT plus the excitation sources. The DUT perturbed by the measurements tools is called loaded DUT while the unperturbed DUT is called unloaded. In this subsection first the equipment to perform the measurement is presented, subsequently, the differences between the loaded and the unloaded DUT are briefly reviewed, and the concept of unloaded and loaded resonant frequency, quality factor and shunt impedance are also introduced.

5.2.1 Measurement Tools

In Fig. 5.1, a setup for a probe measurements campaign is shown. One can notice the Vector Network Analyzer (VNA) that is the excitation source and the reading instruments during the measurements. Two Radio Frequency RF cables connect the VNA with the DUT. The excitation source is attached at the extremity of the cable. It can be a probe for probe measurements (described in section 5.3), or a wire for wire measurements, (described in section 5.4). The excitation source is inserted into

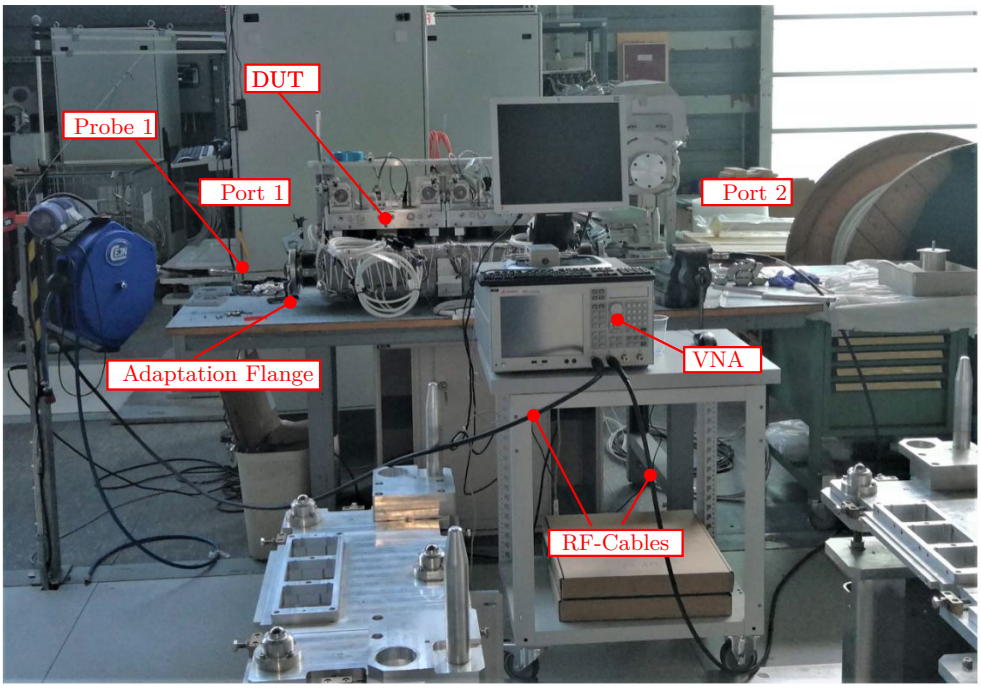

Figure 5.1. Impedance Bench Measurements set-up, probe measurements case. The Vector Network Analyzer (VNA), the RF-Cables, ad the excitation source are shown.

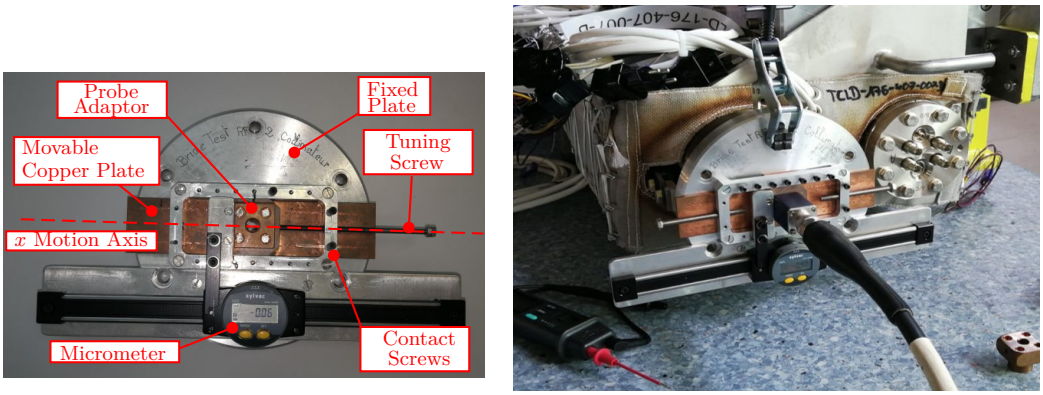

(a) **(b)**

Figure 5.2. (a) Adaptation flange schematic. (b) Adaptation flange installed on DUT for wire measurements

the DUT through an adaptation flange, shown in Fig. 5.2. This flange, clamped to the DUT, is made by a fixed plate in aluminium and a movable plate in copper, the movable part can slide on the fixed part and the electrical contact is ensured by screws to be tighten when the desired configuration is reached. The excitation source is inserted into the device through an hole in the copper plate. A lateral tuning screw and a micrometer rigidly connected with the movable copper plate allow the fine tuning of the source position along the x motion axis.

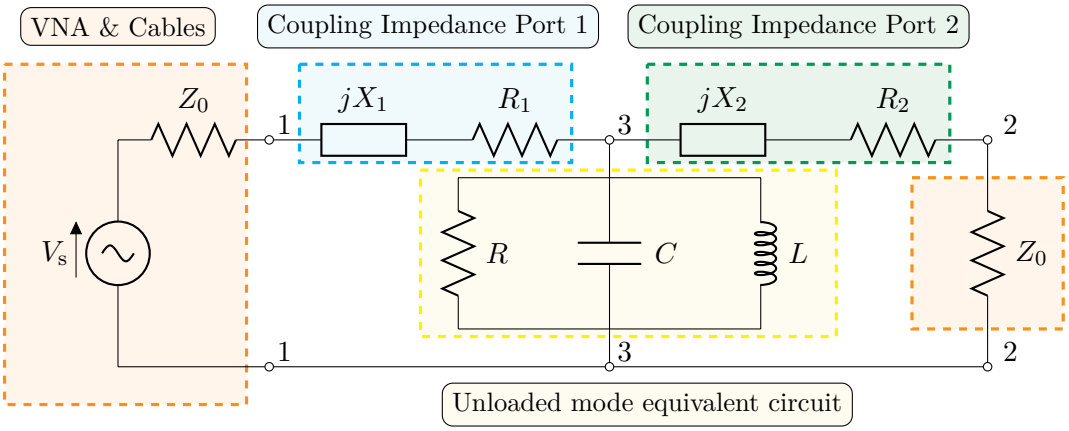

Figure 5.3. Equivalent circuit of a resonator connected to VNA excitation source in a two port configuration in the case the characteristic impedance of the cables connecting the VNA to the DUT is matched to the VNA internal impedance Z_0. Port 1, port 2 and port 3 are indicated, port 1 is excited, port 2 is loaded with Z_0, while port 3 is the port of the unloaded resonator. Images readapted from Kajfez [101].

5.2.2 Equivalent Circuit of a Loaded DUT Mode

Let's consider the case in which only one resonant mode in a loaded DUT is to be analyzed. The resonant mode is characterized by three quantities, already introduced in section 3.2.4, resonant frequency f_r, quality factor Q and shunt impedance R. Following [48], [100] and [101], the equivalent circuit model of the loaded DUT mode has been drawn in Fig. 5.3 in the case of excitation at port 1 and loading at port 2:

- The unloaded resonant mode in the DUT is represented by the circuital elements in the yellow block: the shunt impedance R (already introduced in section 3.2.4), a capacitor C and an inductance L. One can analyse this part of the schematic with simple circuit theory obtaining the unloaded resonant frequency of the mode:

$$f_r = \frac{1}{2\pi\sqrt{LC}} \tag{5.1}$$

  and the unloaded quality factor Q (already introduced in section 3.2.4):

$$Q = 2\pi f_r RC. \tag{5.2}$$

  This is the quality factor that characterizes the mode.

- The excitation source, i.e. the VNA plus the connection RF-cables, is represented by the generator V_s and the two port impedance values Z_0 for port 1 and port 2 respectively.

- The impedances $R_i + jX_i$ is a representation of the coupling mechanism between the DUT mode and the excitation source at the port i.

Thus, it is easy to identify the perturbation elements in the equivalent circuit of Fig. 5.3 as Z_0 and $R_i + jX_i$. The effects of this perturbation elements are that the

measured resonant frequency, shunt impedance and quality factor are different from those of the actual mode [101, 48]. The measured perturbed resonant frequency, shunt impedance and quality factor are called loaded, and they are labeled as f_L, R_L and Q_L to distinguish them from the unloaded resonant frequency, shunt impedance and quality factor f_r, R and Q.

5.2.3 Resonant Frequency

To find the relation between the loaded and unloaded resonant frequency one can work out the equivalent impedance seen by port 2 (the reading port in the circuit of Fig. 5.3), and impose its imaginary part to 0. Thus, the loaded resonant frequency will be a function of the perturbation elements as well.

Let's make an example calculation. In order to simplify the calculation let's suppose the circuit to be loss free, i.e. $R_1 = R_2 = R_s = 0\ \Omega$ and the voltage generator to be ideal (Z_0 on the left is short circuited). The equivalent impedance seen by port 2, Z_e, can be found using the Thevenin's or Northon's theorem for port 2. Under the simplification hypotheses, its expression is:

$$Z_e = \frac{jXX_1}{X + X_1} + jX_2, \tag{5.3}$$

where

$$X = \omega L - \frac{1}{\omega C}, \tag{5.4}$$

$$X_1 = \omega L_1 - \frac{1}{\omega C_1}, \tag{5.5}$$

$$X_1 = \omega L_2 - \frac{1}{\omega C_2}. \tag{5.6}$$

Thus, imposing the resonant condition, i.e. imaginary part of $Z_e = 0\ \Omega$, after some algebraic manipulations one gets:

$$\begin{aligned}\left(\omega L - \frac{1}{\omega C}\right)\left(\omega L_1 - \frac{1}{\omega C_1}\right) + \left(\omega L_1 - \frac{1}{\omega C_1}\right)\left(\omega L_2 - \frac{1}{\omega C_2}\right) + ... \\ ...+ \left(\omega L_2 - \frac{1}{\omega C_2}\right)\left(\omega L - \frac{1}{\omega C}\right) = 0.\end{aligned} \tag{5.7}$$

In order to further simplify Eq. 5.7 let's us assume to use ideal excitation sources with just a capacitor behaviour, i.e. $L_1 = L_2 = 0$ H/m. Solving Eq. 5.7 for ω with this hypothesis, one obtains the resonant frequencies of the loaded resonator:

$$f_L = \frac{1}{2\pi\sqrt{LC}}\sqrt{\frac{C_1 + C_2 + C}{C_1 + C_2}} = f_r\sqrt{1 + \frac{C}{C_1 + C_2}}. \tag{5.8}$$

It is evident from Eq. 5.8 that port 2 sees a loaded resonant mode that has a different resonant frequency with respect to the unloaded resonant mode. This frequency shift depends on the coupling impedance characteristics, C_1 or C_2 in this case. Please note that in case of perfect coupling, i.e. $C_1, C_2 \to \infty$, the resonant frequency of the loaded resonator transforms into the unloaded resonant frequency, as expected.

5.2.4 Quality Factor

To understand the consequences of the DUT mode loading on the mode quality factor first one has to formally define the quality factor. The mode quality factor is the ratio between the total energy stored in the resonant mode U and the energy lost per cycle P/f_r (where P is the dissipated power in the device walls by the mode) [48]:

$$Q = 2\pi f_r \frac{U}{P}. \tag{5.9}$$

Thus, if the energy stored in the mode is fixed, one expects to have lower quality factor if the energy loss per cycle rises, i.e. if there are more losses.

Let's go back to the mode loaded equivalent circuit of Fig. 5.3, without the hypothesis of loss free circuit. The active power delivered by the voltage generator is dissipated in the resistances Z_0, R_1, R_2 and R. On the contrary in the case of an unloaded resonator connected to an ideal generator all the active power is dissipated on R. Thus, when the resonator is loaded, extra losses are introduced, the so called external losses. Considering now the definition of quality factor for a resonant mode given by Eq. 5.9, it is evident that these extra losses increase the energy loss per cycle. Thus, a loaded generator always presents a loaded quality factor Q_L lower than its unloaded one Q.

The relationship between the loaded and the unloaded quality factors is given by:

$$\frac{1}{Q_L} = \frac{1}{Q} + \frac{1}{Q_{ext}}, \tag{5.10}$$

where Q_{ext} is introduced as the quality factor linked to the power losses outside the unloaded resonator, i.e. the power losses due to R_1, R_2 and Z_0 with reference to Fig. 5.3. The ratio between Q_{ext} and Q is indicated with k and is called coupling coefficient [101]:

$$k = \frac{Q}{Q_{ext}}. \tag{5.11}$$

It can be interpreted as the ratio between the active power dissipated in actual resonator and the one dissipated on the external circuit. Eliminating Q_{ext} from Eq. 5.10 using Eq. 5.11 one finally gets the expression of Q in terms of Q_L as:

$$Q = Q_L(1 + k). \tag{5.12}$$

5.2.5 Shunt Impedance

As for the quality factor, also the measured shunt impedance is the one of the loaded DUT mode that is different with respect the shunt impedance of the unloaded mode. To understand this, let's state the formal definition of shunt impedance [48]: the shunt impedance is the ratio between the square of accelerating voltage V_{acc} (the

integral of the axial electric field along the particle trajectory) and power dissipated in the mode P:

$$R = \frac{|V_{acc}|^2}{2P}. \tag{5.13}$$

Supposing that the accelerating voltage remains unchanged for the loaded DUT mode, the extra losses introduced by the measurement tools increase P, leading a lower shunt impedance R_L with respect to the unloaded one R.

5.2.6 Summary

To sum up, in this subsection the impedance measurements tools have been presented and the equivalent circuit of a loaded DUT resonant mode has been analyzed. It was shown that the measurements tools perturb the resonant mode. The effects of this perturbation are: the measured resonant frequency, that is the loaded one, is shifted with respect to the unloaded mode resonant frequency. Furthermore the loaded shunt impedance and the loaded quality factor are decreased with respect to the unloaded value.

5.3 Probe Measurements

Probe measurements are handy and moderately invasive for the device. They provide the resonant frequency of the electromagnetic mode f_r and its quality factor Q. However, they cannot provide the mode shunt impedance and because of that, when possible, they should be performed as a complement to other kinds of impedance measurements as, for instance, the wire measurements, discussed in section 5.4.

5.3.1 Different Probe Shapes

In this kind of measurements the principle is the excitation of the resonant modes in the DUT by mean of probes. They are made by two coaxial conductors separated by a dielectric. The external conductor provides structural rigidity, the internal one is the one to be excited and it is longer than the external one. A schematic of these probe is presented in Fig. 5.4.

In particular, in Fig. 5.4a a probe with a loop termination is represented. It well couples with DUT resonant modes that have a magnetic field component passing through the loop. During the measurements performed for this work, it has been found that this kind of probes is very effective for the detection of low frequency modes. This was observed also in the work of Biancacci et al. [103].

In Fig. 5.4b a probe with straight termination is drawn for different values of the tilt angle θ. This geometry well couples with resonant modes that have an electric field component oriented in the same direction as the probe termination. Thus, with a zero value of the tilt angle θ, longitudinal modes are easily excited, while with $\theta = 90°$ transverse modes are the most stimulated. Both kinds of modes are excited with intermediate tilt angles.

In Fig. 5.5 examples of real probes used for measurements are shown.

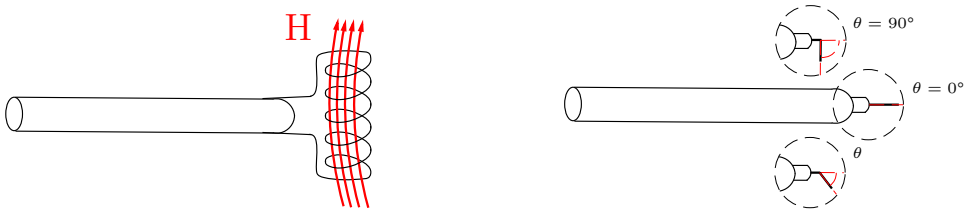

(a) (b)

Figure 5.4. (a) Probe with loop termination. (b) Probe with straight termination at different tilt angles.

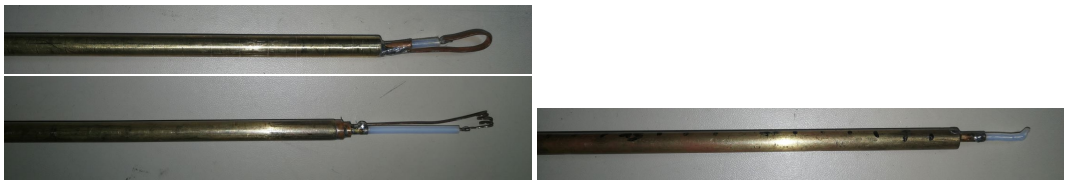

(a) (b)

Figure 5.5. Real probes used for measurements. (a) Probe with loop termination. (b) Probe with straight termination.

5.3.2 Measurements Set-Up

The set-up for this kind of measurements is straightforward, and it is illustrated in Fig. 5.6. Once the two adaptation flanges are put in place at the two ports of the DUT, the probes, connected to the VNA with the RF cables, are inserted in the DUT. The probes are excited by the VNA and they excite electromagnetic resonant modes inside the DUT structure.

In Fig. 5.7 a cartoon of the measurement set-up installed on a pill-box cavity is displayed. The probe insertion axis, the z axis, is highlighted. The adaptation flanges allow for the translational motion of the probe along this axis. Thus, the probe can be inserted in the DUT with arbitrary depth d (obviously limited by the probe length). Further, also rotational motion around the insertion axis is permitted. Considering an arbitrary reference configuration, one can call α the rotation angle around the z axis of the current configuration with respect to the reference configuration. Further, also transverse motion is allowed by the flange.

These degrees of freedom are extremely helpful during the measurements. Indeed, rotating the probes of an angle α allows to align the probe termination in the direction of the resonant mode electric or magnetic field components, so maximizing the mode excitation. Obviously, during the measurements campaign the orientation of the electric or magnetic field modes is not known and it has to be detected. Thus, a scan for different α values must be done in order to obtain maximum coupling. On the other hand, variations of the probe depth d enable to investigate on modes resonating in different position inside the DUT and, as it will be shown in section 5.3.4, to discriminate spurious modes due to the probe insertion in the DUT from the proper one due only to the DUT.

With the set-up shown in Fig. 5.6, measurements can be done in reflection or

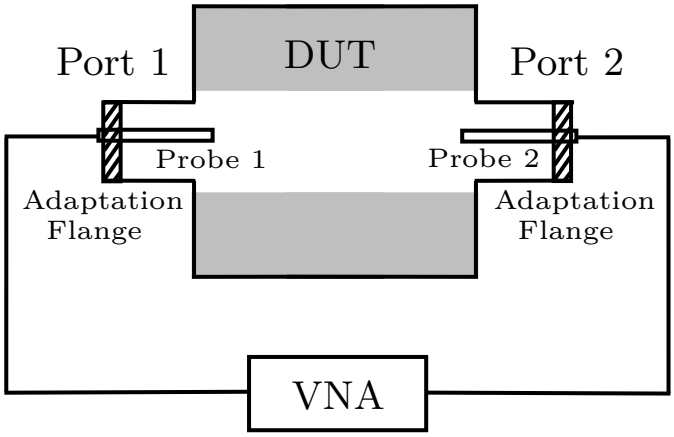

Figure 5.6. Schematic representation of the probe measurements set-up, two probes are inserted at the ports of the DUT thought the adaptation flanges, camped.

.

in transmission. In the first case the the DUT is excited from port 1 and from the same port the response is read. For this kind of measurements there is no need of a second port, i.e. of a second probe. In the transmission type measurement two ports are necessarily required, the DUT is excited from port 1 and the response is read from port 2, or viceversa. This is the case represented in Fig. 5.3.

5.3.3 Measurements and Post Processing

Measurements Reading

Measurements reading is straightforward. The VNA returns the scattering parameters of the DUT. The devices treated in this work are reciprocal structures, thus, they are described by a symmetric scattering matrix S, i.e. $S = S^T$. Therefore, for a two port network one is only interested on three elements over four: S11,S22, S12 or S21. The identity S12 = S21 can be used as an index of the procedure correctness.

Critical parameters to read are the reflection parameters, in the two port case S11 and S22. Indeed, they behave as shown in Fig. 5.8:

- At frequencies for which no resonant modes are present in the DUT the transmission line is an open circuit, i.e. all the input power is reflected back and the reflection coefficients are close to zero dB.
- At frequencies for which resonant modes exist in the structure only little input power is reflected back, the majority of it is absorbed to excite and feed the resonant modes in the structure. This effect results in a decrease of the reflection coefficients at the mode resonant frequency.

Thus, looking at the reflection parameters, the mode resonant frequencies can be estimated.

Similar information can be deduced from the the transmission parameters (S12 or S21 in a two port case). Indeed it is clear that all the probes that can excite a

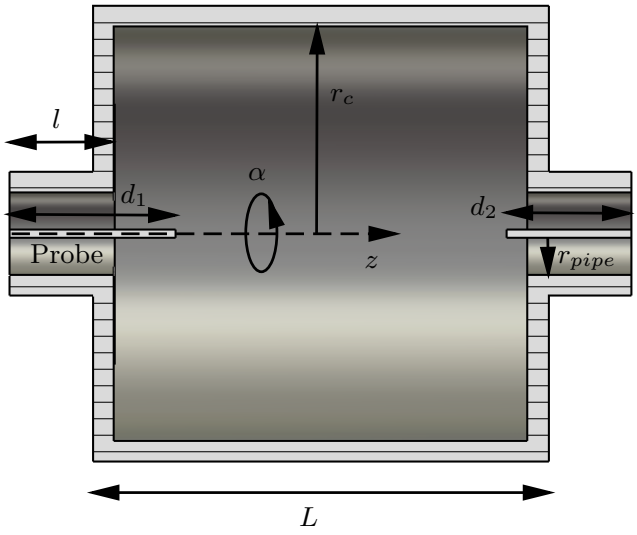

Figure 5.7. Representative cartoon of the probe measurements set-up for a pill box cavity. All the geometrical quantities are drawn: r_c the internal radius of the cavity, l the length of the in/out pipe, d_1 the left probe insertion depth, d_2 the right probe insertion depth, r_{pipe} the internal radius of the in/out pipe, L the length of the cavity, z the insertion axis of the probes (in this case the simmetry axis of the pill-box) and α the rotation angle of the probe respect to an arbitrary reference configuration.

.

resonant mode in the structure can also be excited by that resonant mode. Thus, with reference to Fig. 5.6, let's consider a configuration for which both probe 1 and probe 2 are able to excite only one particular mode in the DUT structure. Let's further consider the case for which only probe 1 is power fed:

- At frequencies far from the resonant mode, all the input power is reflected back and there is no power transmitted from probe 1 to probe 2: the transmission parameter is $-\infty$ if measured in dB (for real measurement, due to the measurement noise, the transmission parameters have values around $-100, -140$ dB).
- At the resonant mode frequency, part of the power used to feed probe 1 excites the DUT resonant mode, the latter in turn couples with probe 2 that absorbs part of the power in the resonant mode. The net effect is power transmitted from port 1 to port 2 and this reflects in an increase of the magnitude of the transmission parameters at the resonant frequency, as can bee seen in Fig. 5.8.

However, a mode could be visible in reflection but not in transmission. This is particularly true for collimators (discussed in section 7.2.1). Their geometry is complex and resonant modes can be localised in specific region (like the entrance cavity) that are excitable by only one of the probes.Since the mode has no coupling with the other probe it cannot be detected looking at the magnitude of the transmission coefficients.

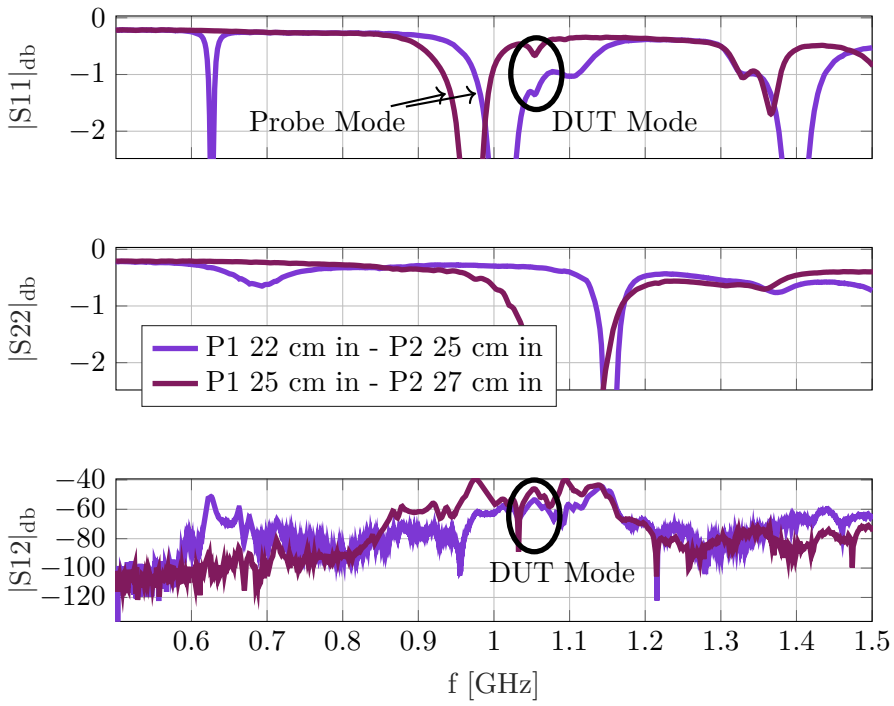

Figure 5.8. Scattering parameters registered by two loop probes P1 and P2 for different insertion values in a collimator. Example of a device resonant mode detected in the reflection parameter S11. When the probes (P1 and P2) are moved, the spurious probe mode modify their resonant frequency, while the device modes keep resonating at the same frequency. The resonant mode is also visible in the transmission parameter S12.

.

Postprocessing

Probe measurements return the loaded mode resonating frequency f_L and the loaded quality factor Q_L. Usually, the shift between the loaded and the unloaded resonant frequencies is so small that has no consequence, [101]. Thus, one can consider $f_r \cong f_L$ and read directly the resonant frequency as the frequency at which S11 or S22 have a minimum or the one at which S12 or S21 have a maximum.

Slightly more complex is the estimation of Q from Q_L. The loaded quality factor is given directly from the VNA, as shown in Fig. 5.9.

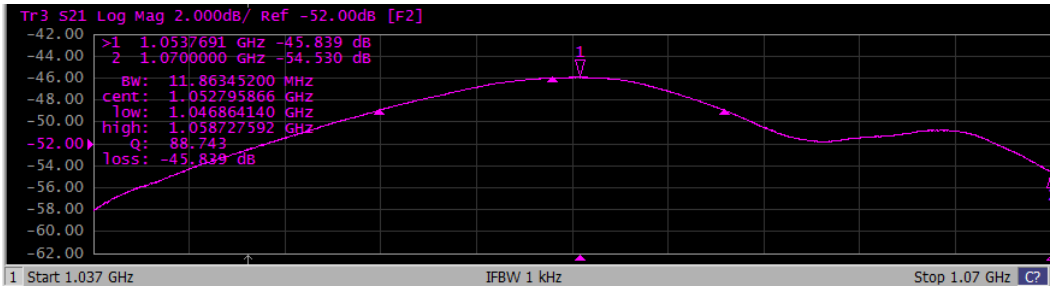

Figure 5.9. Example of loaded quality factor measurement directly by the VNA.

.

The loaded quality factor Q_L is obtained as the ratio of the resonant frequency f_r and the difference of the 3 dB frequency f_1 and f_2 at each side of the resonance [100]:

$$Q_L = \frac{f_0}{f_1 - f_2}. \tag{5.14}$$

Once Q_L is found, according to Eq. 5.12, the coupling coefficient k is needed for the Q estimation. The coupling coefficient can be obtained both from the reflection scattering parameters S11 and S22, or from the transmission scattering parameters S12, [100]. In this thesis, when possible, the transmission parameters are used to estimate k, since the procedure is faster.

For two ports transmission measurements the coupling coefficient is [101]:

$$k = k_1 + k_2, \tag{5.15}$$

where k_1 is the input coupling coefficient relative to the external losses of port 1 (Z_0 and R_1 with reference to Fig. 5.3) and k_2 is the output coefficient relative to the external losses of port 2 (Z_0 and R_2 with reference to Fig. 5.3). The magnitude of the transmission parameter at the resonant frequency f_0 can be written as a function of the coupling coefficient k_1 and k_2 as [101],:

$$|\mathrm{Sij}(f_0)|_{\mathrm{lin}} = \frac{2\sqrt{k_1 k_2}}{1 + k_1 + k_2}, \tag{5.16}$$

where $|\mathrm{Sij}(f_0)|_{\mathrm{lin}}$ is the linear modulus of one of the transmission parameters.

If the hypothesis of weak and approximately equally strong coupling at both ports is done, thus, $k_1 = k_2$ and from Eq. 5.15 one has $k = 2k_1 = 2k_2$. Equation 5.16 can be inverted as [99]:

$$k = \frac{|\mathrm{Sij}(f_0)|_{\mathrm{lin}}}{1 - |\mathrm{Sij}(f_0)|_{\mathrm{lin}}}. \tag{5.17}$$

For the specific case of probe measurements, the condition of weak and approximately equally strong coupling is ensured with the retraction of the probe at the two ports until the minimal value of S11 and S22 for which the mode is still visible in transmission is obtained, [103]. Once k is known, one obtains the unloaded Q from the loaded one using using Eq. 5.12.

5.3.4 Limitations

In this section some of the limitations of this measurement method are presented. Since the resonant mode frequency shift and the variation in the quality factor due to the mode loading have been already discussed in the previous sections, the rest of this section focuses on the spurious resonant modes introduced in the DUT structure with the insertion of the probe. Note that such modes are due only to the probe insertion, they are not present in the unloaded DUT. The section reviews also known methods to discriminate probe modes from the proper DUT modes and how to suppress them.

It is well know from the electromagnetic theory that a metallic stick short circuited at an extremity and free in the other resonates electromagnetically with mode wavelength λ dependent on the stick length d according to:

$$\lambda = \frac{4d}{n}, \tag{5.18}$$

where n is a natural odd number. This kind of resonances are called "lambda quarter resonances". The electric and magnetic field map of this kind of modes is reported in Fig. 5.10 and 5.11, respectively.

In the measurement set-up the probe behaves as the just discussed metallic stick. Indeed, it is short circuited at the extremity where there is the adaptation flange and free in the other. This means that in the measurements one sees both the proper DUT electromagnetic modes and the lambda quarter resonances due to the probe. Fortunately, it is easy to distinguish the lambda quarter modes from the DUT ones: Inserting or retracting the probes from the DUT the lambda quarter resonances modify their resonant frequencies while the DUT modes resonate always at the same frequencies.

This is shown in Fig. 5.8, where one can see a probe mode and a DUT mode. In the picture two measurements with different values of the probe insertion depth d are superimposed. The shift in resonant frequency of the probe mode is visible, while it is not detectable for the DUT mode.

These spurious modes could be also damped by absorbing foam at the shorted edge of the probe, i.e. to the internal surface of the adaptation flanges, where the probe mode magnetic field is maximum.

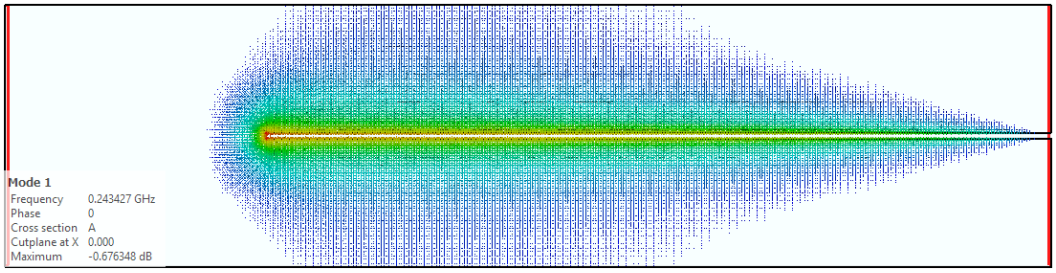

(a)

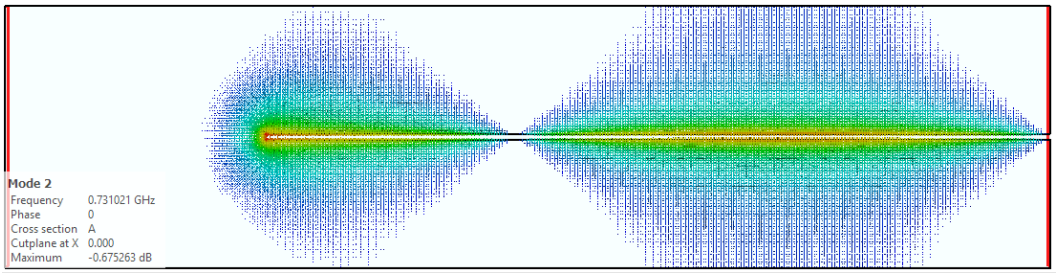

(b)

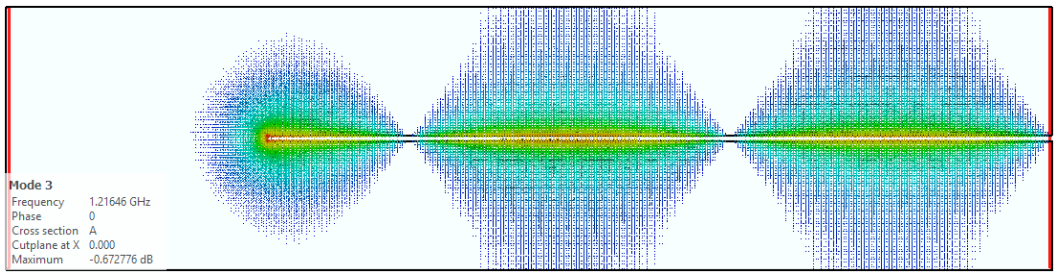

(c)

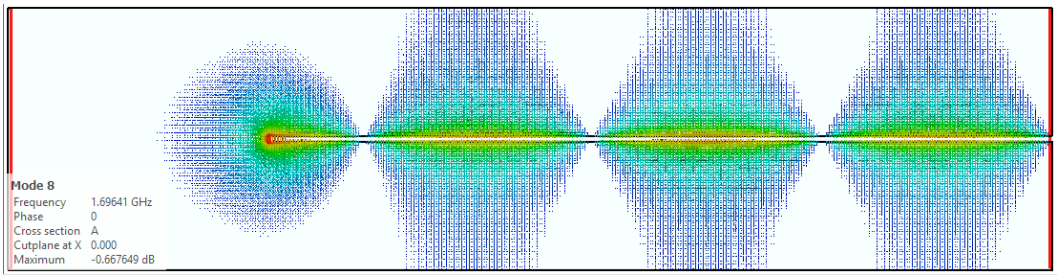

(d)

Figure 5.10. Electric Field map of the first four lambda quarter modes for a stick of length $d = 0.3$ m in vacuum.

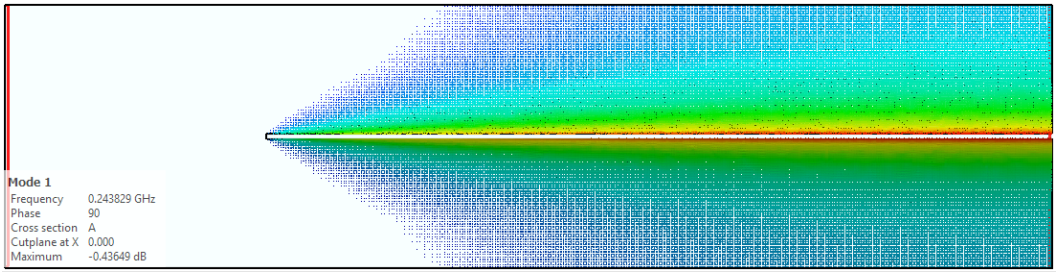

(a)

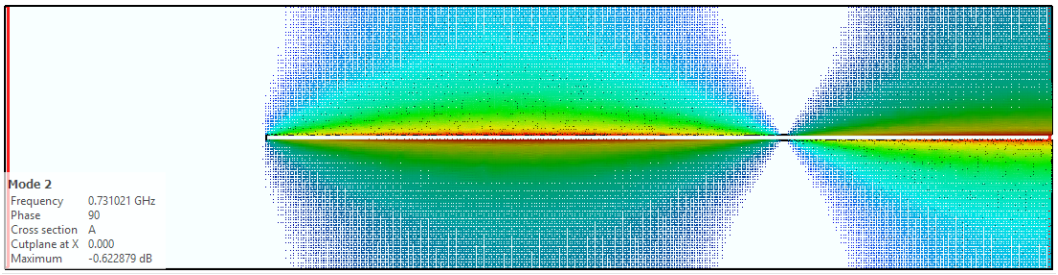

(b)

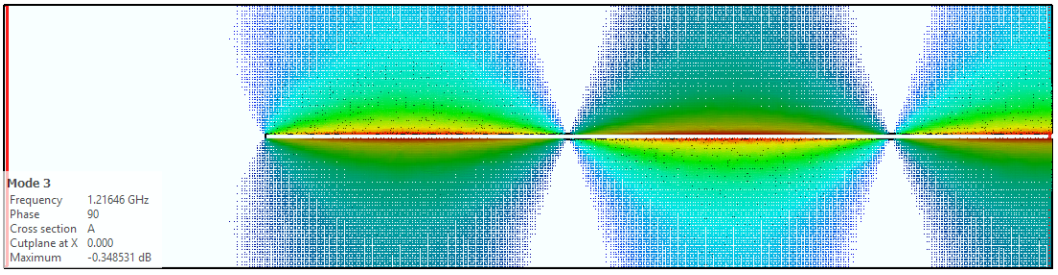

(c)

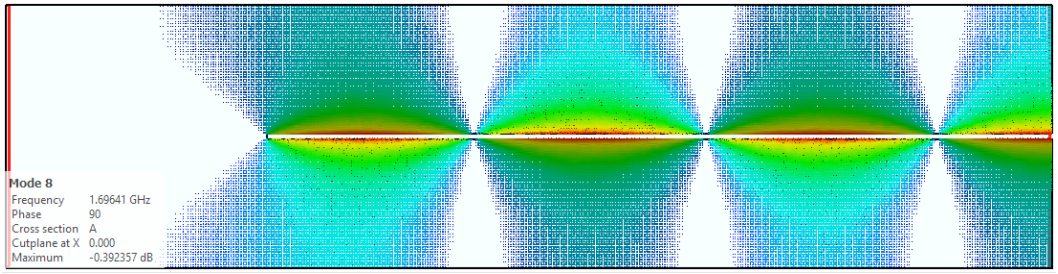

(d)

Figure 5.11. Magnetic field map of the first four lambda quarter modes for a stick of length $d = 0.3$ m in vacuum.

5.4 Wire Measurements

This measurement method was introduced in the 70's, by Faltens et al. [104] and Sand and Ress [105]. It relies on the fact that an ultrarelativistic beam generates an electromagnetic field distribution similar to the one of a transverse electric (TE) mode of a coaxial wire. An improved wire method was proposed by V. G. Vaccaro [106]. Nowadays the latter has become a standard practice at CERN and in other laboratories to estimate device impedances. Wire measurements can be used to measure both the longitudinal and the transverse impedance. They provide the mode resonant frequency, the quality factor and the shunt impedance. In this section wire measurements are described having the Kroyer et al. work [99] as a baseline. First the measurement set-up is explained, then examples of data acquisition are shown and the post-processing to obtain the coupling impedance from measurements is discussed. As a last point the limitations of the method are addressed.

5.4.1 Measurement Set-Up

The principle of this kind of measurements is simple: a copper wire is inserted into the DUT, the transmission parameter Sij is measured and used to compute the longitudinal impedance. Knowing the longitudinal impedance for different wire locations allows to compute the transverse impedance, as it is discussed in section 5.4.2.

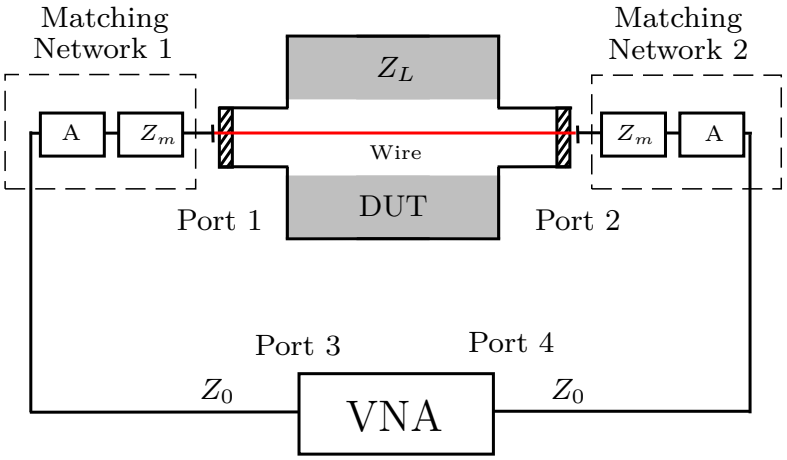

Figure 5.12. Wire measurements set-up. The impedance matching network formed by the matching impedance Z_m and the attenuator A is shown. The characteristic impedance of the transmission line formed by the DUT plus the wire is indicated with Z_L.

The set-up for this kind of measurements is depicted in Fig. 5.12. As can be seen it is slightly more involved if compared with the probe measurement set-up due to the matching network that is needed to avoid wave reflection inside the DUT. Indeed the VNA and its cables generally have an impedance of $Z_0 = 50\ \Omega$, while the DUT with the stretching wire inside can be modelled as a transmission line that, most of the time, has an impedance Z_L higher than Z_0. In order to better understand the reason of this matching structure, an example is discussed. With reference to

Fig. 5.12, let's suppose the matching network to be not present at all and let's suppose to analyse only the S12, i.e. port 1 is fed while port 2 is reading. The power inserted in port 1 flows from port 3 trough the RF-cable with line impedance Z_0. In the hypothesis in which there is no matching network 1 it arrives at port 1 to the DUT that has a line impedance Z_L. The power that is not reflected back because of the mismatch enters the DUT. At the DUT exit, port 2, in the hypothesis in which there is no matching network 2, i.e. there is a mismatch between the DUT line impedance Z_L and the VNA cable one Z_0, power is reflected into the DUT from port 2, flowing towards port 1. However, when the power reflected at port 2 reaches port 1 there is again mismatch and some power is again reflected back into the DUT. This generates a series of waves travelling inside the DUT. This makes difficult the computation of the longitudinal impedance since such oscillations have to be removed in the post-processing (refer to section 5.4.2).

For the example under discussion the problem is solved if the matching network 2 is inserted between port 4 and port 2. Indeed, in this case, when the power that flows from port 1 arrives at port 2 it is not reflected back but is completely absorbed by line formed from the matched network 2 plus the VNA. Obviously, considering the case in which port 2 is feed and port 1 is reading all the previous considerations are still valid. In this case, in order not to have waves reflections in the DUT the matching network 1 has to be put between port 3 and port 1. Since for this work port 1 and 2 have been used alternatively as feeding and reading port, one can understand the measurements set-up reported in Fig. 5.12.

Matching Network

Several matching techniques exist [99], and for this work one-way resistive matching has been chosen because it is fast to set up and, further, power dissipation is not an issue. In Fig. 5.12 a schematic of the configuration of a one-way resistive matching network is reported. The network is made by a series resistor Z_m and a 10 dB attenuator, A. To guarantee the matching the following condition has to hold:

$$Z_m = Z_L - Z_0. \tag{5.19}$$

It is called one-way resistive matching because there is matching only from the DUT toward the VNA (with reference to Fig. 5.12). If power travels from the VNA to the DUT it is partially reflected at the location of the resistance Z_m, this is the reason why the attenuator is present. It reduces the reflection that goes back to the VNA because of the mismatch between Z_m and Z_0.

Line impedance of the DUT

From what was said in the previous subsection, and from Eq. 5.19 it is clear that to perform wire measurements one has to know both Z_L and Z_0.

Generally, the VNA and its cables have a known impedance specified by the manufacturer ($Z_0 = 50\ \Omega$ in all the cases discussed in this thesis) while the DUT line impedance Z_L depends on the geometry of the DUT itself and can be found using well know formulae.

For a coaxial line (circular beam pipe with a wire inside) [99]:

$$Z_L/\Omega = 60 \ln\left(\frac{D}{d_w}\right) \tag{5.20}$$

where D is the beam pipe diameter and d_w is the wire diameter.

Another useful relationship is the one for a wire between two parallel plates spaced by D:

$$Z_L/\Omega = 60 \ln\left(1.27\frac{D}{d_w}\right). \tag{5.21}$$

The last one is a good approximation of the line impedance of a collimator.

Another method to obtain Z_L is a direct time domain reflectometry (TDR) measurement, [107]. This method has to be applied when the DUT has complex geometry for which no approximate formulae exist, while in case they exist, it can be used to check the validity of the used expression. An example of time domain reflectometry for a TCLD collimator (discussed in detail in section 7.2) is reported in Fig. 5.13. In the figure, the characteristic line impedance is reported as a function of s (s is measured in meters being the product of the reflected signal time of flight and the speed of light [107]) for different apertures of the collimator jaws. After the TDR is performed, the value of Z_m is obtained by Eq. 5.19. The matching networks are built by welding two resistor Z_m at the beginning and at the end of the wire and connecting the two attenuators.

5.4.2 Measurements and Post-Processing

A qualitative reading of this kind of measurements is straightforward. Once the set-up is done the quantity to look at is the measured magnitude of the scattering transmission parameter Sij. A typical trend of $|\mathrm{S12}|_{\mathrm{dB}}$ is reported in Fig. 5.14 for a collimator. One can distinguish a uniform cyclic behaviour perturbed by some irregularities. These irregularities are the resonant modes while the uniform wiggling baseline is given by the waves reflection inside the DUT. They should not be present because of the matching network, however, it is useful to stress that, for the BIDs that have movable parts inside, the mismatched oscillating behaviour is difficlut to avoid. This is due to practical reasons. The movable part motion strongly influences the line impedance of the DUT Z_L. Obviously, the device coupling impedance has to be analysed for several configuration of the movable parts, i.e. for several value of Z_L. However, according to Eq. 5.19, for every value of Z_L there is a different value of Z_m. Thus, in order to have always a perfect matching, one should remove the current resistor and weld a new one every time that the DUT movable part configuration is changed, and this is not practical. A compromise to work around the problem is computing all the values of Z_m required for a perfect matching and taking the mean value, [103]. However, as anticipated, this means that the matching network is perfectly working only in the mean configuration, and all the other configurations will be approximately matched, thus, showing oscillating behaviour.

Decoupling the contribution of the resonant modes to the Sij from the one of the reflected waves is relatively easy. It is done applying the relation:

$$\mathrm{Sij}_P = \frac{\mathrm{Sij}}{\mathrm{Sij}_{\mathrm{REF}}} \tag{5.22}$$

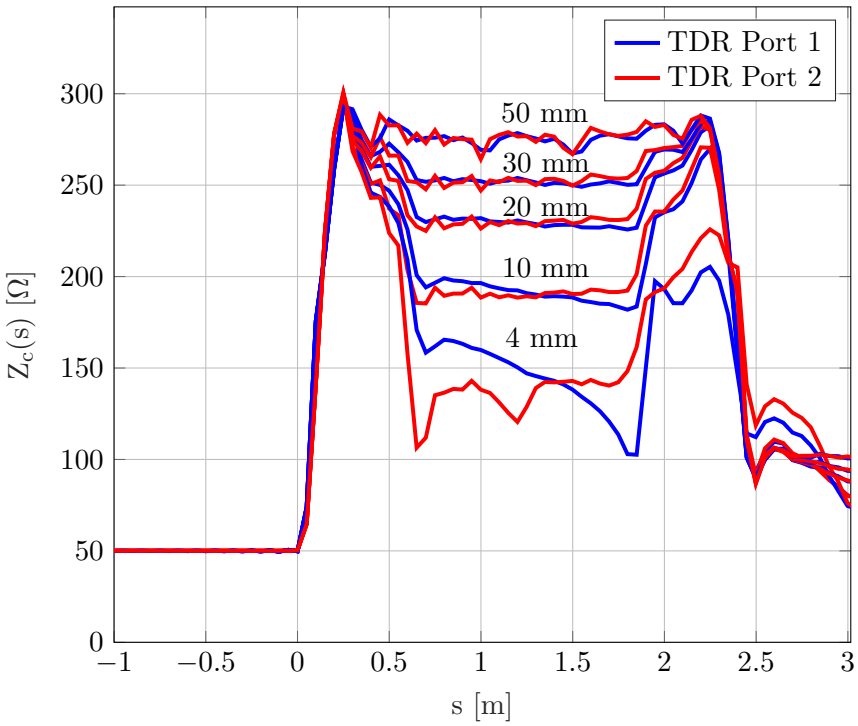

Figure 5.13. Time Domain Reflectometry for a TCLD collimator (discussed in section 7.2) for different jaw apertures (distance between the collimator jaws). The characteristic impedance stays constant to the value of 50 Ω for negative distances. It grows sharply up to 300 Ω around 0.2 m, then, after a slight decrease, it has an almost constant behaviour up to 2 m where it increases again to decay sharply at 2.5 m. The first sharp increase represents the collimator entrance section, with reference to Fig. 7.4a the part where the RF-fingers are located. The zone where the characteristic impedance is constant is the gap between the jaws, and the second step represents the contribution of the exit part, again where the RF-fingers are located. For a jaw aperture of 4 mm, the central part of the characteristic impedance is not constant and symmetric as it should be. This could be due to misalignment of the wire that is not perfectly laying on the beam trajectory.

where Sij are the measured data and $\mathrm{Sij}_{\mathrm{REF}}$ is the response of an ideal reference line without modes, i.e. the wiggling part of Sij. The response of the reference line can be simulated or calculated using approximated analytical models. Furthermore, another method to obtain $\mathrm{Sij}_{\mathrm{REF}}$ is a local polynomial or Fourier series fitting of the data Sij [103]. The degree of the polynomial, or the order of the interpolating Fourier series has to be high enough to capture the wiggling behaviour but not so high to capture also the oscillation due to the mode. In this work, to compute $\mathrm{Sij}_{\mathrm{REF}}$, a weighted fit of the measured data with a Fourier series of eighth order was done. A lower weight was given to the frequency region around the mode resonant frequency.

Once the contribution of the resonant mode to Sij has been isolated in Sij_P, the transmission scattering parameter can be transformed directly into impedance using the log formula [108]:

$$Z_z = -2Z_L \ln(\mathrm{Sij}_P). \tag{5.23}$$

It has to be noted that several formulae to transform the measured transmission scattering parameters into impedance exist [99, 109]. The log formula, Eq. 5.23, was chosen among others because, despite it is not the most accurate [109], it is the most versatile. Its application is not restricted to a limited frequency range and it can be applied both to long and short structure[1] [99].

In Fig. 5.15 an example of wire measurements post processing is shown.

5.4.3 Longitudinal and Transverse Impedance

Equation 5.23 gives the longitudinal impedance in the wire position. As discussed in section 5.2.1, the flanges allow to move the wire along the axis parallel to the micrometer, that is the x axis of Fig. 5.2. It is intended that x is the transverse wire position and that $x = 0$ mm corresponds to the situation for which the wire is on the beam golden orbit. If the longitudinal impedance is known for at least three different transverse wire positions, transverse impedance can be found via the Panofsky Wenzel relation as in Kroyer et al. [99] or in Biancacci et al.[103]. The longitudinal impedance of the DUT for n different wire positions, i.e. $[Z_1, Z_2, Z_3\ ..., Z_n]$ at $[x_1, x_2, x_3,\ ..., x_n]$ is fitted with a parabola $\alpha x^2 + \beta x + \gamma$. The transverse impedance is obtained from the coefficient of this parabola as:

$$Z_t = \frac{c\alpha}{w}, \tag{5.24}$$

where α is the coefficient of the second order term of the parabola, c is the light speed and $w = 2\pi f$, in which f is the particular chosen frequency.

5.4.4 Limitations

In this section the limitations of this method are briefly described. A deeper discussion can be found in [110] and [57].

[1] Long and short structures are defined comparing the device physical length with the wavelength associated to the highest investigate frequency.

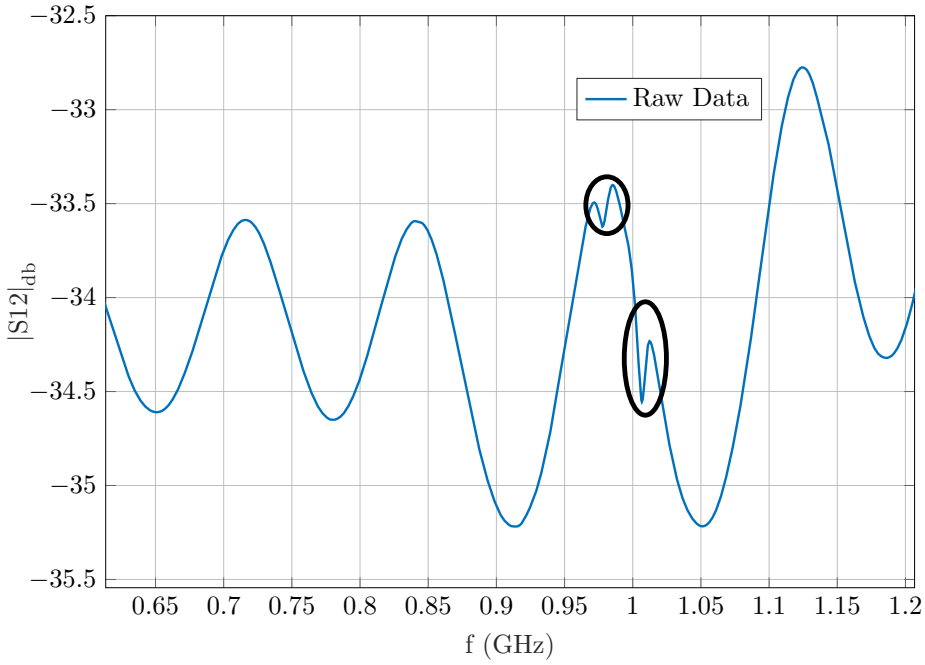

Figure 5.14. Example of data wire acquisition for a collimator. The acquired row data, $|S12|_{dB}$, is shown as a function of frequency. One can distinguish a uniform cyclic behaviour perturbed by some irregularities, highlighted in black. These irregularities are the resonant modes while the uniform wiggling baseline is given by the waves reflection inside the DUT due to the approximated matching.

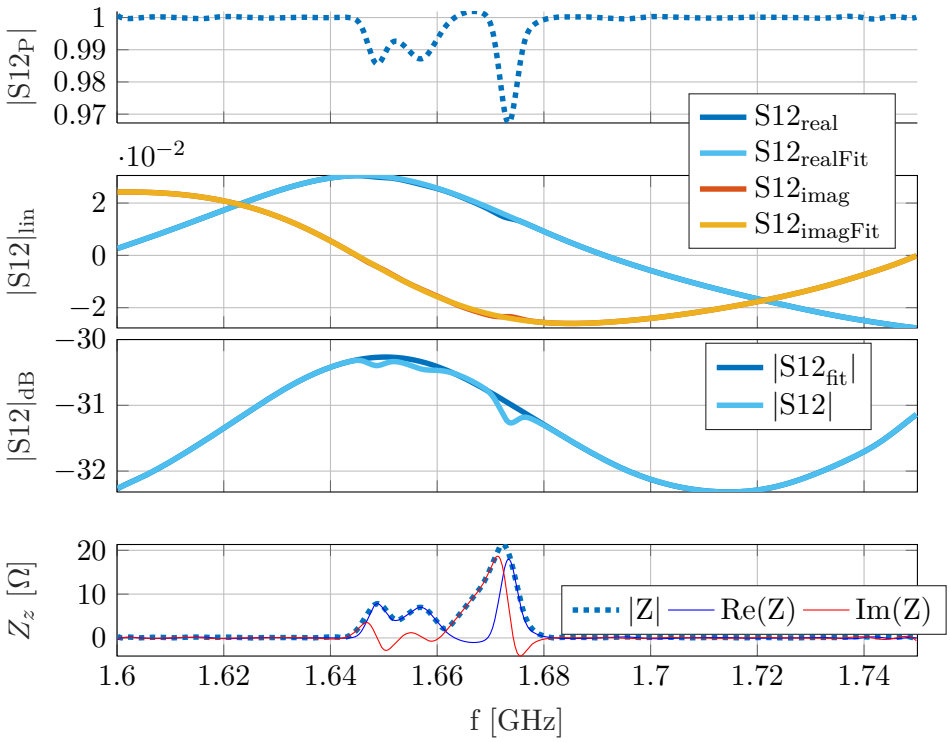

Figure 5.15. Example of wire acquisition post-processing for a collimator. In the second and third graph, the acquired row data ($S12_{real}$,$S12_{imag}$,|S12|) have been fitted with a Fourier series of order eight to obtain the wiggling baseline. This was possible with a weighted fitting with low weight at the mode frequencies. In the top graph it is shown the transmission parameter with the removed baseline. It is clearly possible to see the resonant modes. Finally in the bottom graph, the impedance obtained from the transmission scattering parameter using the log formula Eq. 5.23 is reported.

The wire measurement is an invasive method, since a wire has to be inserted into the DUT. During the wire insertion and the extraction operations there is the risk of damaging the device internal parts . Then, there is also the risk of introducing into the DUT dust or impurities (small pieces of materials for instance), polluting it from a vacuum perspective. The wire is also an electromagnetically invasive method. This point was studied in the work of Panniello [111, 110]. He found that, the presence of the conducting wire in the device forces the electric field of the DUT resonant modes to be perpendicular to the wire (at least in the regions close to the wire). This is usually a strong perturbation for the electric field patterns of the longitudinal modes, i.e. those DUT modes that would have an electric field mainly directed parallel to the wire. The effect of the perturbation is a detuning, i.e. the measured resonating mode frequency (the loaded one) can differ significantly from the unloaded resonant frequency. The detuning of the mode resonant frequency is a limitation of the probe measurements as well, however, in the wire measurements this effect is more pronounced and cannot be neglected.

Furthermore, the wire allows TEM modes with zero cut-off frequencies that would not be present in the DUT without the wire inserted. These modes take out electromagnetic energy from the DUT through the wire. This is a mechanism of dissipation that appreciably decreases the loaded quality factor and shunt impedance of the DUT modes that resonates at frequencies below the device entrance and exit pipe cutoff frequency (this result was reobtained by Zannini [57]). This decreasing in the quality factor and shunt impedance is to be summed to the decrease due to the losses on the wire. Panniello [110] found also that, above the device pipe cutoff frequency, the dissipation effects of the TEM modes introduced by the wire have a negligible influence. Indeed, above the pipes cutoff frequency, energy can evacuate the vacuum chamber trough the DUT entrance and exit pipe also without the wire.

The main conclusion of Panniello [110] is that the wire method gives precise impedance estimation only for modes resonating at frequencies higher than the cutoff frequency of the inner and outer pipes of the measured device. Below the pipes cutoff frequency, the wire method could bring to errors in the mode impedance estimation. These errors depends on the coupling between the wire and the mode, for high coupling, the mode is strongly perturbed by the wire and the error on the impedance estimation is large (usually, longitudinal modes resonating in the path of the wire are the most perturbed). Vice versa, if there is low coupling between the mode and the wire, the impedance estimation can be considered accurate also below the entrance and exit pipes cutoff frequency. This aspect can be checked by simulating the DUT wire measurements set-up (the DUT with the wire inside) and comparing it with simulations of the simple DUT.

5.5 Beam Position Monitor Measurements

Beam position monitors (BPM), are used to measure the longitudinal beam profile and the transverse positions of the bunches [112]. They are non-destructive diagnostic devices made by a couple (or more) of insulated metal plates (electrodes) one facing each other. The BPMs measure the charge induced on the plates when the bunch (or a part of it) is passing between them. This allow to measure the longitudinal

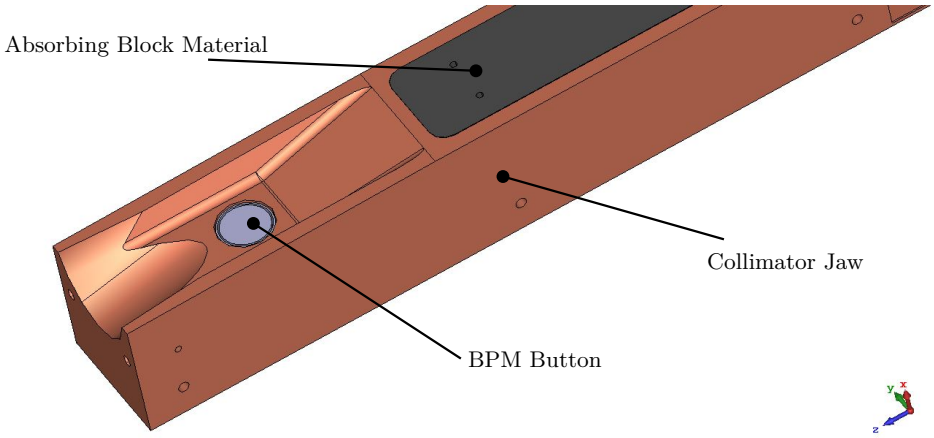

Figure 5.16. Example of a BPM plate on a collimator jaw.

profile of bunches. Furthermore, If a bunch is closer to one of the electrode, the signal registered in that electrode is larger than the signal registered by the other electrode, this allows to estimate the bunch transverse position. A BPM in the jaw of a collimator is reported in Fig. 5.16. The BPM plates are electromagnetic probes, and during the accelerator operations, they are only used as reading ports. However, in impedance bench measurements they can be used also as excitation ports.

Thus, BPM impedance measurements are basically probe measurements. They have the big advantage to be noninvasive. Indeed, for this kind of measurements the excitation sources does not perturb the device because the BPMs are already part of it. Thus, they do not have the problem of the loaded and unloaded quantities.

However, the drawback of this kind of measurements is the fact that the BPM position in the device is fixed. Thus, BPMs can detect only modes that have field component close to their installation region. This means that, if no mode is visible with the BPM measurements one cannot conclude that there is no mode in the device. Further, another limitations is the fact that, at the writing time, among the new CERN BIDs, only some collimators have BPM.

An example of transmission measurements from two BPMs is shown in Fig. 5.17 where the scattering paramenter S12 is reported.

5.6 Conclusions

This was a background chapter. Some basic concepts of RF engineering were introduced: the resonant mode quality factor, shunt impedance and resonant frequency, distinguishing them between loaded and unloaded. Subsequently, the CERN impedance measurements equipment was presented, followed by some of the techniques used in this work to measure device impedance, i.e. probes, wire and BPM measurements. For each one of them the data acquisition and post-processing was discussed as well as the limitations.

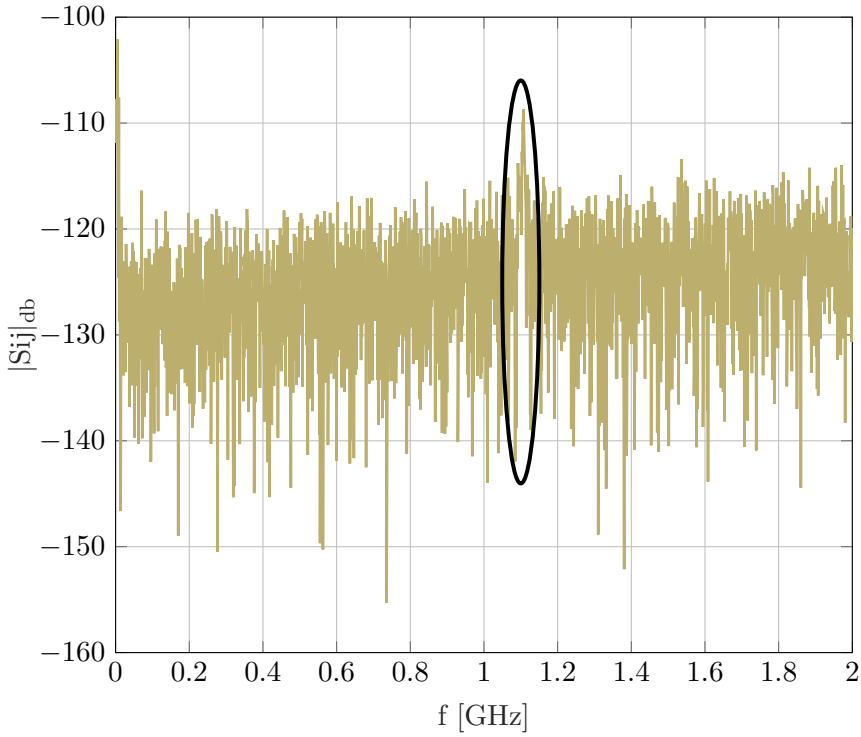

Figure 5.17. Example of BPM measurements, a mode around 1.1 Ghz is highlighted by the black circle.

Chapter 6

Impedance Minimization of LIU Devices

6.1 Introduction

This chapter contains original material partially published as light peer review proceeding in several conferences, [113],[114],[115],[116].

As already said in chapter 1, during the coming years the CERN accelerator complex will be upgraded to improve its performance. An increase of the beam energy, intensity and brightness is foreseen in the framework of the projects LIU (LHC Injection Upgrade) [17] and HL-LHC (High Luminosity Large Hadron Collider) [16]. A large number of systems, equipment and devices will be redesigned taking into account the challenging new situation. Particularly, the raised intensity of the HL-LHC beams may lead to beam instabilities and high RF-heating. Thus, extra attention needs to be paid to electromagnetic and thermo-mechanical interactions between the beam and its surroundings. In this context, the beam-device coupling impedance is a driver for the new device design. Its evaluation and minimization is essential during the early design phase to avoid beam instabilities, reduce beam losses and minimize impedance induced heating.

Both the material and geometrical features that lead to a high impedance devices[1] are well known by the impedance community along with the way to cure them: Day [117] reported some impedance mitigation techniques, Chao discussed the resistive wall impedance in details [46], while Palumbo et. al [38] and Y. Chin [118] discussed various high impedance geometric features. However, implementing the curing methods from the device design may not be trivial. Real components have to fulfill their functional requirements, in addition to easy manufacturing and integration, size and cost constraints. Those points may be in conflict with an impedance optimized design. In this case, a compromise has to be reached, i.e. the design is to be modified reducing impedance as much as possible, satisfying the requirements.

[1] In section 3.2.3 it was discussed how impedance can be divided into two contributions, the one due to the geometry of a device (geometric impedance) and the one due to the electromagnetic properties of the materials that compose the device (resitive wall impedance, due to the electrical resistivity of the material and to the presence of ferromagnetic materials).

6.1.1 Scope and Structure Of the Chapter

In the context outlined in the previous section, the main scope of this chapter is to show a way to minimise the device impedance satisfying the device functional requirements.

The chapter has the following structure: Section 6.2 reviews the high impedance features most commonly encountered in BID designs and the guidelines to cure them. The section reports some schematic examples of the curing methods, and it analyses their longitudinal impedance before and after the cure implementation.

Subsequently, as an original contribution of this work, examples of applications of this guidelines on real LIU devices are shown (LHC devices are discussed in chapter 7).

In section 6.3 the Proton Synchrotron Booster absorber/scraper (PSBAS) is discussed. The design iterations to go from the preliminary high impedance design to the final low impedance one are reported. Further, also the thermo-mechanical simulations performed to assess the response of the device in operation conditions are reported.

Section 6.4 discusses the Proton Synchrotron internal Dump (PSD) impedance optimisation process and the thermo-mechanical simulations on the device to assess the impedance RF-heating effects.

Section 6.5 reports the impedance analysis on the Proton Synchrotron Ralentisseur.

Finally, section 6.6 concludes the chapter summarising the main points.

6.2 Guidelines For Low Impedance Designs

This section discusses common high impedance features in BIDs and the way to cure them. First the high geometric impedance features of devices are discussed. Their effects are analyzed and a possible simple and cost-effective design modification to eliminate them, or at least to reduce their detrimental impact, is proposed. Then effects of the materials on the impedance are discussed.

6.2.1 Methodology

For the current investigation a careful analysis of the design of various mechanical devices under development at CERN was carried out. Some of these devices, in their preliminary design, exhibited common geometric high-impedance features, well documented in literature [38], [118]. These features were deeply investigated through numerical simulations with the aim of eliminating them or reducing their effects with modifications to the device design. They were considered individually and modelled in the CAD (computer aided design) tool of a Finite Integration Technique (FIT) software. Their basic geometrical features were considered as parameters in order to characterize the effects of their variation. The software used for the impedance simulations was CST Particle Studio® [56]; its time domain solver, Wakefield [60], is a well known and tested tool at CERN for device impedance computation [57], [49].

6.2.2 Geometric High Impedance Feature: Abrupt Changes of Section in Components

Abrupt changes of section were often recurring in the preliminary design of the analyzed devices. However, they should be avoided because they generate electromagnetic trapped modes visible as well defined peaks in the impedance curve, (refer to Fig. 6.2).

In order to investigate the effects of the abrupt changes of section, the geometry shown in Fig. 6.1 was simulated. The radius of the small pipe was considered fixed ($r_a = 5$ mm) while the radius of the larger pipe, r_b was parametrized. The longitudinal impedance of the abrupt change of section is reported in Fig. 6.2 for different value of the radius r_b. Compared to the case $r_a = r_b$, i.e. no section changes, for $r_b > r_a$ an increase in the impedance can be observed. In the case $r_b = 10$ mm no trapped modes are visible at the investigated frequencies. However, the same Fig. 6.2 shows that for $r_b \geq 35$ mm trapped modes start to appear. Further, the more r_b increases the more the observed modes shift to lower frequencies raising their impedance peak value. This finding agrees with well known results, [38]. The key parameter of the phenomenon is the pipes radii ratio r_b/r_a. By increasing it, the frequency of the resonant modes decreases while their impedance peak value increases.

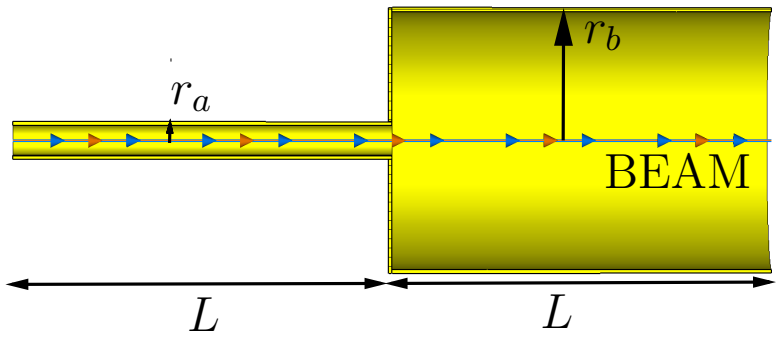

Figure 6.1. Abrupt section change geometry model: $r_a = 5$ mm, $L = 100$ mm, $r_b =$ parametrized.

An easy solution to the problem is tapering. To investigate its effects, the geometry of Fig. 6.1 was modified, adding a conical connection of length L_t between the two pipes as illustrated in Fig. 6.3. The radius of the small pipe, the length of the pipes and the length of the conical taper were considered fixed ($r_a = 5$ mm, $L = 100$ mm, $L_t = 50$ mm) while the radius of the larger pipe, r_b was parametrized. The results of the simulations, the longitudinal impedance for different values of the radius r_b, is reported in Fig. 6.4. In the case $r_b > r_a$ there is an impedance increase in comparison to the case $r_a = r_b$, i.e. no section changes. The non tapered configuration has the same qualitative behaviour. For $r_b = 10$ mm no trapped modes are visible at the investigated frequencies, in this case virtually no differences can be found between tapered and not tapered configurations. As for the configuration without taper (Fig. 6.2) for $r_b \geq 35$ mm trapped modes start to appear, although

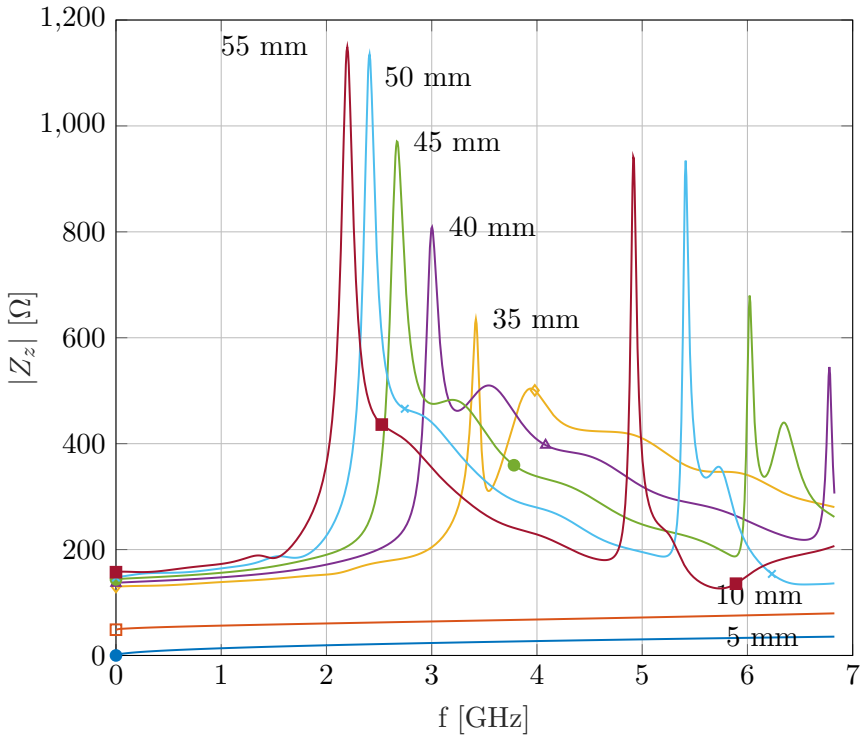

Figure 6.2. Abrupt section change configuration. Longitudinal impedance modulus computed for different values of r_b (they are indicated in the figure), the value of $r_a = 5$ mm was considered fixed.

the beneficial effects of the taper results in lower impedance peak values. This can be clearly seen comparing the results of the abrupt section change geometry (Fig. 6.2) with the ones of the tapered configuration (Fig. 6.4). Further, considering the r_b value which leads to the worst case scenario (i.e. the highest considered r_b) we investigated the effects of variation in the taper length. The result is shown with a dashed line in Fig. 6.4, revealing the beneficial effects of a longer taper which further decreases the peak impedance of the modes. A good practice in use at CERN is to have tapered change of sections with a tapering angle not higher than 15 degrees [117], except if strictly required by the design. An example of taper application for impedance reduction can be found in the PSD in section 6.4.

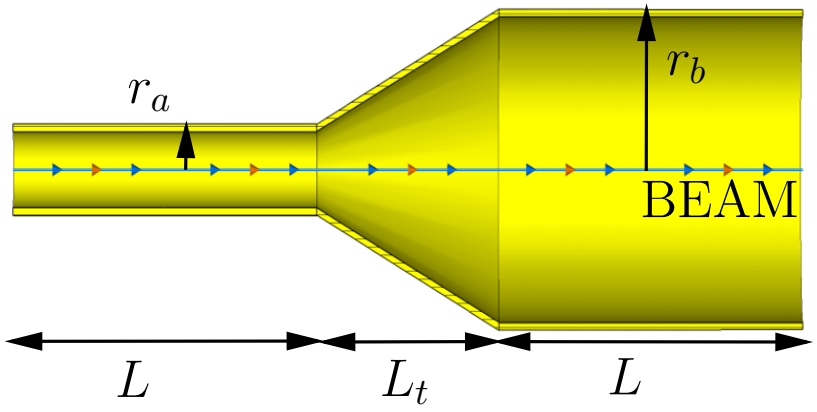

Figure 6.3. Tapered section change geometry model: $r_a = 5$ mm, $L = 100$ mm, $L_t = 50$ mm, r_b = parametrized.

6.2.3 Geometric High Impedance Feature: Gap

Gaps and absence of electrical connections among components are other, quite common, high impedance features found in the preliminary analyzed designs. Gaps should be avoided because they create capacitive effects leading to high impedance values at low frequencies, which are very dangerous for RF heating. In order to study their effects the geometry shown in Fig. 6.5 was simulated. The length and the radius of the pipes were considered fixed ($r = 5$ mm and $L = 100$ mm) while the gap between the pipes, g, was parametrized.

Impedance simulations results are reported in Fig. 6.6 for different values of g. The capacitive effects of the gap results in high impedance at very low frequencies. The impedance peak values increase with the distance between the pipes. This is consistent with the results obtained in [118]. Other peaks at higher frequencies can be seen from Fig. 6.6. According to [118], they map trapped modes in the gap.

The easy solution to the detrimental effects of a gap is the gap elimination by connections. Figure 6.7 shows the same geometrical layout of Fig. 6.5 with the addition of two symmetrical electrical connections between the two pipes. For simulations the length and the radius of the pipes were considered fixed ($r = 5$ mm and $L = 100$ mm) while the gap between the pipe, g, was parametrized. The

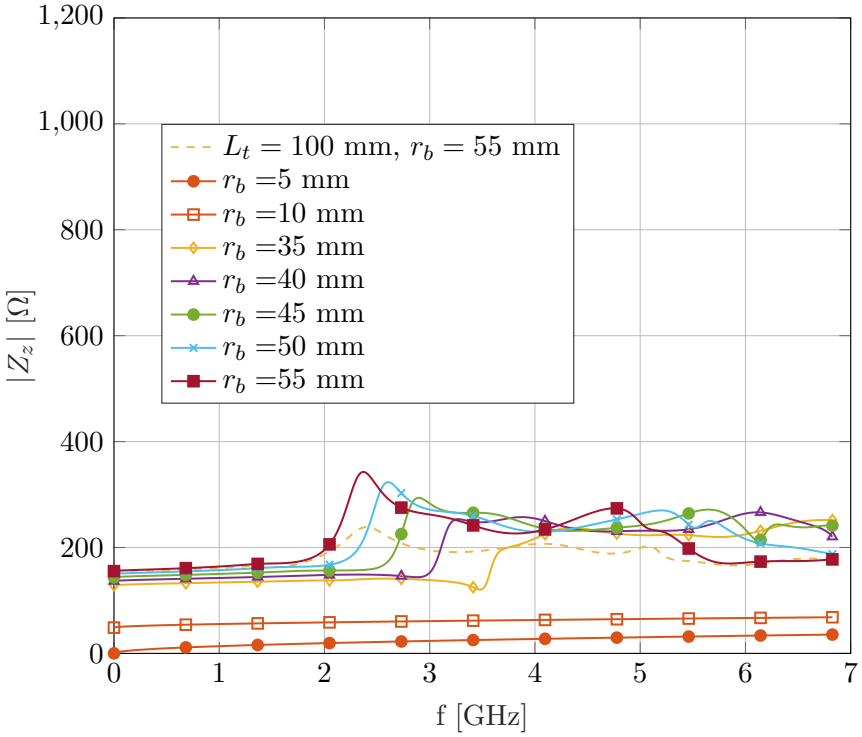

Figure 6.4. Tapered section change configuration. Longitudinal impedance modulus for different values of r_b.

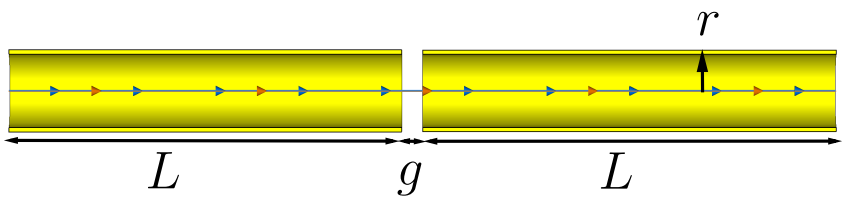

Figure 6.5. Open gap model geometry: $r = 5$ mm, $L = 100$ mm, $g =$ parametrized.

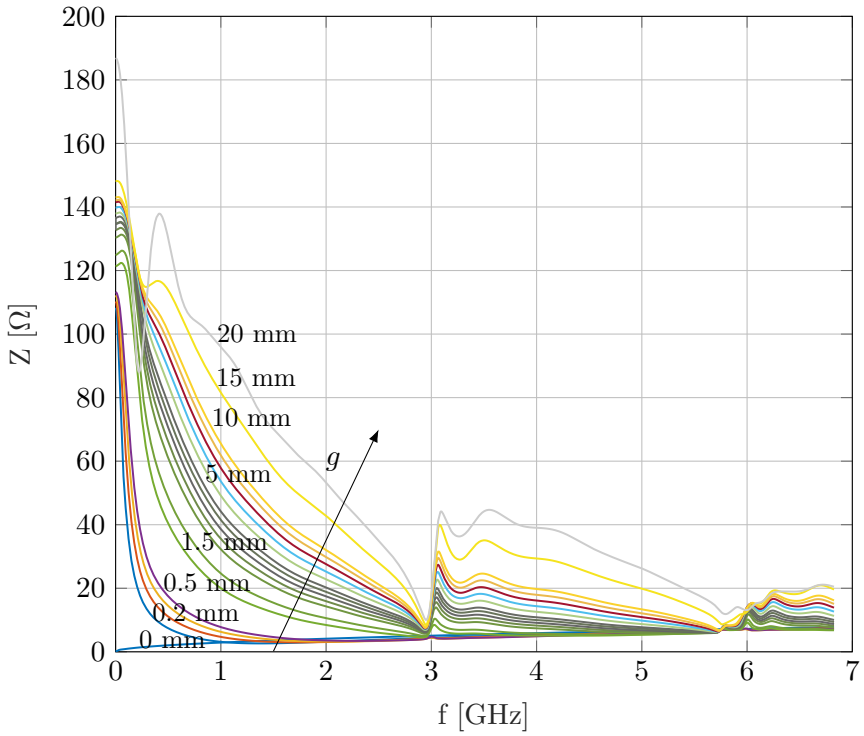

Figure 6.6. Open gap model geometry, longitudinal impedance modulus computed for different values of g.

obtained results, reported in Fig. 6.8, demonstrate the effectiveness of applying connections. Comparing the impedance of the open gap geometry, Fig. 6.6, with the impedance of the same geometry with connections, Fig. 6.8, one notices that impedance at very low frequencies is drastically reduced for all gap sizes when connections are added. However, in the connected geometry a new trapped mode is present, around 2 GHz. It was not found in the open gap configuration. This mode strongly depends on the contacts shape and on the number of connection points and it can be shifted to higher frequencies simply adding more contact points. Impedance behaviour for frequencies higher than 3 GHz seems not to be affected by the connections. During the design phase, gaps should be always avoided by some kind of connection, and RF-fingers are usually used for that. An example of their use can be found in section 6.3 where the PSBAS is discussed.

6.2.4 Geometric High Impedance Feature: Parasitic Cavities

The last high impedance feature noticed during the design analysis was the presence of parasitic cavities. Every empty volume that is directly seen by the beam potentially behaves like a parasitic cavity, i.e. it extracts energy from the beam in order to excite its resonant modes. This leads to really high peaks in the impedance curve of the device and it is very dangerous due to long range instability effects [46] and RF-heating. The bigger the empty volume the lower the mode resonating frequency, thus, in general, if an empty volume is needed for device working reasons, it should

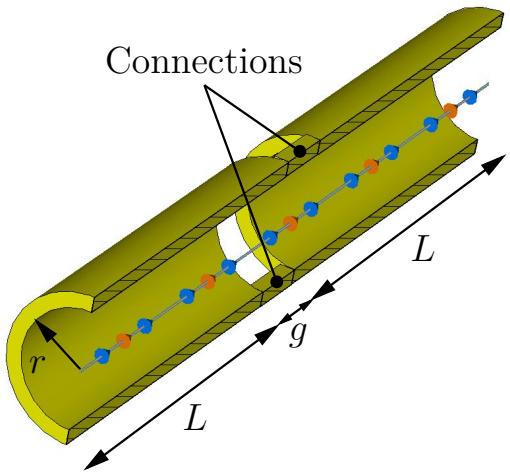

Figure 6.7. Gap with connections. Geometry: $r = 5$ mm, $L = 100$ mm, $g =$ parametrized.

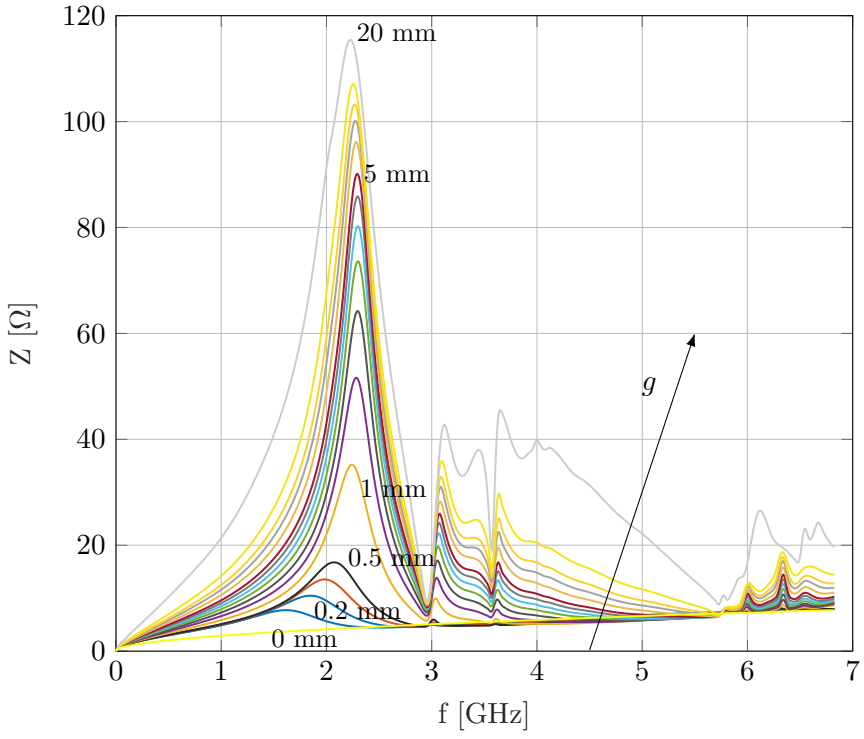

Figure 6.8. Gap with connections. Longitudinal impedance modulus for different values of g.

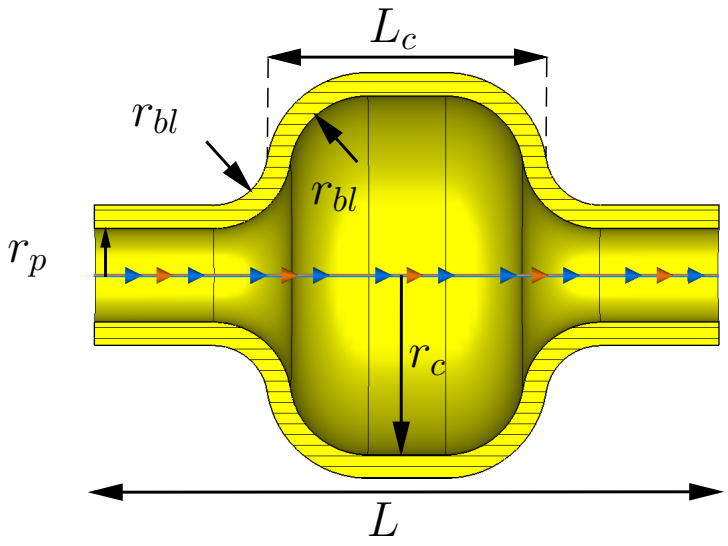

Figure 6.9. Unshielded cavity. Geometry: $r_p = 60$ mm, $L = 800$ mm, $r_{bl} = 100$ mm, $L_c = 300$ mm, $r_c = 230$ mm.

be the smallest possible.

It is well recognized in literature that in the case of a cavity, a key role is played by the wall material, particularly the electrical conductivity σ strongly influences the peak impedance of the mode. The cavity geometry shown in Fig. 6.9 was simulated considering different wall materials.

The longitudinal impedance modulus of the mode that resonates at the lowest frequency is reported in Fig. 6.10.

The most common way to eliminate this contribution is the use of RF-shieldings. An RF-shielding is a metal screen that blocks electromagnetic interactions between the beam and the empty volume. It can have different shapes in order to better fit the geometry it has to shield. An example of shielding is proposed in Fig. 6.11, where the geometry of the previous parasitic cavity (refer to Fig. 6.9) has been modified adding ten metallic tubes on a circle connecting the inner pipe with the outer one.

The results of the electromagnetic simulations on the shielded cavity geometry, in Fig. 6.12, show a striking impedance reduction of about 6 orders of magnitude if compared with the results of the no-shielded configuration of Fig. 6.10. This is due to the fact that the particle beam does not see any more the empty volume, and the resonant mode disappears. A pratical example of af an RF-shielding can be found in section 6.3 where the PSBAS impedance design optimization is discussed, in section 7.3 where the TDIS is discussed or in section 7.2, where the TCLD is discussed.

6.2.5 Material High Impedance Feature

As already seen in section 3.2.4, the resistive wall impedance is directly dependent on the electric conductivities and of the vacuum chamber wall materials and on their distance from the beam. The greater the distance of the wall from the beam the

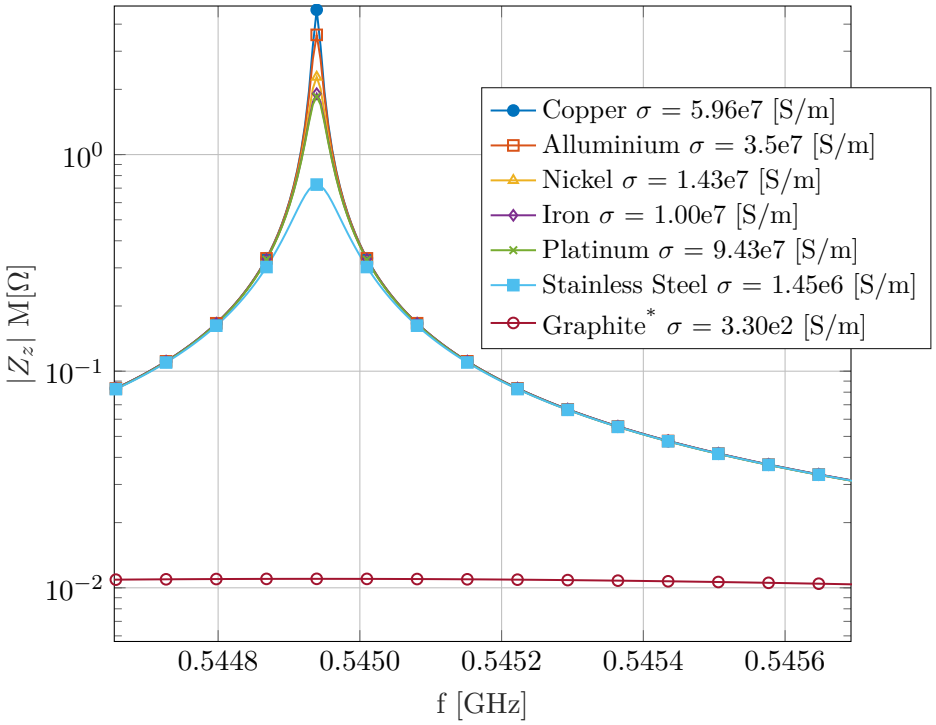

Figure 6.10. Unshielded cavity. Longitudinal impedance computed for different values of the material electrical conductivity σ. Logarithmic scale.

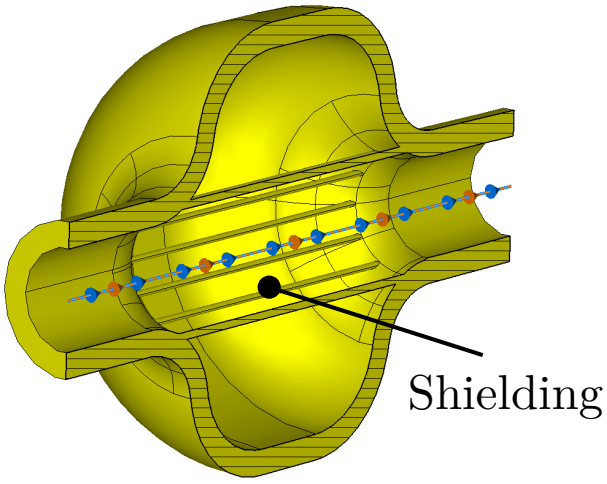

Figure 6.11. Shielded cavity geometric model.

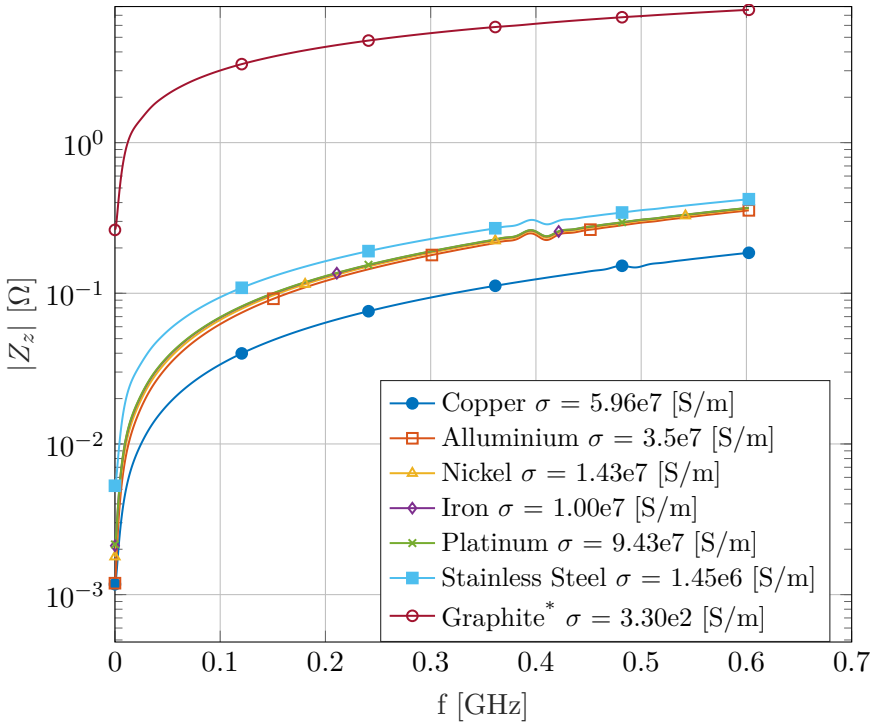

Figure 6.12. Shielded cavity. Longitudinal impedance modulus computed for different values of the material electrical conductivity σ. Logarithmic scale.

smaller the impedance, the higher the wall conductivities the smaller the impedance. However, these two dependencies are not equivalent. Indeed, looking at the resistive wall longitudinal impedance expression for a cylindrical beam pipe, Eq. 3.6, one realizes that it scales with the inverse of the beam wall distance and with the inverse of the square root of the vacuum conductivities. This means that, if one wants to halve the resistive wall impedance, one has to double the beam wall distance or one has to build the vacuum chamber with a material that has four times the conductivity of the current material. Note that when the beam passes close to a material the electron cloud phenomenon could also develop [43]. As for the impedance, it can lead to heating and beam instabilities. The parameter that indicates if the chosen material is prone to generate electron cloud is the secondary electron emission curve, that indicates how many electrons are irradiated by the material if it is bombarded with an electron of a given energy. Some curves of secondary electron emission for common technical materials are reported in the work of Baglin et. al [119]. In general, one should choose a material with high conductivity and poor electron emission curve. It is also important to consider that surface treatment and thermal treatment can decrease or increase the electron emission curve [119].

Another important effect is due to the presence of ferromagnetic materials in the device. These materials could be needed to damp a resonant trapped mode in the device that it is not possible to eliminate with geometrical modifications. In this case the ferromagnetic material should be put inside the mode fields but as far as possible from the beam. Furthermore, ferromagnetic materials heat up when

they have to dissipate the resonant mode energy. Thus, a good heat evacuation system has to be considered around these materials. An example of a device with ferromagnetic material used to damp an electromagnetic resonant mode is the new cylindrical TOTEM roman pot [88], discussed in chapter 4. Ferrites are also used in beam kickers, devices that have to generate fast rising magnetic fields that deviates ("kick") the beam modifying its trajectory [57]. Kickers are used, for example, for the beam injection and extraction operations.

6.2.6 Impedance Guidelines: Conclusions

In this section the high impedance features, both geometric and material related, were reviewed. Regarding the former, the section has shown how, abrupt changes of section, lack of electrical connections among the device components and empty volumes directly seen by the beam generates resonant modes. Solutions to avoid such modes has been reviewed, as tapering, RF-contacts, and RF-shieldings, and their beneficial effects were shown by simulation results. Regarding the material related high impedance characteristics, it was concluded that to lower resistive wall impedance the beams should pass far from the vacuum chamber wall or/and the latter has to have high conductivity. Moreover, it was briefly discussed also the problem of secondary electron emission for high conductive materials. Finally the ferromagnatic material impact on impedance was analyzed. Such materials should be put as far as possible from the beam, or they have to be well shielded. They also have to be inside the resonant mode that they have to damp.

6.3 The Proton Synchrotron Booster Absorber Scraper

This section summarizes conceptual design studies on the new Proton Synchrotron Booster Absorber/Scraper (PSBAS), a device aimed at cleaning the beam halo at the very early stage of the PSB acceleration. The section outlines the steps performed to fulfil the component design requirements. It discusses the impedance optimisation performed on the design. Furthermore, it discusses thermo-mechanical effects as a consequence of the beam-matter collisions, simulated with the FLUKA Monte Carlo code and ANSYS® finite element software; and the impedance minimization study performed to prevent beam instabilities and to reduce RF-heating on the device.

6.3.1 Introduction

The beam cleaning system (collimation and scraping) is essential for the entire CERN accelerator chain. This system absorbs unstable external beam particles, i.e. beam halo, in controlled areas preventing them from irradiating against sensitive equipment, minimizing the risk of damage [23]. In the framework of the CERN HL-LHC [16] and the LIU [17] projects, the beam intensity will be increased and the current cleaning system needs to be upgraded accordingly. In this context, Cieslak-Kowalska et al. [120] have demonstrated that the present scraping device in the PSB, the windows beam scope, will not be able to scrape the high intensity LIU beams. This section presents the conceptual design of its upgrade: the PSBAS.

The PSBAS will represent the major aperture restriction of the PSB. It will scrape up to 6% of the total number of protons ($2.95\ 10^{12}$ [17]) for a LIU beam during the very early stages of acceleration (kinetic energy per nucleon up to 200 MeV). It must be able to survive a direct accidental beam impact and its impedance has to be minimized. Further, in order to correctly scrape the beam halos (a description of halos is given in section 7.2.1) the PSBAS geometry has to follow the beam transverse envelope shape (i.e. the square root of the beta function) and its longitudinal evolution inside the device itself (the complete requirements list can be found in the document [121]). To fulfil the outlined requirements the preliminary design shown in Fig. 6.13a was conceived. The two graphite masks, cylinders with a truncated squared based pyramid holes to follow the beam β function, are the actual beam scraper. They can be positioned in two working configurations (Fig. 6.13a) according to the operational requirements: movable mask out provides a wide aperture for the initial beam commissioning while movable mask in limits the aperture for an optimal beam cleaning during nominal operation. However, the preliminary design was found not optimal from an impedance perspective and it needed to be optimized. The performed optimisation studies are reported in this section. Further, the thermo-mechanical studies to evaluate the effects of the beam scraping and the RF-heating are reported as well.

6.3.2 Impedance Reduction Campaign

To reduce the PSBAS impedance, an iterative loop was implemented from the initial PSBAS design simulating the device impedance, identifying the problematic geometries and modifying the mechanical drawing accordingly.

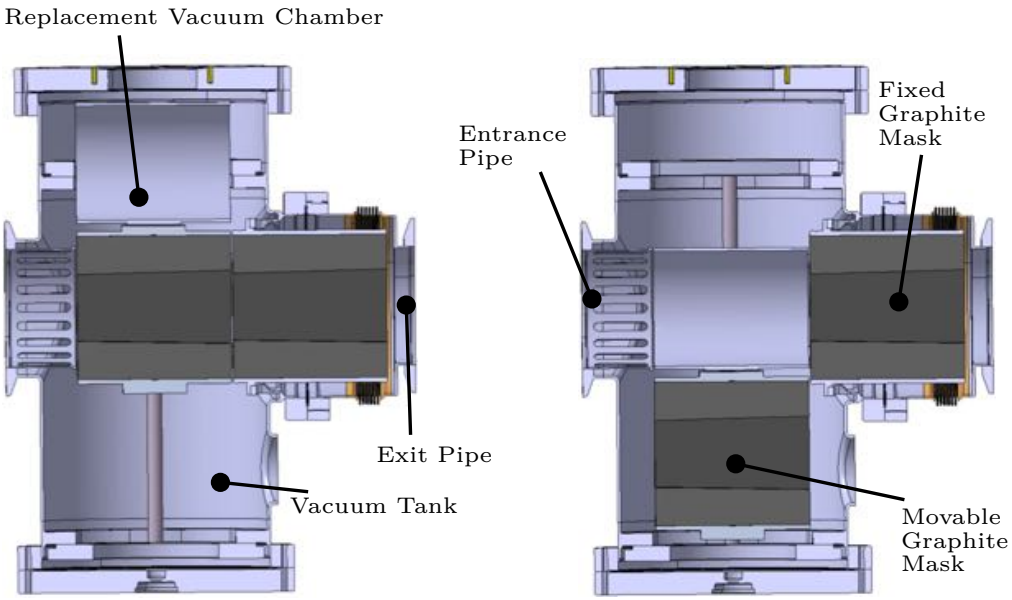

(a)

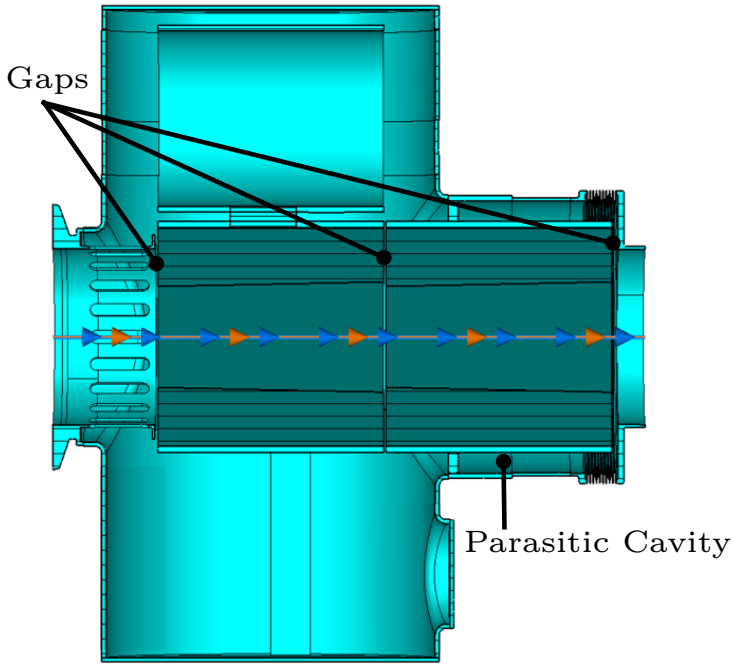

(b)

Figure 6.13. Different Geometries of the PSBAS: preliminary and final low impedance design. (a) Preliminary PSBAS design: Working configuration and nomenclature. (b) Preliminary PSBAS design: CST model and high impedance features.

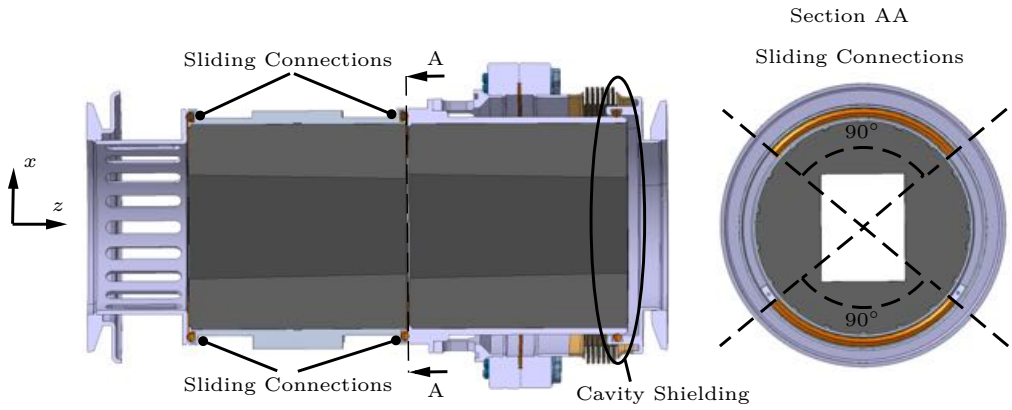

Figure 6.14. Final low impedance PSBAS design: Section view and detail of the sliding connections.

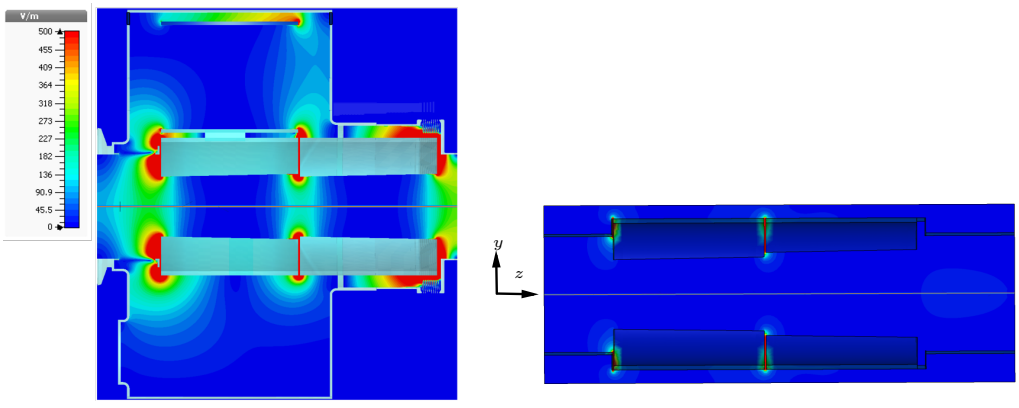

(a) **(b)**

Figure 6.15. (a) PSBAS preliminary design, electric modes field shapes. (b) PSBAS final design, electric modes field shapes (scale on Fig. 6.15a).

The electromagnetic properties of the equipment were assessed through simulations with CST Particle Studio®.

The high impedance characteristics of the PSBAS preliminary design are shown in Fig. 6.13b on the CST simulated model. To allow an easy motion of the movable graphite mask, the latter was not electrically connected to the rest of the device along the beam path direction. Thus, gaps were present in this design, leading to the generation of resonant electromagnetic modes trapped in the gaps, refer to Fig. 6.15a. Moreover, such a design presents an unshielded empty volume around the fixed graphite mask. It is important to stress that in the preliminary PSBAS design, shown in Fig. 6.13a, some impedance mitigation measurements were already taken: in configuration mask out, the replacement vacuum chamber was acting as a shielding against the vacuum tank, a potential parasitic cavity, preventing it from resonating. However, this was not sufficient and the impedance behaviour of the device turned out to be unacceptable. Indeed, the discussed high impedance features generated trapped modes at frequencies lower than 0.4 GHz. The latter is considered as the acceptable lower limits for modes in the PSB machine [122]. Therefore, the preliminary PSBAS design, was not impedance compliant. A new design, presented in Fig. 6.14 was conceived.

A comparison between the results of the electromagnetic simulations, electric modes field shapes and device impedance, for the preliminary design and for the impedance improved design are shown in Fig. 6.15a and 6.16.

As a part of the work done for this thesis, some modifications to the PSBAS preliminary design were proposed in order to eliminate the low frequency resonant mode:

- Electric sliding connections, between movable and fixed parts, were added to eliminate the resonant modes in the gaps shown in Fig. 6.15a.
- The parasitic cavity was shielded by a geometry modification.

This led to an impedance compliant design, shown in Fig. 6.14, eliminating the modes at low frequencies and so decreasing the maximum impedance of the device of three orders of magnitude if compared with the previous performances. The results of the electromagnetic simulations, field shapes of the electric modes and device impedance, are shown in Fig.s 6.15b and 6.16. Note that in both the final and preliminary PSBAS design there are abrupt changes of section between the graphite masks and the pipes. No attenuation method was applied to reduce their effects because, due to operational and space constraints, it was impossible to add tapers. However, despite this, with the curing methods applied, it was possible to drastically reduce the impedance at low frequencies.

6.3.3 Impedance Optimized Final Design

This section discuss in detail the the final, impedance optimised, PSBAS design reported entirely in Fig. 6.17. In configuration mask out, the replacement vacuum chamber works as RF-Shielding, preventing the tank from trapping electromagnetic resonating modes. The electrical connections between the fixed mask housing and the out pipe (Fig. 6.17 Detail 2) shields the empty volume between the bellow

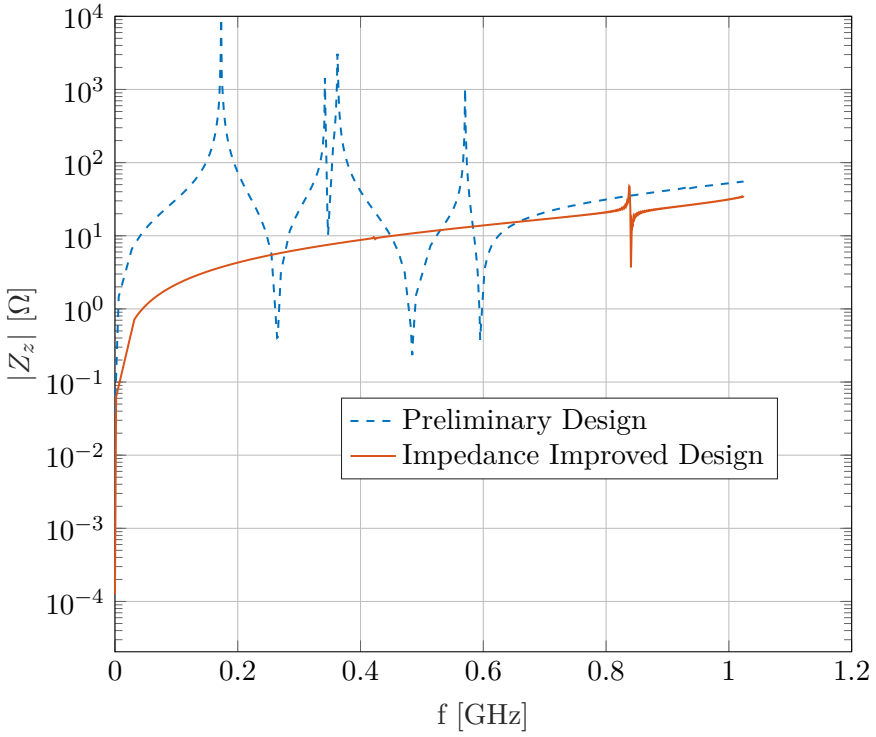

Figure 6.16. PSBAS final vs PSBAS preliminary design, Longitudinal Impedance Modulus. Logarithmic scale.

and the housing-itself avoiding trapped resonating electromagnetic modes inside. This connection is made of a ring of stainless steel material with two copper spirals mounted on it, which is installed inside a circular groove, machined in the fixed mask housing. This allows an easy assembling of the components guaranteeing the electrical contact at all times. The movable components, the replacement vacuum chamber and the movable mask with its housing, are separated from the fixed components, in pipe and fixed mask housing, by a gap of 2 mm. However, they are electrically connected by means of sliding connections. As shown in Fig. 6.17, detail 1 and 3, there are copper wire spirals inserted on grooves realized on the replacement vacuum chamber and on the movable mask housing. They provide a path for the image currents and limit the detrimental effects of the trapped electromagnetic resonant modes in the gaps.

The real and imaginary parts of the longitudinal and transverse impedance of this design are shown in Fig. 6.18. The longitudinal impedance of the scraper is negligible with respect to the PSB impedance, thus, no longitudinal beam instability issues are expected [123]. Furthermore, the transverse impedance of the scraper is three orders of magnitude smaller than the global transverse impedance of the PSB [124]. In the transverse plane, there is not a relevant effect on the rise time of the head-tail instabilities [46] in the z-x plane, where the PSBAS impedance contribution is maximum. This is shown in Fig. 6.19, where the rise time of the first two unstable beam modes is plotted. Thus, the device has negligible impact also on transverse beam instabilities.

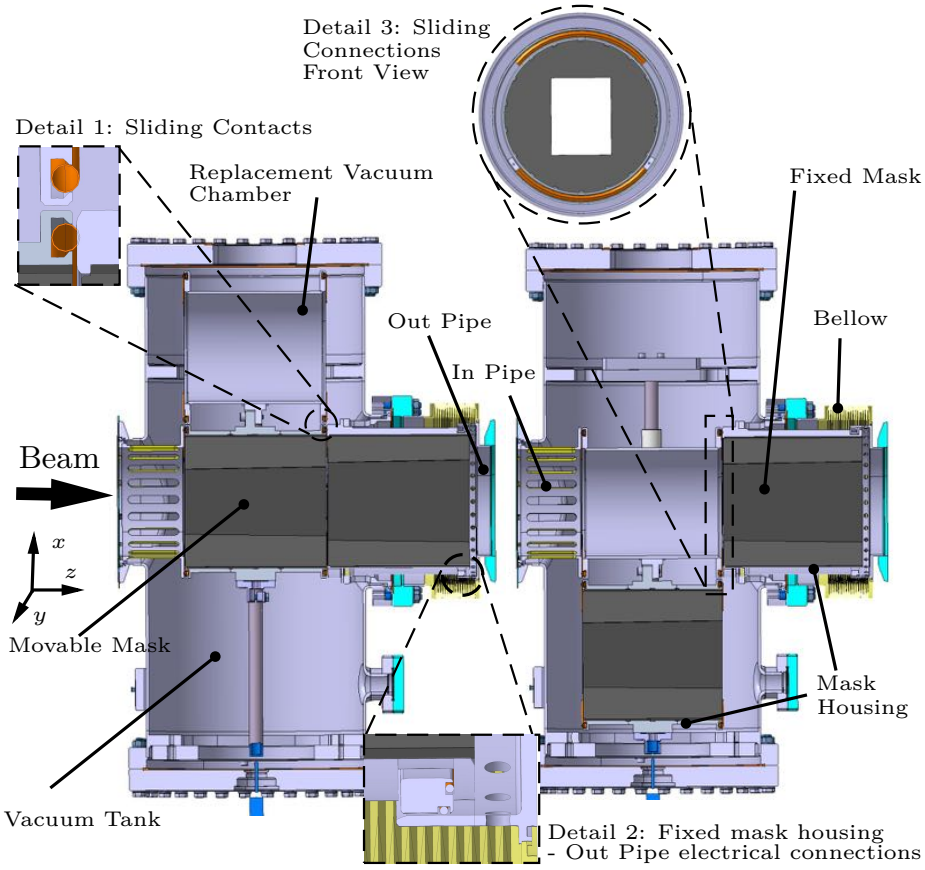

Figure 6.17. Final design of the impedance optimized PSBAS with nomenclature and details of the electrical connections. The two working configurations are also shown: movable mask in (left) and movable mask out (right).

6.3.4 Impedance RF-Heating

Also the RF-heating, the heating flux deposited in the material by the circulating beam through electromagnetic interactions, was computed for the PSBAS. The 3D map of the dissipated power was obtained following the procedure described in chapter 4 and it has been plotted in Fig. 6.20 for the scenario 1 movable mask in (refer to the next section). The total estimated RF-heating for the device is 0.43 W, only 1.69% of the power deposition due to nuclei matter interaction (refer to the next subsection 6.3.5).

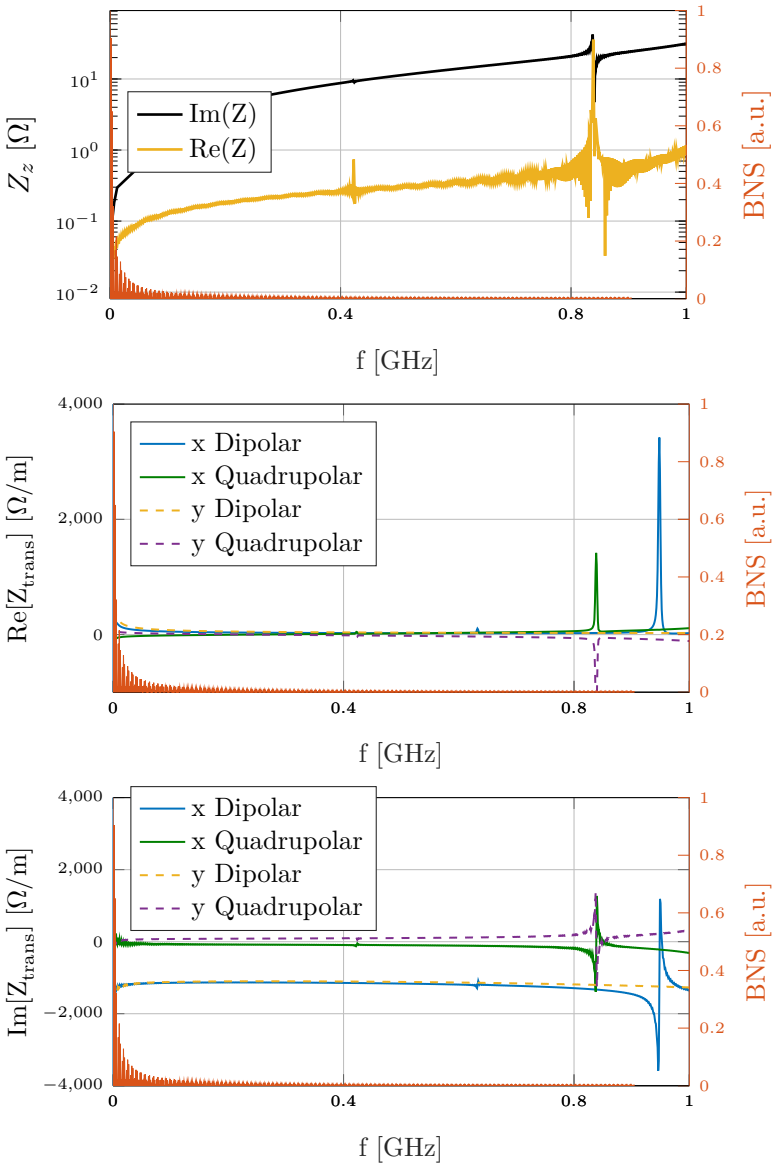

Figure 6.18. Real part of the longitudinal (log scale) and the transverse (linear scale) impedance with the PSB beam normalized spectrum (BNS) in linear scale.

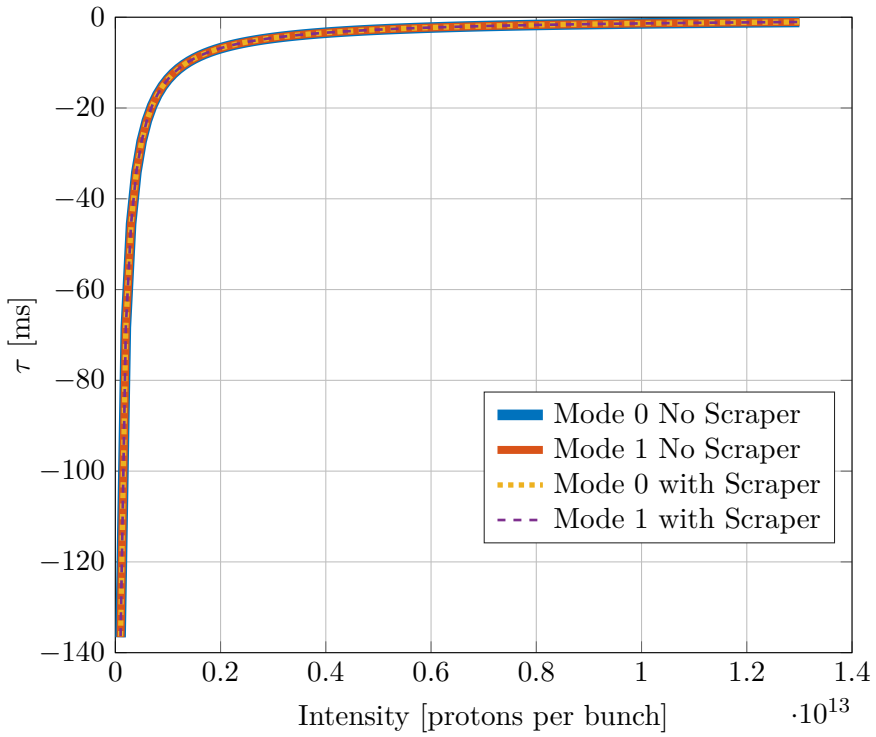

Figure 6.19. Comparison of the PSB rise time of the first two modes of the head-tail instabilities in the horizontal plane with and without the PSBAS, courtesy of Rijoff [114].

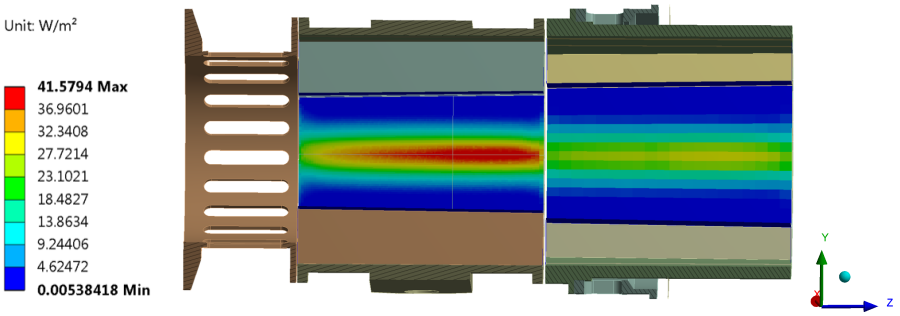

Figure 6.20. RF-heat flux imported in ANSYS® [73]. It can be noted that in the movable mask there are higher local power fluxes than in the fixed mask. This was expected because the movable mask has a smaller aperture with respect to the fixed mask. Thus, being the graphite closer to the beam, it experiences a higher local power flux.

6.3.5 Thermomechanical Studies

The incidence of the proton beam on the scraper material results in an energy deposition on the scraper as a consequence of beam particles-material interaction. The time duration of the beam impact is very short and very localized. Under these conditions, materials suffer non-uniform and sudden temperature increases that can generate high stress levels. These thermo-mechanical phenomena must be considered in the design of the PSBAS.

According to the LIU project, the beam injection and extraction kinetic energies in the PSB complex are set to 160 MeV and 2 GeV, respectively, [17]. Among the possible beam scenarios in the PSB, three representative cases were identified for the design of the PSBAS (see Table 6.1). The first two scenarios were assumed to happen routinely, scraping the halo of the beam at low energies. The last scenario is an accidental direct impact at high energy.

Beam-matter interaction was simulated using the FLUKA Monte Carlo code [125, 126]. The two absorber masks, as well as the surrounding components, susceptible to receive primary or secondary particles after the beam-masks interaction, were modelled. Low-density materials were selected for masks and housings (i.e. graphite and Ti_6Al_4V alloy, respectively). This is a compromise between thermo-mechanical and residual radiation requirements. Stainless steel 316L was chosen for the rest of the components. Figure 6.21 shows the energy deposition due to scraping in scenario 1. FLUKA simulations revealed that the incident primary particles are completely stopped in one graphite mask under nominal conditions (scenarios 1 and 2) with scenario 1 being the most energetic (average power deposition during the pulse was equal to 25.42 W). In the impact scenario, the beam particles traverse the masks losing around 5.5% of its initial energy. The 3D energy density map obtained from FLUKA and the impedance RF-heating heat flux (Fig. 6.20) were imported to the software ANSYS®, to analyze the thermo-mechanical behavior of the device. Preliminary simulations under nominal conditions showed temperatures over 80°C in the graphite. This could produce out-gassing compromising the vacuum in the PSB. In the vacuum tank a dynamic vacuum pressure of 10^{-8} mbar or below has to be maintained [121], so, the outgassing must be minimized reducing the graphite temperature. Due to this, copper braided connectors between tank and housings were simulated. This reduced the graphite temperature below 63 °C (see Fig. 6.22).
Moreover, a press-fitting technique is planned to be used between the masks and the housings. This technique ensures a good thermal contact and confers a beneficial pre-compression state to the graphite masks. Further simulations demonstrated the

Table 6.1. Beam scenarios for the PSBAS design [121]

Scenario		**1**	**2**	**3**
Kinetic energy [MeV]		160	181	2000
Intensity [p/pulse]		$2 \cdot 10^{13}$	$2.8 \cdot 10^{12}$	$2 \cdot 10^{13}$
Pulse time [s]		1.2	1.2	$2.4 \cdot 10^{-7}$
Size [mm]	σ_x	9.08	3.92	4.84
	σ_y	11.15	4.40	4.96

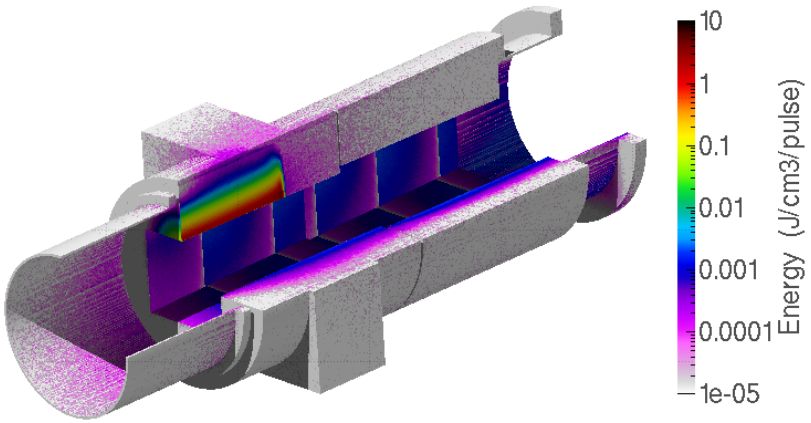

Figure 6.21. 3D view of the energy deposited for vertical scraping in Scenario 1 obtained from FLUKA simulations, courtesy of Britz [114].

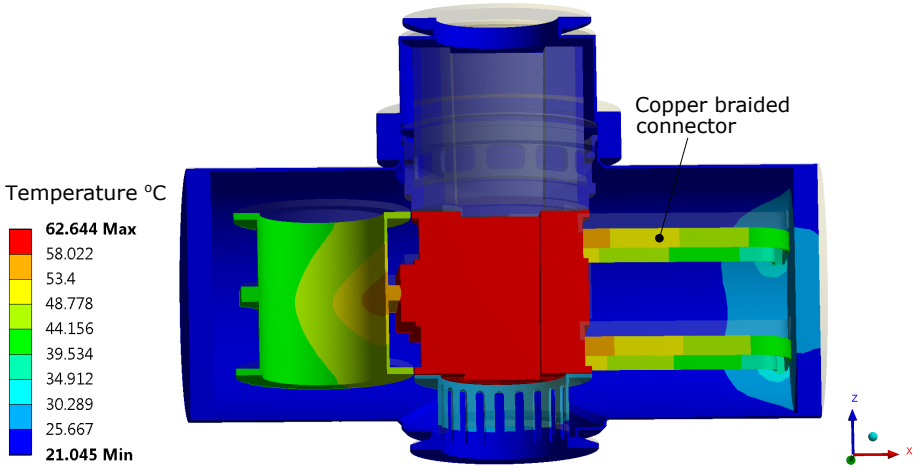

Figure 6.22. Temperature distribution at the steady state for scenario 1 and config. 1 considering the beam-matter interaction and impedance effect.

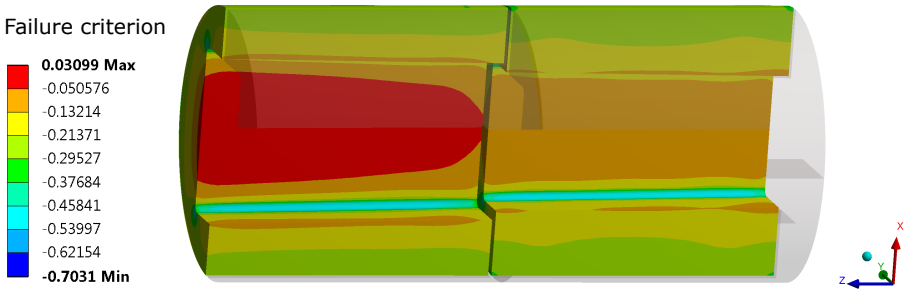

Figure 6.23. Christensen failure criterion [127] for scenario 1 and config. 1 at the steady state (a value superior or equal to positive unity implies material failure).

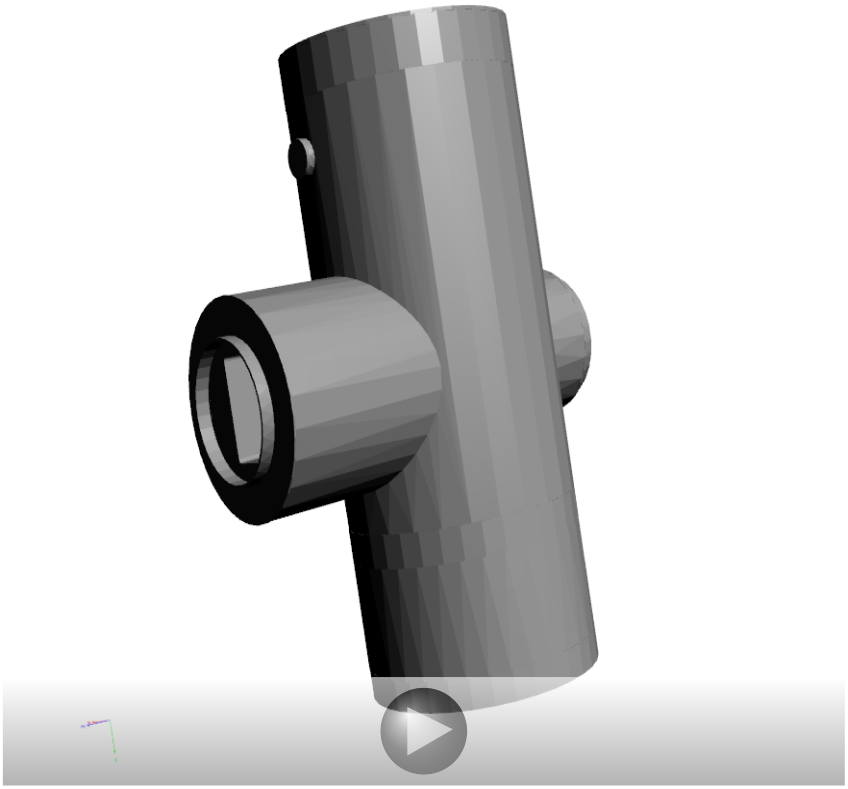

Figure 6.24. A 3D schematic model of the PSBAS. If the figure does not appear interactive, please enable this function and click on it or use a recent version of Adobe Reader.

mechanical safety of the design under nominal conditions (see Fig. 6.23).

6.3.6 Conclusion

In this study, the main features of the PSBAS conceptual design were summarized and its quality in the LIU framework was assessed. The electromagnetic simulations showed that the PSBAS has low impedance and negligible effects on beam dynamics. Furthemore, the impedance design improvement iterations were reported. The thermo-mechanical studies demonstrated that the PSBAS is able to withstand the worst case accidental or operational scenario. In the latter case, the design was optimized to minimize the graphite temperature and so the induced outgassing, as demanded by the vacuum constraints, [121]. Further, the mechanical stresses induced by the temperature distributions are well below the ultimate strength and the yield limit of the materials, making the design robust and reliable.

Further studies will benchmark the obtained results against real measurements taken on a prototype under construction at CERN at the writing time.

6.4 The Proton Synchrotron Internal Dump

6.4.1 Introduction

The intensity of the beams in the Proton Synchrotron (PS) is foreseen to be doubled with respect to the current situation after the long shutdown 2 (LS2), 2019-2020 [17]. In this scenario, the two current internal dumps, which are responsible for stopping the beam if needed or requested, have to be replaced. It has been proved that they cannot cope with the new post LS2 high intensity beams [128]. The design of the new devices, able to absorb and stop the new intense beams, has been recently completed and it is currently in the prototyping phase [76, 129]. The new PS dumps are scheduled to be installed before May 2020. The initial design of the device presented high impedance, this can generate beam instabilities and high RF-heating [46]. The preliminary design of the PSD was found not impedance compliant and an impedance reduction campaign was carried out at CERN [115]. The design of the new PS dump was electromagnetically simulated to individuate the reasons of such a high impedance. It was modified in order to decrease the electromagnetic coupling between the beam and the device. The operations of simulation and design modification were iteratively repeated until the impedance of the PS dump was under the beam instability threshold [130, 131]. This section, after the presentation of the preliminary device geometry and materials, reviews the impedance reduction campaign that led to the last PS dump design. Subsequently, it focuses on the impedance heating induced by the beam on the device and it reports the results of a thermal simulation to asses RF-heating effects.

6.4.2 Impedance Reduction Campaign

The preliminary design of the PSD is shown in Fig. 6.25. The device is made by a graphite and Copper Cromium Zirconium (CuCr1Zr) core, non visible in the reported simplified model, attached to an arm that allows a rotatory motion around the rotatory axes (shown in Fig. 6.25, right). The core is at rest position out of the

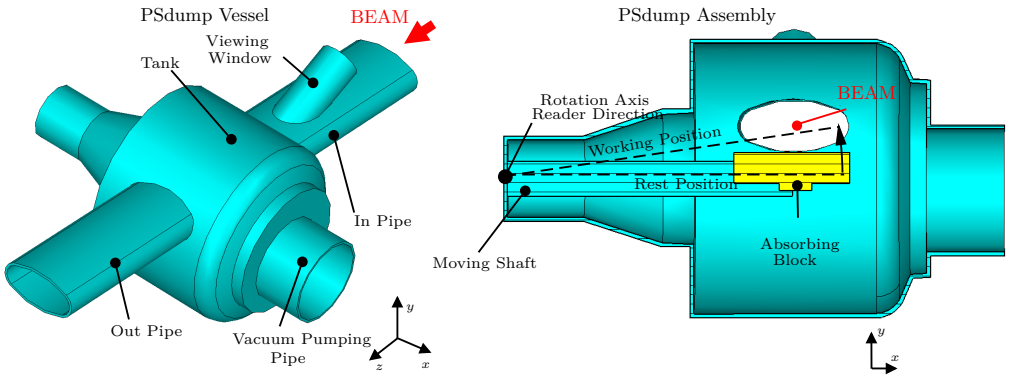

Figure 6.25. Preliminary design of the PS dump with nomenclature. Left: The vacuum vessel, the beam propagation direction is highlighted. Note that the beam is propagating along the z axis. Right: assembly of the core inside the vessel in the rest position. This is a simplified model for the electromagnetic simulations.

beam trajectory and, when triggered, has to enter into the beam trajectory to dump the beam. The core and the arm are installed inside a vacuum vessel.

This preliminary design was not optimal from an impedance perspective. The longitudinal impedance of the preliminary PSD design, as given from the wakefield solver, is reported in Fig. 6.26. In the same figure also the shunt impedance given from Eigenmode is reported[2]. The tank was behaving like a parasitic cavity and the impedance simulations revealed trapped modes with high shunt impedance at frequencies excitable by the LIU PS beams (below 0.7 GHz). The shunt impedances of these modes were found to be above the stability threshold for the PS beams, i.e. they would have generated longitudinal beam instabilities.

Several are the high impedance features found in the preliminary design, however, the major one is the empty volume of the vessel that behaves like a parasitic cavity. According to the low impedance beam device guidelines previously exposed, a shielding would have been the best option to prevent the tank from resonating. However, installing a shielding on the preliminary design would have been a major modification and it would have required a substantial amount of money and time to be performed. Thus, it was decided to explore alternative ways to lower the impedance below the beam instability threshold. The first mitigation measure was to design a new tank with reduced volume to move resonant modes to higher frequencies. A comparison between the geometry of the preliminary and the smaller tank is reported in Fig. 6.27. The longitudinal impedance and the shunt impedance for the PSD with the new tank are reported in Fig. 6.28. Comparing the impedance of the PSD with the new tank (refer to Fig. 6.28) with the impedance of the PSD with the preliminary vessel (refer to Fig. 6.26), shows that the new tank leads to a general reduction of the shunt impedances. In particular, for the modes at low frequency, the shunt impedance of the mode at 131 MHz was decreased by a factor 3 while the one of the mode at 375 MHz was decreased by a factor 2.

However, the impedance behaviour of the PSD design with the new vessel was still considered unacceptable because the low frequency modes had still a shunt impedance that was above the beam instability threshold. The most dangerous mode, the one with the highest shunt impedance, was found to be the one resonating at 372 MHz. Studying its pattern it could be identified as a mode resonating in the gap between the dump core and the vessel, refer to Fig. 6.29. RF-contacts were not considered as a solution to close the gap, since, considering the dump motion, it was not possible to guarantee perfect contacts between the RF-contacts and the vessel after every beam dump. Since the mode resembled a capacitive mode between two plates (the dump core lateral surface and the vessel internal surface), the beam pipe aperture size at the vessel wall was tapered to reduce the surface on which the mode was resonating, refer to Fig. 6.29. Considering the impedance of the PSD with the smaller and tapered vessel, reported in Fig. 6.30, tapering led to a frequency shift of the mode resonant frequency from 372 to 385 MHz, and a decrease of the mode shunt impedance from 44 to 27 kΩ, 38.6 % reduction, producing only negligible changes in the other modes. Two taper structures were investigated, a circular and an elliptical one, since the performance of both the tapering were similar the circular

[2]The shunt impedance computed with Eigenmode needs to be divided by two to be compared with the Wakefield results. This is due to a different convention between the two solvers.

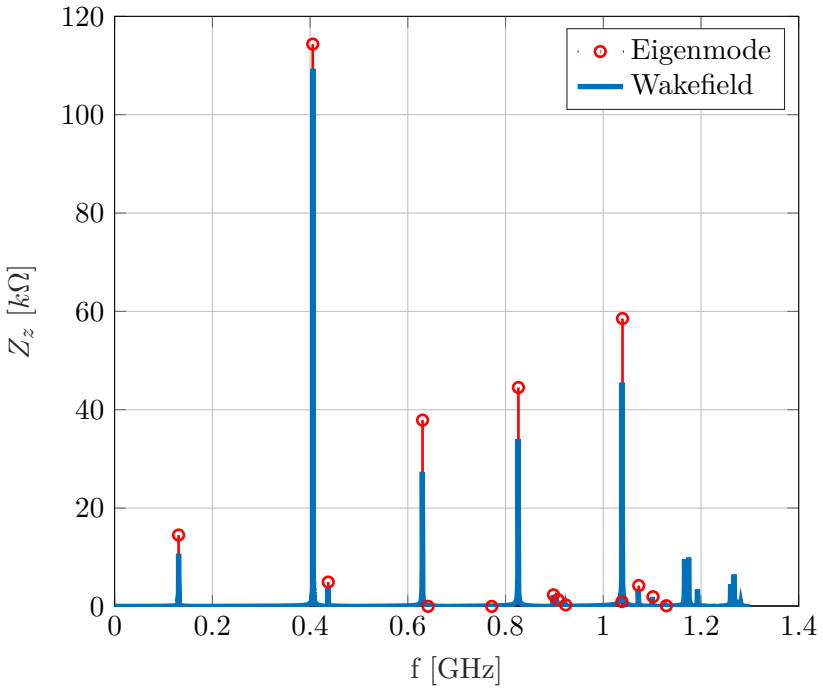

Figure 6.26. Longitudinal impedance obtained from the Wakefield solver (blue solid line) and shunt impedance of the first 15 resonant modes obtained from Eigenmode solver (red stem) for the preliminary PSD design.

taper was chosen because easier to manufacture.

6.4.3 Impedance Improved Final Design

In this section a detailed analysis of the final impedance improved PSD design is reported. The impedance improved geometry is presented in Fig. 6.31. The main part of the dump is the dump core ($180 \times 230 \times 40$ mm^3) [129], made by two blocks of different materials: Copper Cromium Zirconium (CuCr1Zr) and Graphite. They have to stop and absorb the particle beam. Inside the core, a system of cooling pipes in stainless steel is hipped [132, 129] to the CuCr1Zr block. This boosts the efficiency of the heating exchange between the dump core and its cooling pipes, in which water flows at 22 °C. The dump core and the cooling system is mounted on a movable shaft. The extremity of this shaft can rotate moving the core from its rest position to the working position, i.e. the core is put into the beam trajectory so that the beam is completely absorbed (see Fig. 6.31 right). The core and its shaft are assembled into a vacuum vessel, as shown in Fig. 6.31 right.

The impedance of the final device desing was estimated using the commercial software CST studio suite. The impedance obtained from Wakefield and Eigenmode solver was compared as a benchmark and little differences were found. In Fig. 6.32 the model used for electromagnetic simulation of the improved impedance design is shown. In table 6.2 the value of the electrical conductivity for each material has been reported, along with its thermal physical properties that are used in section 6.4.5. In Fig. 6.33, the results of the electromagnetic analysis, that is the real part of the

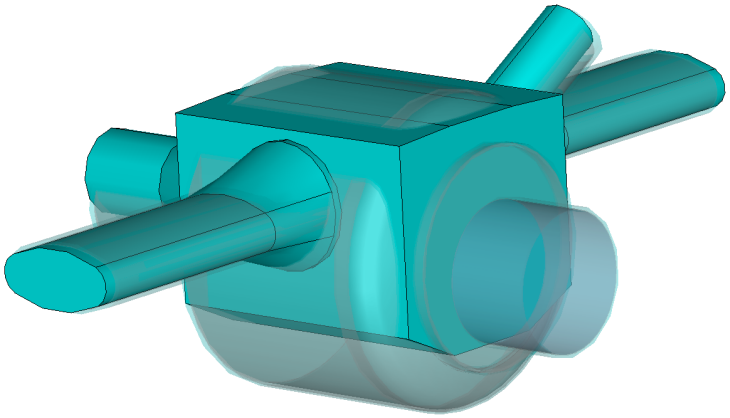

Figure 6.27. Comparison between the old PSD vessel, transparent, and the impedance improved one. The empty volume in the device has been reduced to the minimum needed for the dump core motion. In the picture also the tapers at connection between the tank wall and the pipe are shown. They are needed to decrease the shunt impedance of one of the mode in the PSD.

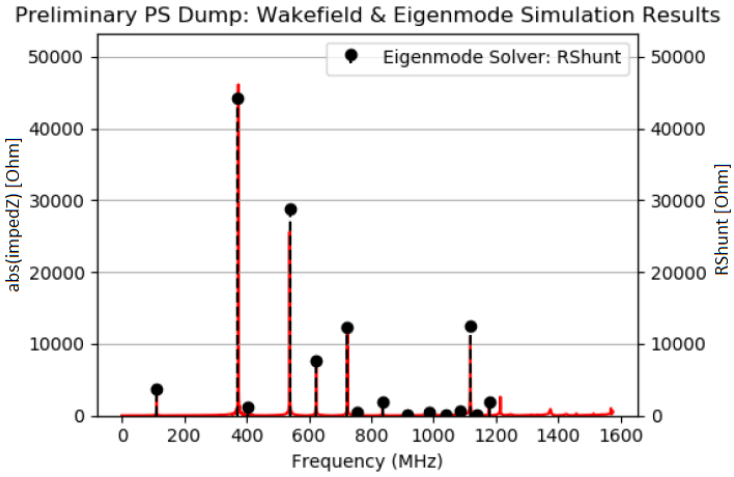

Figure 6.28. Longitudinal impedance obtained from the wakefield solver (red solid line) and shunt impedance obtained from eigenmode solver (black stem), for the PSD design with the new squared vessel. Image taken from Popovic et al. [115].

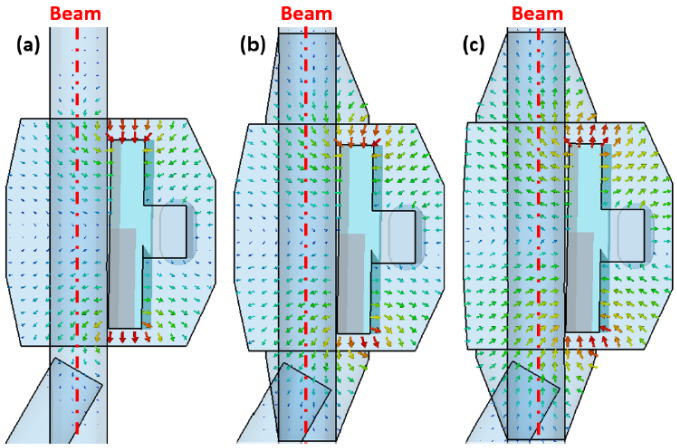

Figure 6.29. Electric field patters for the 385 MHz mode in the impedance improved tank, without taper (a), with elliptical taper (b), with circular paper (c). The beam path is the red line. Image taken from Popovic et al. [115].

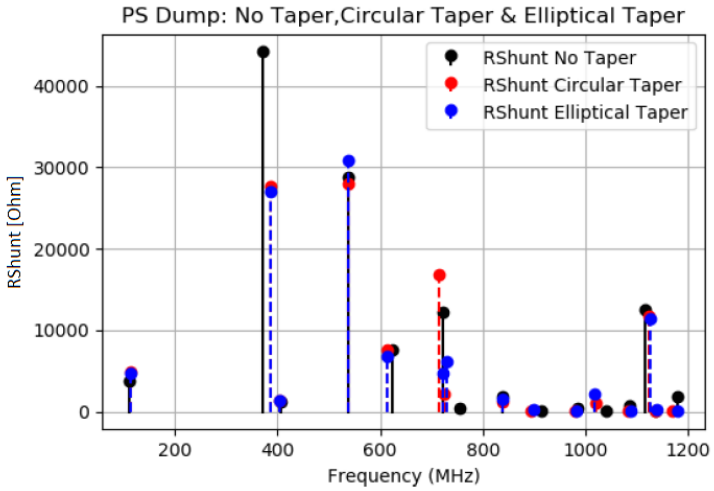

Figure 6.30. Eigenmode simulations results: shunt impedances as a function of frequency for the the PSD with the volume-reduced vessel, for different taper configurations. Image taken from Popovic et al. [115].

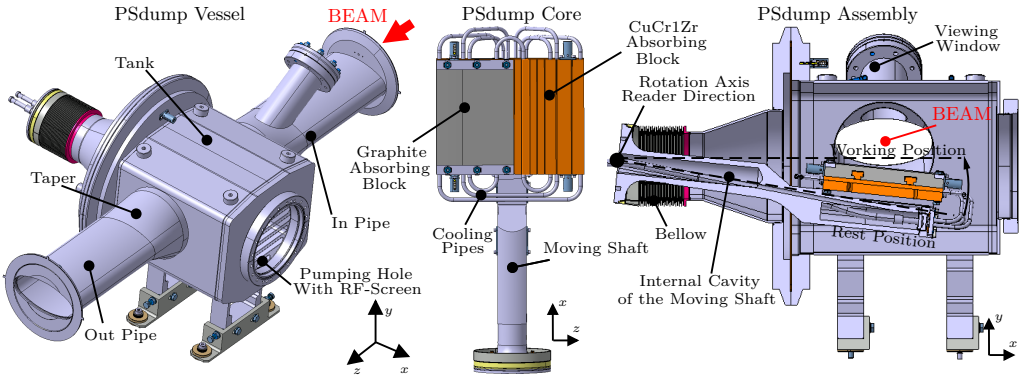

Figure 6.31. Design of the PS dump with nomenclature. Left: The vacuum vessel, where the beam propagation direction is highlighted. Note that the beam is propagating along the z axis. Center: The PS dump core, with the blocks of Copper Cromium Zirconium (CuCr1Zr) and Graphite that have to absorb the PS beams. Right: assembly of the core inside the vessel in the rest position. Note that the internal cavity of the moving shaft opens to the environment. Thus, this cavity contains air at room temperature.

impedance obtained with the Eigenmode solver, which is slightly more pessimistic than the one obtained trough the Wakefield solver, is reported along with the power spectrum and the normalized beam power spectrum (NBPS, defined in the next section).

Table 6.2. Material Physical Properties at 25 °C

Material	$\sigma_c \left[\frac{\mathrm{S}}{\mathrm{m}}\right]$	k $\left[\frac{\mathrm{W}}{\mathrm{Km}}\right]$	C $\left[\frac{\mathrm{kJ}}{\mathrm{Kkg}}\right]$	$\rho \left[\frac{\mathrm{kg}}{\mathrm{m}^3}\right]$
SS 304L	$1.34 \cdot 10^6$	13.3	0.48	7962
Graphite	$1.00 \cdot 10^5$	24.0	0.71	2250
CuCr1Zr	$5.96 \cdot 10^7$	401	0.39	8930

The impedance is characterized by strong resonant modes. This was expected because the geometry of the device presents empty volumes and the PSdump core and the moving shaft acts as an antenna. Unfortunately, neither the PSdump core can be modified nor the volumes removed since these features are needed for the functionality of the device. Despite the modes, the PSD improved design has an impedance that is below the instability threshold, both in the transverse [131] and in the longitudinal planes [130][3].

6.4.4 RF-heating

The beam structure, i.e. bunch length, bunch number and interbunch distance is constantly changing in the PS. To compute the RF-heating a worst case scenario approach was adopted, i.e. the beam with the larger frequency spectrum which run

[3]Regarding the longitudinal beam instabilities only the coupled bunch instability was considered. At the writing moment a model for the microwave instabilities in the PS is currently being developed and the impact of the PSD on this kind of instabilities is not known.

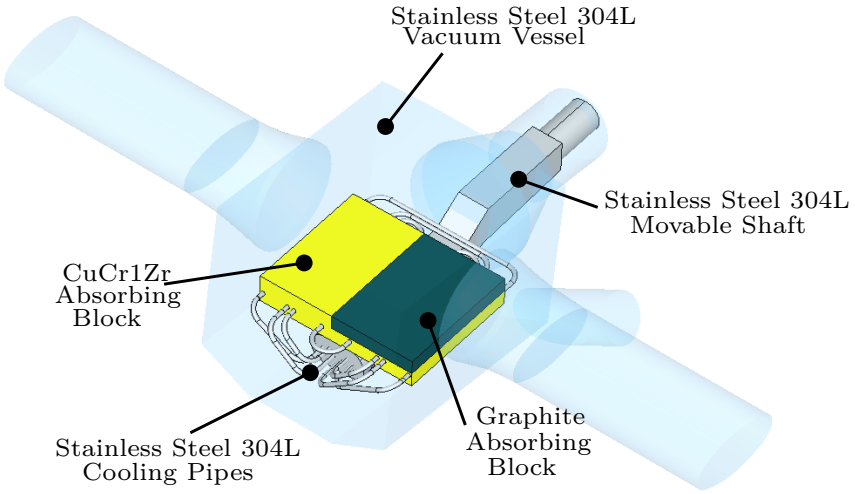

Figure 6.32. CST model of the new PS dump. The vacuum vessel is represented as transparent.

into the machine for more than 0.5 s was considered among the PS beams. The parameters reported in table 6.3 represent this scenario. The total beam intensity

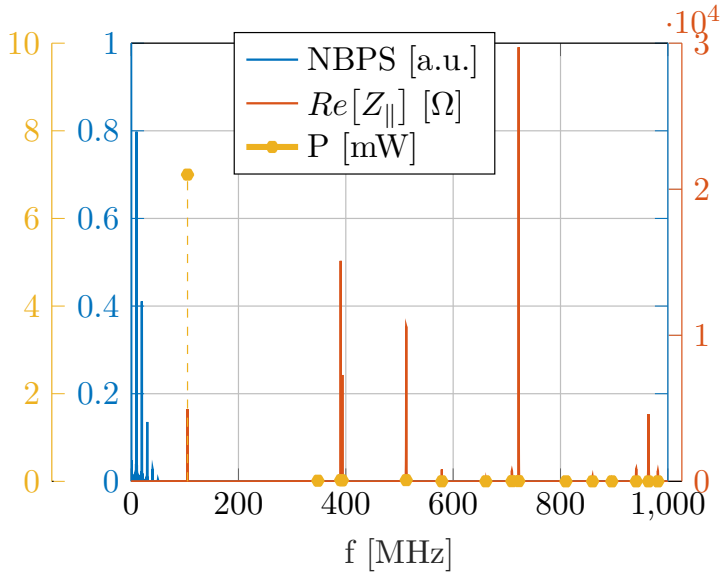

Figure 6.33. Normalized beam power spectrum [adimensional units] (NBPS), dissipated power spectrum and real part of the impedance. Colors refer to different scales. Comparing the impedance value reported in this figure with the one reported in Fig. 6.30, one can notice a discrepancy between the shunt impedance of the resonant modes. This is because the dump model simulated to produce the results in Fig. 6.30, to run faster, was not considering the cooling pipes, while the results reported here do. The effects of the cooling pipes is positive for impedance, it decreases the shunt impedance of the modes at lower frequencies.

was set to $N_{beam} = 2.4 \cdot 10^{13}$ protons. In Fig. 6.33 the Normalized Beam Power Spectrum ($|\Lambda(p\omega_0)|^2$, NBPS) is reported.

Table 6.3. Bunch parameters selected for the impedance heating calculation, worst case scenario

Shape	Length (4σ)	Interbunch Distance	γ	N Bunches
gaussian	30 [ns]	100 [ns]	27.74	18

An analysis of the beam dissipated power has also been performed in order to obtain the dissipated power spectrum. A sensitivity analysis technique has been used, i.e. the resonant modes' frequencies have been randomly moved with respect to the initial value, obtained by simulations within a range of ±10 MHz to study the coupling between beam spectrum and longitudinal device impedance. The power dissipated by every mode for an average case and for a worst case scenario was computed. In Fig. 6.33 the power dissipated in the worst case scenario is reported as a function of frequency. At the frequency values of the first resonant mode, 105 MHz, the NBPS is not totally null and there is a small coupling with the real part of the impedance function, giving a dissipated power of 7mW. The power dissipated on the other modes can be considered negligible.

6.4.5 Thermal Simulations

The power dissipated on the device, around 7 mW, seems rather small. However, it has to be taken into account that this power is flowing into the PS dump continuously while the beam is circulating in the accelerator. In specific operational scenarios beams run for several hours in the PS machine uninterruptedly. Thus, this rather small power is applied for a long period of time. Further, it is crucial to know the areas in which this power fluxes into the device. Indeed, if the flux is concentrated in small regions where no cooling system is present, also low values of deposited power could increase appreciably the temperature. This could potentially lead to material outgassing, ablation or even cracking. This latter case can happen if the temperature gradient between cold and hot zones is so large to generate intense mechanical stresses. Since a dump is a critical component for an accelerator and because of the reasons listed above, the analysis on the PSD was carried out with thermal simulations.

The method exposed in chapter 4 was used to obtain the map of the dissipated power on the PS dump.

Every mode below 1 GHz was considered and for each one of them a 3D dissipated power map was obtained. All these contributions were summed up to compute the final power flux. The 95% of the total power deposited in the PS dump is deposited on the PS dump core and on the PS dump shaft, specifically in the shaft and in the cooling tubes. In Fig. 6.34 the power flux experienced by the core and the shaft is shown.

Always considering a worst case scenario approach, a thermal steady state simulation was run. It is implicit in the steady state simulation the assumption

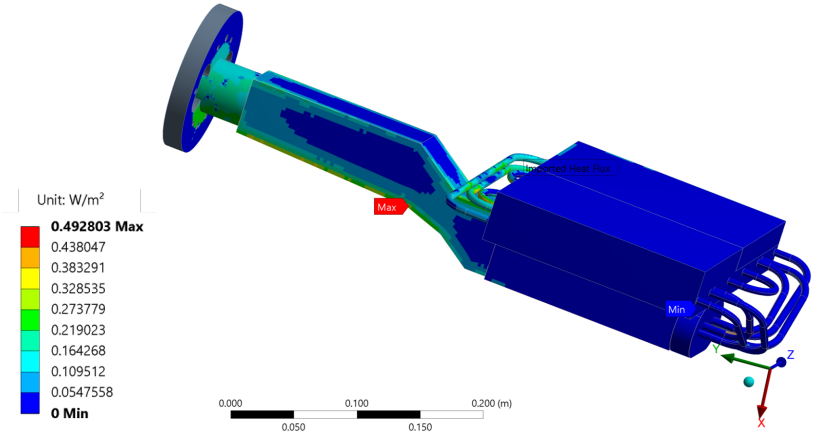

Figure 6.34. Impedance induced power flux on the core and the shaft.

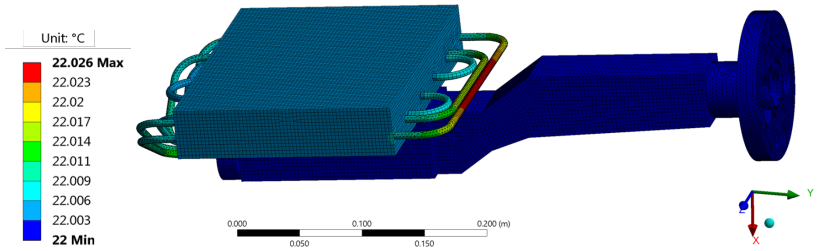

Figure 6.35. Core and shaft temperature at steady state.

that the 7 mW are deposited continuously till the equilibrium is reached. This is a pessimistic scenario because between the extraction of a PS beam and the injection of a new one there is a time interval in which no beam is circulating. Thus, no impedance induced power is deposited in the device.

The only simulated cooling mechanism was the convection on the internal surfaces of the shaft, 5 W/Km^2. The cooling system was ignored. This represents the case of a pump failure. The temperature results are shown in Fig. 6.35. The maximum temperature increase is clearly negligible being less than 1°C. Thus, the PSD is not expected to have any problem because of RF-heating.

6.4.6 Conclusions

This section reported on the analysis done on the impedance heating effects for the new design of the proton synchrotron dump. First, the impedance optimization campaign of the preliminary design was discussed. Then the impedance simulations of the final design have been revised and the computed 3D induced RF-heating map was presented. Finally, the thermal effects of the impedance heating is estimated in a worst case scenario. The device is found with an impedance below the beam instability threshold and the RF-heating is not expected to affect the device functionality.

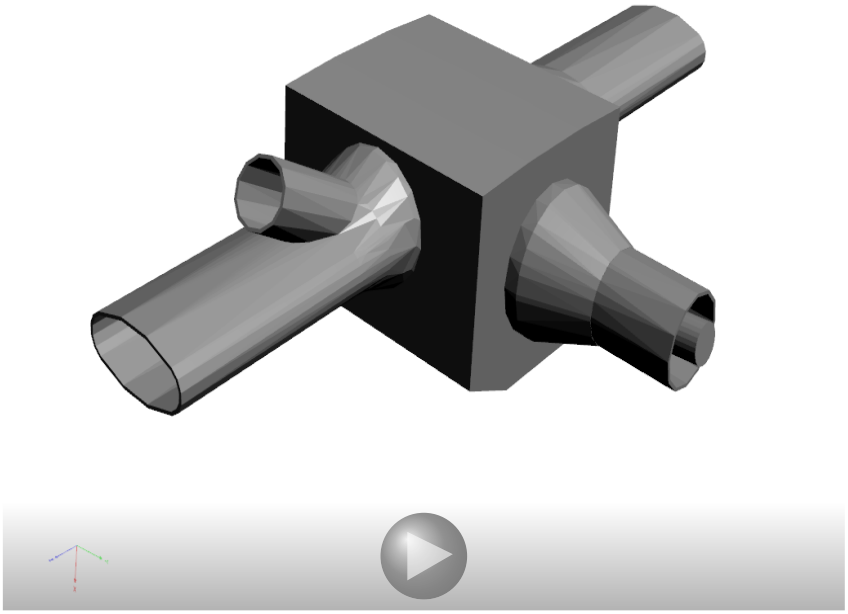

Figure 6.36. A 3D, schematic model of the final PSDUMP. If the Figure does not appear interactive, please enable this function and click on it or use a recent version of Adobe Reader.

6.5 The Proton Synchrotron Ralentisseur

6.5.1 Introduction

The ralentisseur is a BID currently installed in the PS. Its main function is to protect the Secondary Emission Monitors grids (SEM-grids) [133], beam diagnostic devices made by a ceramic frame crossed by wires, that measure beam profile and emittance. A picture of a SEM-grid is reported in Fig. 6.37a. The SEM-grids are movable devices inserted in the beam trajectory during the beam commissioning phase. They work on a single passage mode, i.e. the beam can pass only once through the grids otherwise they could be damaged [134]. The ralentisseur is located downstream with respect to the grids and it dilutes the beam after the first passage into the grids to prevent that the high intensity beam impacts again the same grid during the second turn, [134]. In Fig. 6.37b a schematic of the ralentisseur location is reported.

The currently installed ralentisseur is made by a pure tungsten plate that moves in and out from the beam trajectory with the SEM-grids inside a stainless steel vacuum chamber [135]. A model of the device is reported in Fig. 6.38. Its active part, the tungsten plate, is not mechanically designed for the new LIU high intensity beams [136] and it has to be substituted with a geometrically identical plate made by a tungsten alloy (inermet [137]). The new ralentisseur is planned to be installed before the end of LS2.

Three different designs were proposed, the final one was selected having the lowest impedance. This section presents the impedance analysis performed on these designs. For the analysis, both the wakefield and the eigenmode solvers of the CST studio suite software were used.

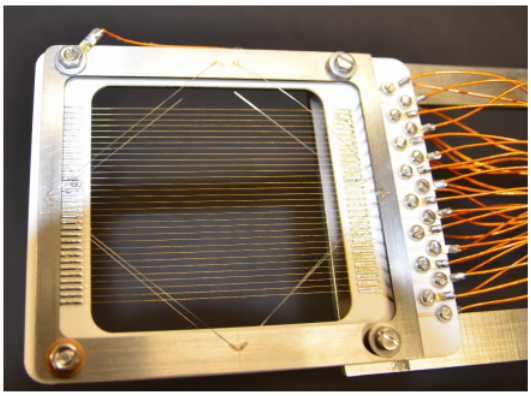

(a)

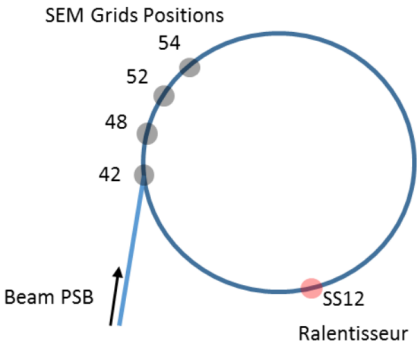

(b)

Figure 6.37. (a) Example of a SEM grid, image courtesy of Fernandez [133]. (b) SEM-grids and ralentisseur position in the PS accelerator, image courtesy of Romagnoli et al. [134].

6.5.2 Design One: The Current ralentisseur design with new Inermet Plate

The easiest solution for the design was a substitution of the old tungsten plate with a new one in the current ralentisseur tank. This design is shown in Fig. 6.38. As

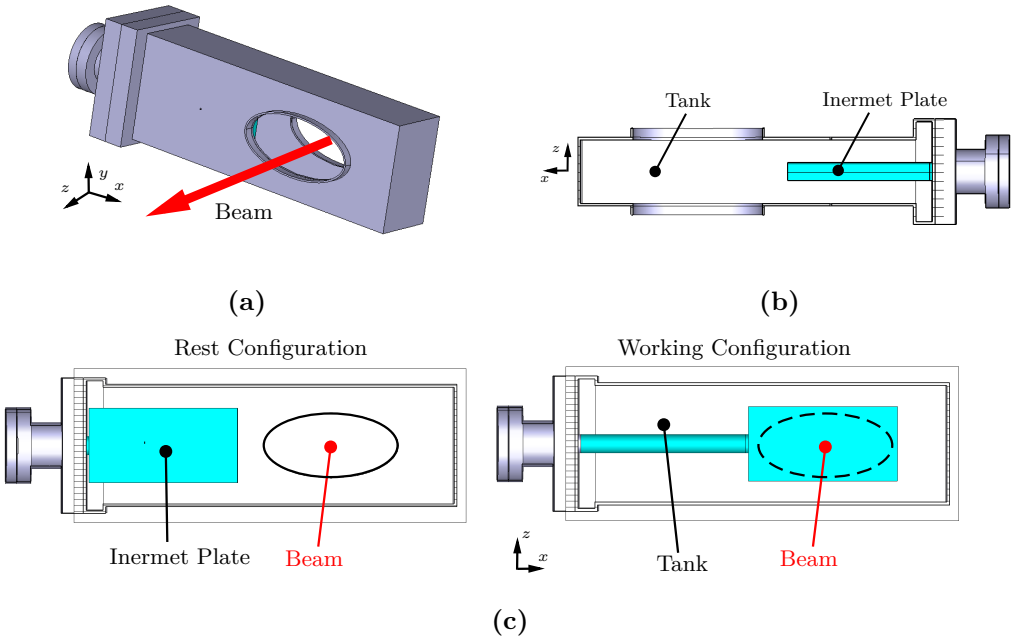

Figure 6.38. (a) Ralentisseur design one, isometric view. (b) Ralentisseur design one cut, view form top. (c) Ralentisseur design one cut, view form side, the two configurations of the ralentisseur are highlighted.

already said it is made by a movable inermet plate in a vacuum chamber.

The longitudinal impedance of this design was investigated with the wakefield and eigenmode solvers of the CST studio suite software. The eigenmode solver was used also to estimate the transverse impedance. The longitudinal impedance, up to 1.5 GHz, of the device obtained from the wakefield solver is reported in Fig. 6.39. In the same figure also the shunt impedance value of the modes computed by eigenmode are reported, and the agreement between the results of the two solvers is excellent. The longitudinal impedance curve presents two peaks at 1.19, 1.44 GHz. They are two resonant modes trapped in the ralentisseur cavity. The transverse impedance, computed with Eigenmode, is reported in Fig. 6.40. As for the longitudinal impedance, the high shunt impedance transverse modes are located at frequencies higher than 1 GHz.

Both the longitudinal and the transverse resonant modes have frequencies well above the frequencies that the LIU PS beams can excite (approximately up to 0.7 GHz), thus, they are not a concern both from a beam dynamics and an RF-heating perspective.

These modes are produced by two factors: the empty volume of the vacuum chamber of the ralentisseur behaves like a cavity, and the tungsten plate has no connections with its vacuum chamber except in the extremity were the plate is held. However, the volume of the vacuum chamber is the minimum to allow the motion of the plate with a margin of safety, and since the modes are at high frequency with respect to the PS beam excitable frequencies, the installation of extra connections between the tungsten and the vacuum chamber is not required.

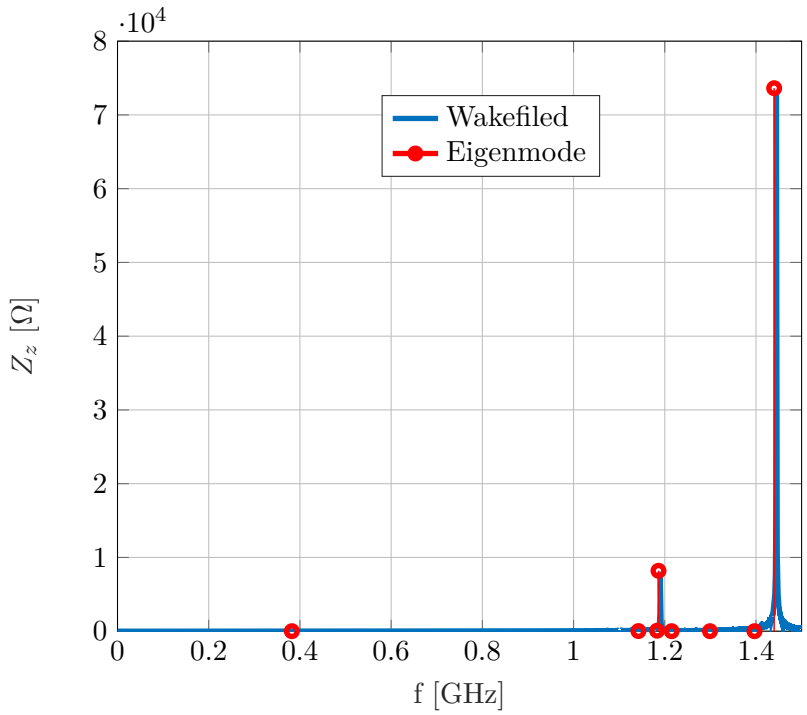

Figure 6.39. Ralentisseur design one, longitudinal impedance absolute value, CST Wakefield and Eigenmode solver.

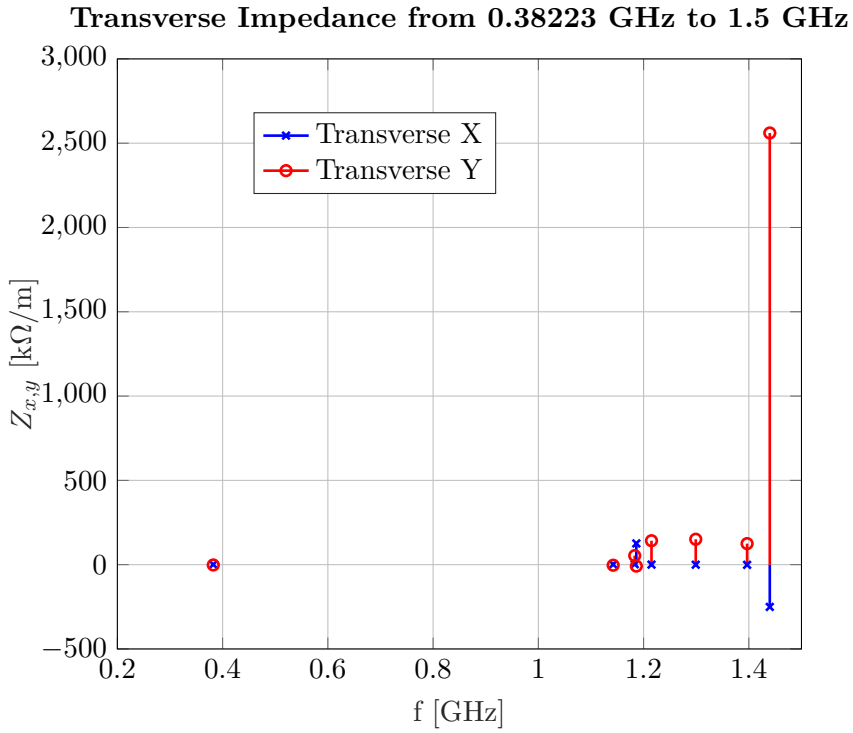

Figure 6.40. Ralentisseur design one, transverse impedance, CST Eigenmode solver.

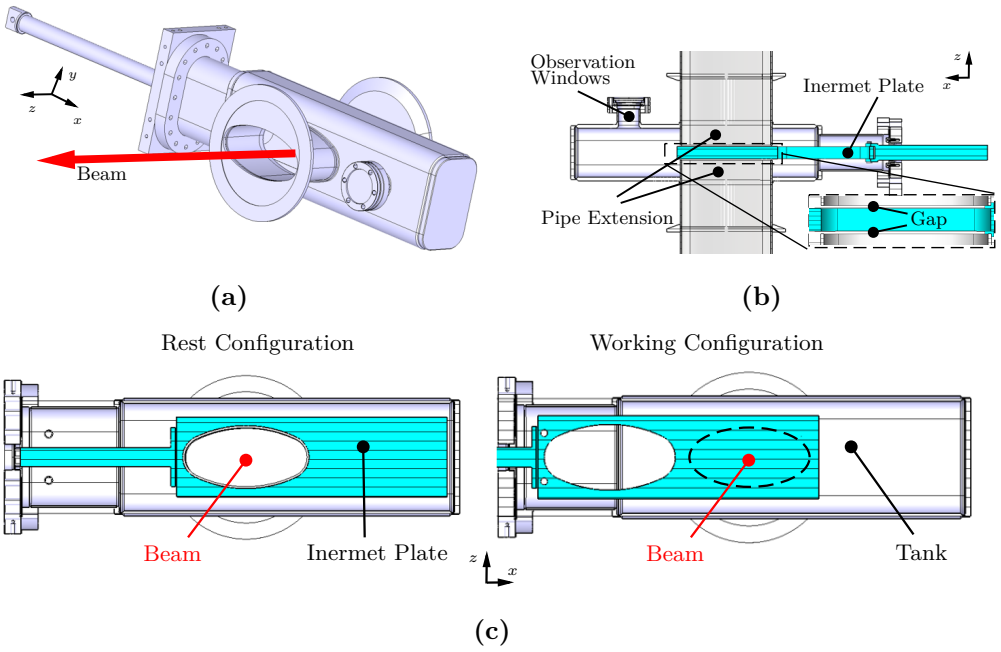

Figure 6.41. (a) Ralentisseur design two, isometric view. (b) Ralentisseur design two cut, view form top. The pipe extension to shield the tank empty volume is highlighted. (c) Ralentisseur design two cut, view form side. The two configurations of the ralentisseur are highlighted.

6.5.3 Design Two: Preliminary new design of the PS ralentisseur

The design two is shown in Fig. 6.41. With respect to design one (shown in Fig. 6.38) the tungsten plate is longer and there is a hole in it to allow the beam to pass when the system is in parking position.

This design of the ralentisseur was elaborated to improve the robustness of the device. In the ralentisseur tank there is vacuum, the pressure difference between the the environment and the internal ralentisseur tank would naturally push the plate inside. The external motor, is preventing this motion. However, in case of problems with the external motor the plate would be pushed completely inside. With the design two, this aspect is not critical since, also with a problem in the motor, the ralentisseur plate would be out of the beam trajectory and the PS could continue to operate. On the contrary, in case of a motor problem in the design one, the tungsten plate would be in the beam orbit. Thus, this design is more robust with respect to the current one because its default position is the rest configuration, i.e. the tungsten plate out of the beam trajectory.

However, with reference to the low impedance guidelines, the bigger volume of the device vacuum chamber was expected to trap resonant modes with lower frequencies with respect to the ones of design one, that has smaller vacuum chamber. To prevent the expected low frequency modes from resonating, the inner and the outer pipes were extended up to a distance of 1 mm from the tungsten plate to act as a shielding. However, this 1 mm gaps were not electrically closed with movable RF-contacts. Indeed, this would have required a very precise control of the motion

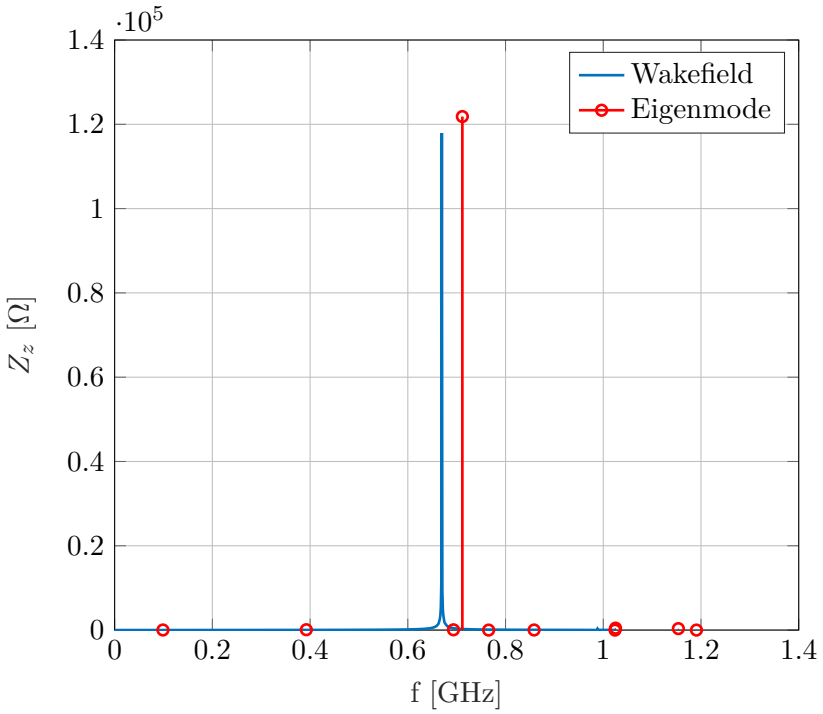

Figure 6.42. Ralentisseur design two, longitudinal impedance, CST Wakefield and Eigenmode solver. The discrepancy in the mode frequency between the two solvers is due to the fact that in the Wakefield geometric model the blends of the vessel were simplified while this was not done in Eigenmode model. Thus, the Wakefield simulations see the tank with a slightly larger volume and present the resonant mode at a slightly lower frequency with respect to Eigenmode.

of the absorbing plate, increasing dramatically the cost of the device.

The longitudinal impedance of the design two of the PS ralentisseur, up to 1.5 GHz, obtained from the Wakefield solver is reported in Fig. 6.42. In the same figure also the shunt impedance value of the modes computed by Eigenmode are reported, and the agreement between the results of the two solvers is good. The discrepancy in the mode frequency between the two solvers is due to the fact that in the Wakefield simulations the blends of the vessel were simplified while this was not done in the Eigenmode simulation. Thus, the Wakefield simulations saw the tank with a slightly larger volume and present the resonant mode at a slightly lower frequency with respect to eigenmode. The longitudinal impedance curve presents one resonant mode at 0.71 GHz. The transverse impedance, computed with Eigenmode is reported in Fig. 6.43. The design as it is, it is not impedance compliant, bacause the mode at 0.71 GHz can be excited by the LIU PS beams and it could be harmful both from a beam dynamics and from an RF-heating perspective.

6.5.4 Design Three: The Optimized new design of the PS ralentisseur

The design presented in this subsection is an impedance optimization of design two. The geometry of the device is reported in Fig. 6.42. With respect to design two, the

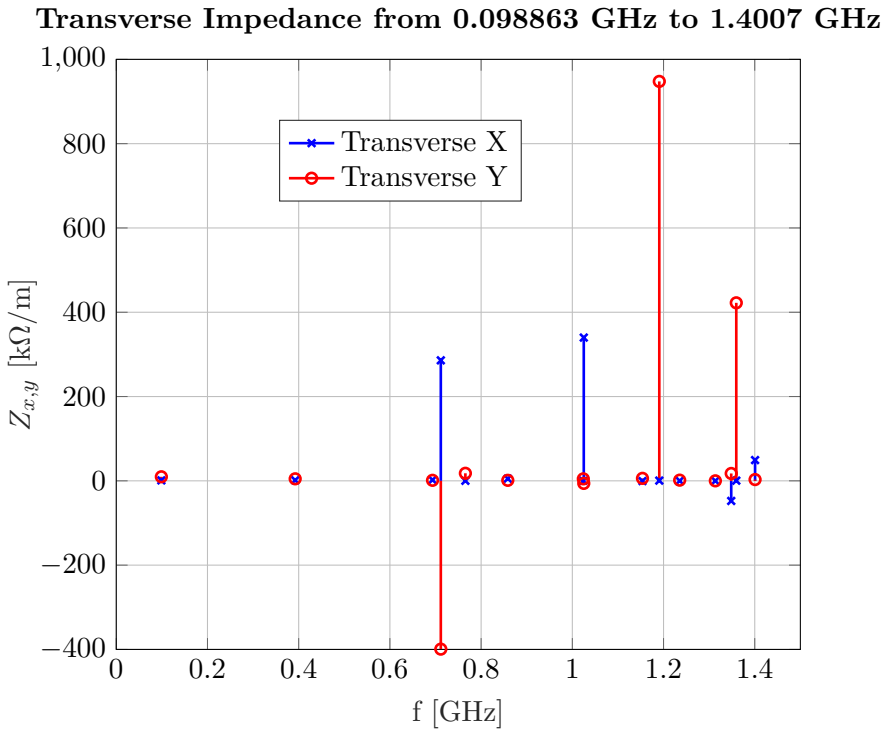

Figure 6.43. Ralentisseur design two, transverse impedance, CST Eigenmode solver.

length on the inermet plate was halved, and this allowed to decrease also the vacuum vessel dimensions, with the results of shifting resonant modes to higher frequencies. On the tungsten plate extremity far from the motor, a system of RF-contacts was inserted. They guarantee the electrical contact between the plate and the vacuum vessel when the ralentisseur is in parking position.

The longitudinal impedance of this design computed with the Wakefield solver is reported in Fig. 6.45 where also the shunt impedances of the modes computed with the Eigenmode solver are reported. The agreement between the two solvers is excellent. The transverse impedance computed with eigenmode is also reported in Fig. 6.46. In both the longitudinal and transverse impedance, there is only one resonant mode at 1.53 GHz with substantial impedance. This frequency is far higher than the frequency that the LIU PS beams are able to excite, and thus, the mode is not expected to represent a problem form a beam dynamics and RF-heating point of view.

6.5.5 Impedance analysis on the PS Ralentisseur, Conclusions

In this subsection the proposed new ralentisseur designs have been analysed from an impedance perspective. Design two was found not impedance compliant. By applying the impedance guidelines discussed in section 6.2 it was possible to modify design two into an impedance optimized design with good eletromagnetic performance: design three. The optimized design (design three) turned out to be very similar to the current device design (design one), and the impedance performance of the

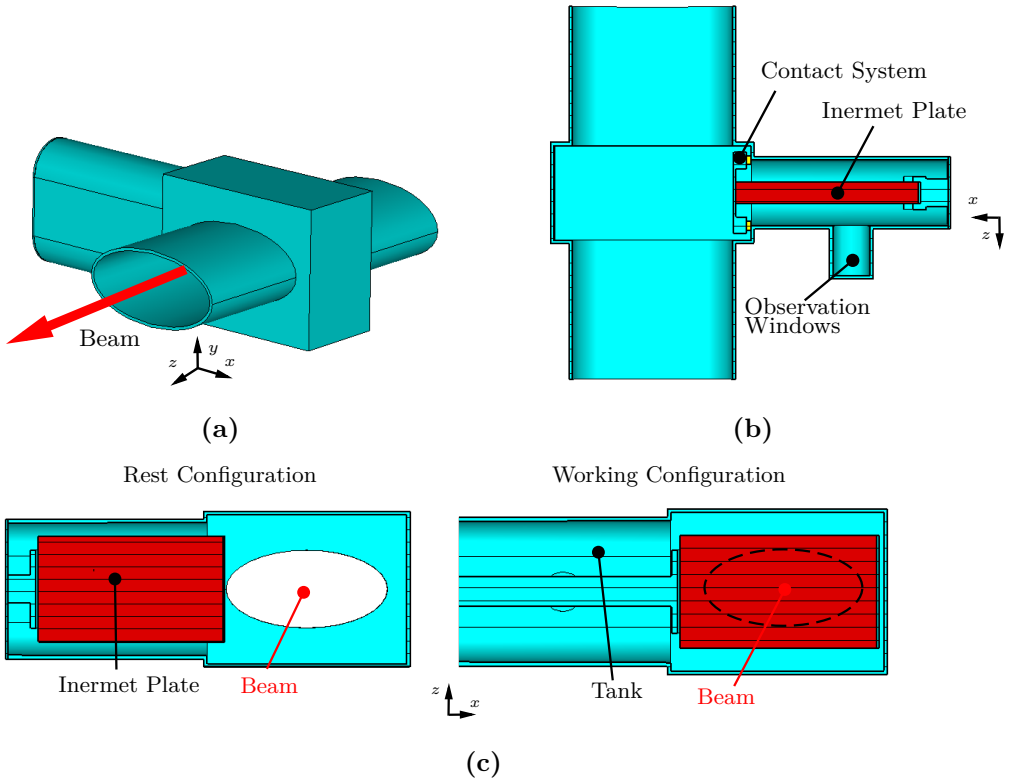

Figure 6.44. (a) Ralentisseur design three, isometric view. (b) Ralentisseur design three cut, view form top. The contact system to reduce the empty volume of the vacuum tank is highlighted. (c) Ralentisseur design three cut, view form side. The two configurations of the ralentisseur are highlighted.

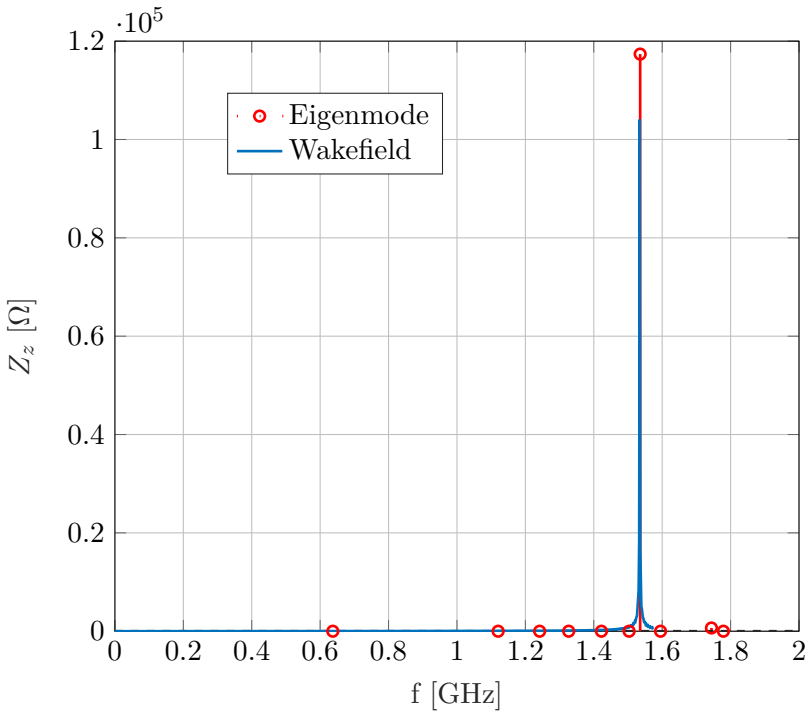

Figure 6.45. Ralentisseur design three, longitudinal impedance, CST Wakefield and Eigenmode solver.

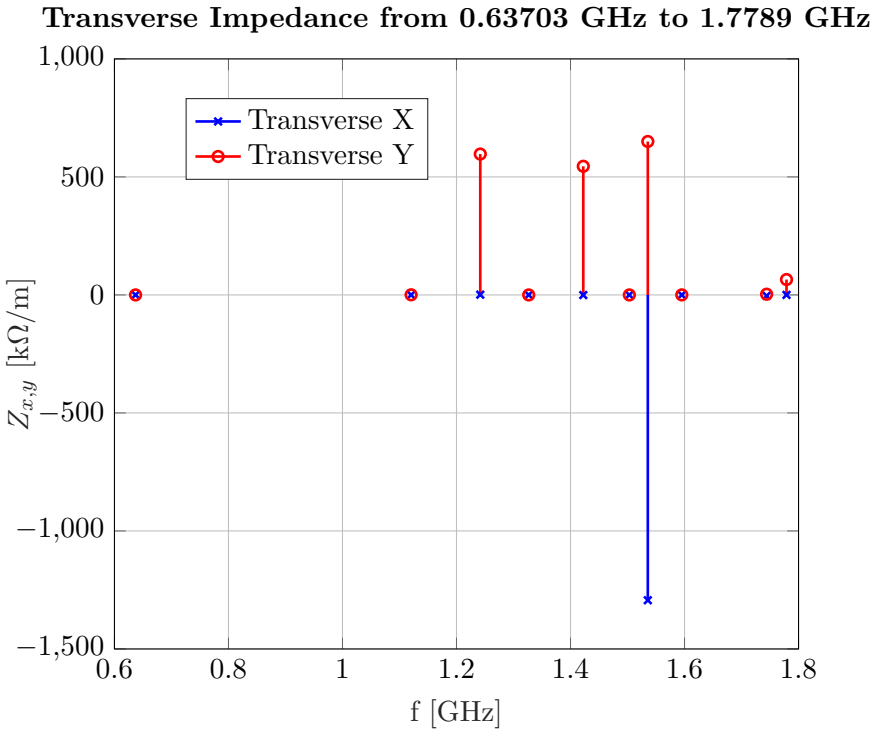

Figure 6.46. Ralentisseur design three, transverse impedance, CST Eigenmode solver.

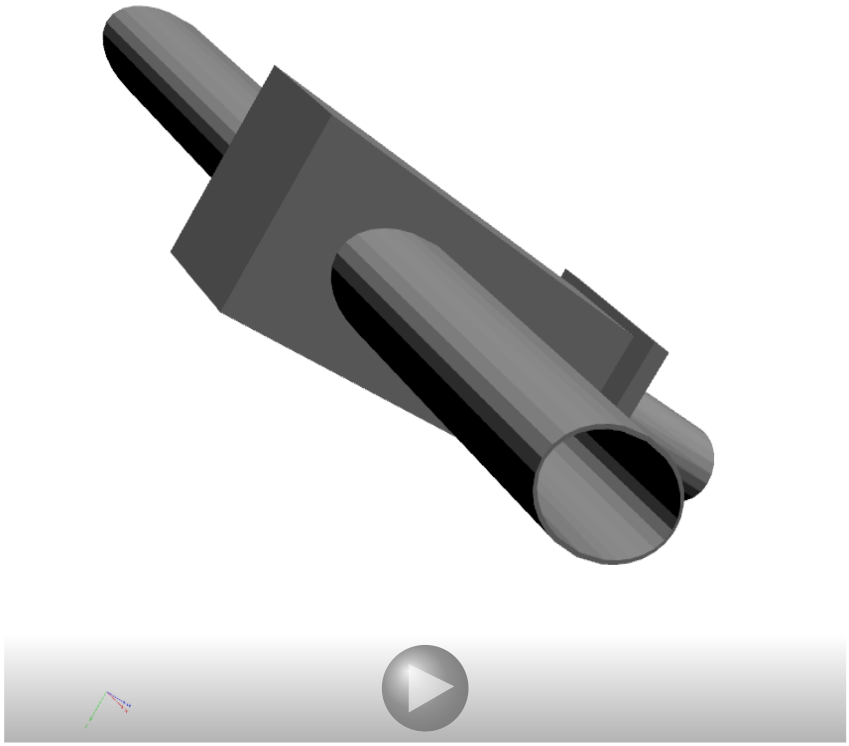

Figure 6.47. A 3D, schematic model of the final Rallentiseur. If the figure does not appear interactive, please enable this function and click on it or use a recent version of Adobe Reader.

actual design is only slightly worse than the optimized design (both designs have a resonating mode around 1.45 GHz with shunt impedance about 80 kΩ, but the current ralentisseur design presents also a resonant mode at 1.19 GHz with a shunt impedance of 10 kΩ). Considering the cost of realisation and installation of the new optimized design, it was concluded that it is not worth to make it. Also the design two of the ralentisseur was rejected, considering its problematic impedance and the fact that the current ralentisseur motor has never experienced a failure in the past years. The design one was selected. The current vessel can be used, the material of the absorbing plate will be changed from pure tungsten to inermet. This will allow the PS ralentisseur to fulfil its requirement of diluting the LIU PS beams to protect the SEM-grid.

6.6 Conclusions

Prior work has documented the importance of reducing the impedance of accelerator devices and so of the whole machine [38], [49]. In this section, the most common high impedance geometric features usually present in a preliminary device design were analyzed and simple and cost-effective way of modifying geometries to obtain

low impedance designs were reviewed. Subsequently, these methods were applied to improve the impedance performance of complex devices: the Proton Synchrotron Booster Absorber Scraper, the Proton Synchrotron internal dump and the Proton Synchrotron Ralentisseur. For the Proton Synchrotron Booster Absorber Scraper, a striking impedance reduction of almost three orders of magnitude between the preliminary and the final design was obtained. The impedance of the Proton Synchrotron internal dump was driven below the beam instability threshold. Finally, the process of selection of a low impedance design for the ralentisseur was shown.

Chapter 7

Impedance and Thermo-Mechanical Analysis of HL-LHC Devices

7.1 Introduction

This chapter contains original material partially published as light peer review proceeding in two conferences [138],[139].

The CERN accelerator complex has been undergoing upgrades to improve its performance. In the framework of the HL-LHC (High Luminosity LHC) [16] and LIU (LHC Injection Upgrade)[17] projects, an increase of the beam brightness and intensity is foreseen [16]. Several systems have to be redesigned and rebuilt to survive the new demanding situation.

With the foreseen higher beam intensity, the minimization of the device impedance is one of the driver for the design of new equipment. Indeed, the impedance reduction avoids beam instabilities that are more easily triggered with higher particle beam intensity.

Furthemore, a device with high impedance can be subjected to excessive impedance induced heating. This is particularly true for the beam intercepting devices (BIDs), such as dumps, collimators and absorbers/scrapers. They usually operate in close proximity to the particle beam, they are made by materials with limited electrical conductivity and have complex geometries because composed of movable parts. If the BIDs impedance is not minimized, they may experience strong electromagnetic interaction with the beam circulating in the accelerator. This interaction causes an energy deposition in the equipment (RF-heating), proportional to the square of the bunch intensity and to the device impedance, as discussed in section 3.3.

BIDs have to deal also with another beam intensity related phenomenon: the Nuclei-Matter Interactions (NMI). BIDs are usually responsible for absorbing a large part of the beam energy (beam dumping) or the removal of the unstable peripheral beam particles (beam scraping). Thus, they are directly exposed to beam impacts and particle irradiation. It is well known that the incidence of the proton beam on the device material results in an energy deposition in the material itself, and this effect also increases with the beam intensity [140, 141].

Thus, during the design of a BID for a high intensity machine, as for instance HL-LHC, all these factors should be considered, and the effects of the device impedance on the beam and of the impedance induced heating and nuclei matter interaction on the device have to be assessed from an early design phase.

7.1.1 Scope and Structure of the Chapter

This chapter presents the results of the electromagnetic simulations performed to characterize the impedance of two HL-LHC devices: the LHC injection dump (TDIS) and the Low Dispersion Collimator (TCLD). Also, the results of the impedance measurements performed on the TCLD are reported and compared with the simulation results. Furthemore, the chapter discusses the analysis made to characterize the thermo-mechanical response of the TDIS to NMI and impedance induced heating in a RF-contacts failure scenario.

The TCLD is discussed in section 7.2. First the scope and the geometry of the device are reported. Then, the results of the electromagnetic simulations are discussed. Subsequently, the most significant results of the measurement campaign performed on the device are reported and compared with the simulation results.

The TDIS is discussed in section 7.3. The scope of the device, its functionality, its location in the CERN accelerator complex and its geometry are presented. Subsequently, the results of the electromagnetic and thermo-mechanical simulations are shown. First the thermomechanical response of the device to a beam impact on one of the jaws is discussed. Subsequently, the impedance of the device is analyzed for two different TDIS configurations, with and without the RF-contacts. The thermal effects of the impedance induced heating on the TDIS is also investigated for the configuration without RF-contacts.

7.2 The Target Collimator Long Dispersion Suppressor (TCLD)

7.2.1 Introduction

A particle accelerator is always built considering a reference trajectory, also known as golden orbit, and the accelerator is shaped around this orbit. The golden orbit has to be swept by a charged particle with specific timing, i.e. the particle has to be at a specific point of the orbit at a specific time. For instance the particle, to have the maximum energy gain, has to traverse the RF-cavity at the time in which the electric field is at its maximum and it is directed in the same direction of the particle speed. A particle that is moving exactly on the golden orbit with the right timing is called synchronous, ideal or reference particle. Particle accelerators work with a large number of particles, that can have different positions and velocities with respect to the ideal particle. Substantial effort is put to keep these differences as small as possible. However, some beam particles (a minority in normal operations) can have very different speeds or very different positions with respect to the ideal particle[1]. Thus, in a real machine one can distinguish two regions in the beam: a core region with particles that have velocities and positions close to the ideal particle, and a beam halo (or tail) region, populated by off-energy, off-position particles.

Those halo particles, in particular in proton machines, are very difficult to control, since the accelerator is thought to work with core particles and, without a safety system, they finish to irradiate randomly some machine components. This situation should be avoided for several reasons: the irradiated component may be activated, and if this is a component that needs regular human maintenance, the radiation could cause critical issues . Further, if the accelerator has superconducting magnets, the energy deposition due to irradiation can cause them to quench.

This is why the majority of the high energy particle accelerators have a cleaning and collimation system. The core part of this system are collimators, equipment that aims at absorbing the beam halo in controlled areas so that the irradiation and energy deposition is safely concentrated in those areas. The conceptual scheme of a collimator is easy: it is made by blocks of material (collimator jaws) that are inserted into the halos to absorb them. An example of beam core, beam halo and collimator jaws is reported in Fig. 7.1. An in-depth discussion on beam cleaning and on the LHC collimation system can be found in the work of Redaelli [23].

This section discusses a particular kind of collimator, the Target Collimator Long Dispersion Suppressor (TCLD) which has to be installed in the HL-LHC between two 11 Tesla magnets. Its main goal is to clean the off momentum particles and avoid magnet quench [23], as shown in Fig. 7.2.

In section 7.2.2 the geometry of the TCLD is presented.

In section 7.2.3 the results of the electromagnetic simulations are shown.

In section 7.2.4 the results of the measurements campaign performed on the TCLD are shown and, when possible, they are compared with the simulation results.

Finally, section 7.2.5 presents a discussion on the performed measurements and simulations and section 7.2.6 concludes recalling the main points.

[1]For more quantitative detail on beam dynamics the reader can refer to the work of Chao [46], Wiedemann [65], Holzer [142, 143] and Salvant [49].

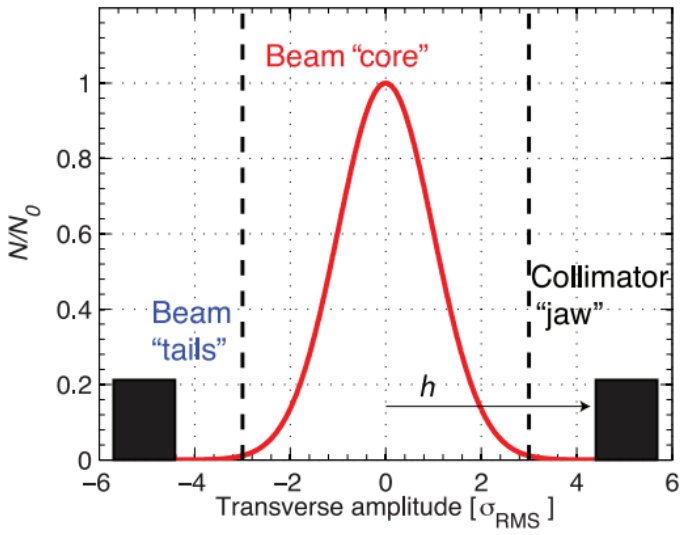

Figure 7.1. Transverse gaussian distribution of beam particles N, normalized with respect to the maximum N_0 (red line). The beam halos, indicated as tails in this figure, are shown. They may be intercepted by collimator jaws shown as black rectangles. The jaw distance from the beam core is indicated with h. Courtesy of Redaelli [23].

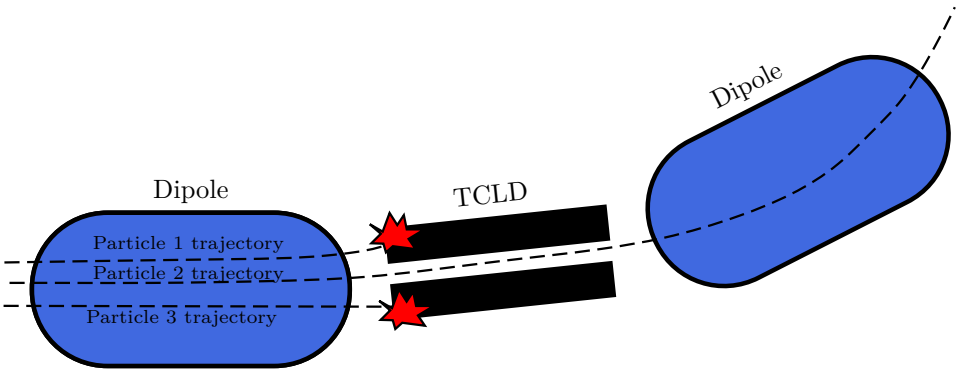

Figure 7.2. Cartoon representation of the TCLD working principle, top view. Particle 1 has lower energy than the ideal particle, i.e. lower magnetic rigidity, thus, the bending action of the dipole is stronger on this particle and its trajectory is bent so that it impacts on the jaw of the collimator. Particle 3 has a higher energy than the ideal particle, i.e. higher magnetic rigidity, the bending action of the dipole is weaker on this particle and its trajectory has only a little bending so that it impacts on the jaw of the collimator. Particle 2 has an energy almost equal to the ideal particle energy, the bending action of the dipole is such that this particle manages to pass inside the TCLD opening and in the next dipole.

7.2.2 Geometry

The assembly of the TCLD and the 11 T dipoles is shown in Fig. 7.3. The CAD model and a picture of the real assembly is also shown. From the figure, it can be seen that the collimator shares its position with a cryostat needed to connect the cooling circuits of the two superconducting dipoles. In Fig.s 7.4, 7.5 and 7.6 the two critical components for impedance of the 11 T dipoles and the TCLD collimator assembly (the TCLD itself and the connections between the dipole RF-screen and the TCLD) are shown in detail.

Figure 7.4 shows the TCLD collimator. Its core is made by two movable jaws, jaw 1 and jaw 2, made with a copper alloy (glidcop), where the tungsten absorbing blocks are installed. The jaws are connected to the In and Out flange of the vacuum tank by a system of RF-fingers, reported in yellow in Fig. 7.4a. On each jaw a cooling system is present and two BPMs are installed. The signal collected from the latter transit trought the BPM cables up to the BPM output plug. The BPM cables have a rigid shielding in stainless steel that isolates them from the environment and is flexible enough to accommodate shape variation of the cable due to the jaw motion. The space between the two jaws, where the beam passes, is screened from the rest of the vacuum tanks empty volume by a lateral RF-shielding, which should prevent the vacuum tank to resonate electromagnetically. This lateral RF-shielding is connected with the tank by lateral RF-fingers, visible in Fig. 7.4b and better shown in Fig. 7.5a. Finally, in Fig. 7.4b also the connections between the jaw and the motors are reported.

In Fig. 7.5a, a sectional cut on the plane yz of the device is shown. The jaw is seen from the x axis perspective. It is possible to better distinguish the lateral RF-contacts that connect the lateral RF-shielding and the vacuum tank, the RF-fingers that connect the jaw with the in or out flange, the BPM button, and the lateral RF-screen. Further, in the figure the outgassing holes in the tungsten blocks are reported. They are needed during the bake out of the component (during the bake out all the device is heated up so that the surface and bulk impurities of the materials are out gassed and pumped out of the device). The holes could represent an issue for impedance. However, their are not facing the beam axis directly, thus they should not perturb the beam. In Fig. 7.5b, a sectional cut on the plane xy of the device is shown. The jaws are seen from the z axis perspective. The RF-system that keeps the connection between the jaws is visible from the picture. The lateral RF-screens are fixed on jaw 2, the latter can move parallel to the x axis, and the distance between the beam and jaw 2 is labeled by h_2. Lateral RF-fingers are installed on jaw 1. They are always touching the lateral RF-screens guaranteeing the electrical contacts. Like jaw 2, jaw 1 moves on an axis parallel to the x axis and its distance from the beam is labeled by h_1. When jaw 1 and jaw 2 move, the lateral RF-contacts slide on the RF-screen keeping the electrical connection.

In Fig. 7.6 the transition pipe from the magnet to the collimator is shown. The possible risk for impedance is linked to the change of section and the cavity like structure that forms after it. However, the impedance simulations performed on this component did not reveal any resonant mode in the frequency range excitable by the HL-LHC beams, i.e. at frequencies below 1.5 GHz. These analyses are not discussed in this thesis. The interested reader can find them in the following reference [144].

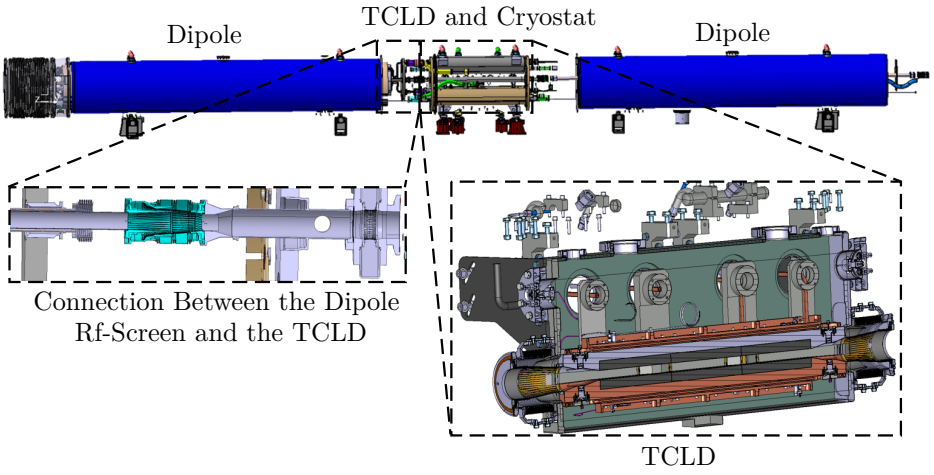

(a)

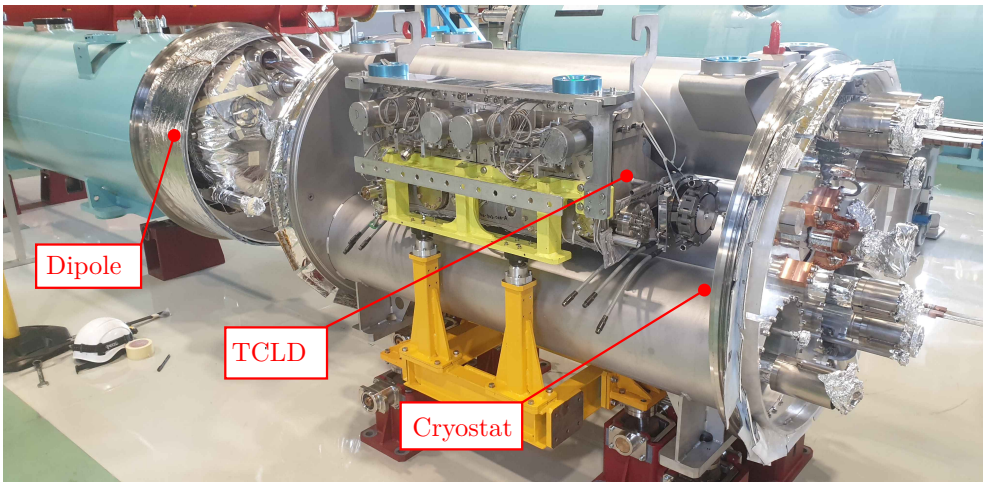

(b)

Figure 7.3. (a) CAD model of the assembly of the cryostat and the TCLD and the 11 T dipoles. The critical components for impedance are highlighted: the TCLD itself and the connections between the dipole RF-screen and the the TCLD. (b) TCLD collimator mounted on its support integrated with the cryostat.

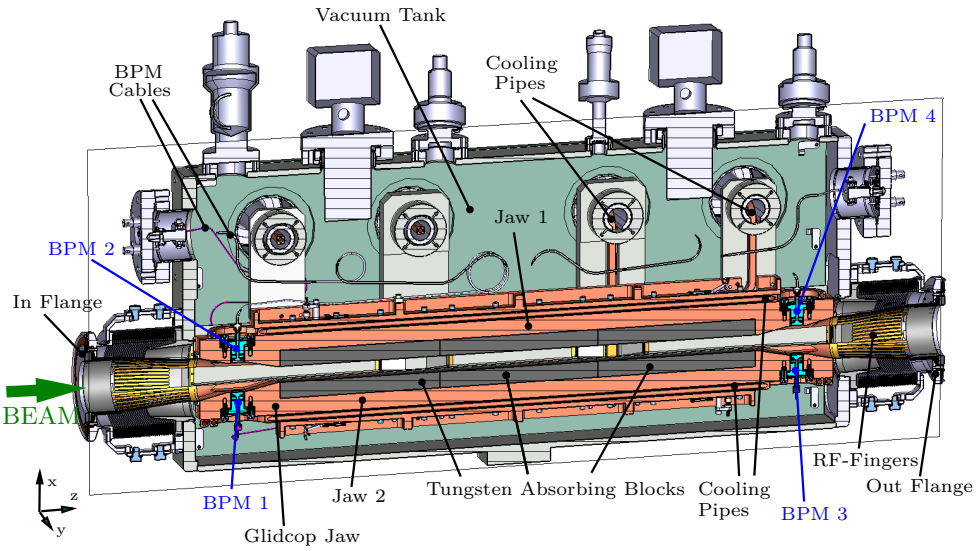

(a)

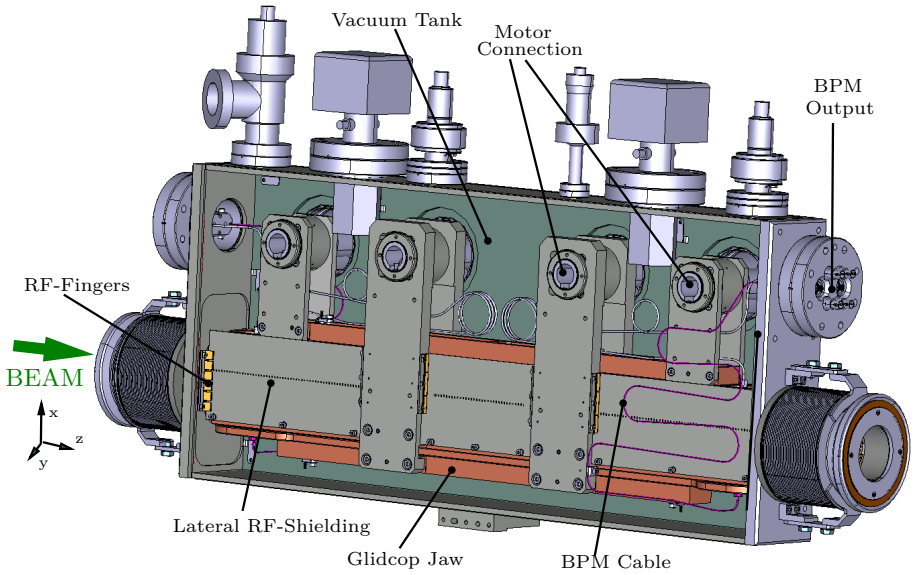

(b)

Figure 7.4. TCLD geometry. The nomenclature of the BPM buttons is indicated in blue.

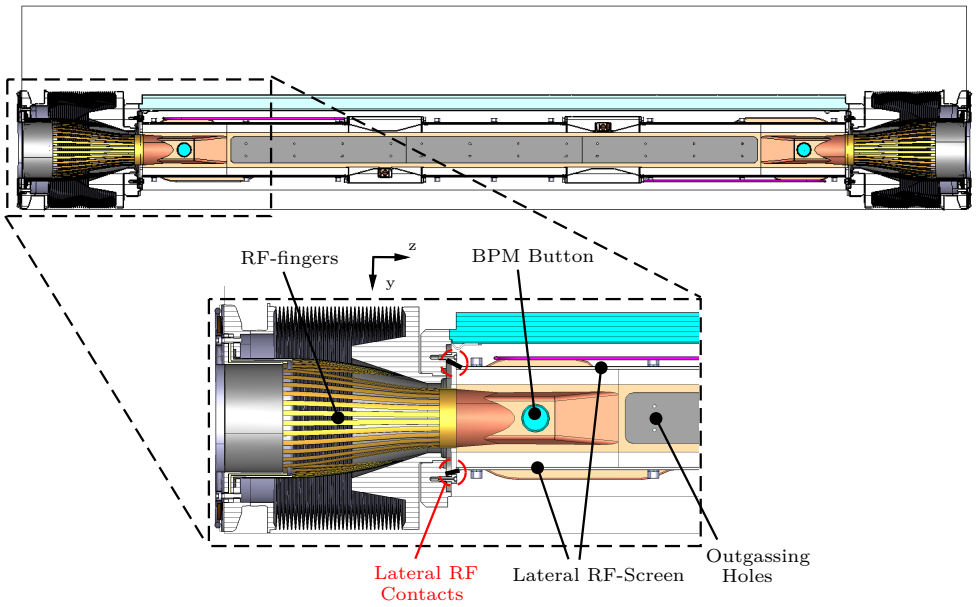

(a)

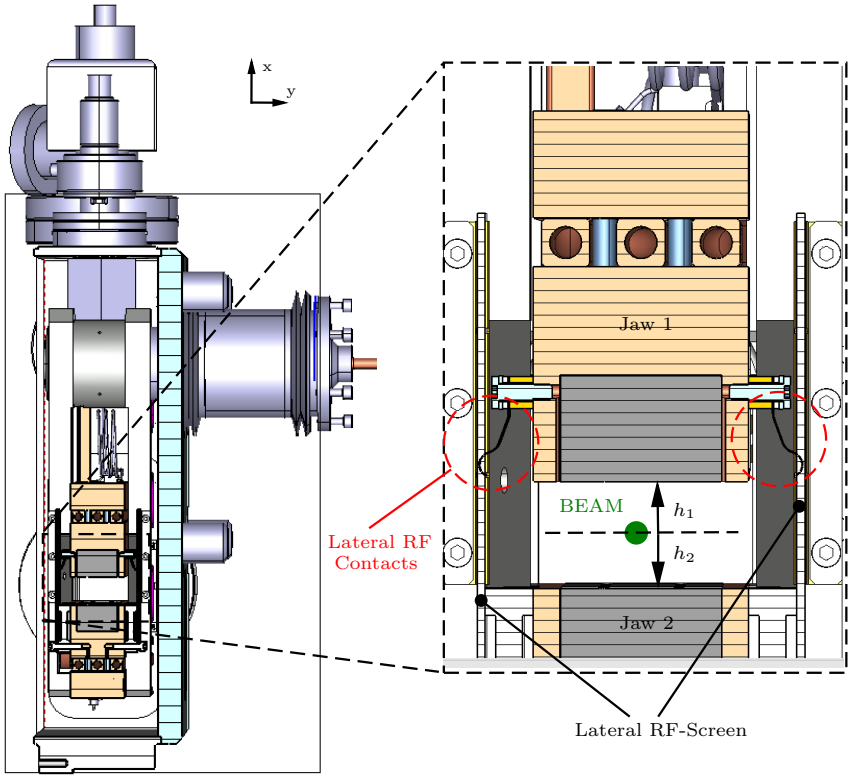

(b)

Figure 7.5. TCLD cut views and RF-contacts system. (a) yz section cut. (b) xy section cut, the distance from the beam and the jaws (h_1 and h_2) is highlighted.

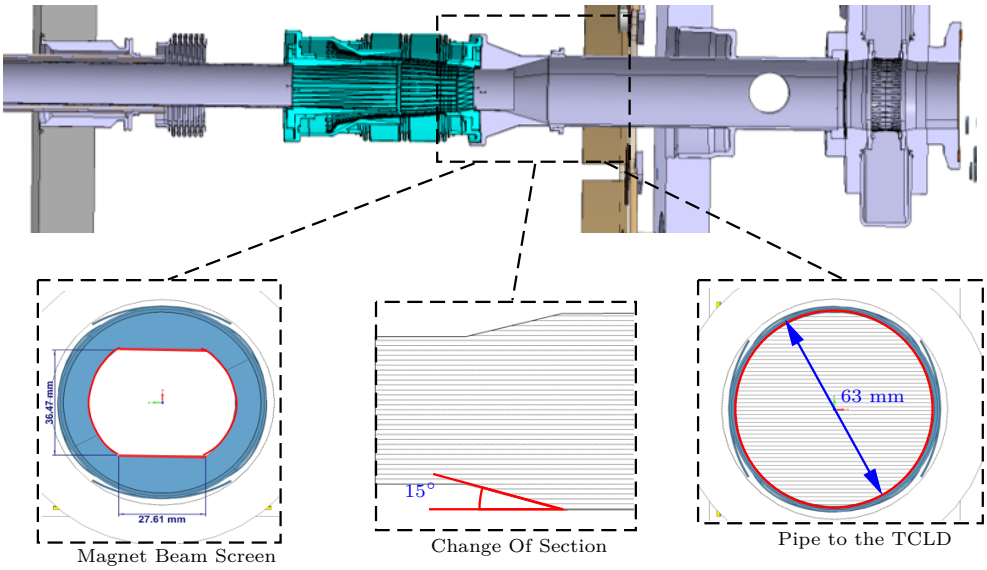

Figure 7.6. Transition pipe from the magnet RF-screen, on the left, to the TCLD on the right. The change of section and the formed cavity like structure could be detrimental for the device impedance. However, they are not a problem in this case since the electromagnetic resonant modes trapped in the change of section resonate at frequencies above 1.5 GHz [144]. The latter is considered as the upper limit of the frequencies excitable by the LHC beams.

7.2.3 Electromagnetic Simulations

The electromagnetic simulations were performed using the CST studio suite solvers Eigenmode, Wakefield, and Time Domain. The model used for the electromagnetic simulations, reported in Fig. 7.7, was obtained from the CAD model for production shown in Fig. 7.4, eliminating all the details not critical for impedance simulations, i.e. chamfers, screws and small surfaces, that would have slowed down the simulations and complicated the task of the mesher without giving significative contributions to the results. The material conductivities used in the simulations are reported in table 7.1. Several cases of jaw aperture were investigated, and they are reported in Table 7.2 and labeled as configuration 1, 2, 3 and 4. In particular, the case $h_1 = h_2 = 20$ mm was deeply investigated since visible transverse modes appear from the measurements for this configuration, refer to section 7.2.4.

Table 7.1. Electrical conductivities of the material used in the TCLD CST model.

Material	Conductivity [S/m]
Stainless Steel 316L	$1.34e6$
Tungsten	$7.70e6$
Copper	$5.96e7$
Copper Nickel	$5.40e6$
Glidcop	$5.37e7$

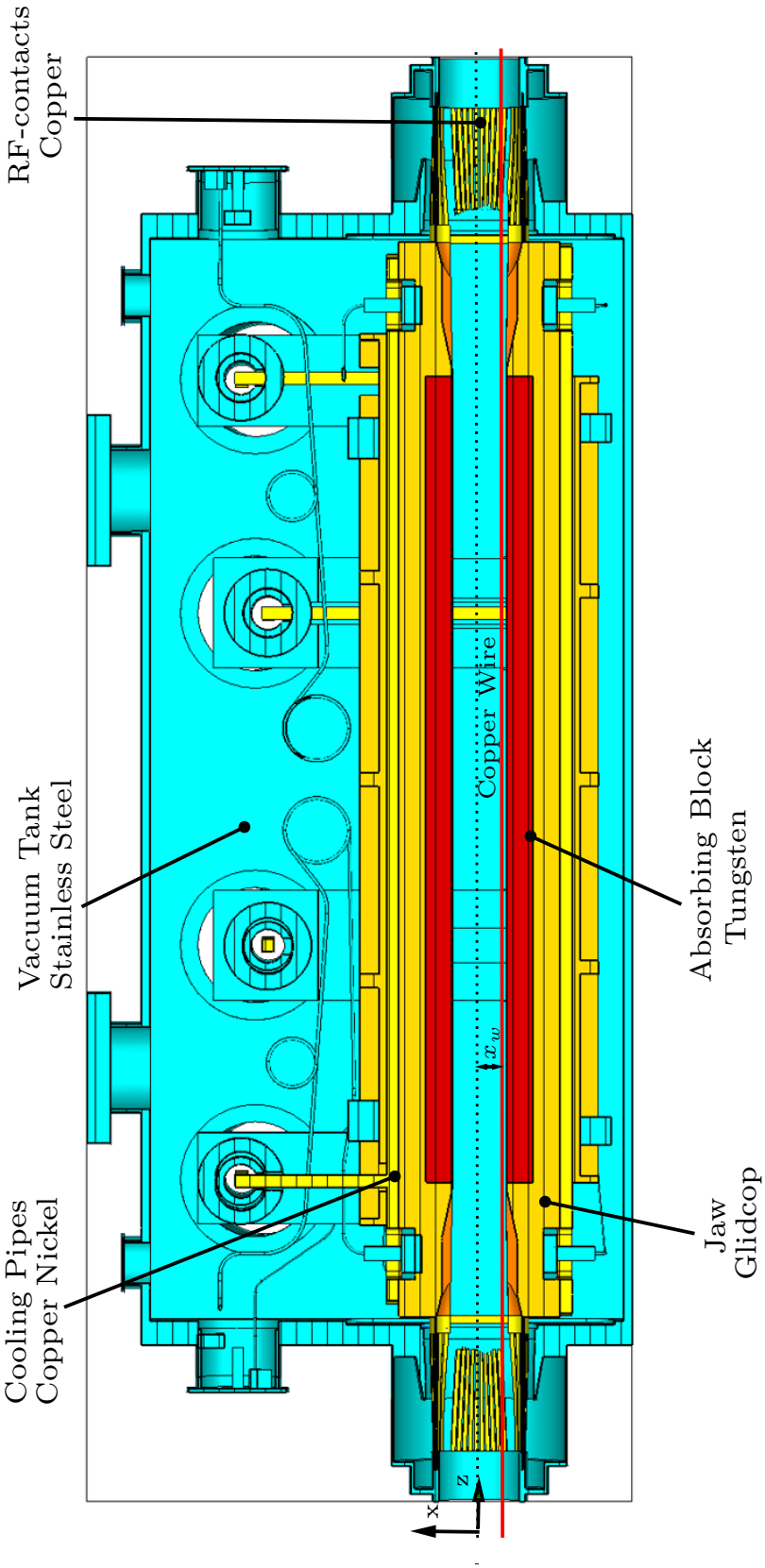

Figure 7.7. TCLD model for electromagnetic simulations. The wire, used to simulated the wire measurements set-up, is shown in red. For the Wakefield and Eigenmode simulations the wire was not simulated. The distance between the copper wire and the z axis is indicated as x_w.

Table 7.2. Simulated TCLD Jaw apertures.

Configuration	Solvers Used	h_1 [mm]	h_2 [mm]
1	Eigenmode, Wakefield	2	2
2	Eigenmode	11	5
3	Eigenmode	5	11
4	Eigenmode, Wakefield, Time transient	20	20

In all cases the Eigenmode solver was used to compute both the longitudinal and the transverse impedance, and when possible also Wakefield simulations were run. For the particular configuration $h_1 = h_2 = 20$ mm also time domain simulations were run to reproduce the wire measurements set-up and investigate the electromagnetic impact of the wire in the device. The wakefield simulations and the time domain simulations were time consuming (from 1 to three weeks) depending on the chosen wake length. For final simulations, hundred times the length of the device (the TCLD is approximately 1.5 m long) was used.

The longitudinal and transverse impedance computed for configuration 1 are reported in Fig.s 7.8 and 7.9. Figure 7.8 reports the longitudinal impedance obtained from the CST Wakefield and the Eigenmode solver. The agreement between the two solvers is rough with respect to the resonant frequencies of the modes: both of them predict the strongest longitudinal modes at frequencies around 1.2 GHz, however, the resonant frequencies of the modes found by wakefield do not match the resonant frequencies of the modes found by eigenmode. This may be due to the different meshes used by the two solvers (wakefield hexahedrons, eigenmode tetrahedrons), or to the different boundary conditions applied at the entrance and at the exit of the device (with the Eigenmode solver it is not possible to define an open, without reflection, surface). However, despite the disagreement with respect to the resonant frequencies, the value of the shunt impedances R_s between the Eigemode and Wakefield resonant modes agree. The shunt impedance of the modes remains limited under 500 Ω, and should not represent a cause of beam instabilities or RF-heating. Figure 7.9 reports the transverse impedance computed using the Eigenmode solver. In the frequency range of interest, between 0 and 1.5 GHz it is always below 200 kΩ/m. As for the longitudinal impedance, this transverse impedance should not represent a cause of beam instabilities.

In Fig. 7.10 and 7.11 the longitudinal and transverse impedance for configuration 2 is explored by eigenmode simulations and in Fig. 7.12 and 7.13 the same is done for configuration 3. Also in this case both the longitudinal and the transverse impedances remain limited, and as for configuration 1, the results of the simulations do not show any potential issue regarding beam instabilities nor impedance induced heating.

A more in-depth study was done for configuration 4, to benchmark the simulations results against measurements taken on an assembled TCLD (refer to the next subsection 7.2.4). In Fig.s 7.14 and 7.15 the longitudinal impedance of the TCLD in configuration 4, computed by the Eigenmode and the Wakefield CST solvers, is reported. Both the solvers give the strongest electromagnetic resonant modes around 1 GHz. However there is not perfect agreement between resonant frequencies and shunt impedances. Further, the Wakefield solver gives a non negligible resonant

mode around 1.2 GHz that seems not found by the Eigenmode solver. Finally, both the solvers report also a non negligible mode for a frequency close to 1.65 GHz and 1.55 GHz. The magnitude of the shunt impedance of these modes can be considered low and not dangerous from beam dynamics and beam induced heating perspectives.

In Fig.s 7.16, 7.17 and 7.18 the transverse impedance obtained from the Eigenmode solver in the x and in the y axis is considered. Transverse modes are present on the x and y axis around 1 GHz, and they are limited in absolute magnitude to 10-20 kΩ/m. Other transverse modes on the y axis develop around 1.3 GHz, always limited to 20 kΩ/m, and finally around 1.5 GHz other, smaller, resonant modes on the x axis are present. The dipolar impedance along the x axis for the TCLD in configuration 4 is shown in Fig. 7.19. It was obtained with the Wakefield solver following the work of Zannini [57]. There is agreement between Eigenmode and Wakefield in the resonant frequencies of the modes around 1 GHz. Furthermore, the agreement between the two solvers regarding the shunt impedances of the strongest transverse modes, the ones around 1 GHz, is within a factor 2.

In Fig. 7.20 the result of the Time Transient CST solver, used to simulate the wire scan measurements is reported, i.e. the TCLD has been simulated with a 0.5 mm diameter wire inside (refer to Fig. 7.7) that acts as excitation source. The simulations have been repeated for several x_w positions of the wire. The results of these simulations show strong perturbation around 1 GHz, three peaks are clearly visible from Fig. 7.20, and this agrees with the finding of Eigenmode and Wakefield that predict resonant modes around 1 GHz. Furthemore, there is a variation on the peak value of the scattering parameters if the wire position is changed. This implies that these modes could be transverse ones. Also this observation agrees with the finding of Wakefield and Eigenmode simulations that show the strongest transverse mode along the x axis around 1 GHz. The reported data are noisy because of the limited simulated time span, 100 ns, used to obtain results in a reasonable time (one month approximately). Indeed the number of mesh used in the simulations is around 132 milions.

Finally, in Fig.s 7.21 and 7.22 the electric field map of two modes, the one at 0.98 GHz and the one at 1.66 GHz are displayed. In both cases the modes resonate between the RF-fingers and the tank or directly between the different RF-fingers.

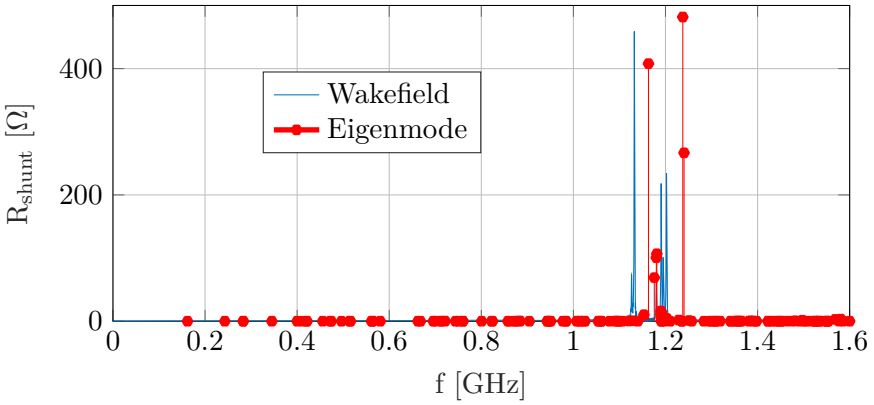

Figure 7.8. TCLD Longitudinal Impedance from Wakefield and Eigenmode solver, $h_1 = h_2 = 2$ mm.

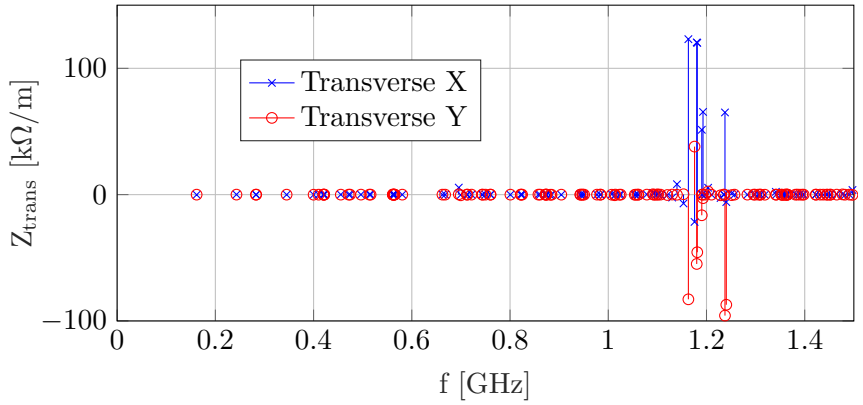

Figure 7.9. TCLD transverse impedance from Eigenmode solver, $h_1 = h_2 = 2$ mm.

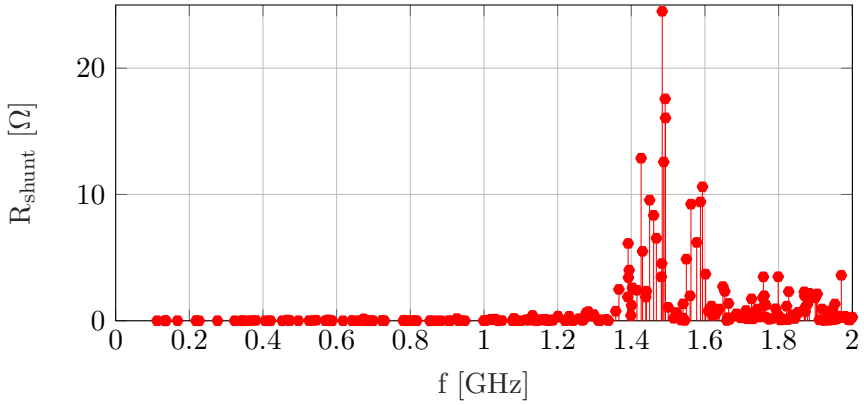

Figure 7.10. TCLD longitudinal impedance from Eigenmode solver, $h_1 = 11$ mm, $h_2 = 5$ mm.

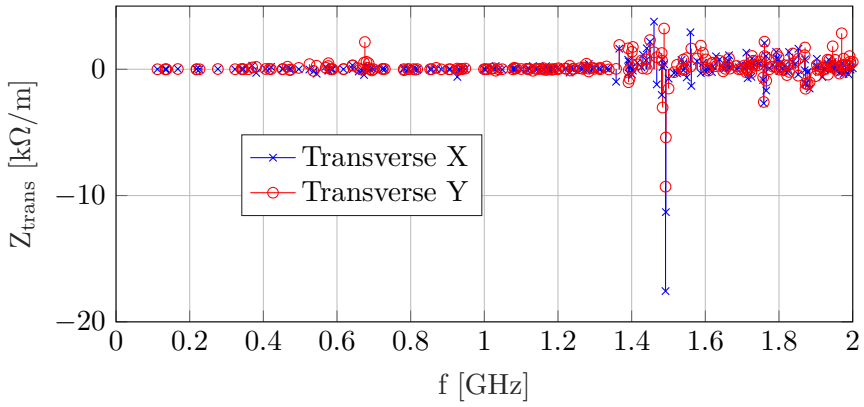

Figure 7.11. TCLD transverse impedance from Eigenmode solver, $h_1 = 11$ mm, $h_2 = 5$ mm.

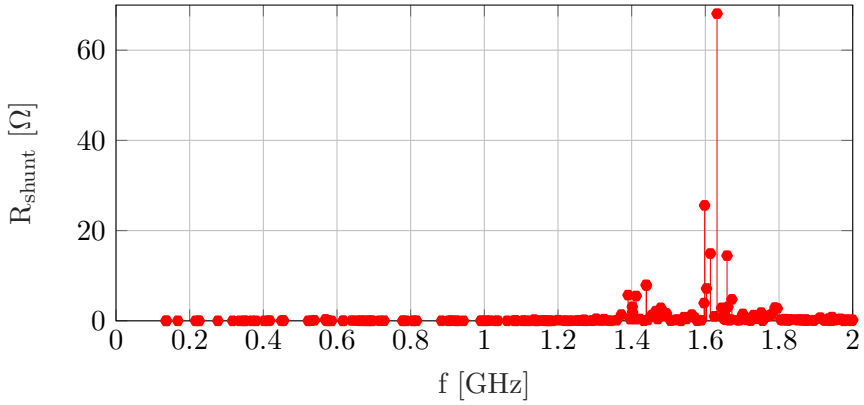

Figure 7.12. TCLD longitudinal impedance from Eigenmode solver, $h_1 = 5$ mm, $h_2 = 11$ mm.

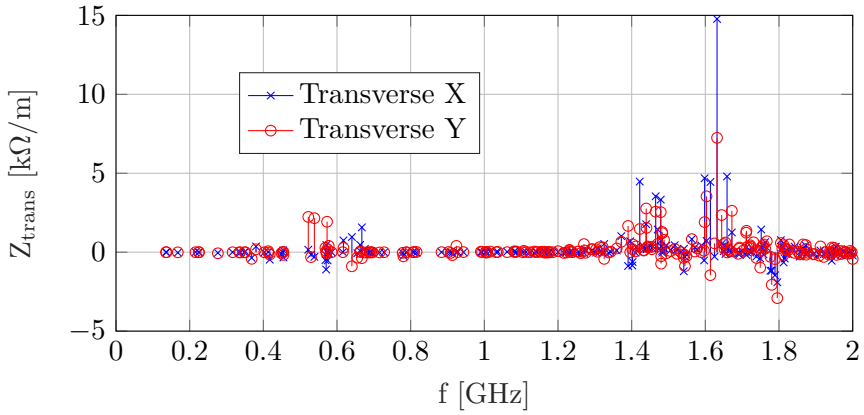

Figure 7.13. TCLD transverse impedance from Eigenmode solver, $h_1 = 5$ mm, $h_2 = 11$ mm.

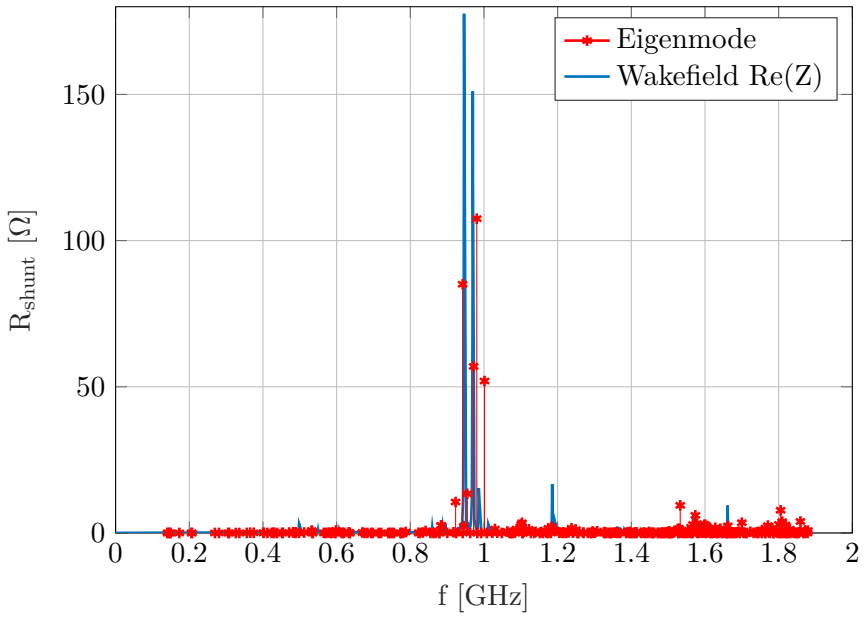

Figure 7.14. TCLD Longitudinal Impedance from Wakefield and Eigenmode solver, $h_1 = h_2 = 20$ mm.

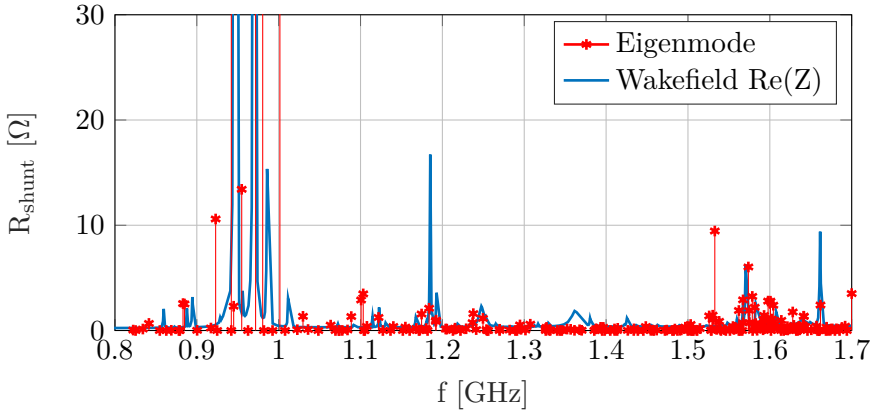

Figure 7.15. Zoom, TCLD Longitudinal Impedance from Wakefield and Eigenmode solver, $h_1 = h_2 = 20$ mm.

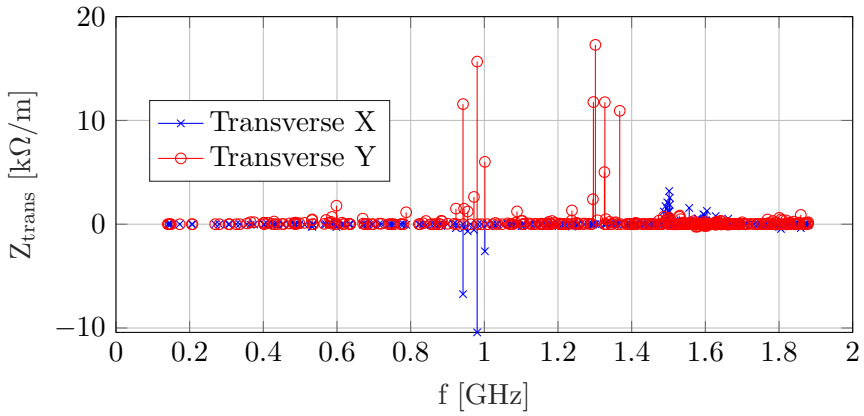

Figure 7.16. TCLD transverse impedance from Eigenmode solver, $h_1 = h_2 = 20$ mm.

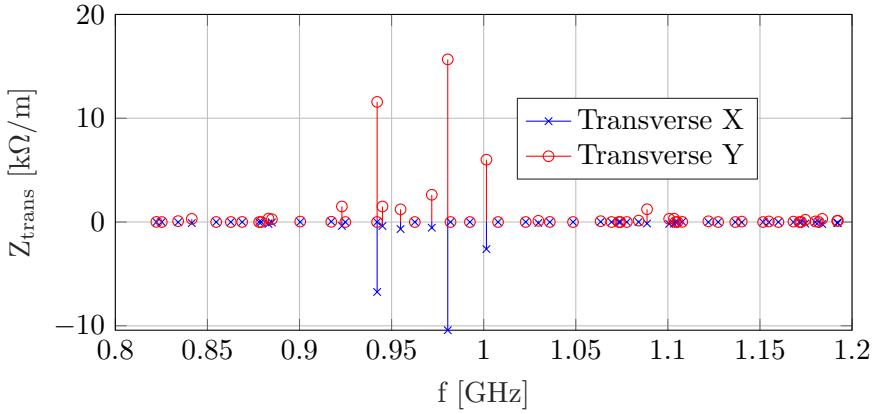

Figure 7.17. Zoom around 1 GHz, TCLD transverse impedance from Eigenmode solver, $h_1 = h_2 = 20$ mm.

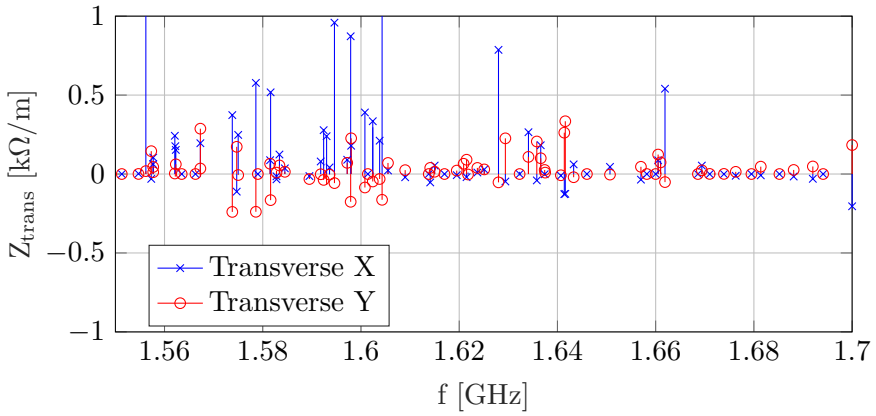

Figure 7.18. Zoom around 1.65 GHz, TCLD transverse impedance from Eigenmode solver, $h_1 = h_2 = 20$ mm.

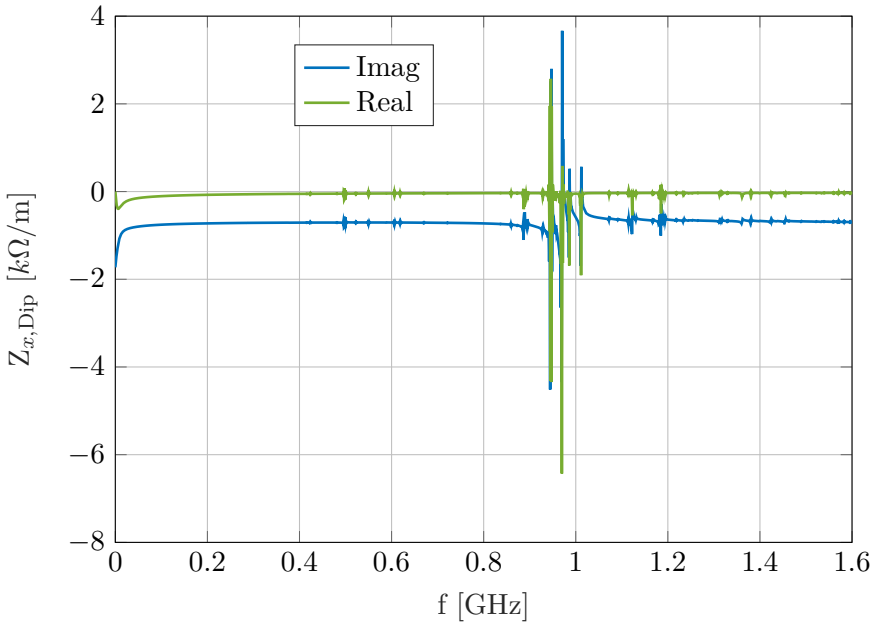

Figure 7.19. TCLD x dipolar impedance from CST wakefield solver, $h_1 = h_2 = 20$ mm. The mode with transverse real shunt impedance approximately 2 kΩ/m, is affected by noise, the noise fluctuations lead to the real negative shunt impedance value of -4 kΩ/m.

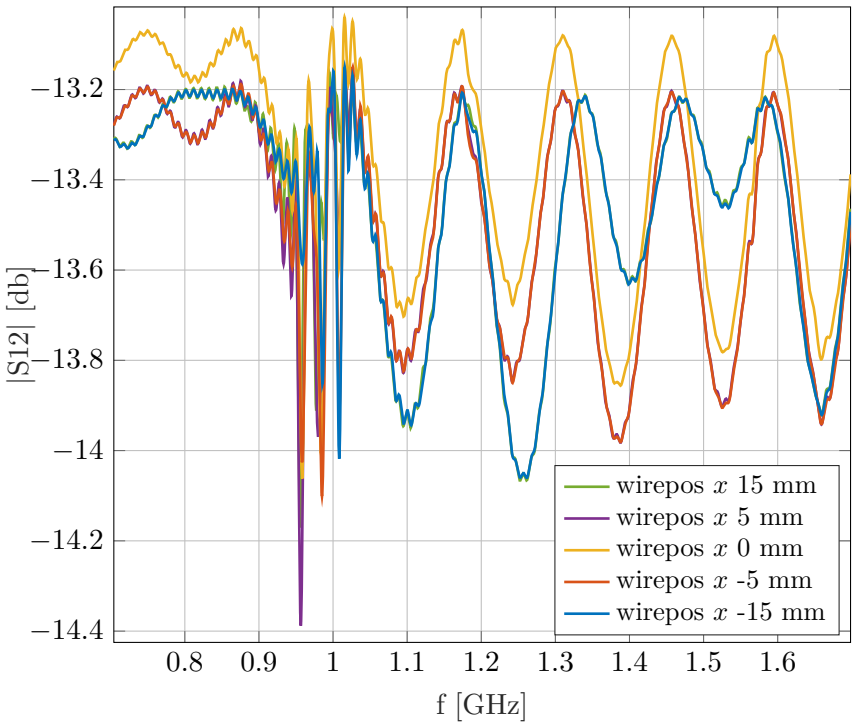

Figure 7.20. TCLD transmission parameter S12 from time transient solver, $h_1 = h_2 = 20$ mm.

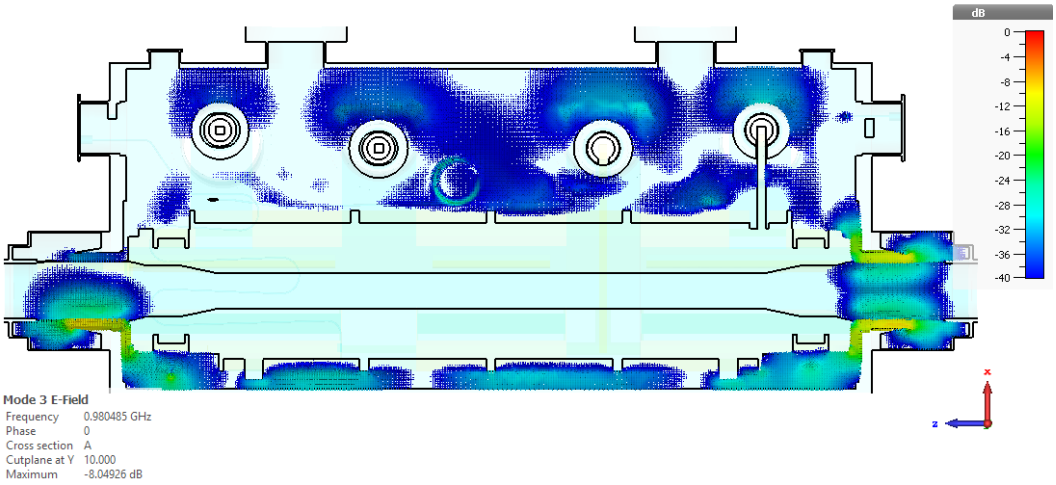

Figure 7.21. TCLD configuration 4, $h_1 = h_2 = 20$ mm, electric field map of the 0.98 GHz mode. The mode resonates the most in the space between the RF fingers and the tank at the in and out pipe of the collimator.

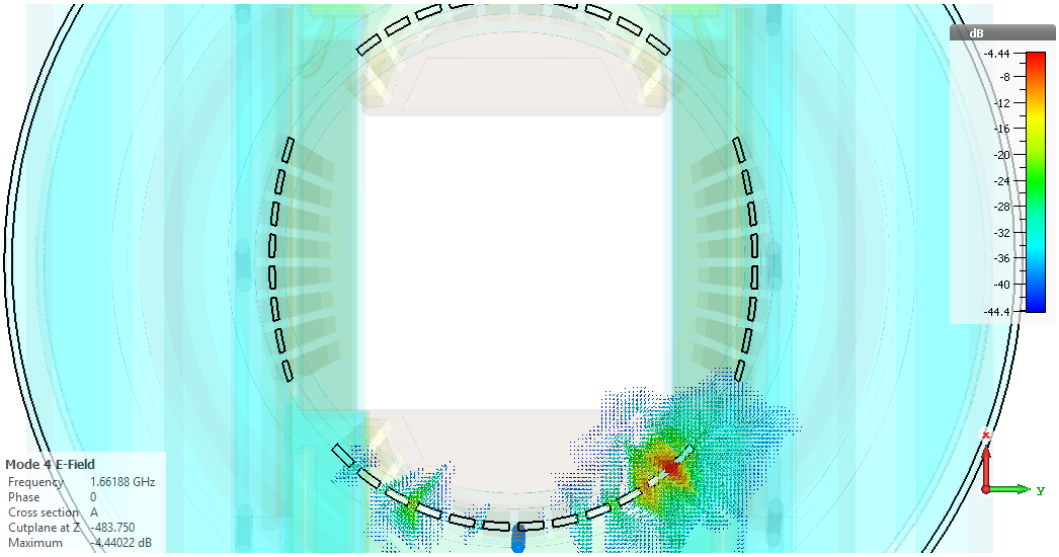

Figure 7.22. TCLD configuration 4, $h_1 = h_2 = 20$ mm, electric field map of the 1.66 GHz mode. The mode resonates the most in the space between the the RF fingers.

7.2.4 Impedance Bench Measurements

In this subsection the results of the measurements performed on the TCLD are reported. First the probe measurements are discussed, subsequently the results of the BPM measurements are presented and finally the results of the wire measurements are reviewed. Two TCLDs were measured, a prototype and a pre-series. In the industrial world, a prototype is the first fully functional device built using a design. On a prototype are performed all the possible tests to characterise its behaviour. The latter should be as close as possible to the one defined during the design phase. If the prototype does not behave as expected it can be due to assembly and manufacturing issues but also to overlooked aspects in the design phase. If the prototype characterisation is positive one can pass to the series production. The manufacture and assembly techniques used to built the prototype may be different from the one used to built the same device in the series production. Thus, on the first device produced in series, the so called pre-serie device, several tests are run again, this time to look specifically for non conformities. The probe measurements and BPM measurements result, reported in this chapter, are relative to the pre-serie TCLD while wire measurements were performed only on the TCLD prototype. It was not possible to perform the wire measurements on the TCLD pre-serie because this kind of measurement is invasive, and since the pre-serie is to be installed into LHC, the risk of polluting the device by inserting external materials or scratching the internal surfaces had to be minimized.

Probe Measurements

The probe measurement procedure was described in section 5.3, and the experimental set-up for this kind of measurements is shown in Fig. 7.23.

In Fig. 7.24 the scattering parameters, reflection (S11, S22) and transmission (S12) of the TCLD in configuration 4, for frequencies below 0.5 GHz and for different values of the probe insertion length, are shown. The reported measurements were performed with loop probes, that were found more sensitive to low frequency modes, as already observed by Biancacci et al. [145]. The black dashed lines in the figure mark the resonant frequency of some of the device modes. In Fig. 7.24, in the S12 plot, the resonant frequencies obtained by simulations (Eigenmode) are also shown at an arbitrary fixed value of -175 db for comparison purposes. There is a general good agreement on the measured and simulated resonant frequencies: for every measured mode frequency a simulated one falls within a 20 MHz range. The only exception is the resonant mode at 0.19 GHz. It can be noted that the reflection parameters exhibit a wiggling behaviour, and this can be due to a calibration issue that was not possible to remove during the measurements. This wiggling behaviour made it difficult to recognise the mode track on the reflection parameters. However, the mode presence is clear in the transmission parameters that present a peak at the frequency of the resonant modes.

Frequencies higher than 0.5 GHz were investigated. There were particular focus on the region between 0.8 and 1.2 GHZ since, according to the simulations (configuration 4), the strongest resonant modes of the device are located in this frequency range.

In Fig. 7.25 the transmission and reflection scattering parameters measured with loop probes inserted both 40 cm inside the TCLD in configuration 4 are shown. The transmission parameter was filtered with a low pass filter to remove the noise. The filtered data were used to compute the resonant quality factor of the mode as described in section 5.3.3. Figure 7.26 shows an example of Q acquisition. The three green dots represent the maximum of the curve and the two points of the curve located at -3 db from the maximum allow to compute loaded and unloaded quality factor applying Eq.s 5.12, 5.14 and 5.17.

In the Tables 7.3, 7.4 and 7.5 the resonant frequency, the loaded and unloaded quality factor and the coupling coefficient are reported for the mode in which the measurement was possible.

Finally, it is possible to say that the probe measurements support the simulation results by finding device resonant modes in the expected frequency range.

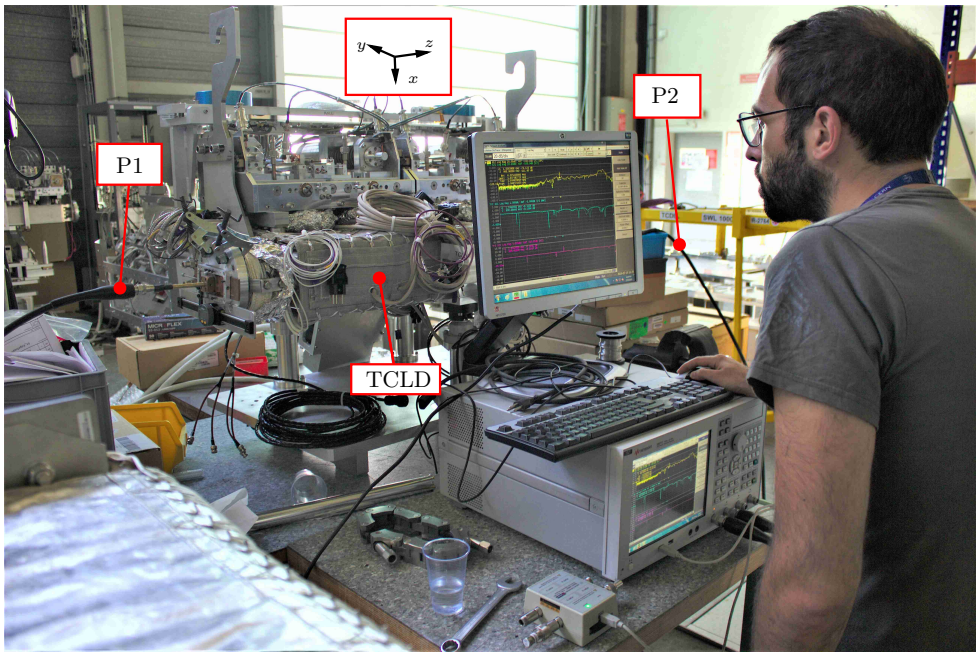

Figure 7.23. Probe measurements set-up. The two probes P1 and P2 are inserted into the collimator: alternatively one probe is fed and the other is used as a pick up alternatively to read the device response and obtain the scattering parameters. In the picture the reference system, the same used in Fig. 7.4, is shown. The figure shows also an example of totally confused operator.

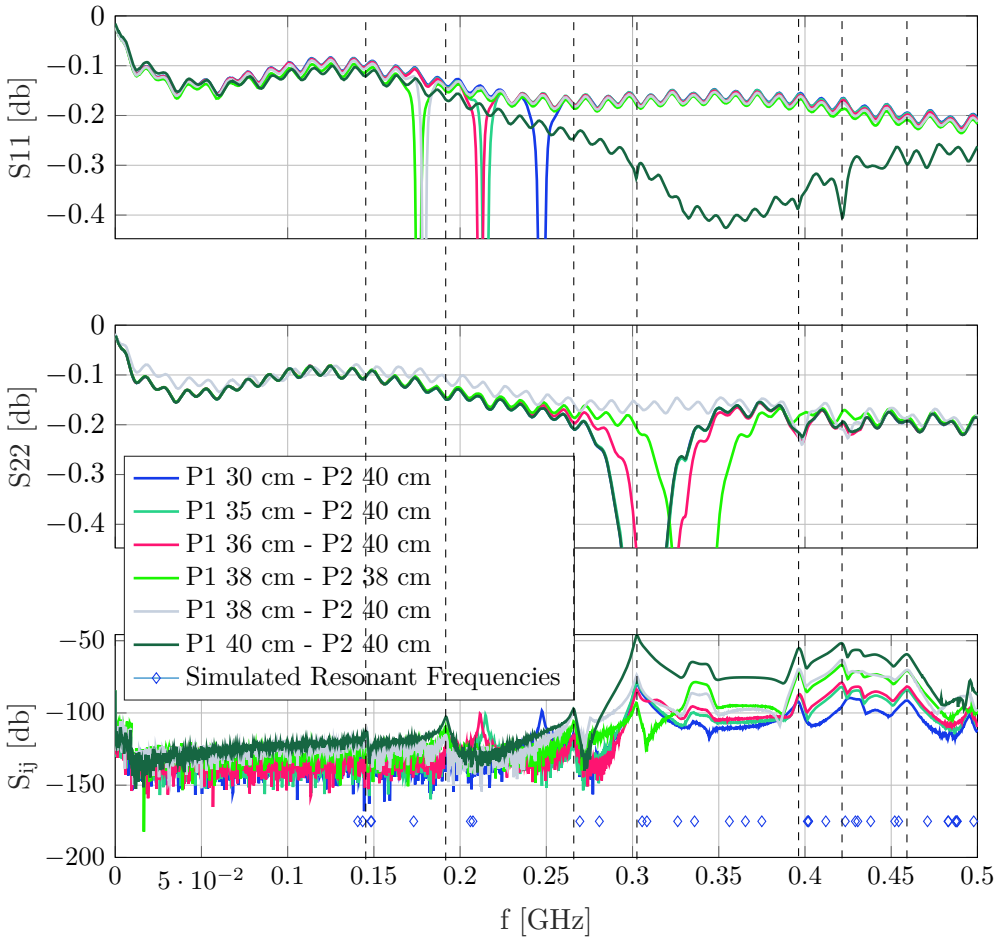

Figure 7.24. Scattering parameters, reflection (S11, S22) and transmission (S12) of the TCLD in configuration 4 for frequencies below 0.5 GHz and for different values of the probe insertion length. The measurements were done with loop probes. The black dashed lines mark the resonant frequencies of some of the device modes. In the S12 plot, the resonant frequencies obtained by simulations (Eigenmode) are also shown at a fixed value of -175 db. There is a general good agreement between the measured and simulated resonant frequencies. For every measured mode frequency a simulated one can be found within 20 MHz range. The only exception is the resonant mode at 0.19 GHz. In the figure also some probe lambda quarter mode is visible, they are characterised by the out of scales reflection parameters.

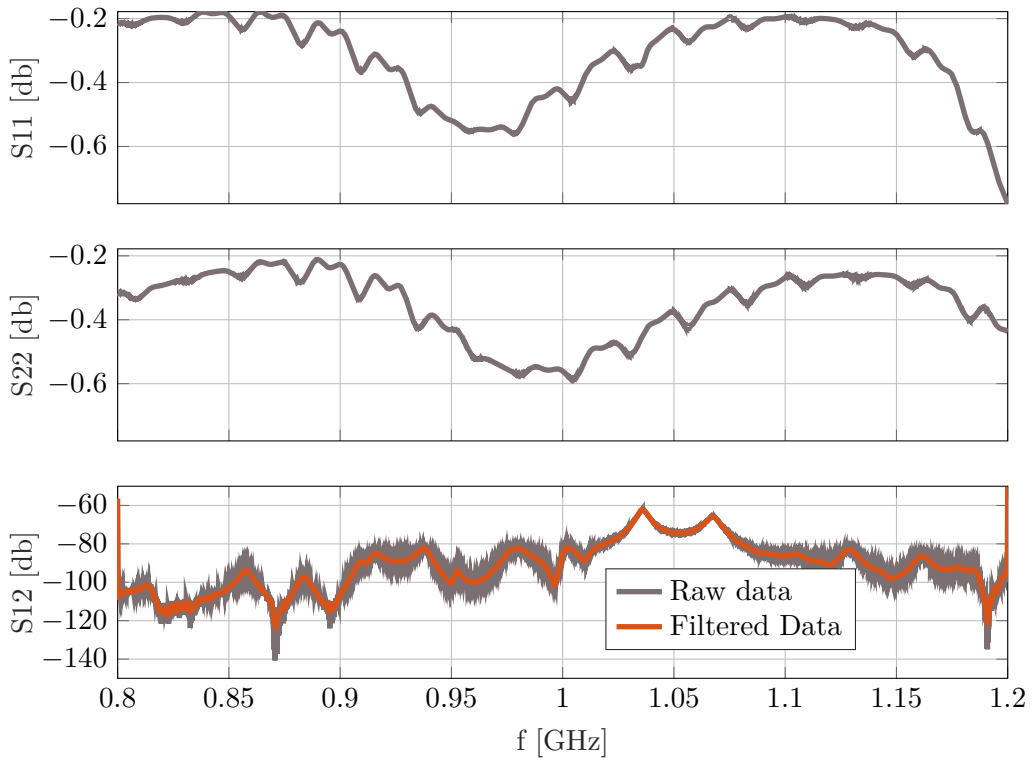

Figure 7.25. Scattering parameters, reflection (S11, S22) and transmission (S12) of the TCLD in configuration 4 for frequencies between 0.8 and 1.2 GHz and for probe insertion lengths of 40 cm. The measurements were done with loop probes. The transmission parameters have been filtered to remove the noise and allow a better characterization of the resonant mode quality factor.

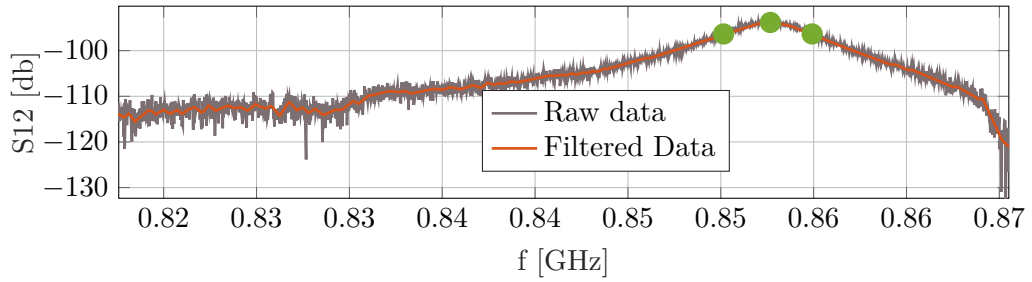

Figure 7.26. Example of Q acquisition. The three green dots represent the maximum of the curve and the two points of the curve located at -3 db from the maximum. These points allow to compute the loaded and unloaded quality factors.

Table 7.3. TCLD configuration: $h_1 = h_2 = 20$ mm

f_r[GHz]	Q_l	k	Q
0.192	87.226	7.411E-06	87.227
0.396	135.253	1.751E-03	135.490
0.421	86.252	2.590E-03	86.475
0.459	81.741	1.071E-03	81.828
0.858	180.144	2.037E-05	180.147
0.884	190.558	1.364E-05	190.560
0.916	141.574	5.652E-05	141.582
0.938	193.985	7.849E-05	194.000
0.953	361.231	2.080E-05	361.239
1.002	183.223	8.099E-05	183.238
1.036	252.530	7.847E-04	252.728
1.068	195.223	5.090E-04	195.323
1.129	183.448	7.179E-05	183.462
1.162	180.905	4.793E-05	180.914

Table 7.4. TCLD configuration: $h_1 = h_2 = 15$ mm

f_r[GHz]	Q_l	k	Q
0.859	226.968	8.437E-06	226.970
0.893	257.542	1.037E-05	257.545
0.913	265.163	1.412E-05	265.167
0.936	165.323	1.301E-05	165.325
0.968	162.541	2.727E-05	162.545
1.004	210.805	4.220E-05	210.814
1.188	188.609	2.480E-04	188.655

Table 7.5. TCLD configuration: $h_1 = h_2 = 25$ mm

f_r[GHz]	Q_l	k	Q
0.859	231.474	8.507E-06	231.476
0.893	224.387	9.954E-06	224.389
0.912	254.238	1.384E-05	254.242
0.936	214.223	1.389E-05	214.226
0.968	162.541	2.727E-05	162.545
1.003	208.624	4.198E-05	208.633
1.188	190.804	2.486E-04	190.851

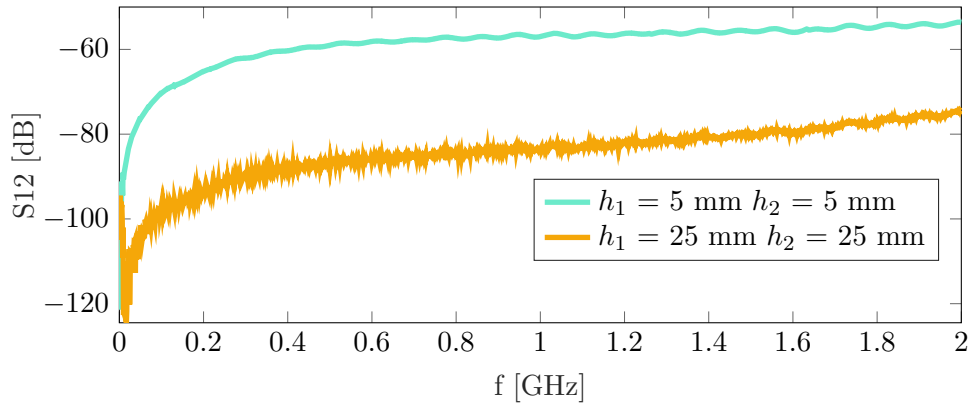

Figure 7.27. Transmission scattering parameters, with BPM 3 - BPM 4 plugged in, at different TCLD jaw configurations.

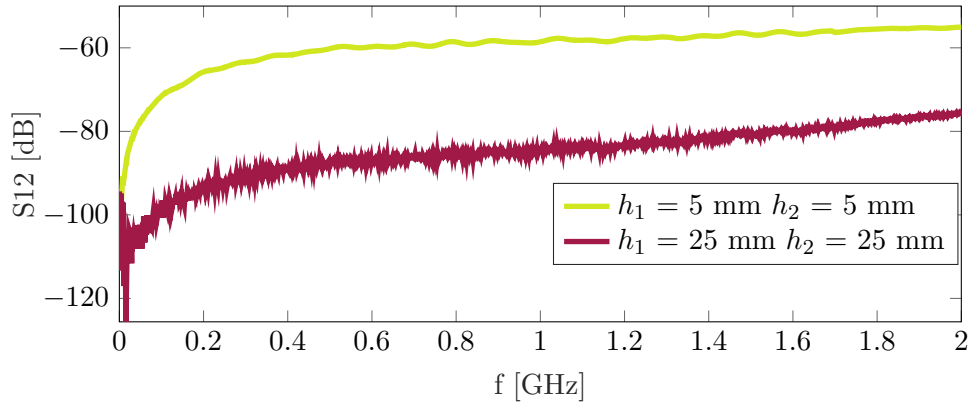

Figure 7.28. Transmission scattering parameters, with BPM 1 - BPM 2 plugged in, at different TCLD jaw configurations.

BPM Measurements

In the TCLD there are four BPMs, two per jaws. Their exact location is shown in Fig. 7.4a. The figure also indicates the labelling of the different BPMs. The beam position monitors can be plugged to the VNA via the BPM output port, Fig. 7.4b, so that they can excite the device and read its response, in particular its transmission parameter S12 or S21. In order to have a transmission measurement one has to connect to the VNA at least a couple of BPMs. One can distinguish between "facing BPMs couples", where the two BPMs are positioned one in front of the other, and "non-facing BPM couples". With the nomenclature defined in Fig. 7.4a, the facing BPM couples are BPM 3 - BPM 4 and BPM 1 - BPM 2. All the other combinations form non facing BPM couples. Facing couples were used as a checking tool in the performed measurements. If the hardware is correctly working, a capacitive coupling should be the expected output signal connecting a BPM facing couples to the VNA. The transmission scattering parameter as a function of frequency for the facing BPM couples are reported in Fig. 7.27 for BPM 3 - BPM 4 and in Fig. 7.28 for BPM 1 - BPM 2, for different TCLD jaw configurations. The behaviour of the

curves in both figures is similar: there is a minimimum at the lowest frequencies, followed by a sharp increase that gradually turns into a linear growing behaviour. This is the behaviour expected by a capacitor, which acts as an open circuit at low frequency, i.e. with very low transmission scattering parameters, which increase at higher frequencies. Further, comparing the scattering parameters in Fig. 7.27 and in Fig. 7.28, one can see that the response read from the facing couples is the same if the same jaw configuration is compared. This was also expected, since the two facing BPM couples are identical. Thus, one concludes that the BPMs are correctly working as far as concern impedance measurements. The scattering parameters as a function of frequency for the non facing BPMs are reported in Fig.s 7.29 - 7.40 for different jaw configurations of the TCLD, as indicated in the figures.

For small apertures, $h_1 = h_2 = 1-2$ mm, refer to Fig.s 7.29 and 7.30, it is possible to see modes around 1.2 GHz as bumps on the flat noise figure. Modes around this frequency were expected by simulations, refer to Fig. 7.8. For $h_1 = h_2 = 2$ mm, bumps at 1.45, 1.65 and 1.70 GHz appear. They could represent resonant modes. If the value of $h_1 = h_2$ is increased up to 5 mm, according to Fig.s 7.31 and 7.32, there are still modes around 1.2 GHz, and the modes at 1.65 GHz start to be more visible. It is interesting to compare Fig.s 7.31 and 7.32. They show the transmission scattering parameters at the same TCLD configuration for different BPM couples. Different couples of BPMs read different device responses. For instance the bumps due to the modes are very clear for the BPM couple 1-3 while they are more noisy for the couple 2-4. This may be explained considering that these modes may resonate more in the region where the BPMs 1 and 3 are, i.e. near jaw 2 of the collimator. For $h_1 = h_2 = 10$ mm, Fig. 7.33, there are still modes visible around 1.2 GHz and around 1.70 GHz. For $h_1 = h_2 = 15$ mm, Fig. 7.34, there is clearly one mode appearing a frequencies below 1.2 GHz , while the modes at 1.2, 1.3 and 1.6 GHz are more visible. Comparing the scattering parameters for $h_1 = h_2 = 15$ mm of the BPM couples 1-3, Fig. 7.34 and 1-4 Fig. 7.35, one can see that, as before, the scattering parameters for the latter BPM couple do not present well defined bumps differently from S12 of the BPM couple 1-3. The hypothesis that BPMs mounted on jaw 2 can better couple with the excited modes is reinforced. Figures 7.36, 7.37, 7.38 and 7.39 compare the scattering parameters obtained for different couples of BPMs for $h_1 = h_2 = 20$ mm. Regarding BPMs 1-3 and 1-4, Fig.s 7.36, 7.37 clearly show a resonant mode between 1.1. and 1.2 GHz (a mode in that region was expected at least by the Wakefield simulations, Fig. 7.15) and another for frequencies slightly below 1.6 GHz. However, the mode highlighted by the simulations around 1 GHz are not observed by these two BPM couples. On the contrary, Fig. 7.38, BPMs 2-3, presents a bump around 1 GHz, where it was expected because of the simulations. Figure 7.39, reports the transmission scattering parameter of the BPM couple 2-4, and it seems not to reveal any resonant mode. Finally, S12 of the BPM couple 2-3 is presented for $h_1 = h_2 = 25$ mm in Fig. 7.40, only a resonant mode can be surely spotted around 1.6 GHz. One can conclude saying that different couples of BPM couples differently with the device modes and that the measurements support the simulations since the measured modes were in frequency region expected by simulations.

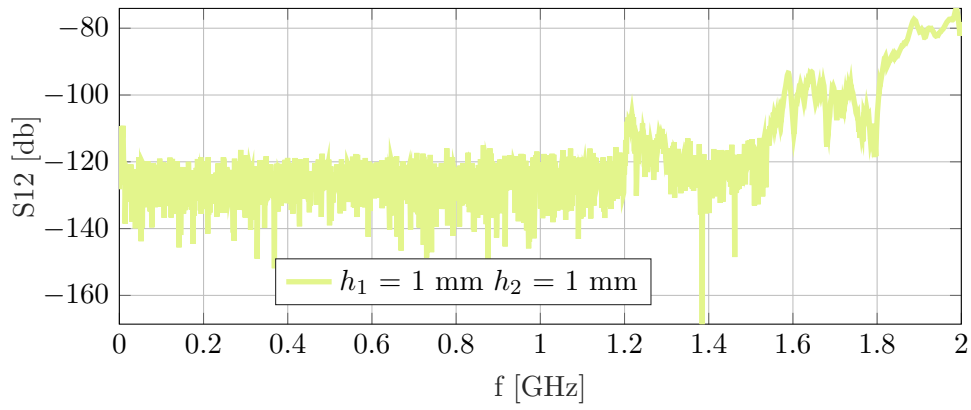

Figure 7.29. Transmission scattering parameters, with BPM 2 - BPM 3 plugged in.

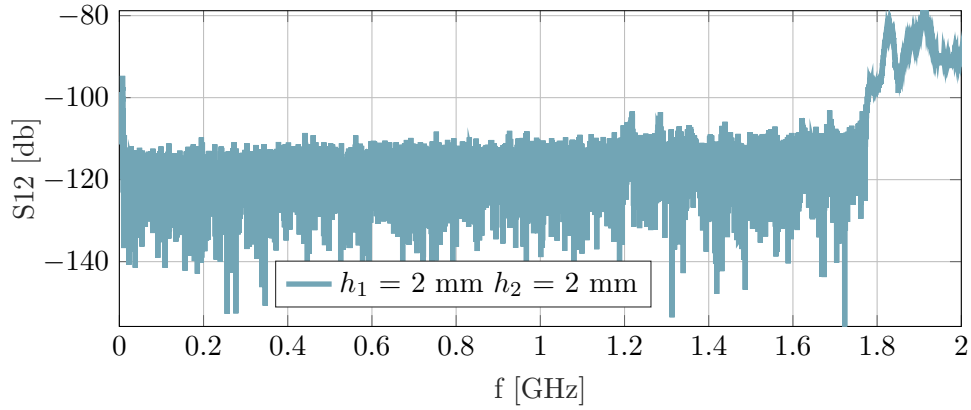

Figure 7.30. Transmission scattering parameters, with BPM 1 - BPM 4 plugged in.

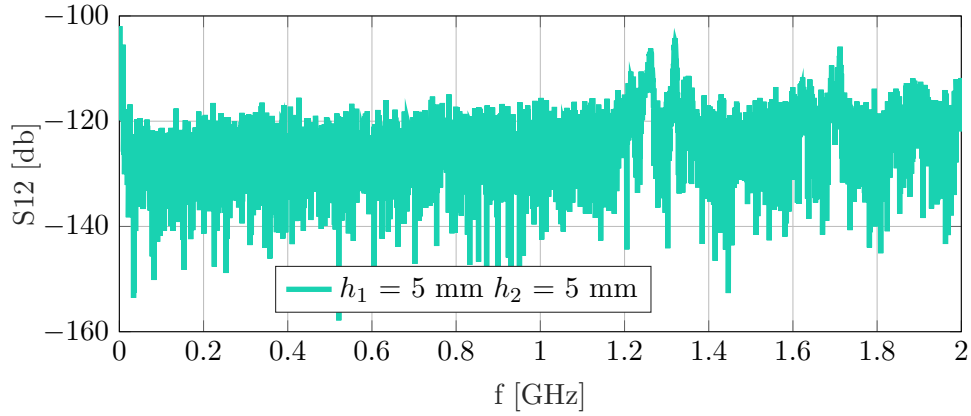

Figure 7.31. Transmission scattering parameters, with BPM 1 - BPM 3 plugged in.

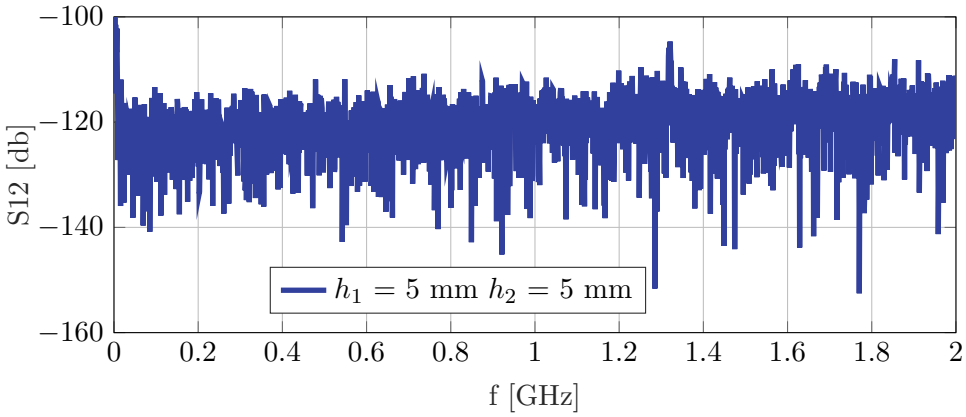

Figure 7.32. Transmission scattering parameters, with BPM 2 - BPM 4 plugged in.

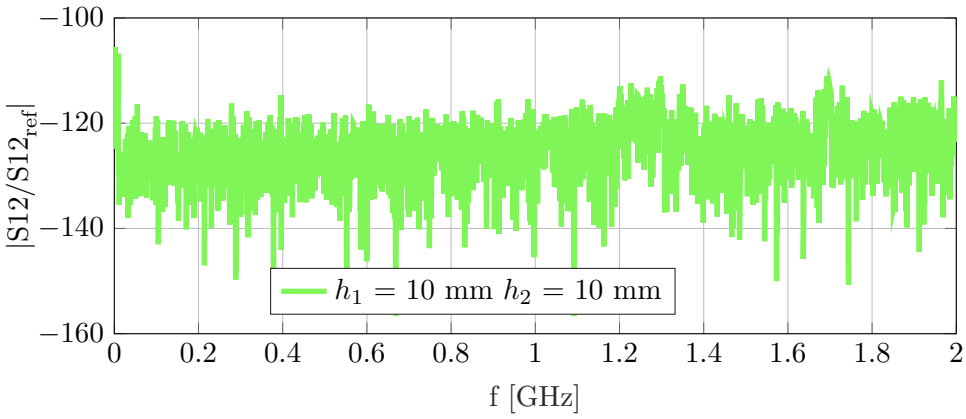

Figure 7.33. Transmission scattering parameters, with BPM 1 - BPM 4 plugged in.

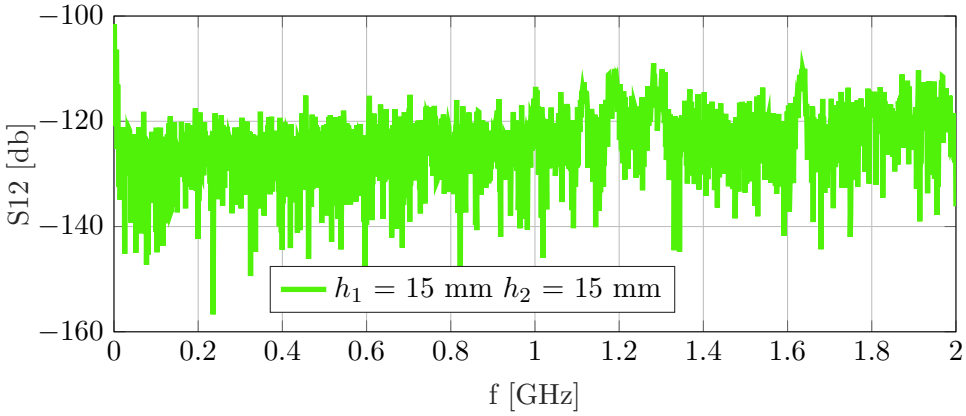

Figure 7.34. Transmission scattering parameters, with BPM 1 - BPM 3 plugged in.

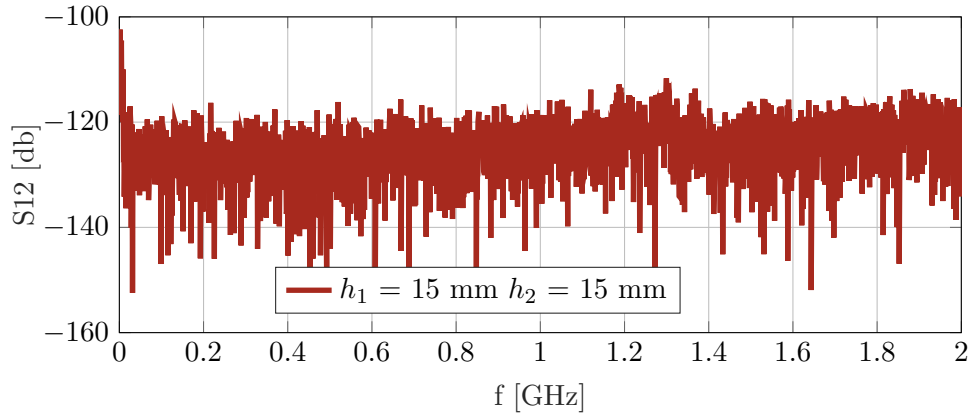

Figure 7.35. Transmission scattering parameters, with BPM 1 - BPM 4 plugged in.

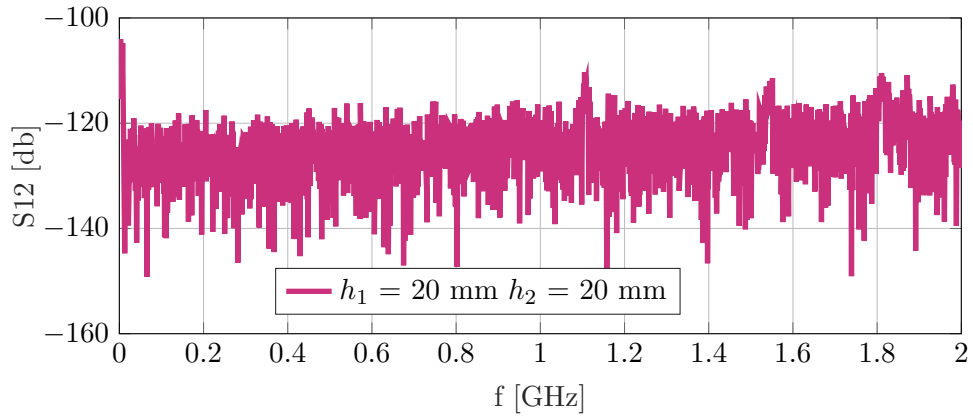

Figure 7.36. Transmission scattering parameters, with BPM 1 - BPM 3 plugged in.

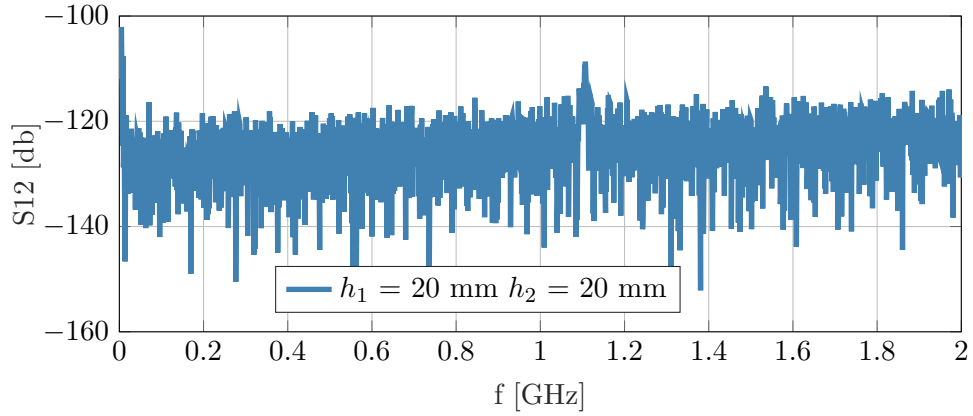

Figure 7.37. Transmission scattering parameters, with BPM 1 - BPM 4 plugged in.

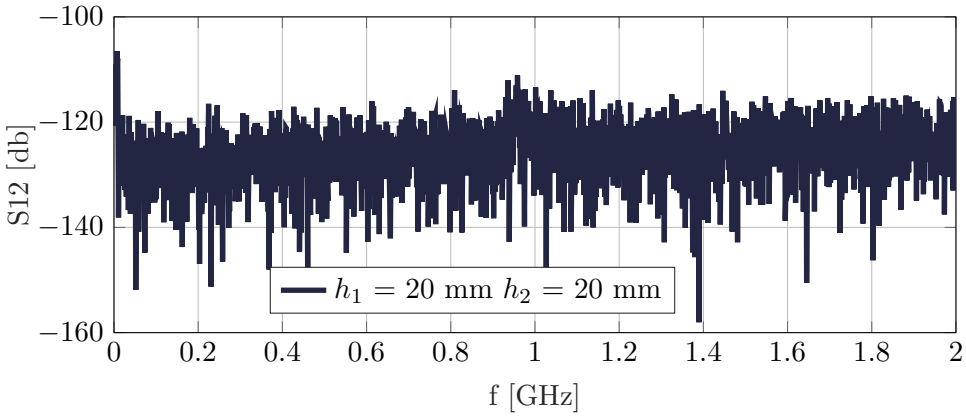

Figure 7.38. Transmission scattering parameters, with BPM 2 - BPM 3 plugged in.

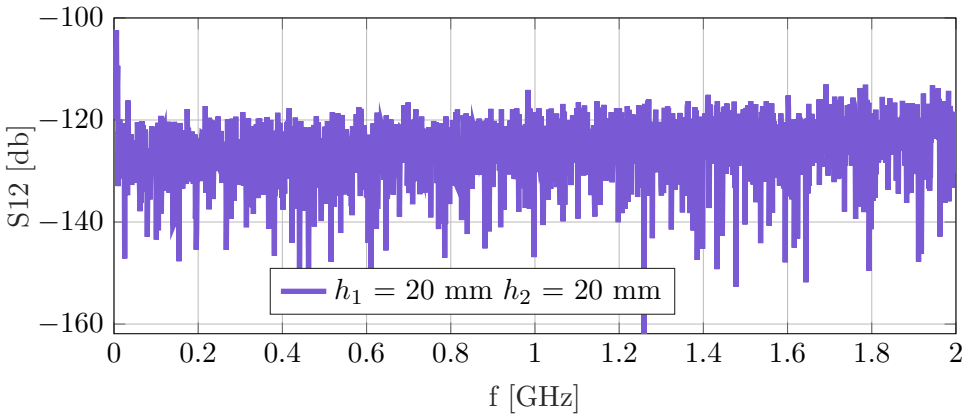

Figure 7.39. Transmission scattering parameters, with BPM 2 - BPM 4 plugged in.

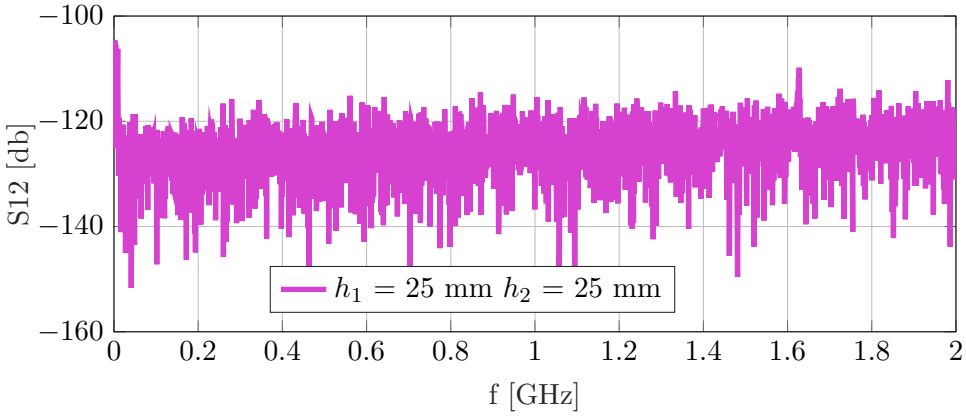

Figure 7.40. Transmission scattering parameters, with BPM 2 - BPM 3 plugged in.

Wire Measurements

The wire measurements procedure was described in section 5.4. In this subsection the results of the measurements and post processing for the TCLD prototype are reported. First, the raw data acquired with the wire scanner measurements for two configurations of the TCLD are shown, $h_1 = h_2 = 2$ mm and $h_1 = h_2 = 20$ mm. The strongest resonant modes are identified from the measurements. Subsequently, the subsection reports the raw data post-processing to find the longitudinal and transverse impedance of these resonant modes, according to what was done by Biancacci et al. [145] and what was reported in section 5.4.2.

In Fig. 7.41 the transmission scattering parameter S12 acquired via wire measurements is displayed for the TCLD prototype in configuration 4 ($h_1 = h_2 = 20$ mm). Several acquisitions for different wire positions along the x axis, x_w (refer to Fig. 7.7) were performed. The top plot shows all the acquisitions for the whole explored frequency range, from 0 to 2 GHz. These data reveal two regions with strong modes (the modes are visible as perturbations of the oscillating S12 behaviour), one around 1 GHz and the other one around 1.6 GHz. A zoom of these regions is reported in Fig. 7.39 in the middle and the bottom plots. Both in the regions around 1 GHz and 1.66 GHz, three resonant modes can be identified. The intensity of these modes, i.e. the difference between the peak of the perturbation and the wiggling baseline, varies with the wire position making them potential transverse modes along x. These resonant modes were expected by simulations, refer to Fig.s 7.15, 7.17 and 7.18.

In Fig. 7.42 the transmission scattering parameter S12 acquired via wire measurements is reported for the TCLD prototype in configuration 1 ($h_1 = h_2 = 2$ mm). Several acquisitions for different wire positions along the x axis were performed. The top plot shows all the acquisitions for the whole explored frequency range, from 0 to 2 GHz. In these data one resonant mode around 1.25 GHz can be clearly identified. The region is magnified in Fig. 7.42 in the bottom plot. Also for this TCLD configuration, resonant modes around that region were expected by simulations, refer to Fig.s 7.8 and 7.9.

The following figures report the results of the post-processing of the raw data just presented.

Figure 7.43 reports the post processing of the scattering parameters, the meaning of each single plot is better discussed in section 5.4.2. In this subsection one is particularly interested on the bottom plot, where the longitudinal impedance of the TCLD in configuration 4 is shown for the frequency region around 1 GHz. One can see that there are three resonant modes at frequencies really close each other. In Fig. 7.44, the measured longitudinal impedance is compared with the simulated one. The agreement is reasonable, the Eigenmode solver seems to be able to find the measured mode resonating around 1.01 GHz with the right shunt impedance. Regarding the measured mode resonating at 0.98 GHz both the Eigenmode and the Wakefield individuate modes in that frequency region. However, while the Wakefield seems to find a mode with the right shunt impedance at 0.985 GHz, the Eigenmode solver overestimates of about one order of magnitude the measured shunt impedance, but it has a better agreement in frequency, 0.98 GHz. However, neither the Eigenmode nor the Wakefield solver can find the measured mode resonating at around 0.99 GHz with the correct shunt impedance.

The variation of the longitudinal impedance with the wire position was investigated to understand if the identified modes are transverse. In this case a parabolic behaviour should appear [103]. In Fig.s 7.45, 7.46 and 7.47 the peak values of the longitudinal impedance obtained at the mode frequency are reported for the three modes around 1 GHz for different wire positions. Those points have been fitted with a parabolic fit, that is also plotted in the figures, and the coefficient of the second order term of the fit is used to compute the transverse impedance (refer to section 5.4.2). In the figures, for each mode, the value of the computed tranverse impedance is reported. Also in this case, comparing the results of the measurements with the simulations (refer to Fig. 7.17) one can see that the simulations overestimate the transverse impedance. The same post processing is repeated for the three modes in the 1.6 GHz region. In Fig. 7.48 the longitudinal impedance of the three modes around 1.65 GHz is reported. In Fig.s 7.50, 7.51 and 7.52 the transverse impedance of these modes is computed.

In Fig. 7.49 a superposition of the real part of the longitudinal impedance obtained by Eigenmode and Wakefield simulations and from the measurements is displayed. In this case the magnitudes of the resonant modes estimated by the measurements and the simulated ones well agree. However, the resonant frequencies of the modes differ between simulations and measurements. For example, the mode measured at 1.657 GHz can be reasonably associated with the mode simulated at 1.662 GHz, since they have similar longitudinal shunt impedance and the simulated transverse impedance for this mode is 0.54 kΩ (refer to Fig. 7.18) that is within a factor 2 with respect to the measured transverse impedance 0.94 kΩ, refer to Fig. 7.51. The mode measured at 1.649 GHz could be associated with the mode simulated at 1.575 GHz, because of the close longitudinal impedance (measured 7.5 Ω, simulated 6.25 Ω) and the close transverse impedance (measured 0.52 kΩ, refer to Fig. 7.51, simulated 0.375 Ω, refer to Fig. 7.18). It has to be noticed that a discrepancy of about 100 MHz between simulated mode and measured one is huge, a normal value should be within the 20 MHz. This discrepancy may be explained by some oversimplification performed on the simulated CAD model.

Different is the mode measured at 1.647 GHz: this cannot be easily associated with any simulated ones.

7.2.5 Discussion

In the previous sections the results of the impedance simulations and the impedance measurements performed over the TCLD have been shown. In particular, it was shown that the simulations can reasonably predict the frequency at which the modes with the highest longitudinal and transverse impedance are. However, in some cases they overestimated both the longitudinal and transverse impedance, while in some other cases the simulated modes present a non negligible frequency shift with respect to the measured ones. One possible reason for this behaviour is linked to the complexity of the analyzed device. Indeed, the simulations report that the modes in the frequency regions of interest, around 1 GHz and around 1.65 GHz, resonate between the RF-fingers and the tank or between the RF-fingers itself, refer to Fig.s 7.21 and 7.22. These parts are extremely difficult to model since they are flexible parts and their shape and configurations can be different from the expected

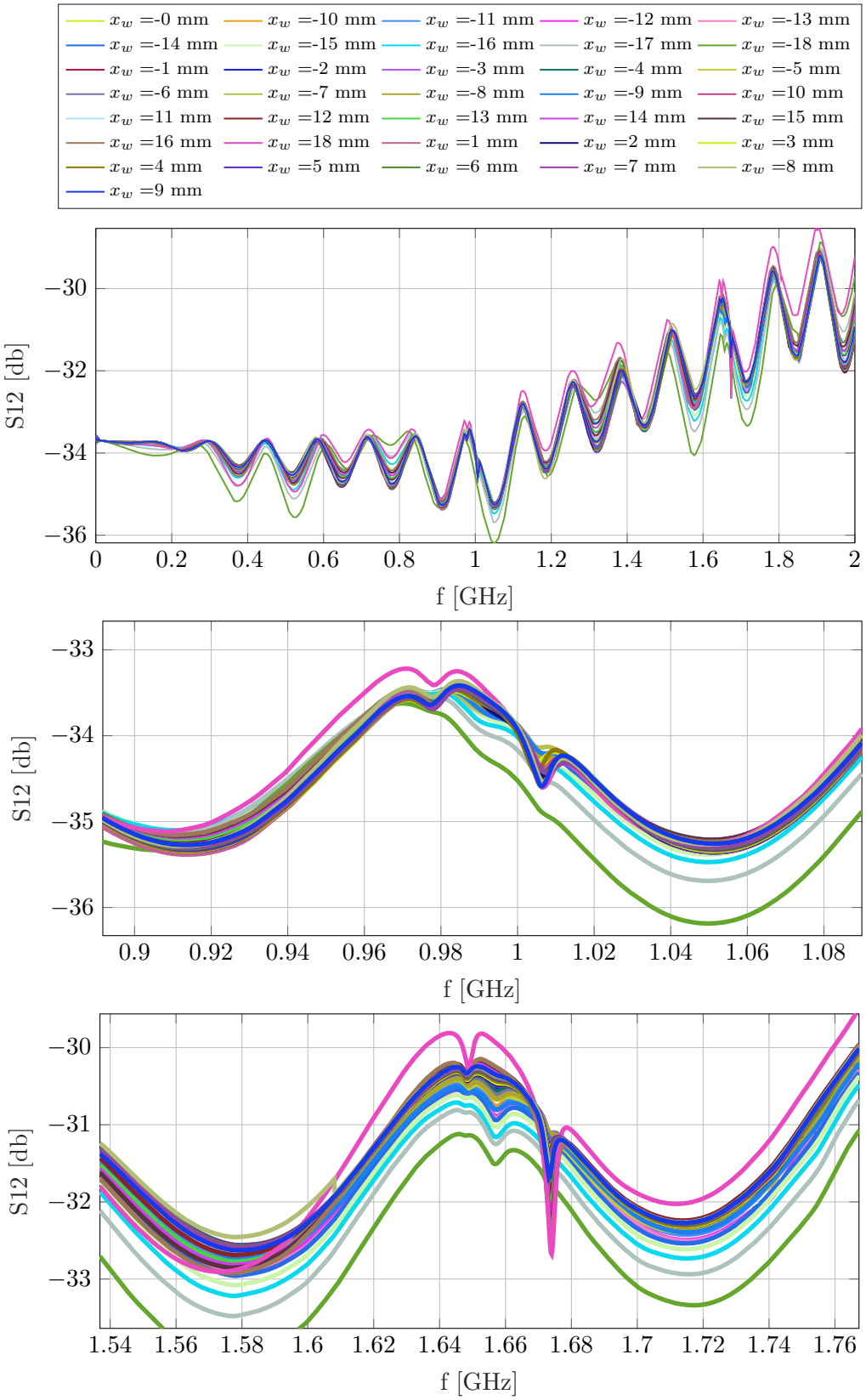

Figure 7.41. Transmission scattering parameters, with wire scanner for TCLD configuration 4, x_w is the wire position on the x axis, $x_w = 0$ mm means the wire is at the center. Top plot: entire frequency range scan, from 0 to 2 GHz. Middle and bottom plots: zoom around the areas with the strongest modes.

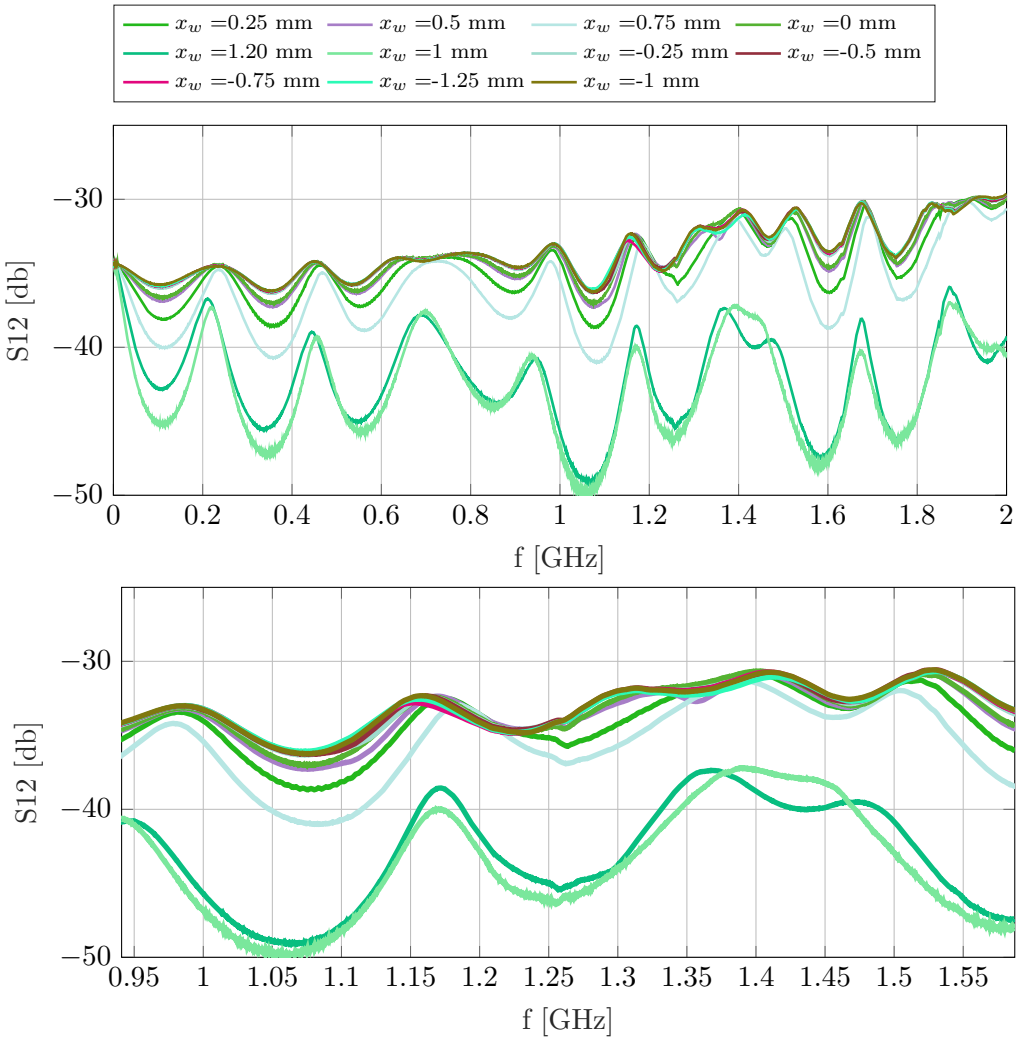

Figure 7.42. Transmission scattering parameters, with wire scanner for TCLD configuration 1, x_w is the wire position on the x axis, $x_w = 0$ mm means the wire is at the center. Top plot: entire frequency range scan, from 0 to 2 GHz. The bottom graph is a zoom around the areas with the strongest modes, 1.25 GHz in this case.

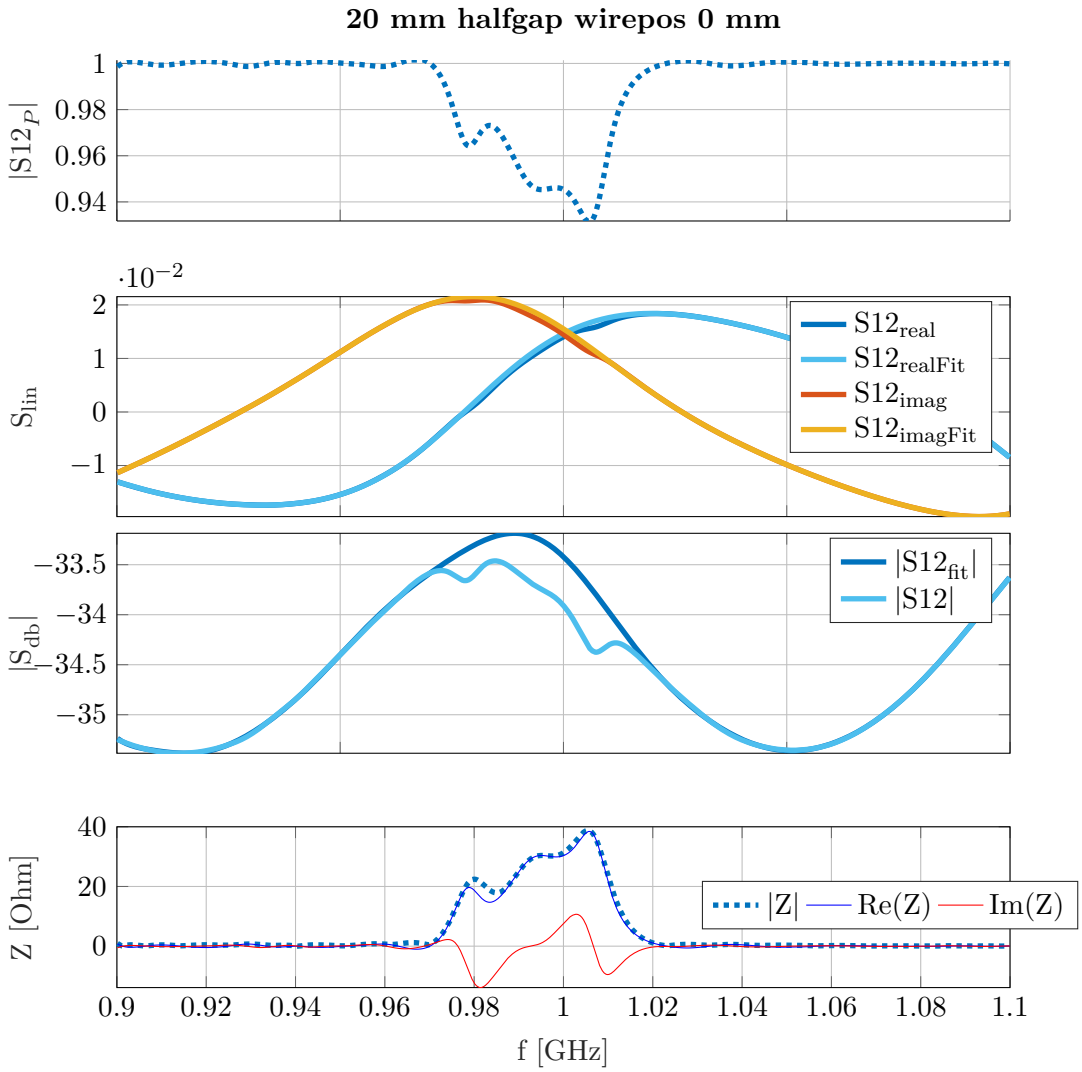

Figure 7.43. Impedance reconstruction from the transmission parameter acquired with the wire measurements for the TCLD in configuration 4. The wire was positioned at $x_w = 0$ mm, thus the reconstructed impedance is supposed to be longitudinal impedance. The significance of every subgraph was already explained in section 5.4.2.

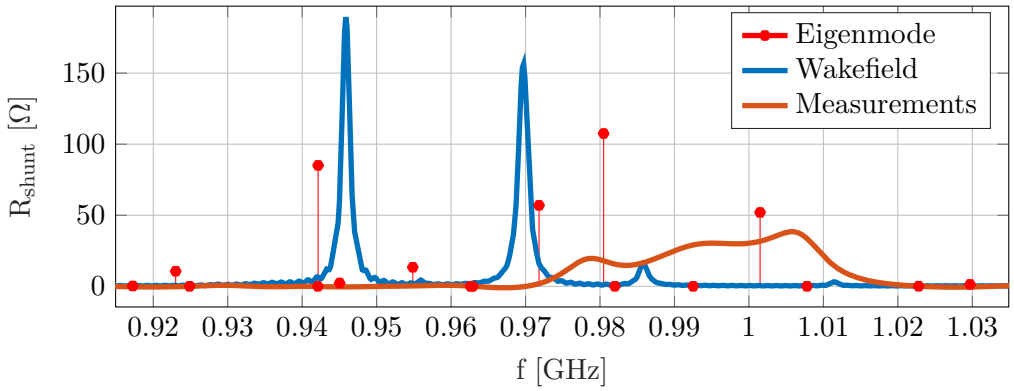

Figure 7.44. Real part of the longitudinal impedance obtained from the Eigenmode solver, the Wakefield solver and the measurements post-processing.

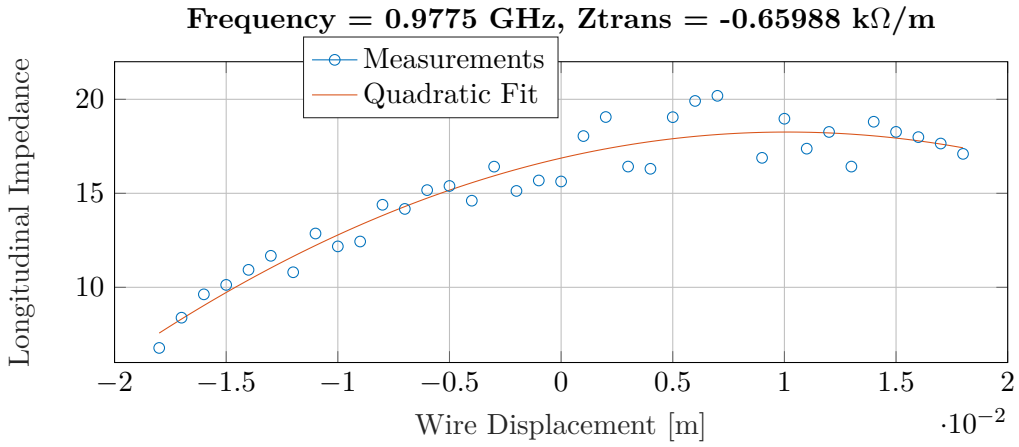

Figure 7.45. Longitudinal impedance as a function of the wire displacement along the x axis. The parabolic fit, to obtain the transverse impedance, is also shown.

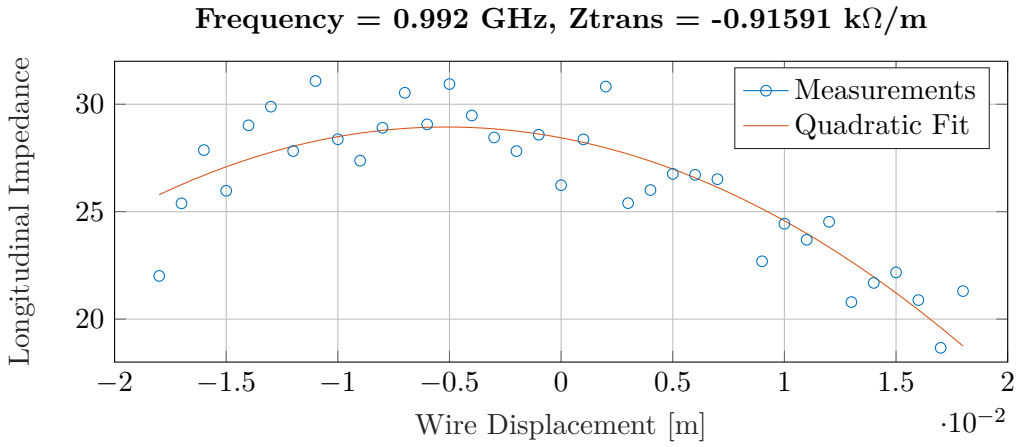

Figure 7.46. Longitudinal impedance as a function of the wire displacement along the x axis. The parabolic fit, to obtain the transverse impedance, is also shown.

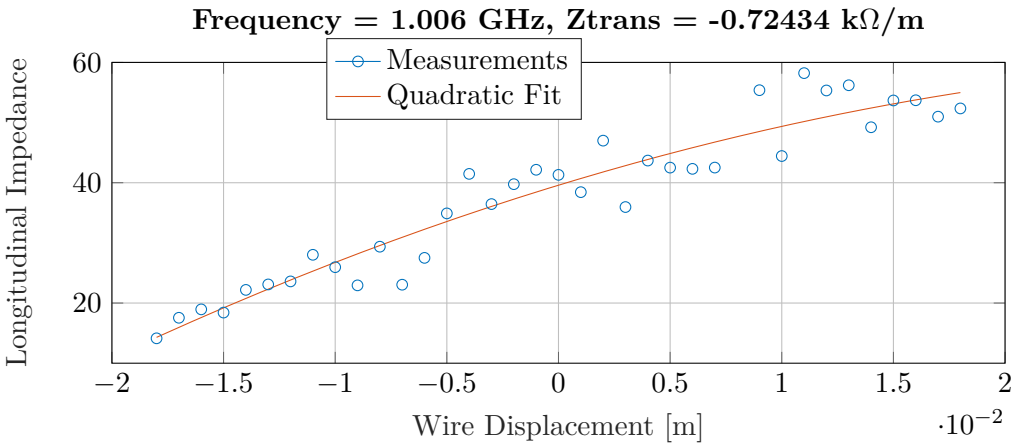

Figure 7.47. Longitudinal impedance as a function of the wire displacement along the x axis. The parabolic fit, to obtain the transverse impedance, is also shown.

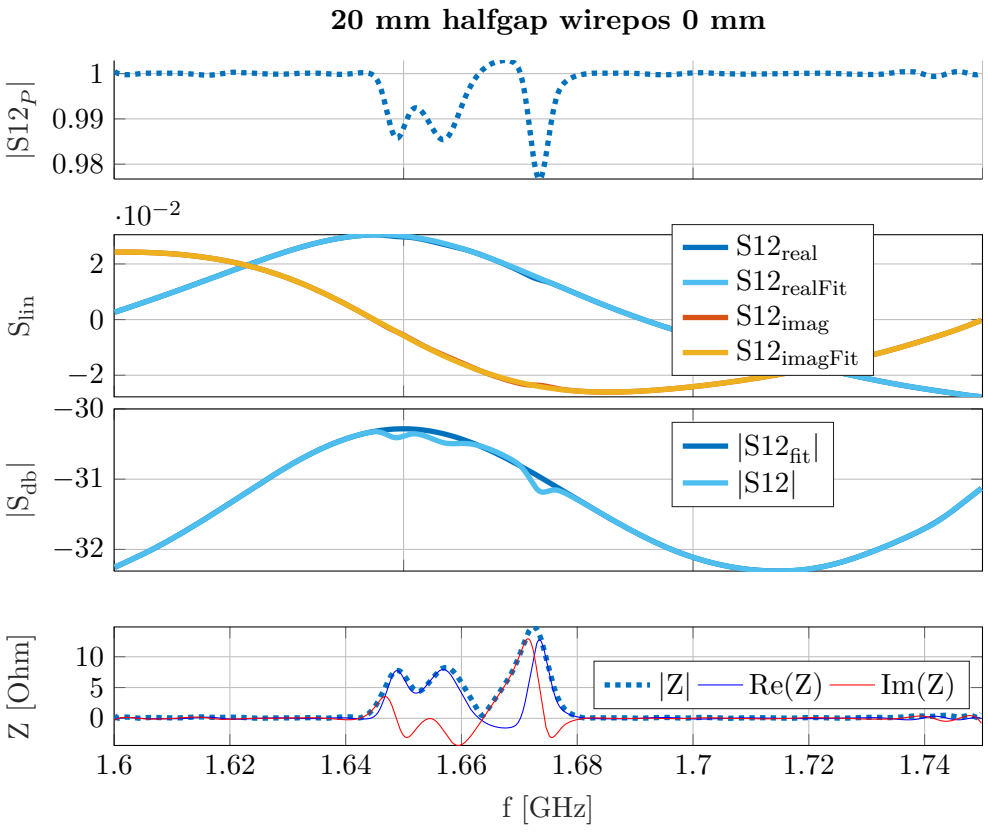

Figure 7.48. Impedance reconstruction from the transmission parameter acquired with the wire measurements for the TCLD in configuration 4. The wire was positioned at $x_w = 0$ mm, thus the reconstructed impedance is supposed to be longitudinal impedance. The significance of every subgraph was already explained in section 5.4.2.

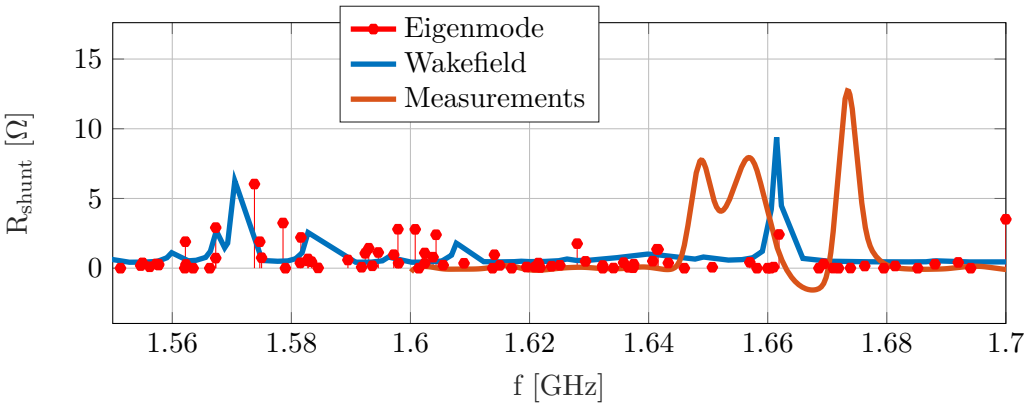

Figure 7.49. Real part of the longitudinal impedance obtained from the Eigenmode solver, the Wakefield solver and the measurements post-processing.

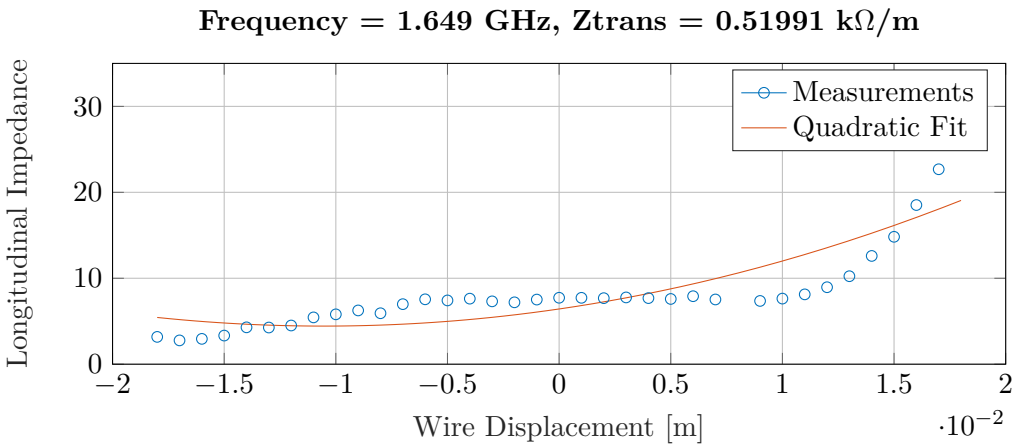

Figure 7.50. Longitudinal impedance as a function of the wire displacement along the x axis. The parabolic fit, to obtain the transverse impedance, is also shown. As can be seen, this mode seems not to be a transverse one, since the parabolic fit does not capture well the behaviour of the impedance as a function of the wire displacement.

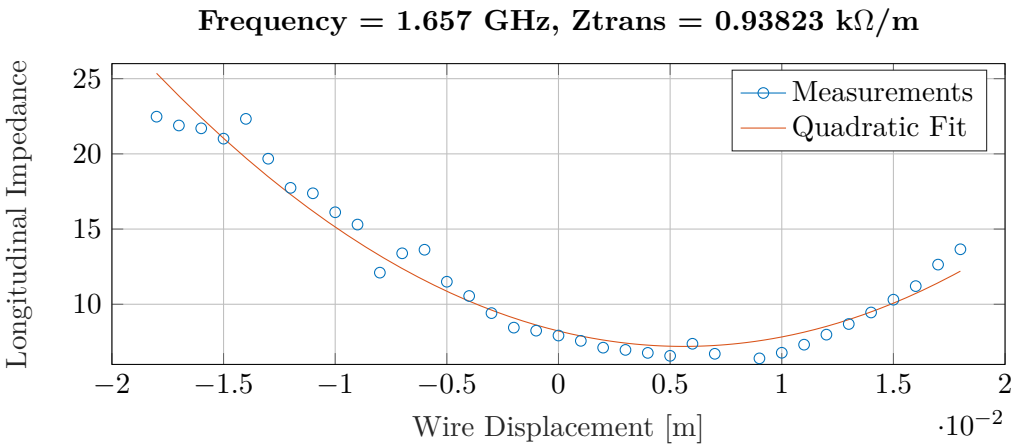

Figure 7.51. Longitudinal impedance as a function of the wire displacement along the x axis. The parabolic fit, to obtain the transverse impedance, is also shown.

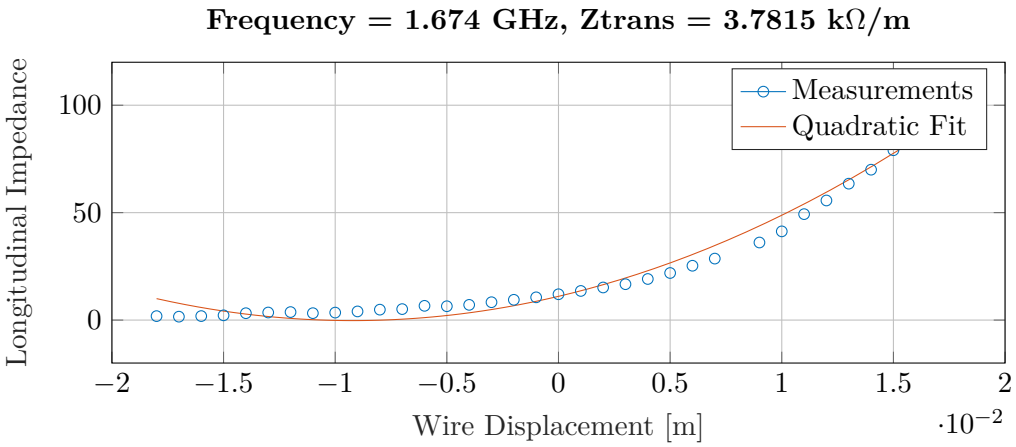

Figure 7.52. Longitudinal impedance as a function of the wire displacement along the x axis. The parabolic fit, to obtain the transverse impedance, is also shown.

ones after some cycles of aperture and closure of the jaws. Thus, this could be an explanation to the observed discrepancies. In future works a sensitivity analysis of the dependence of the device impedance on the way in which the fingers are modelled should be performed.

Furthermore, one can notice that there is agreement between the probe measurements, the wire measurements and the BPM measurements. They are all pointing out to the fact that, for the TCLD in configuration 4, there are two main frequency regions where the modes resonate in the device, around 1 GHz and around 1.66 GHz. This result was not trivial considering the fact that the different measurements were performed on two TCLD assemblies, the prototype and the pre-serie. Thus, one can also conclude that the changing in the manufacturing and assembly procedure from the prototype to the pre-series did not affect the impedance of the device.

7.2.6 Conclusions

In this subsection the TCLD was presented: first its functions, geometry and material and then the simulations and the measurements performed to assess its impedance. The simulations were able to well predict the frequency regions where the modes with the strongest longitudinal and transverse impedance were present in the device, their results reasonably match with the probe measurements, BPM measurements, and wire measurements. However, in some cases, the simulations overestimated both the longitudinal and transverse impedances, while in some other cases the simulated modes present a non negligible frequency shift with respect to the measured ones. However, neither in the measurements nor in the simulations, the impedance of the device was found able to cause beam dynamics or RF-heating issues. Thus, the device can be considered impedance compliant. This was officially stated during the 31st CERN Impedance Working Group [146].

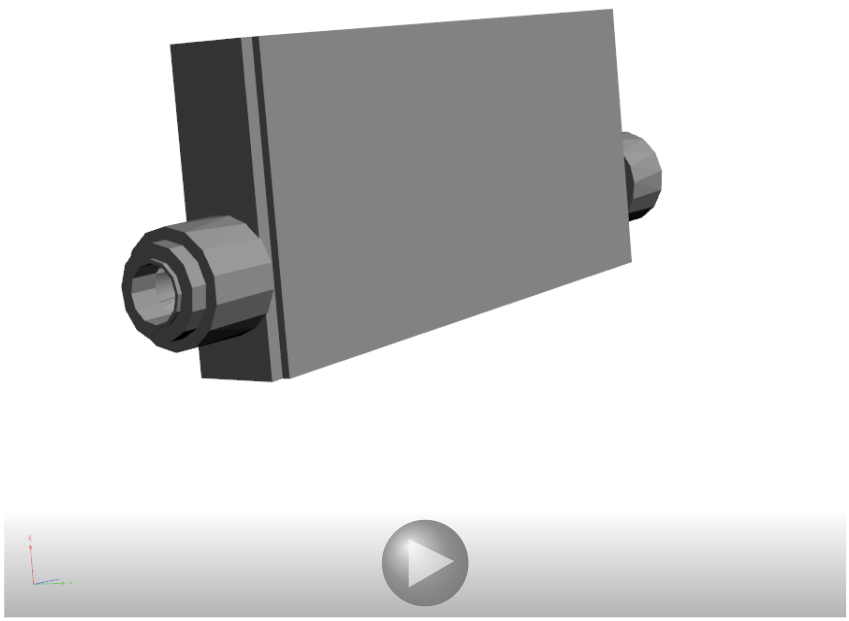

Figure 7.53. A 3D, schematic model of the final TCLD. If the figure does not appear interactive, please enable this function and click on it or use a recent version of Adobe Reader.

7.3 The New LHC injection Dump (TDIS)

The TDIS (Target Dump Injection Segmented) is a dump/absorber aimed at protecting downstream LHC equipment during the injection phase. Since the LHC stores two counter rotating beams, two SPS-to-LHC injection lines feed the machine with beams. Thus, two of these devices will be installed in the LHC ring, immediately downstream the injection kickers of the SPS-to-LHC [78] transfer lines. The device will absorb the injected beam in case of an injection kicker malfunctions [79]. Furthermore, the TDIS will be used as a dump for the proton beam during commissioning operations [79].

The TDIS has been developed as an improved version of the current injection dump, the Target Dump Injection (TDI) [78]. In 2015 and in the LHC first operational run (2009-2013), the TDI experienced severe issues, as structural damage and jaws deformations [147]. These issues are believed to be due to unexpected, excessive RF-heating [70], increased by several device non conformities. To avoid such problems, in the TDIS a new system of RF-contacts and RF-shielding (see Fig. 7.54b and 7.54c) will be implemented. These systems are tought to decrease the RF-heating load of the high intensity/brightness HL-LHC beams [148].

The geometry of the TDIS is presented in Fig. 7.54 and described in detail in the work of Carbajo et al. [78]. The core of the TDIS are two vertically movable jaws (upper and lower jaw with a length of about 4.5 m), divided into three segments (about 1.5 m each), each of them composed of absorbing blocks of different materials. The three segments of a jaw are separated by gaps of 15 mm (see Fig. 7.54a and 7.54c). This arrangement limits jaw bending and deformation allowing unconstrained thermal expansion at the gaps. This makes the TDIS design mechanically more robust if compared with the TDI (made only with one long jaw and so more subjected to bending).

In the TDIS (and in the TDI) there are two counter-rotating beams circulating at all time: the injected beam, that is passing between the jaws, and the circulating one, traversing the device in the RF-screen [149, 150], Fig. 7.54b. During the injection phase the jaws have a half-gap of 4 mm with respect to the injected beam reference orbit, refer to Fig. 7.54b. If the orbit of the injected beam differs more than the allowed tolerance from the expected one, the beam will impact against the jaws so it is dumped. After the injection phase the TDIS jaws are completely open (half-gap 55 mm) [79].

As anticipated, this section reports two different analysis. First, the thermo-mechanical effects of a beam impact on one of the TDIS jaw is investigated, this case corresponds to a triggered beam dump or to an accidental magnet misfiring scenario. In this context, there is only NMI related heating. The section shows that the TDIS can withstand the impact of the injected beam.

Subsequently, the device impedance characterization is discussed. In particular, the impedance of the TDIS with and without RF-contacts is compared. The case of TDIS without RF-contacts simulates a failure scenario in which all the RF-contacts detach and the image current path is interrupted. The results show that the TDIS with the RF-contacts has better impedance performances with respect to the TDIS without RF-contacts. The RF-contacts failure scenario is further investigated computing the impedance induced heating and simulating its

related thermo-mechanical effects. It is shown that the TDIS could withstand the temperature and the mechanical stresses that develop in this failure scenario without any other major failure.

The impedance of the device in the scenario with and without the RF-contacts and the related impedance induced heating was characterized considering only one beam, the injected one, passing into the device and not two counter rotating ones. At the moment of the analysis the theory to take into account the two beams RF-heating (refer to chapter 3) was not elaborated. This case was indeed the one that triggered its development.

7.3.1 The Accidental Beam Impact Scenario

The TDIS will cope with different failure scenarios of the SPS-to-LHC injection magnets [79] that can arise during the injection phase until the LHC ring is completely filled. In such failure cases, the proton beam is misdirected resulting in a wrong insertion trajectory and an impact against the absorbing blocks of the TDIS jaws [151, 149]. Two main types of accidents could occur during the lifespan of the device [79]. They are defined by the impact parameter b (Fig. 7.54b), that is the distance between the beam impact position and the jaw free surface, (Fig. 7.54c).

- Grazing (small impact parameter, $0 \leq b \leq \sigma_y$, where σ_y is the transverse root mean square beam dimension on the y axis of Fig. 7.54c): the proton beam impacts the graphite block at a small depth (compared to the beam core dimension) with respect to the jaw free surface. Most of the energy is deposited on the material surface.
- Central impact (large impact parameter, $b >> \sigma_y$): the proton beam impacts the front end of the graphite block. Most of the energy is deposited in the material bulk.

Furthermore, in both cases only one jaw, either the upper or lower one is expected to receive the beam impact. Thus, the thermo-mechanical response of only one jaw has been investigated. The jaw model is shown in Fig. 7.54b. The beam-matter interaction was simulated using the FLUKA Monte Carlo code [125, 126]. Subsequently, the 3D dissipated energy density map, obtained from FLUKA, was imported as a thermal load into the software ANSYS® [73], to analyze the thermo-mechanical behavior of the device.

Both in the grazing impact scenario and in the central impact one the first jaw segment experiences the highest temperatures. The thermal analysis revealed that a grazing impact may lead to a rise of the absorbing blocks temperature up to 1392°C in the first impacted graphite block (see Fig. 7.55) whilst the other jaw components experience a negligible increase in temperature. This is due to the fact that most of the energy is deposited in the first impacted graphite block, on its jaw free surface, far from other components. A temperature of 1392°C is not critical for the graphite, as it can tolerate up to 2800°C [152] without deteriorating its mechanical properties. The maximum mechanical stresses induced by the thermal gradients are also localized in the first impacted graphite block. Since graphite is a brittle material, the Christensen criterion [127] was used to assess its mechanical resistance. The local Christensen coefficient (this is an adimensional quantity) is

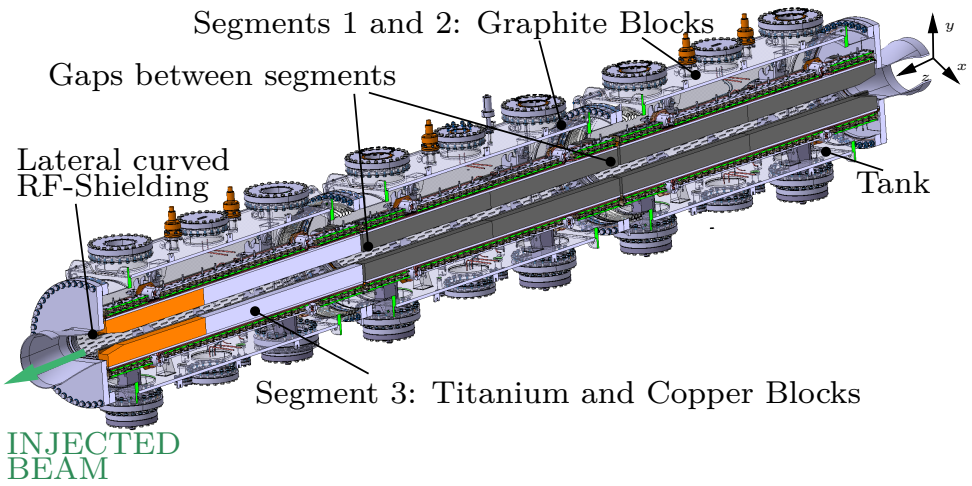

(a)

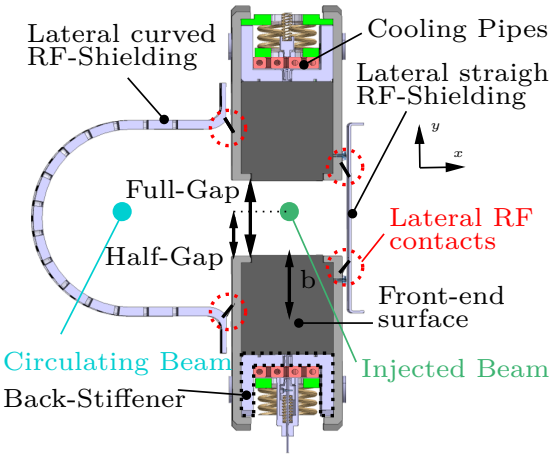

(b)

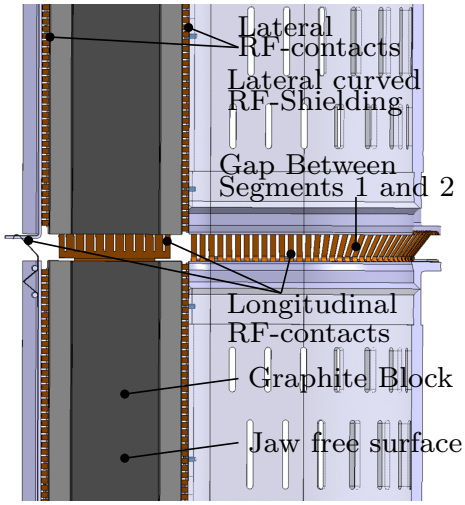

(c)

Figure 7.54. (a) Complete TDIS design Geometry. (b) Section view in x-y plane. The main components are labeled. (c) Section view in x-z plane. The main components are labeled.

shown for the graphite block in Fig. 7.56. The fact that this coefficient remains locally below 1 guarantees the mechanical robustness of the block.

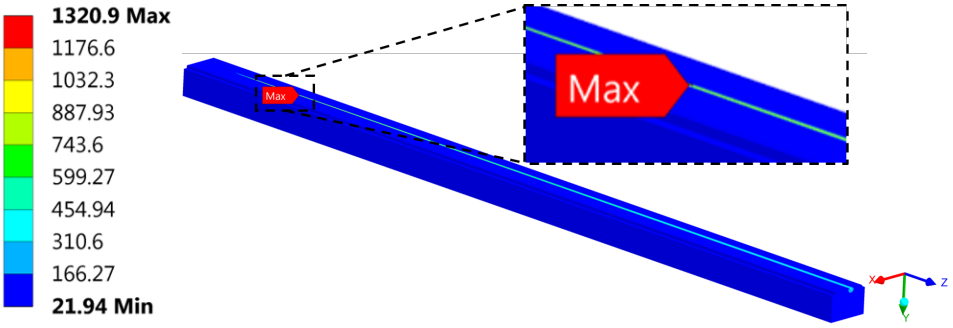

Figure 7.55. Surface temperature [°C] of the graphite block due to grazing impact. The high temperature is extremely localized on a longitudinal line in the jaw free surface. The beam is impacting the jaw moving along the positive z direction.

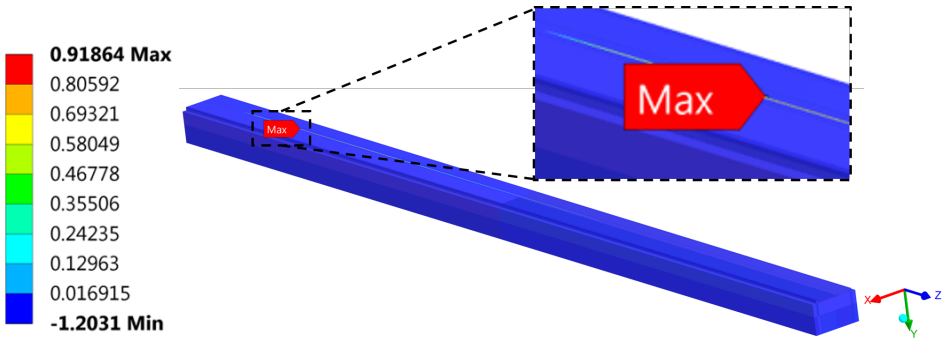

Figure 7.56. Christensen coefficient [adimensional unit] on the graphite block due to grazing impact. A value superior or equal to 1 implies material failure. However, 0.91 is acceptable because of the conservative assumption of considering the static yield stress at room temperature as maximum tensile limits. Indeed, the static yield stress for the graphite increases with temperature within a temperature range up to, approximately, 2500 °C [153]. Like the high temperature, the stresses are also extremely localized on a longitudinal line in the free jaw surface.

Regarding the central impact scenario, the thermal analysis has shown that the most dangerous thermal gradient develops in the molybdenum alloy (TZM) back-stiffener, which reaches a peak temperature of 215°C (see Fig. 7.54b and 7.57), and in the oxygen-free copper cooling pipes (see Fig. 7.54b), which reaches a peak temperature of 92°C. Mechanical analyses have revealed significant stresses in these two key components. They have shown that the pipes are likely to undergo some minor plastic deformation as a consequence of the thermal gradients caused by the particle shower energy deposition. However, this is not expected to be detrimental for the device function, given the high ductility of the material. For the back-stiffener, the Finite Element Analysis (FEA) shows that, in the event of a central impact, it will be subjected to mechanical stresses of 340 MPa. This stress value is below the elastic limit of the TMZ for that temperature which is 455 MPa [153] (resulting in a safety margin of 1.33). It must be noted that this is a conservative approach.

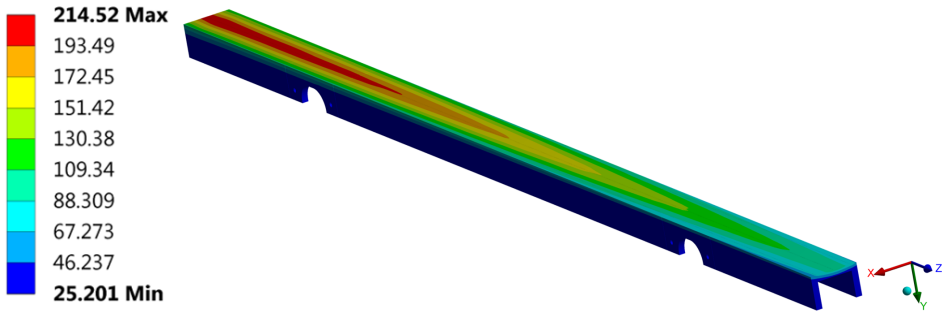

Figure 7.57. Surface temperature [°C] of the back stiffener due to the particle shower after the central impact.

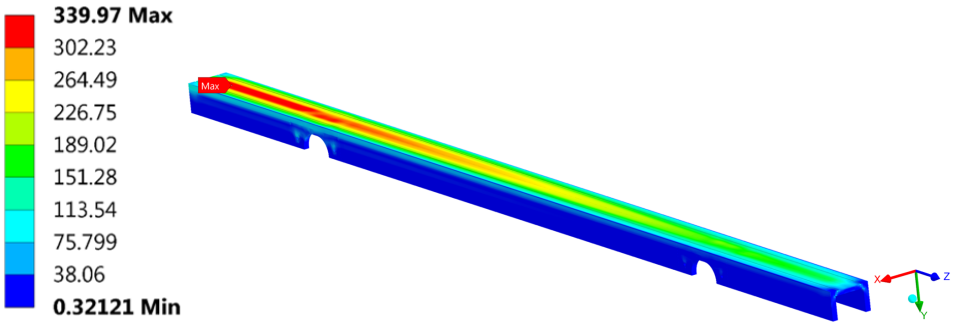

Figure 7.58. Surface Stresses [MPa] of the back stiffener due to the thermal gradient.

Indeed, the energy deposition due to the beam impact is very localized in space and takes place in an extremely short time scale (strain rate[2] $1.6 \cdot 10^2$ [s^{-1}]). Thus, a dynamic behavior for the TZM must be considered, i.e. elastic waves are generated in the material because of the sudden sharp temperature increase and the induced localized material expansion immediately after the beam impact [22]. In this case, the maximum stress obtained by the simulation must be compared with the dynamic yield strength for TZM, which is significantly larger than the static one [154]. Thus, if the static yeld stress of the TMZ is well above the maximum mechanical stress developed by the thermal gradient, the TDIS is expected to be able to withstand the HL-LHC beam impact without failures.

7.3.2 Device Impedance Characterization and RF-heating Thermo-mechanical Effects

Subsequently to the beam impact analysis, the case in which the injected beam traverses the device in between the two jaws was explored.

First, the TDIS was characterized from an impedance perspective. Subsequently, the TDIS thermo-mechanical response to a worst case scenario was investigated. The impedance of the TDIS was studied for two device configurations, TDIS with and without RF-contacts. The first configuration represents the normal working

[2]The strain rate is the speed at which a given strain develops, the higher the strain rate the faster the component deformation.

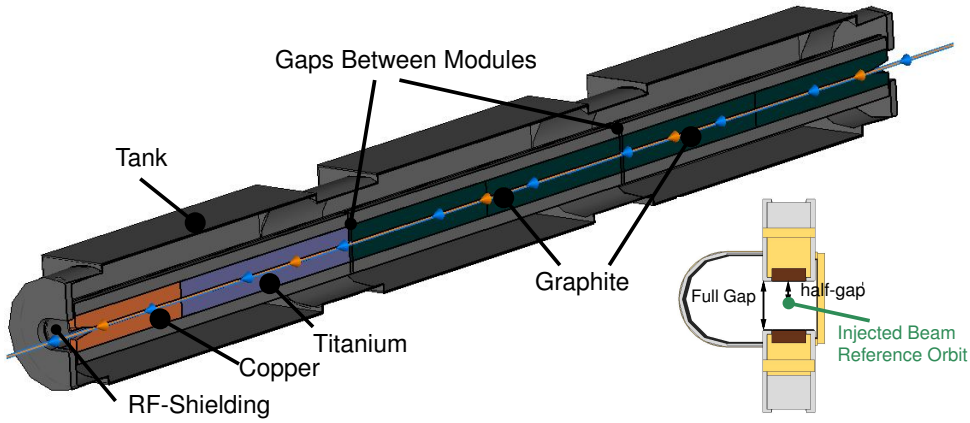

Figure 7.59. TDIS Model in CST.

condition for the TDIS, the second configuration represents a RF-contacts failure scenario, where all the RF-contacts detach and the image currents do not have a defined path anymore. As expected, the impedance perfomance of the device was found to be worse in the RF-contacts failure scenario. Furthemore, excluding an impact due to beam dumping, the main sources of heat loads for the TDIS are: direct beam load due to the scraping of secondary halo, and impedance heating. The latter can be further divided into resistive wall heating and resonant modes (RMs) RF-heating. The load of the three sources is at a maximum during the injection phase, when the jaws of the TDIS are at their minimum half-gap, 4 mm, and in the pessimistic assumption of a failure of the longitudinal RF-contacts between the jaws modules gaps. Indeed, the power deposited by the beam halos and by resistive wall effects decreases by increasing the beam-jaw distance, and the next section will prove that in the 4 mm half-gap configuration the RM heat load is also maximum.

Thus, the simulated worst case scenario, the one with the highest heat load, was that of an RF-contacts failure at the beam injection, i.e. with minimum jaw half-gap of 4 mm.

Note that since the TDIS functional specifications were preliminary when this analysis was performed, a value of 5 mm for the minimum half-gap was used instead of the current accepted value of 4 mm [79]. This have to be kept in mind in the results analysis, especially for transverse RW impedance. However, given the small difference between the values and the fact that only longitudinal impedance and RF-heating are considered in the analysis that are presented following the section, the conclusions of this study remain valid.

7.3.3 Electromagnetic Simulations

In order to evaluate the TDIS longitudinal coupling impedance and its heating effects, electromagnetic simulations were performed. The geometrical model for CST simulations (Fig. 7.59), was obtained carefully simplifying the complex mechanical TDIS drawing, preserving only the features deemed important for the electromagnetic computations, so reducing simulation time.

The TDIS was analyzed with different RF-contacts configurations and for different half-gap apertures[3]. In Fig. 7.60 the impedance of the TDIS obtained by CST wakefield [60] simulations for 5 mm half-gap is reported for the cases with and without longitudinal RF-contacts with the HL-LHC beam spectrum. For the scenario with

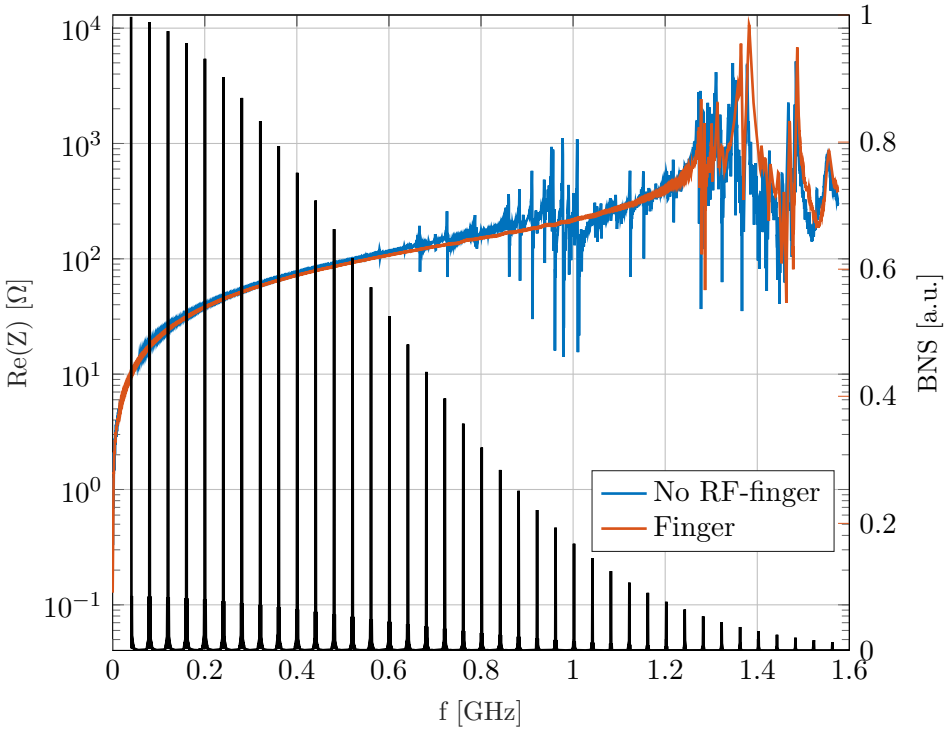

Figure 7.60. Beam normalized spectrum (BNS) in black, linear scale, and real part of the longitudinal impedance in log scale, with 5 mm half-gap.

contacts, there are no trapped resonant modes inside the structure below 1.25 GHz. Indeed, the electric contacts prevent trapped modes below the cutoff frequency of the LHC pipe. In the scenario without RF-contacts, several trapped modes are present below 1.25 GHz. There is a clear contribution to the longitudinal impedance in the beam spectrum frequency range. The impact of the absence of longitudinal contacts was then further investigated: the shunt impedance of every trapped mode obtained by the CST eigenmode solver [60] was compared with the results of the wakefield solver, Fig. 7.61. The agreement between the two different methods is good for the resonant frequencies, however, it is rough with respect to the shunt impedances.

Following the conservative approach, to compute the RM heating power, the eigenmode results in the scenario without RF-contacts were used. The power was numerically computed for the HL-LHC beam considering Eq. 3.25. Furthermore, a sensitivity analysis of the impedance induced power was performed. For each considered jaw aperture an impedance curve was estimated. The impedance peaks (i.e the resonant modes) were individually moved from their original frequencies within a range of ±10 MHz to obtain the maximum coupling with the HL-LHC beam

[3] An extensive study on the topic can be found in the work of Mazzacano [155]

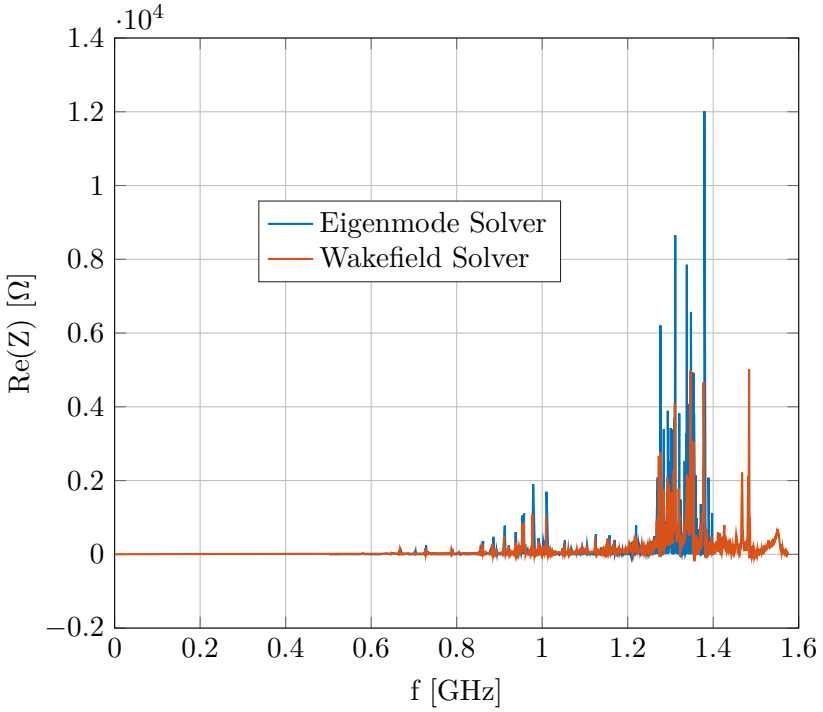

Figure 7.61. Real part of the TDIS longitudinal impedance, with 5 mm half-gap.

spectrum, i.e. the maximum power loss. Figure 7.62 shows the RM RF-heating spectrum for different TDIS half-gap configurations. Despite the similar appearance, the 5 mm half-gap configuration is the most critical with a total deposited power on the device of 1003 W (704 W for the 25 mm half-gap case). Analyses of the resistive wall impedance heat load have demonstrated that, as expected, the worst case scenario is at 5 mm half-gap with a total dissipation of 798.3 W in addition to the RM load.

7.3.4 Thermo-mechanical Simulations For the RF-contacts Failure Scenario

Following what was exposed in chapter 4, the thermo-mechanical simulations on the TDIS were carried out in ANSYS. The main goal was to verify that in the worst case scenario the TDIS local mechanical stresses were at least 20% lower than the yield stress (for ductile materials) or the ultimate strength (for brittle materials) and that the graphite blocks temperature remained below 50 °C, in order to avoid outgassing issues [156].

The heat loads considered are listed in Table 7.6. They occur for the duration of the injection phase (around 30 minutes) simultaneously. Other heat loads are negligible, e.g. heating effect due to e-cloud phenomena at a jaws half-gap of 5 mm [157], or not associated with the injection phase.

For the RM RF-heating, the 3D map obtained following chapter 4 was used. In the thermo-mechanical simulations the same geometrical model of the electromagnetic simulations was used with only slight modifications. In particular, the RF-contacts

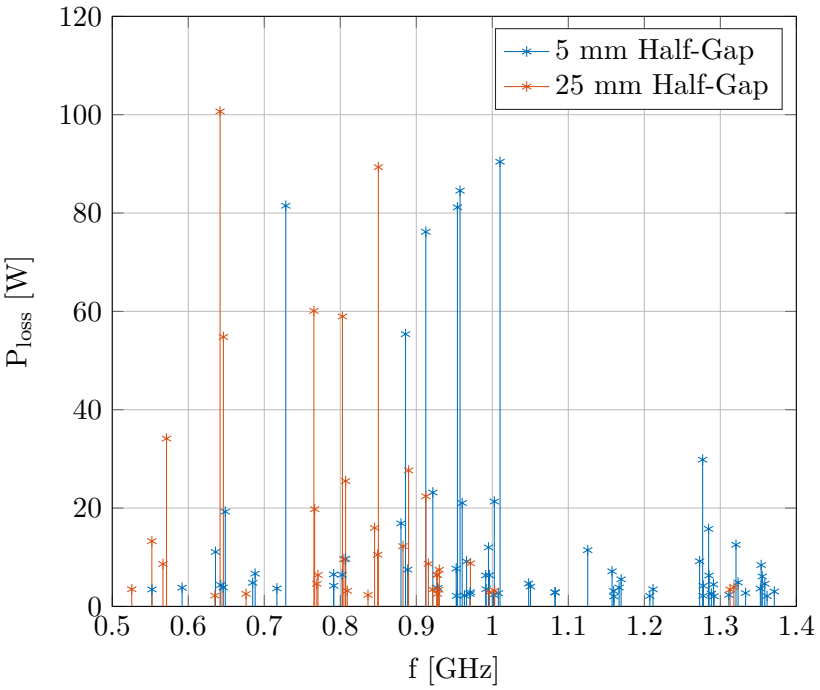

Figure 7.62. Power losses due to trapped resonant modes in the TDIS .

Table 7.6. Applied Heat loads

Source	Heat load [W]	Affected Element
Secondary halos	580 [79]	Jaws free surface
Resistive Wall	798.3	Jaws free surface
RF-heating	1003.6	Entire TDIS

were reintroduced in order to have a realistic representation of the contact failure case, i.e. the contacts are present in the device but they lose the physical contact with device parts on their non fixed side. Both secondary halo and resistive wall impedance heating was applied as a constant heat flux on the jaws free surfaces facing the beam, refer to Fig. 7.54c. The former was considered as evenly spread on the jaw free surfaces while the latter was applied according to the resistivity of the material (i.e. 75% of the load on the jaw graphite free surfaces and 25% on the jaw titanium-copper free surfaces). The considered heat dissipation systems were: conduction, radiation, on all the free surfaces, and convection, only on the external surfaces of the tank. Furthermore, the TDIS cooling apparatus, a system of identical pipes for each jaw in which 0.135 m^3/s of water at 27 °C flows, was also simulated. The global temperature map is plotted in Fig. 7.63. In this figure the component with the highest temperature has been removed to optimize the scale for readability. It is important to note that, the graphite remains below the 50 °C threshold for vacuum acceptance.

The peak temperature at the end of the injection stage is observed on the lateral straight RF-shielding (Fig. 7.54b) on the longitudinal RF-contacts between the

two graphite modules. It is reported in Fig. 7.64. Regarding mechanical stresses, the maximum value is localized on the same component on which the maximum temperature develops some centimeters downstream: at the connections of the lateral straight RF-shielding with the tank, Fig. 7.65. This is due to the fact that the maximum temperature is on a gap. At this point the material is unconstrained and free to expand; whereas, the connection points between the tank and the straight shielding fully constraint rotational and translational degrees of freedom. This limits deformations and increases stresses on the lateral straight RF-shielding. However, the maximum Von Mises stress value in the TDIS, 85 MPa is well below the yield strength of the lateral RF-shielding material, stainless steel 314L, of 250 MPa. Thus, the study concluded that also in the RF-contacts failure scenario there is no risk of any other major failure in the TDIS.

7.3.5 Conclusions

This section reviewed the electromagnetic and thermo-mechanical analysis performed to assess the quality of the new Target Dump Injection Segmented.

In this section, the impedance of the TDIS was characterized. The design was found robust from an impedance perspective given the absence of trapped RM in the structure for frequencies up to 1.25 GHz.

Furthermore, two critical scenarios were discussed: an accidental case of beam impact on the device and another accidental case of complete longitudinal RF-contacts failure during the beam injection. The TDIS was found able to cope with the former scenario. Regarding the latter one, despite the fact that our findings have highlighted some possible critical areas at the segment gaps, neither the developed temperatures or the related mechanical stresses seem to be high enough to cause problems, demonstrating the high quality of the design. Future studies should repeat the analysis done here taking into consideration the two counter rotating beams traversing the device. It was not possible to do so in this work since the two counter rotating beams formalism (chapter 2) was still not elaborated at the time of this analysis. Further, future studies should also consider the actual gap of 4 mm in between the jaws.

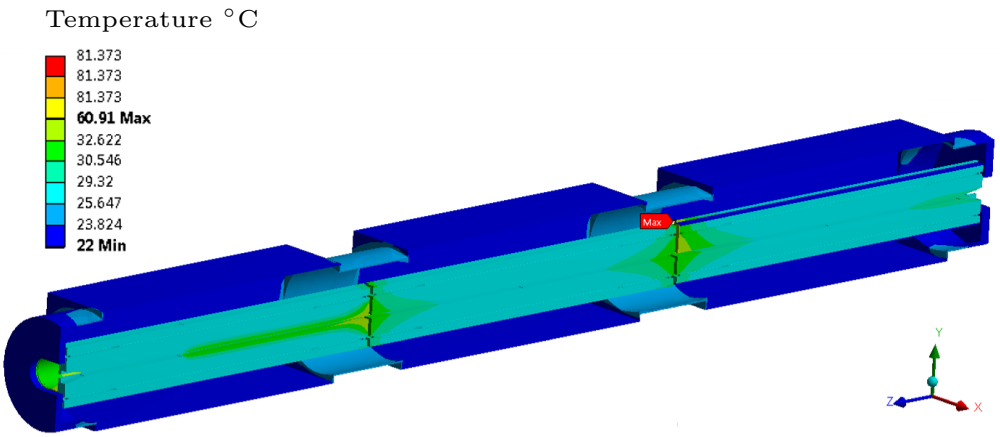

Figure 7.63. Global temperature distribution.

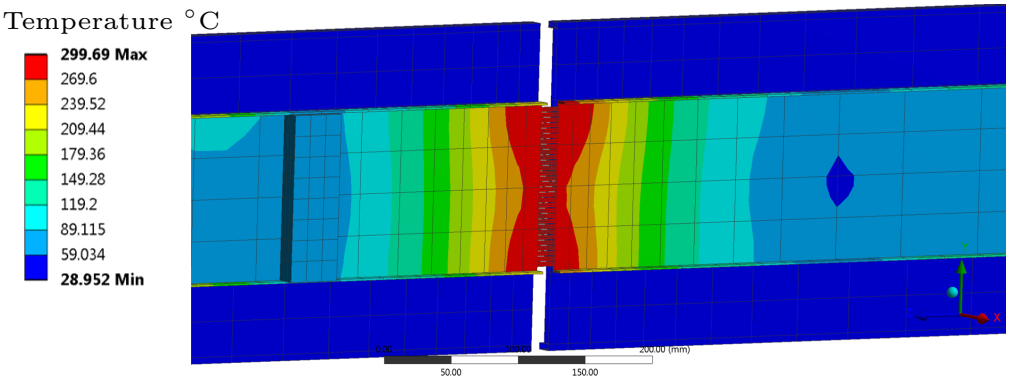

Figure 7.64. Detail of the hottest region in the TDIS: the lateral straight RF-shielding. The maximum temperature is reached in the gap between the graphite modules, on the RF-contacts.

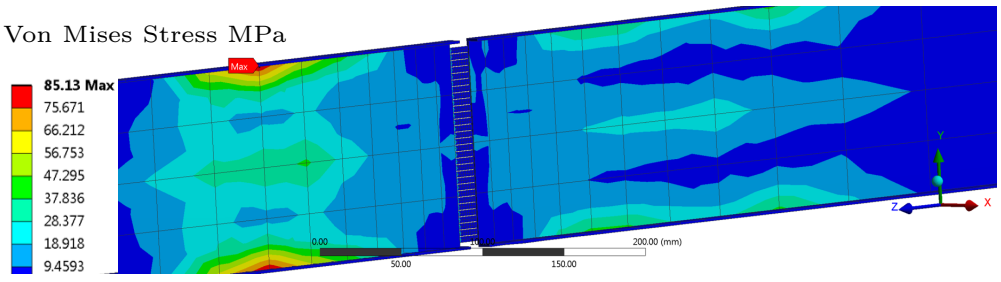

Figure 7.65. Stresses distribution maximum. Lateral straight RF-shielding, gap between the graphite modules.

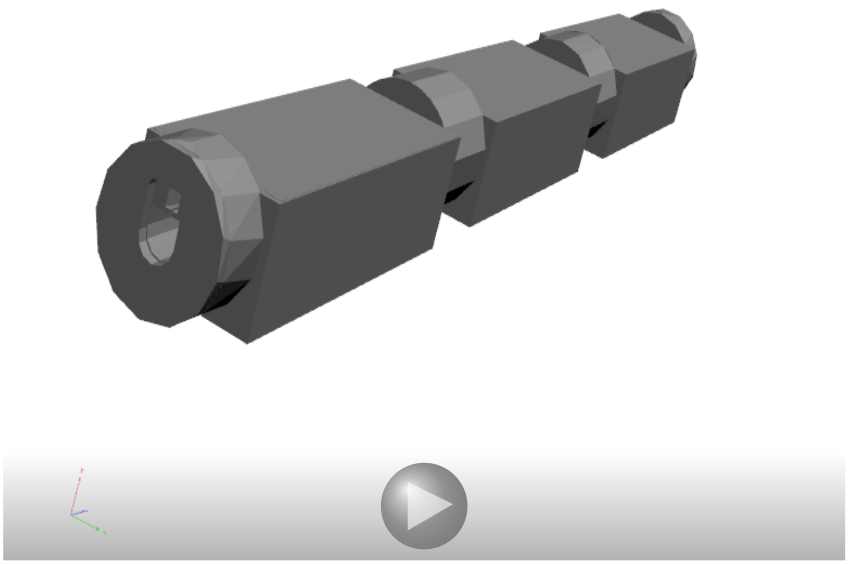

Figure 7.66. A 3D, schematic model of the final TDIS. If the figure does not appear interactive, please enable this function and click on it or use a recent version of Adobe Reader.

7.4 Conclusions

This chapter reviewed the electromagnetic and thermo-mechanical analysis performed to assess the quality of two HL-LHC devices, The TCLD and the TDIS.

The impedance of both was characterized by simulations and it was assessed it was not an issue neither for beam instabilities nor for RF-heating.

The TCLD simulations were bench-marked with wire, probe, and BPM measurements. Despite some small discrepancies in resonant frequencies and shunt impedances, there is reasonable agreement between measurements and simulations. The agreement among the different measurements types, performed on the TCLD prototype and on the TCLD pre-serie, allows to assess that the manufacturing and assembly procedure did not impact the impedance of the device with respect to the design.

The TDIS design was found robust from an impedance perspective given the absence of trapped RM in the structure for frequencies up to 1.25 GHz. Furthemore, the TDIS was found able to cope with two different failure scenarios, beam impact on one of the jaw and RF-contacts detaching at the beam injection. Future studies should repeat the analysis taking into consideration the two counter rotating beams traversing the device.

Chapter 8

Conclusions and Future Work

This thesis has discussed about design problems and solutions for beam intercepting devices, with special focus on impedance minimization.

As a first step, in chapter 1, the justification for building new beam intercepting devices for the CERN particle accelerators was given. It was discussed that, in order to produce more results for physics, the CERN accelerator complex needs an upgrade to increase the instantaneous luminosity. This can be achieved increasing beam intensity and beam brightness, and, as a direct consequence, also the beam stored energy. Two main projects were launched to reach the high luminosity goal: HL-LHC and LIU. It was shown that, in the framework of these two projects, several beam intercepting devices had to be redesigned and rebuilt since they will not be able to perform their tasks with the new more intense and more energetic beam. Further, since BIDs are among the machine components with the highest impedance and since high impedance components may lead to beams instabilities and RF-heating, in the redesign of the BIDs impedance minimization was a key aspect.

Subsequently, in chapter 2 the wakefield theory was reviewed and also original contributions were discussed. The chapter has reviewed the wakefield concept in general. It has distinguished between co-moving and counter-moving wakefield and it has reported the already well known co-moving wakefield theory, introducing longitudinal and transverse wakefunction, wakepotential, beam dissipated energy and beam induced heating. Original contributions for the counter-moving wakefield have been presented. In particular a definition of counter-moving wakefunction has been given as well as a formalism to compute the counter-moving wakepotential and the related beam induced heating. Some examples of counter-moving wakefunction and wakepotential have been discussed: the wakepotential computed by the PIC and the Wakefield solver of the commercial CST software has been benchmarked against the wakepotential obtained semi-analytically with very good agreement. This has assessed the capacity of the CST software to simulate the counter-rotating problem and it is a good indication that the proposed analytical definition of counter-moving wakefunction works. Furthermore, the problem of the beam induced heating of two counter-rotating beams traversing the same vacuum chamber has been extensively addressed. The formalism exposed in this work was able to explain the results obtained by simulations and to reobtain results of previous studies. It was possible to compute the RF-heating power of a vacuum chamber as a function of the delay

between the counter-rotating beams entrance. This is a critical point to obtain the worst case scenario that a device could experience, and, according to it, to design the device cooling system.

Also chapter 3 was both a background and a results chapter. The definition of longitudinal and transverse impedance was introduced and the energy and power dissipated in a device by one or two counter-rotating beams was expressed as a function of impedance in the frequency domain. As original contribution, the chapter presented the derivation of a formula to identify the entrance delay between two beams into a vacuum chamber that maximizes or minimizes the dissipated power and energy transferred from the beam into the vacuum chamber. It was shown that these entrance delays are frequency dependent. The example of one mode in a pill-box cavity was discussed. In that case the derived equations were able to predict the entrance delays between two beams that lead to the maximum or minimum value of dissipated power in the device. This tool, if the time entrance delay between the beams is fixed, can be used to easily detect modes in the device that could be intensified constructively because of the passage of the two beams, allowing to take the due modifications on the design. In the appendix it was also shown how to compute the beam entrance delay in an accelerator given the position of the device to analyze.

Chapter 4, as result chapter, illustrated an accurate multi-physics approach to simulate the local RF-heating mechanical and thermal effects on accelerator devices. It explained the work flow of the method and showed examples of its use. Furthermore, the proposed method was successfully benchmarked against temperature experimental data taken during the LHC fill 4381 on the cylindrical TOTEM Roman Pot. The thermal transient and steady state simulations well reproduced the temperature evolution of the roman pot during the LHC run. The results were found robust against variation of cooling parameters such as surface emissivities, convection coefficients or contact properties. The method could identify critical points in the design of the Roman Pot. To summarize, the proposed method revealed itself capable to simulate the local thermal effects induced by impedance on a device and it was used to understand the possible design improvements. This method could be a key approach to deal with RF-heating design problems of future high intensity, low emittance particle accelerators.

Chapter 5 was a background chapter. Some basic concepts of RF engineering were introduced; the resonant mode quality factor, shunt impedance and resonant frequency, distinguishing them between loaded and unloaded. Subsequently, the CERN impedance measurement equipment was presented, followed by some of the techniques used in this work to measure device impedance, i.e. probe measurements, wire measurements and BPM measurements. For each one of them the data acquisition and post-processing were discussed as well as the limitations.

Chapter 6 was a result chapter. The most common high impedance geometric features usually present in a preliminary device design were analyzed and simple and cost-effective way of modifying geometries and/or materials to obtain low impedance designs were proposed. These low impedance design guidelines can be summarized in five main points:

- Guarantee the electrical continuity of the device in the beam propagation

direction, i.e. avoid gaps between parts of the same components.

- Minimize the empty volumes in the equipment and, when necessary, shield them with RF-shielding. This avoids the empty volumes to start resonating as parasitic resonant cavities. In eliminating empty volumes, keep in mind that the distance of the material with respect to the beam has to be the highest possible, this reduces the resistive wall impedance.

- Minimize change of section in the equipment and, when possible, guarantee smooth transition between the different sections.

- Use materials with high conductivity wherever possible and check if they could generate electron cloud issues.

- Ferromagnetic materials could be used to damp electromagnetic resonant modes. However, they should be in the resonant mode field but as far as possible from the beam orbit.

These guidelines were applied to improve the impedance performance of complex devices: the Proton Synchrotron Booster Absorber Scraper, the Proton Synchrotron internal dump and the Proton Synchrotron Ralentisseur. For the Proton Synchrotron Booster Absorber Scraper, a striking impedance reduction of almost three orders of magnitude between the preliminary and the final design was obtained. The impedance of the Proton Synchrotron internal dump was reduced below the beam instability threshold. Also, the process of selection of a low impedance design for the ralentisseur was shown.

Finally, chapter 7 reviewed the electromagnetic and thermo-mechanical analysis performed to assess the electromagnetic and thermomechanical performances of two HL-LHC devices, The TCLD and the TDIS. The impedance of both the devices was characterized by simulations and it was assessed it was not an issue nor for beam instabilities neither for RF-heating. The TCLD simulations were benchmarked with wire, probe, and BPM measurements. Despite some small discrepancies in resonant frequencies and shunt impedances there is reasonable agreement between measurements and simulations. The agreement among the different measurements types, performed on the TCLD prototype and on the TCLD pre-serie, allows to assess that the manufacturing and assembly procedure did not impact the impedance of the device. The TDIS design was found robust from an impedance perspective given the absence of trapped RM in the structure for frequencies up to 1.25 GHz. Furthemore, the TDIS was found able to cope with two different failure scenarios, beam impact on one of the jaw and RF-contacts detaching at the beam injection. Future studies should repeat the analysis taking into consideration the two counter-rotating beams traversing the device.

To summarize, the thesis has exposed general methodologies for the design of beam intercepting devices taking into account their impedance minimization, the thermo-mechanical impedance induced effects on the device and the nuclei matter interaction between the particle beam and the device.

The goals of the work, reported in section 1.6, are here restated for the seek of completeness:

1. Study, development and application of general principles for the mechanical design of low impedance devices. Impedance simulations of the developed designs. Prototype Construction. Test of the principles, benchmark of the simulations against measurements taken on device prototypes,

2. Development of physical models, methodologies and tools to analyse and quantify the RF-heating on components and the induced local thermo-mechanical effects,

The first goal was reached with the elaboration and the application of the impedance reduction guidelines to LIU devices and with the analysis and the measurements performed on the HL-LHC devices. The second one was reached with the elaboration of the method described in chapter 4 for the simulations of thermo-mechanical effects due to impedance induced RF-heating, and with the original contribution on the problem of the counter-rotating beams.

About this last point, the given result, despite very encouraging, revealed that the problem of determining the wakefield of two counter-rotating beams traversing the same vacuum chamber is more complex than expected. Thus, future studies will continue the work done on this thesis to better understand what are the consequences of the difference in transient co-moving and counter-moving wakefunction found in chapter 2 on the RF-heating and on the beam instabilities.

Further, future studies should also apply the knowledge acquired on the counter-rotating beams problem to better simulate the impedance induced heating in the TDIS and understand and avoid possible related issues.

The thesis is concluded with a flow diagrams, Fig. 8.1, readapted from Weiland et al. [39], that reports the work flow to design a BID from an impedance perspective.

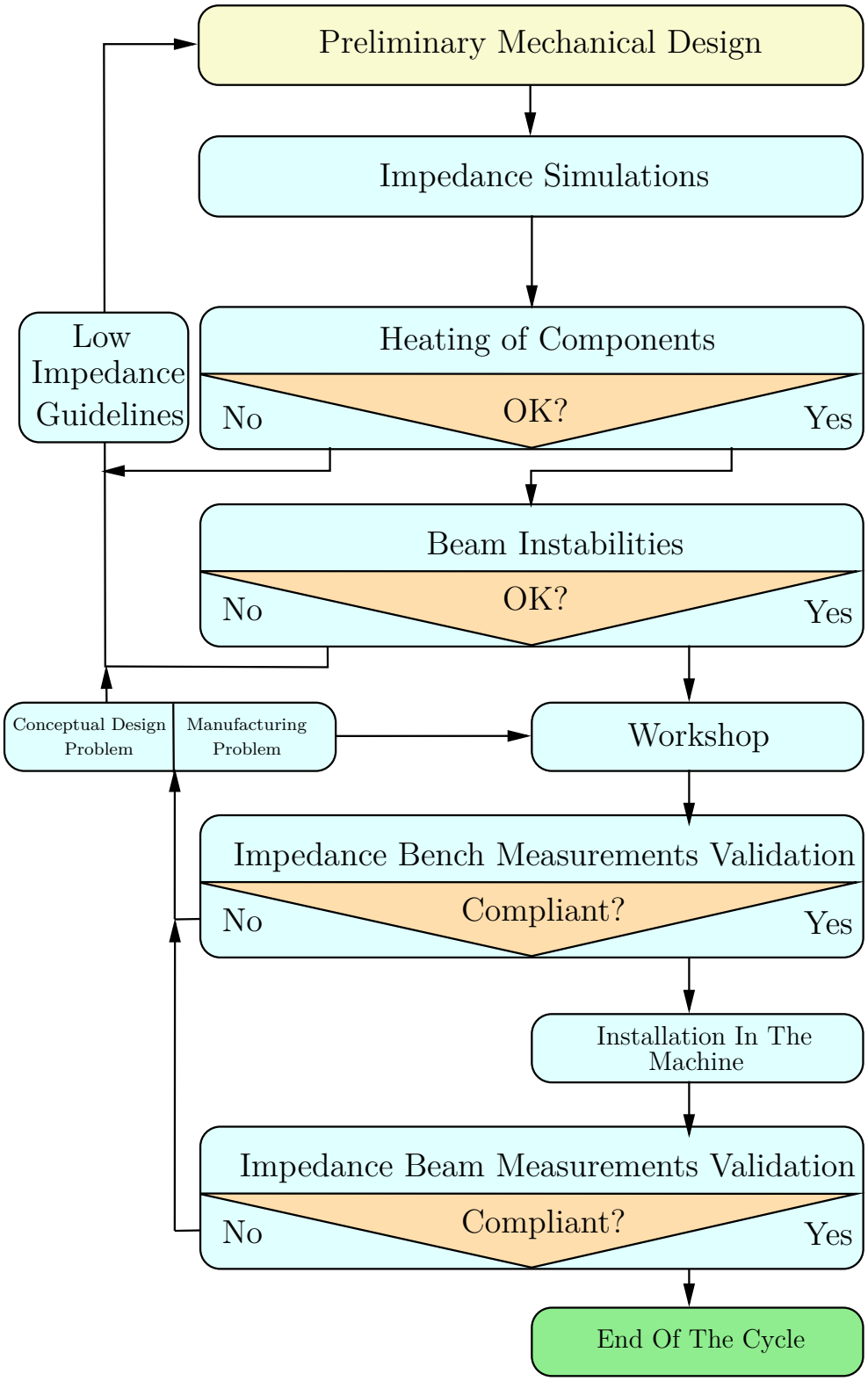

Figure 8.1. Design procedure for any accelerator component. Image readapted from Weiland and Wanzenberg [39].

Appendix A

Computing the Beams Entrance Delay

This is a brief appendix that shows how the entrance delay between two beams in a device, $\Delta t_{b_1 b_2}$, can be computed once the position of the device to study in the accelerator is known.

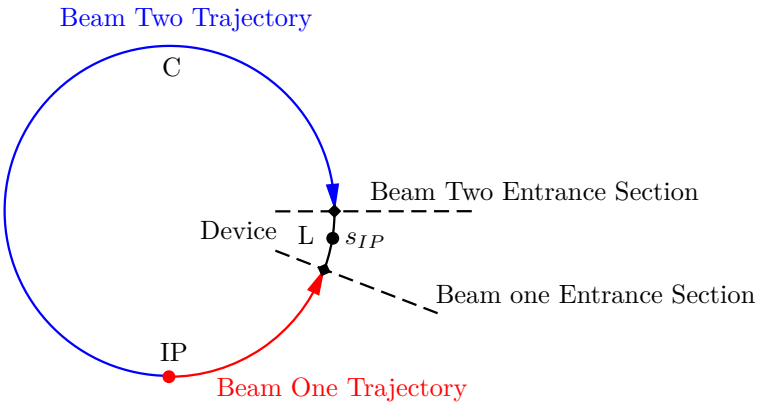

Figure A.1. Schematic drawing of a circular accelerator. C is the accelerator circumference. A generic device, of length L, having a center at a distance s_{IP} from the interaction point IP is shown. Two beams are moving into the accelerators. They are identical and they are both moving with the same speed v. The different path that the two beams have to do to enter into the device are shown.

In Fig. A.1, a schematic drawing of a circular accelerator is displayed. Let's define C as the total accelerator circumference, and let's consider a generic device, of lenght L, having a center at a distance s_{IP} from the interaction point IP.

Two identical beams are moving into the accelerator, with the same speed v. If one sets $t = 0$ as the time at which the two beams collide at the IP, one can say that for $t \geq 0$ they start moving away from the IP in different directions, refer to Fig. A.1.

Let's recall that beam one enters into the device when it crosses the beam one entrance section, while beam two enters into the device when it crosses the beam two entrance section. Thus, one can say that beam one enters into the device at the

time t_{1i}:

$$t_{1i} = \frac{s_{IP} - \frac{L}{2}}{v}, \tag{A.1}$$

and beam two enters into the device at the time t_{2i}:

$$t_{2i} = \frac{C - s_{IP} - \frac{L}{2}}{v}. \tag{A.2}$$

Thus, applying the definition of entrance delay between the beams one has:

$$\Delta t_{b_1 b_2} = t_{2i} - t_{1i} = \frac{C - 2s_{IP}}{v}. \tag{A.3}$$

It is interesting to observe that the two beams entrance delay does not depend on the length of the device, but only on the position of the device center inside the accelerator and on the length of the accelerator. The distance from the nearest interaction point s_{IP} can be found easily for the CERN equipment in the CERN layout database [158].

Bibliography

[1] Adobe Acrobat User Guide, "Interacting with 3D models", 2019. [Online]. Available: https://helpx.adobe.com/acrobat/using/interacting-3d-models.html

[2] P. J. Bryant, "A Brief history and review of accelerators", in *CAS-CERN Accelerator School: 5th general accelerator physics course, Jyvaskyla, Finland, 7-18 Sep 1992: Proceedings. 2 vol.*, 1992, pp. 1–16.

[3] O. Barbalat, "Applications of particle accelerators", in *CAS-CERN Accelerator School: 5th general accelerator physics course*, Jyvaskyla, Finland, 1992, pp. 841–853.

[4] O. S. Bruning, P. Collier, P. Lebrun, S. Myers, R. Ostojic, J. Poole, and P. Proudlock, *LHC Design Report*, ser. CERN Yellow Reports: Monographs. Geneva: CERN, 2004. [Online]. Available: http://cds.cern.ch/record/782076

[5] The ALICE Collaboration, "The ALICE experiment at the CERN LHC", *JINST*, vol. 3, p. S08002, 2008.

[6] The ATLAS Collaboration, "The ATLAS Experiment at the CERN Large Hadron Collider", *JINST*, vol. 3, p. S08003, 2008.

[7] The CMS Collaboration, "The CMS Experiment at the CERN LHC", *JINST*, vol. 3, p. S08004, 2008.

[8] The LHCb Collaboration, "The LHCb Detector at the LHC", *JINST*, vol. 3, p. S08005, 2008.

[9] Human Resources Department, "CERN Personnel Statistics 2018", CERN, Tech. Rep., 2019. [Online]. Available: http://cds.cern.ch/record/2677223/files/CERN-HR-STAFF-STAT-2018-RESTR.pdf

[10] P. Muggli and C. Bracco, "Awake, the Advanced Proton Driven Plasma Wakefield Acceleration Experiment", *IPAC 2016 - Proceedings of the 7th International Particle Accelerator Conference*, vol. 829, pp. 2588–2591, 2016.

[11] M. Hori and J. Walz, "Physics at CERN's Antiproton Decelerator", *Progress in Particle and Nuclear Physics (2013)*, 4 2013. [Online]. Available: http://arxiv.org/abs/1304.3721http://dx.doi.org/10.1016/j.ppnp.2013.02.004

[12] n_ToF Collaboration, "n_ToF Website." [Online]. Available: https://ntof-exp.web.cern.ch/ntof-exp/

[13] HiRadMat, "HiRadMat Website." [Online]. Available: https://espace.cern.ch/hiradmat-sps/WikiPages/Home.aspx

[14] CERN official Youtube Channel, "LHC animation: The path of the protons", 2015. [Online]. Available: https://www.youtube.com/watch?v=pQhbhpU9Wrg&t=63s

[15] E. Mobs, "The CERN accelerator complex - 2019. Complexe des accélérateurs du CERN - 2019", in *Bachelor Thesis*. CERN, 7 2019. [Online]. Available: https://cds.cern.ch/record/2684277

[16] G. Apollinari, A. Bejar, O. Bruning, P. Fessia, M. Lamont, L. Rossi, and L. Tavian, *High-Luminosity Large Hadron Collider (HL-LHC): Technical Design Report V. 0.1*, ser. CERN Yellow Reports: Monographs. Geneva: CERN, 2017. [Online]. Available: https://cds.cern.ch/record/2284929

[17] H. Damerau, A. Funken, R. Garoby, S. Gilardoni, B. Goddard, K. Hanke, A. Lombardi, D. Manglunki, M. Meddahi, B. Mikulec, G. Rumolo, E. Shaposhnikova, M. Vretenar, and J. Coupard, "LHC Injectors Upgrade, Technical Design Report, Vol. I: Protons", CERN, Tech. Rep. CERN-ACC-2014-0337, 12 2014. [Online]. Available: https://cds.cern.ch/record/1976692

[18] W. Herr and B. Muratori, "Concept of luminosity", *CAS - CERN Accelerator School: Intermediate Course on Accelerator Physics*, vol. 2, no. 3, pp. 361–378, 2003. [Online]. Available: https://cds.cern.ch/record/941318

[19] S. Fartoukh, "An Achromatic Telescopic Squeezing (ATS) Scheme For The LHC Upgrade", *IPAC 2011 - Proceedings of the International Particle Accelerator Conference*, no. CERN-ATS-2011-161, p. 2088, 9 2011. [Online]. Available: https://cds.cern.ch/record/1382077

[20] R. Calaga, "Crab Cavities for the High-Luminosity Lhc", *SRF2017 - Proceedings of the 18th International Conference on RF Superconductivity*, pp. 695–699, 2017.

[21] LIU Project, "LIU Injectors Beam Parameters." [Online]. Available: https://edms.cern.ch/document/1296306/2

[22] A. Bertarelli, "Beam-induced damage mechanisms and their calculation", *2014 Joint International Accelerator School: Beam Loss and Accelerator Protection, Proceedings*, vol. 002, no. November 2014, pp. 159–227, 2014.

[23] S. Redaelli, "Beam Cleaning and Collimation Systems", in *contribution to the 2014 Joint International Accelerator School: Beam Loss and Accelerator Protection*, 8 2014. doi: 10.5170/CERN-2016-002.403. [Online]. Available: http://arxiv.org/abs/1608.03159

[24] M. Calviani, *Private Comunication*, 2019.

[25] Oliver Aberle On behalf of the LHC Collimation Team, "HL-LHC Collimators: Components for absorbers", in *3rd HiLumi Industry Day*, Warrington - United Kingdom, 2017.

[26] H. Burkhardt, G. Arduini, C. Fischer, J. J. Gras, A. Koschik, D. Kramer, S. Pedersen, and S. Redaelli, "Beam scraping for LHC injection", *Proceedings of the IEEE Particle Accelerator Conference*, pp. 1580–1582, 2007.

[27] J. L. Ristić-Djurović, "Stripping extraction of positive ions from a cyclotron", *Physical Review Special Topics - Accelerators and Beams*, vol. 4, no. 12, p. 123501, 12 2001. [Online]. Available: https://link.aps.org/doi/10.1103/PhysRevSTAB.4.123501

[28] V. Forte, "Performance of the CERN PSB at 160 MeV with H- charge exchange injection", Ph.D. dissertation, Blaise Pascal University, 6 2016. [Online]. Available: https://cds.cern.ch/record/2194937

[29] T. Nilsson, "The ISOLDE facility at CERN", in *Exotic Nuclei and Atomic Masses*. Berlin, Heidelberg: Springer Berlin Heidelberg, 2003, pp. 469–472. [Online]. Available: http://link.springer.com/10.1007/978-3-642-55560-2_165

[30] D. Amorim, "Study of the transverse mode coupling instability in the CERN Large Hadron Collider", Ph.D. dissertation, University of Grenoble Alpes, 2019. [Online]. Available: https://cds.cern.ch/record/2707064

[31] F. Giordano, "Impacto of filling scheme on beam induced RF-heating in CERN LHC and HL-LHC", Ph.D. dissertation, Università degli studi di Napoli Federico II, 2017.

[32] D. Lipka and D. Hamburg, "Heating of a DCCT and a FCT due to wake losses in PETRAIII , simulations and solutions", in *Simulation of Power Dissipation and Heating from Wake Losses Workshop*, Diamond Light Source, Oxfordshire, UK, 2013. [Online]. Available: https://www.diamond.ac.uk/Home/Events/2013/Simulation-of-Power-Dissipation---Heating-from-Wake-Losses.html

[33] N. Mounet, "The LHC Transverse Coupled-Bunch Instability", Ph.D. dissertation, EPFL, 2012. [Online]. Available: https://cds.cern.ch/record/1451296

[34] J. D. Jackson, *Classical electrodynamics*, 3rd ed. New York, NY: Wiley, 1999. ISBN 9780471309321. [Online]. Available: http://cdsweb.cern.ch/record/490457

[35] K. Ng, "Physiscs of Intensity Dependent Beam Instabilities", in *U.S. Particle Accelerator School (USPAS 2002) Long Beach, California, January 14-25*, 2002. [Online]. Available: http://lss.fnal.gov/cgi-bin/find_paper.pl?fn-0713

[36] B. J. Holzer, "Introduction to Particle Accelerators and their Limitations", in *Proceedings of the CAS-CERN Accelerator School: PlasmaWake Acceleration*, vol. 1, no. November 2014, 2016. doi: 10.5170/CERN-2016-001.29. ISBN 9789290834250 p. 29. [Online]. Available: http://dx.doi.org/10.5170/CERN-2016-001.29

[37] K. C. Schindle, "CAS Lectures: SPACE CHARGE", in *Prooceding of CAS - CERN Accelerator School: Intermediate Course on Accelerator Physics,*

Zeuthen, Germany, 2006. doi: 10.5170/CERN-2006-002.305 pp. 305–320. [Online]. Available: https://cds.cern.ch/record/941316/files/p305.pdf

[38] L. Palumbo, V. G. Vaccaro, and M. Zobov, "Wake Fields and Impedance", *lecture given at CERN Advanced Accelerator School*, vol. 041, no. September, p. 70, 9 2003. [Online]. Available: http://arxiv.org/abs/physics/0309023

[39] T. Weiland and R. Wanzenberg, "Wake fields and impedances", in *Frontiers of Particle Beams: Intensity Limitations*. Berlin, Heidelberg: Springer Berlin Heidelberg, 1992, vol. 400, pp. 39–79. [Online]. Available: http://link.springer.com/10.1007/3-540-55250-2_26

[40] P. B. Wilson, "Introduction to wakefields and wake potentials", in *AIP Conference Proceedings*, vol. 184, no. January. AIP, 1989. doi: 10.1063/1.38045. ISSN 0094243X pp. 525–564. [Online]. Available: http://inspirehep.net/record/276612/files/slac-pub-4547.pdf

[41] K. L. F. Bane, P. B. Wilson, and T. Weiland, "Wake fields and wake field acceleration", in *AIP Conference Proceedings*, vol. 127, Stanford Linear Accelerator Center. AIP, 1985. doi: 10.1063/1.35182. ISSN 0094243X pp. 875–928. [Online]. Available: http://aip.scitation.org/doi/abs/10.1063/1.35182

[42] W. Herr and T. Pieloni, "Beam-Beam Effects", *CERN Yellow Reports*, no. 1, pp. 431–459, 1 2016. [Online]. Available: http://arxiv.org/abs/1601.05235%0Ahttp://dx.doi.org/10.5170/CERN-2014-009.431http://arxiv.org/abs/1601.05235http://dx.doi.org/10.5170/CERN-2014-009.431

[43] G. Iadarola and G. Rumolo, "Electron Cloud Effects", in *Proceedings of ICFA Mini-Workshop on Impedances and Beam Instabilities in Particle Accelerators*, vol. 1, no. September 2017, 2018. doi: http://dx.doi.org/10.23732/CYRCP-2018-001.49 pp. 18–22.

[44] J. Wang, "Transverse Two-Beam Instability", CERN, Tech. Rep., 1987. [Online]. Available: https://cds.cern.ch/record/183705

[45] U. Niedermayer, "Bench Measurements and Simulations of Beam Coupling Impedance", in *Proceedings, CAS - CERN Accelerator School: Intensity Limitations in Particle Beams: Geneva, Switzerland, November 02-11, 2015*, no. 4, 5 2018. doi: 10.23730/CYRSP-2017-003.81 pp. 81–106. [Online]. Available: http://arxiv.org/abs/1805.01824%0Ahttp://dx.doi.org/10.23730/CYRSP-2017-003.81http://arxiv.org/abs/1805.01824http://dx.doi.org/10.23730/CYRSP-2017-003.81

[46] A. W. Chao, *Physics of Collective Beam Instabilities in High Energy Accelerators*. Wiley-VCH, 1993.

[47] G. Rumolo, "Beam Dynamics Challenges for the LHC and Injector Upgrades; Beam Dynamics Challenges for the LHC and Injector Upgrades", in *HB2018 - Proceedings of the 61st ICFA Advanced Beam Dynamics Workshop on High-Intensity and High-Brightness Hadron Beams*, 2018.

doi: 10.18429/JACoW-HB2018-MOA1PL02 pp. 0–5. [Online]. Available: http://accelconf.web.cern.ch/AccelConf/hb2018/papers/moa1pl02.pdf

[48] E. Jensen, "RF Cavity Design", in *Contribution to the CAS - CERN Accelerator School: Advanced Accelerator Physics Course*, 1 2014. doi: 10.5170/CERN-2014-009.405. [Online]. Available: http://arxiv.org/abs/1601.05230http://dx.doi.org/10.5170/CERN-2014-009.405

[49] B. Salvant, "Impedance model of the CERN SPS and aspects of LHC single-bunch stability", Ph.D. dissertation, EPFL, Lausanne, 2010. [Online]. Available: http://infoscience.epfl.ch/record/142384

[50] S. Heifets and A. Wagner, "Generalized Impedances and Wakes in Asymmetric Structures", Stanford Linear Accelerator Center, Tech. Rep. January, 1998.

[51] C. Zannini, G. Rumolo, E. Benedetto, M. Garlasche, J. Hansen, E. Métral, B. Riffaud, B. Salvant, W. Weterings, and L. Zuccalli, "Beam coupling impedance considerations on the PSB pumping ports of the new H-injection region", CERN, Tech. Rep., 2014.

[52] W. A. Panofsky, W. K. H.; Wenzel, "Some considerations concerning the transverse deflection of charged particles in radio-frequency fields", *Review of Scientific Instruments*, vol. 27, no. 11, p. 967, 1956.

[53] C. Zannini, G. Rumolo, G. Rumolo CERN, and G. Iadarola, "Power loss calculation in separated and common beam chambers of the LHC", CERN, Geneva, Switzerland, Tech. Rep., 2014. [Online]. Available: https://cds.cern.ch/record/1742192/files/CERN-ACC-2014-0122.pdf

[54] G. Rumolo and C. Zannini, "Beam induced power loss with two beams", CERN, Tech. Rep., 2018. [Online]. Available: https://indico.cern.ch/event/809558/contributions/3372399/attachments/1820527/2977428/Beam_induced_power_loss_with_two_beam_review.pdf

[55] A. Grudiev, "LHC Project Note 413 Simulation and reduction of longitudinal and transverse impedances of a collimation device with two beams in one vacuum chamber", CERN, Tech. Rep., 2008.

[56] CST Studio Suite, "CST Studio Suite Website." [Online]. Available: https://www.3ds.com/products-services/simulia/products/cst-studio-suite/?utm_source=cst.com&utm_medium=301&utm_campaign=cst

[57] C. Zannini, "Electromagnetic Simulation of CERN Accelerator Components and Experimental Applications", Ph.D. dissertation, Polytechnique, École De Lausanne, Fédérale (EPFL), 2013. [Online]. Available: http://infoscience.epfl.ch/record/187002

[58] K. Bane, "The Calculated Longitudinal Impedance of the SLC Damping Ring", SLAC, Tech. Rep., 1988.

[59] K. Bane, "Bunch lengthening in The SLC Damping Rings", SLAC, Tech. Rep., 1990.

[60] CST Solvers, "CST Solvers Website." [Online]. Available: https://www.3ds.com/products-services/simulia/products/cst-studio-suite/solvers/

[61] W. R. Faust, "Transient behavior of a cavity", *Journal of Applied Physics*, vol. 43, no. 10, pp. 3983–3987, 1972.

[62] F. Giordano, G. Rumolo, B. Salvant, L. Teofili, and C. Zannini, "Analysis of the 2 beam power loss in a cavity structure", in *Impedance meeting, 20 Septemeber 2019 (CERN)*. [Online]. Available: https://indico.cern.ch/event/849584/contributions/3571687/attachments/1912131/3160635/Two_beam_power_loss_analysis_impedance_meeting.pdf

[63] G. Rumolo, "Beam Instabilities", in *Contribution to the CAS - CERN Accelerator School: Advanced Accelerator Physics Course, Trondheim, Norway, 18-29 Aug 2013*, 1 2016. doi: 10.5170/CERN-2014-009.199. ISBN ISBN O-471 -55 184-8. [Online]. Available: http://arxiv.org/abs/1601.05201

[64] E. Metral, T. Argyropoulos, H. Bartosik, N. Biancacci, X. Buffat, J. F. Muller, W. Herr, G. Iadarola, A. Lasheen, K. Li, A. Oeftiger, T. Pieloni, D. Quartullo, G. Rumolo, B. Salvant, M. Schenk, E. Shaposhnikova, C. Tambasco, H. Timko, C. Zannini, A. Burov, D. Banfi, J. Barranco, N. Mounet, O. Boine-Frankenheim, U. Niedermayer, V. Kornilov, and S. White, "Beam instabilities in hadron synchrotrons", *IEEE Transactions on Nuclear Science*, vol. 63, no. 2, pp. 1001–1050, 2016.

[65] H. Wiedemann, *Particle accelerator physics*, 4th ed. Springer, 2015.

[66] N. Wheeler, "Simplified production of Dirac Delta Function Identities", pp. 1–18, 1997. [Online]. Available: https://www.reed.edu/physics/faculty/wheeler/documents/MiscellaneousMath/DeltaFunctions/SimplifiedDiracDelta.pdf

[67] B. M. Furman, H. Lee and Zotter, "Energy Loss of Bunched Beams in RF Cavities", SSC Central Design Group, Berkeley, Tech. Rep., 1986.

[68] S. Heifets and B. Zotter, "On the symmetry of the impedance [particle accelerator]", in *Proceedings of the 1999 Particle Accelerator Conference (Cat. No.99CH36366)*, vol. 2. IEEE, 1999. doi: 10.1109/PAC.1999.795467. ISBN 0-7803-5573-3 pp. 1118–1119. [Online]. Available: https://ieeexplore.ieee.org/stamp/stamp.jsp?tp=&arnumber=795467

[69] L. Teofili, M. Migliorati, and I. Lamas, "a Multi-Physics Approach To Simulate the Rf-Heating 3D Power Map Induced By the Proton Beam in a Beam Intercepting Device", *J. Phys.: Conf. Ser.*, vol. 1067, no. 062012, 2018. [Online]. Available: http://iopscience.iop.org/article/10.1088/1742-6596/1067/6/062012/pdf

[70] B. Salvant, O. Aberle, M. Albert, R. Alemany-Fernandez, G. Arduini, J. Baechler, M. J. Barnes, P. Baudrenghien, O. E. Berrig, N. Biancacci, G. Bregliozzi, F. Carra, F. Caspers, P. Chiggiato, A. Danisi, H. A. Day, M. Deile, D. Druzhkin, S. Jakobsen, J. Kuczerowski, A. Lechner, R. Losito, A. Masi, E. Métral,

N. Minafra, A. Nosych, A. P. Marcone, D. Perini, S. Redaelli, F. Roncarolo, G. Rumolo, E. Shaposhnikova, J. Uythoven, A. J. Välimaa, J. E. V. Campelo, C. Vollinger, M. Wendt, J. Wenninger, C. Zannini, J. F. E. Muller, G. Switzerland, and N. Wang, "BEAM INDUCED RF HEATING IN LHC IN 2015", Tech. Rep., 2016.

[71] C. Zannini and ADAM/AVO, "MULTIPHYSICS SIMULATIONS OF IMPEDANCE EFFECTS IN ACCELERATORS MULTIPHYSICS SIMULATION APPLIED CERN-SPS extraction kicker", in *CERN Yellow Reports: Conference Proceedings, 2018*, vol. 1, no. September 2017, 2018, pp. 141–144.

[72] M. Garlasche, "TCP.B6L7.B1: analytical and numerical evaluation of unexpected heating", in *LHC Collimation Working Group #148*, 2012. [Online]. Available: https://indico.cern.ch/event/206398/contributions/404028/attachments/316329/441573/LHCCWG_10092012_TCPB6Heating_Garlasche.pdf

[73] ANSYS, "ANSYS Website." [Online]. Available: https://www.ansys.com/

[74] A. Dallocchio, "Study of Thermo-Mechanical Effects Induced in Solids by High Energy Particle Beams: Analytical and Numerical Methods", Ph.D. dissertation, Turin Polytechnic, 2008. [Online]. Available: https://cds.cern.ch/record/1314219

[75] C. L. Torregrosa Martin, "Comprehensive Study for an Optimized Redesign of the CERN's Antiproton Decelerator Target", Ph.D. dissertation, Valencia, Polytechnic University, 4 2018. [Online]. Available: https://cds.cern.ch/record/2314375

[76] G. Romagnoli, F.-X. Nuiry, J. J. Esala, T. Polzin, J. A. B. Monago, M. Calviani, A. Masi, and V. Vlachoudis, "DESIGN OF THE NEW PS INTERNAL DUMPS , IN THE FRAMEWORK OF THE LHC INJECTOR UPGRADE (LIU) PROJECT Thermo-Mechanical Simulations", *Proceedings, 8th International Particle Accelerator Conference (IPAC 2017): Copenhagen, Denmark, May 14-19*, pp. 3521–3523, 2017. [Online]. Available: http://accelconf.web.cern.ch/AccelConf/ipac2017/papers/wepva109.pdf

[77] I. L. Garcia, N. Biancacci, G. Bregliozzi, M. Calviani, M. I. Frankl, L. Gentini, S. Gilardoni, A. Lechner, A. Perillo-Marcone, B. Salvant, N. V. Shetty, and J. Uythoven, "LHC injection protection devices, thermo-mechanical studies through the design phase", *IPAC 2016 - Proceedings of the 7th International Particle Accelerator Conference*, pp. 3698–3701, 2016.

[78] D. Carbajo Perez, N. Biancacci, C. Bracco, G. Bregliozzi, M. Calviani, M. I. Frankl, I. G. Lamas, L. Gentini, S. Gilardoni, G. Iadarola, A. Lechner, A. P. Marcone, B. Salvant Cern, and G. Switzerland, "OPERATIONAL FEEDBACK AND ANALYSIS OF CURRENT AND FUTURE DESIGNS OF THE INJECTION PROTECTION ABSORBERS IN THE LARGE HADRON COLLIDER AT CERN", *Proceedings, 8th International Particle Accelerator Conference (IPAC 2017): Copenhagen, Denmark, May 14-19*, 2017.

[79] C. Bracco, A. Lechner, D. Carbajo, and A. Perillo, "TDIS - Functional Specification", CERN, Tech. Rep., 2017. [Online]. Available: https://edms.cern.ch/document/1865250/1.0

[80] G. Bertotti, "Magnetic Losses", in *Encyclopedia of Materials: Science and Technology*. Elsevier, 2001, pp. 4798–4804. [Online]. Available: https://linkinghub.elsevier.com/retrieve/pii/B0080431526008391

[81] CST Studio Suite online help, "Eigenmode Solver Overview."

[82] H. Wiedemann, "Impedances in an Accelerator Environment", in *Particle Accelerator Physics Fourth edition*. Springer, 2015, p. 753.

[83] N. e. a. Biancacci, "Update on TDIS impedance and stability studies", in *TDIS internal review*, 2016.

[84] A. Garzelli, "Electromagnetic fields and heat load simulations in ultrahigh vacuum particle accelerator components", in *bachelor thesis and private communication*. University of Rome la Sapienza, 2017.

[85] The TOTEM Collaboration, "The TOTEM Experiment at the CERN Large Hadron Collider", *Journal of Instrumentation*, vol. 3, no. 08, pp. S08 007–S08 007, 8 2008. [Online]. Available: http://stacks.iop.org/1748-0221/3/i=08/a=S08007?key=crossref.53593e597df8991a1dbab233c46bb618

[86] The TOTEM Collaboration, "TOTEM Upgrade Proposal", CERN, Tech. Rep., 2013.

[87] M. Deile, D. Mirarchi, R. Bruce, A. Mereghetti, S. Redaelli, B. Salvachua, B. Salvant, and G. Valentino, "Roman Pot insertions in high-intensity beams for the CT-PPS project at LHC", *IPAC 2016 - Proceedings of the 7th International Particle Accelerator Conference*, no. June, pp. 1473–1476, 2016.

[88] N. Minafra, "RF Characterization of the New TOTEM Roman Pot", *Cern-Totem-Note-2013-003*, no. June, 2013. [Online]. Available: https://cds.cern.ch/record/1557361

[89] M. S. De Jong, F. P. Adams, R. M. Hutcheon, G. F. Morin, and R. J. Bakewell, "Ferrite-Loaded Higher-Order-Mode Absorbers for the MIT-Bates South Hall Ring", 2016, pp. 2016–2018. [Online]. Available: http://accelconf.web.cern.ch/accelconf/e94/PDF/EPAC1994_2016.PDF

[90] C. Vollinger and F. Caspers, "Material Measurement of TT2-111R." [Online]. Available: https://emetral.web.cern.ch/emetral/LRFF/15thMeeting_16-10-12/TalkLRFFmeeting_16102012MatMeasTT2_111R.pptx

[91] A. Tsinganis and F. Cerutti, "Impact of Roman Pot and TCL settings on radiation levels in the LHC IR5 matching section", in *LHC Collimation Working Group # 226*, 2017. [Online]. Available: https://indico.cern.ch/event/677406/contributions/2773349/attachments/1553277/2441509/CWG_Roman_pots_TCLs.pdf

[92] A. Tsinganis and F. Cerutti, "Simulation study of Roman Pot and TCL settings in the LHC IRs 1&5", in *LHC Collimation Working Group # 229*, 2018. [Online]. Available: https://indico.cern.ch/event/713521/contributions/2931527/attachments/1619547/2575752/CWG_Roman_pots_TCLs.pdf

[93] S. I. Woods, T. M. Jung, D. R. Sears, and J. Yu, "Emissivity of silver and stainless steel from 80 K to 300 K: Application to ITER thermal shields", *Cryogenics*, vol. 60, pp. 44–48, 2014.

[94] R. Shurtz and Randy, "Total Hemispherical Emissivity of Metals Applicable to Radiant Heat Testing." Sandia National Laboratories, Tech. Rep., 2018. [Online]. Available: http://www.osti.gov/servlets/purl/1483461/

[95] S. W. Churchill and H. H. S. Chu, "Correlating equations for laminar and turbulent free convection from a vertical plate", *International Journal of Heat and Mass Transfer*, vol. 18, no. 11, pp. 1323–1329, 11 1975.

[96] Mario Deile, "RP insertions 2016: Physics Acceptance & Interaction with Beam Environment", in *Elba Workshop on Forward Physics @ LHC Energy*, 2016. [Online]. Available: https://indico.cern.ch/event/505807/contributions/2162325/attachments/1282542/1906100/elba-lowbetainsertions.pdf

[97] N. Biancacci, A. Huschauer, M. Migliorati, and D. Ventura, "PS impedance localization measurements in 2018", in *Impedance meeting, 12 July 2019, (CERN)*, 2018. [Online]. Available: https://indico.cern.ch/event/834506/contributions/3497089/attachments/1879784/3096744/HSC_PS_impedance_localiation_2018_NB.pdf

[98] N. Biancacci, "Improved techniques of impedance calculation and localization in particle accelerators", Ph.D. dissertation, University of Rome la Sapienza, 2014. [Online]. Available: http://www.infn.it/thesis/thesis_dettaglio.php?tid=9292

[99] T. Kroyer, F. Caspers, and E. Gaxiola, "Longitudinal and Transverse Wire Measurements for the Evaluation of Impedance Reduction Measures on the MKE Extraction Kickers", CERN, Geneva, Tech. Rep., 2007.

[100] J. R. Bray and L. Roy, "Measuring the unloaded, loaded, and external quality factors of one- and two-port resonators using scattering-parameter magnitudes at fractional power levels", *IEEE Proc. of Microwave Antenna Propagation*, vol. 151, no. 4, pp. 345–350, 2004.

[101] D. Kajfez, "Q factor measurements, analog and digital." University of Mississippi Dept. of EE, 2011. doi: 10.1016/j.jorganchem.2007.02.046. ISBN 1608071618. ISSN 0022328X pp. 1–18. [Online]. Available: http://pcaen1.ing2.uniroma1.it/mostacci/didattica/lab_meas_high_freq/store/Cavities/RF_Qmeas_kajfez.pdf

[102] L. Teofili, "Collimator Measurements Procedure", 2019.

[103] N. Biancacci, F. Caspers, J. Kuczerowski, E. Métral, N. Mounet, B. Salvant, A. Mostacci, O. Frasciello, and M. Zobov, "Impedance simulations and measurements on the LHC collimators with embedded beam position monitors", *Physical Review Accelerators and Beams*, vol. 20, 2017.

[104] A. Faltens, E. C. Hartwig, D. Mohl, and A. M. Sessler, "An Analog Method for Measuring the Longitudinal Coupling impedance of a Relativistic Particle Beam with its Environment", in *8th International Conference on High-Energy Accelerators, HEACC 1971.* Proceedings, 8th International Conference on High-Energy Accelerators, HEACC 1971, 1971, p. 338.

[105] M. Sands and J. Rees, "A Bench Measurement of the Energy Loss of a Stored Beam to a Cavity", SLAC, Tech. Rep., 1974. [Online]. Available: https://www.slac.stanford.edu/cgi-wrap/getdoc/slac-tn-05-051.pdf

[106] V. Vaccaro, "Coupling Impedance Measurements: An Improved Wire Method", INFN, Tech. Rep., 1994. [Online]. Available: https://cds.cern.ch/record/276443/files/SCAN-9502087.pdf

[107] J. Strickland, *Time-domain Reflectometry Measurements.* Tektronix, 1970.

[108] L. e. a. Walling, "Transmission-line impedance measurements for an advanced hadron facility", *NIM*, no. A281, p. 433, 1989.

[109] E. Jensen, "An Improved Log-Formula For Homogeneously Distributed Impedance", CERN, Geneva, Switzerland, Tech. Rep., 2000. [Online]. Available: https://cds.cern.ch/record/960162

[110] M. Panniello, "Numerical-Analytical Methods for Particle Accelerators", Ph.D. dissertation, Federico II University, Napoli, Italy, 2009.

[111] M. R. Masullo, V. G. Vaccaro, and M. Panniello, "the Stretched Wire Method : a Comparative Analysis Performed By Means of the Mode Matching Technique", no. January 2011, 2015, pp. 2–5.

[112] A. Gaupp and F. P. Wolf, "Beam position monitors", *Synchrotron Radiation News*, vol. 1, no. 3, pp. 27–31, 5 1988. [Online]. Available: http://www.tandfonline.com/doi/abs/10.1080/08940888808602499

[113] L. Teofili, I. Lamas, and T. L. Rijoff, "DESIGN OF LOW-IMPACT IMPEDANCE DEVICES : THE NEW PROTON SYNCHROTRON BOOSTER ABSORBER SCRAPER (PSBAS)", in *CERN Yellow Rep. Conf. Proc.*, vol. 1, no. September 2017. Geneva: CERN, 2018. doi: 10.23732/CYRCP-2018-001.111 pp. 18–22. [Online]. Available: https://cds.cern.ch/record/2674111

[114] L. Teofili, M. Migliorati, J. Briz, M. Calviani, N. Chritin, J. Esala, S. Gilardoni, J. Maestre, L. Lamas, T. Polzin, and T. Rijoff, "Design of the new proton synchrotron booster absorber scraper (PSBAS) in the framework of the large hadron collider injection upgrade (LIU) project", in *Journal of Physics: Conference Series*, vol. 1067, no. 8, 2018. doi: 10.1088/1742-6596/1067/8/082027. ISSN 17426596

[115] B. K. Popovic, L. Teofili, and C. Vollinger, "Impedance Analysis of New PS Internal Dump Design", in *Proc. 9th International Particle Accelerator Conference (IPAC'18), Vancouver, BC, Canada, April 29-May 4, 2018*, ser. International Particle Accelerator Conference, no. 9. Geneva, Switzerland: JACoW Publishing, 6 2018. doi: doi:10.18429/JACoW-IPAC2018-THPAF052. ISBN 978-3-95450-184-7 pp. 3083–3086. [Online]. Available: http://jacow.org/ipac2018/papers/thpaf052.pdf

[116] L. Teofili and others, "Analysis on the Thermal Response to Beam Impedance Heating of the Post LS2 Proton Synchrotron Beam Dump", in *Proc. 10th International Partile Accelerator Conference (IPAC'19), Melbourne, Australia, 19-24 May 2019*, ser. International Partile Accelerator Conference, no. 10. Geneva, Switzerland: JACoW Publishing, 2019. doi: doi:10.18429/JACoW-IPAC2019-THPTS065. ISBN 978-3-95450-208-0 pp. 4260–4263. [Online]. Available: http://jacow.org/ipac2019/papers/thpts065.pdf

[117] H. A. Day, "Measurements and Simulations of Impedance Reduction Techniques in Particle Accelerators", Ph.D. dissertation, University of Manchester, 2013. [Online]. Available: http://inspirehep.net/record/1296366/files/CERN-THESIS-2013-083.pdf

[118] Y. Shobuda, Y. H. Chin, and K. Takata, "Coupling impedances of a gap in vacuum chamber", *Phys. Rev. ST Accel. Beams*, vol. 10, p. 44403, 2007.

[119] V. Baglin, J. Bojko, O. Gröbner, B. Henrist, N. Hilleret, C. Scheuerlein, and M. Taborelli, "The secondary electron yield of technical materials and its variations with surface treatment", *Particle accelerator. Proceedings, 7th European Conference, EPAC 2000, Vienna, Austria, June 26-30*, vol. 1-3, pp. 217–221, 2000. [Online]. Available: http://weblib.cern.ch/abstract?CERN-LHC-PROJECT-REPORT-433

[120] M. Cieslak-Kowalska, J. L. Abelleira, E. Benedetto, and C. Bracco, "Evolution of High Intensity Beams in the CERN PS Booster after H- Injection and Phase Space Painting", in *Proc. of International Particle Accelerator Conference (IPAC'16), Busan, Korea, May 8-13, 2016*, ser. International Particle Accelerator Conference, no. 7. Geneva, Switzerland: JACoW, 6 2016. doi: doi:10.18429/JACoW-IPAC2016-MOPOR024. ISBN 978-3-95450-147-2 pp. 656–659. [Online]. Available: http://jacow.org/ipac2016/papers/mopor024.pdf

[121] H. Bartosik, G. Di Giovanni, B. Mikulec, and F. Schmidt, "PS BOOSTER BEAM ABSORBER/SCRAPER AFTER LS2", CERN, Tech. Rep., 2018. [Online]. Available: https://edms.cern.ch/document/1578463/2.1

[122] C. Zannini and G. Rumolo, "Updated status of the PSB impedance model", in *125th LIU-PSB Meeting*, Geneva, Switzerland.

[123] S. Albright, C. Zannini, and B. Salvant, "ECRS: 1969773, 2016343, 2019094", in *23rd Impedance Working Group (CERN)*, Geneva, Switzerland, 2018, p. 2. [Online]. Available: https://indico.cern.ch/event/756863/contributions/3145196/attachments/1719099/2774733/AOBECRs.pdf

[124] C. Zannini, G. Iadarola, K. Li, G. Rumolo, B. Jones, and T. L. Rijoff, "Transverse impedance model of the CERN-PSB", *6th International Particle Accelerator Conference, IPAC 2015*, pp. 406–408, 2015.

[125] G. Battistoni and others, "Overview of the FLUKA code", *Annals Nucl. Energy*, vol. 82, pp. 10–18, 2015.

[126] A. Ferrari, P. R. Sala, A. Fasso, and J. Ranft, "FLUKA: A multi-particle transport code (Program version 2005)", INFN, Tech. Rep., 2005.

[127] R. M. Christensen, "A Two-Property Yield, Failure (Fracture) Criterion for Homogeneous, Isotropic Materials", *Journal of Engineering Materials and Technology*, vol. 126, no. 1, pp. 45–52, 1 2004. [Online]. Available: https://doi.org/10.1115/1.1631024

[128] W. Kozlowska and M. Brugger, "PS Internal Dump in the FLUKA Monte Carlo simulations", CERN, Geneva, Switzerland, Tech. Rep., 2015.

[129] G. Romagnoli, F. Nuiry, J. Esala, M. Calviani, S. Gilardoni, A. Masi, J. A. Briz, V. Vlachoudis, Y. Coutron, D. Steyaert, M. Butcher, A. Huschauer, D. Cotte, and J. Hansen, "ENGINEERING DESIGN AND PROTOTYPING OF THE NEW LIU PS INTERNAL BEAM DUMPS", *IPAC2018 - 9th International Particle Accelerator Conference*, pp. 2600–2603, 2019. [Online]. Available: http://inspirehep.net/record/1690188/files/wepmg001.pdf

[130] A. Lasheen, "Longitudinal instability threshold for the new internal dump", in *14th LIU-PS Beam Dynamics WG meeting*, 2018. [Online]. Available: https://indico.cern.ch/event/718539/contributions/2952920/attachments/1627535/2592372/LIU_PS_050418.pdf

[131] D. Ventura, B. K. Popovic, and B. Salvant, "Transverse Impedance of the PS Dump", in *24th Impedance Working Group (IWG)*, 2018. [Online]. Available: https://indico.cern.ch/event/764129/contributions/3171808/attachments/1731990/2799682/PS_Dump.pdf

[132] S. Kalpakjian and S. R. Schmid, *Manufacturing Engineering and Technology*, seventh ed ed. Pearson, 2014.

[133] A. Navarro Fernandez, "Characterization and optimization of CERN Secondary Emission Monitors (SEM) used for beam diagnostics." Ph.D. dissertation, UNIVERSITAT POLITECNICA DE CATALUNYA, 2017. [Online]. Available: https://upcommons.upc.edu/bitstream/handle/2117/105996/TFG_Araceli.pdf?sequence=1&isAllowed=y

[134] F.-X. Nuiry and G. Romagnoli, "FUNCTIONAL SPECIFICATION PS Ring Ralentisseur Functional Specification", CERN, Tech. Rep., 2017.

[135] F.-X. Nuiry, R. Welschen, E. Grenier Boley, M. Butcher, and J. Lendaro, "Replacement of the PS Ring Ralentisseur in the Framework of the LIU Project", CERN, Tech. Rep. April, 2019.

[136] R. Welschen, "Radiation damage and the design of beam intercepting devices at CERN." in *Master Thesis*. Delft University of Technology, 2019. [Online]. Available: http://resolver.tudelft.nl/uuid:e1eefcff-528b-4a7a-b174-b22ce636cafd

[137] Inermet Datasheet Website, "Inermet Datasheet Website." [Online]. Available: https://www.plansee.com/en/materials/tungsten-heavy-metal.html

[138] L. Teofili, M. Migliorati, M. Calviani, D. Carbajo, S. Gilardoni, F. Giordano, I. Lamas, G. Mazzacano, and A. Perillo, "Analysis on the mechanical effects induced by beam impedance heating on the HL-LHC target dump injection segmented (TDIS) absorber", in *Journal of Physics: Conference Series*, vol. 1067, no. 6, 2018. doi: 10.1088/1742-6596/1067/6/062011. ISSN 17426596

[139] L. Teofili, M. Migliorati, D. Carbajo, I. Lamas, and A. Perillo, "Design of the Target Dump Injection Segmented (TDIS) in the Framework of the High Luminosity Large Hadron Collider (HL-LHC) Project", in *61st ICFA Advanced Beam Dynamics Workshop on High-Intensity and High-Brightness Hadron Beams*, Daejeon, Korea, 2018. doi: 10.18429/JACoW-HB2018-TUP2WE04. ISBN 9783954502028 pp. 122–126.

[140] N. V. Mokhov and F. Cerutti, "Beam-Material Interaction", 8 2016. [Online]. Available: http://dx.doi.org/10.5170/CERN-2016-002.83

[141] A. Lechner, "Particle Interactions with Matter", in *Proceedings of the CAS–CERN Accelerator School: Beam Injection, Extraction and Transfer,*, B. Holzer, Ed., vol. 5. CERN-2018-008-SP (CERN, Geneva), 2018, pp. 47–68. [Online]. Available: http://inspirehep.net/record/1723466/files/660.pdf

[142] B. J. Holzer, "Introduction to longitudinal beam dynamics", in *CAS-CERN Accelerator School: Ion Sources - Proceedings*, 2013. ISBN 9789290833956 pp. 47–61.

[143] B. J. Holzer, "Introduction to transverse beam dynamics", in *CAS-CERN Accelerator School: Ion Sources - Proceedings*, 2013. ISBN 9789290833956 pp. 27–45.

[144] L. Teofili, "TCLD latest measurements results", in *31st Impedance Working Group (IWG)*, Geneva, Switzerland. [Online]. Available: https://indico.cern.ch/event/808587/

[145] N. Biancacci, F. Caspers, J. Kuczerowski, E. Métral, N. Mounet, B. Salvant, A. Mostacci, O. Frasciello, and M. Zobov, "Impedance simulations and measurements on the LHC collimators with embedded beam position monitors", *Physical Review Accelerators and Beams*, 2017.

[146] Impedance Working Group Scientific Secretary, "Minutes of the 31st Impedance Working Group (IWG) Meeting", in *Impedance Working Group*, 2019. [Online]. Available: https://indico.cern.ch/event/820005/contributions/3427078/attachments/1844090/3024834/31th_IWG_Meeting_Minutes_ILG_OB_BS_CV.pdf

[147] A. Lechner, "TDI - Past Observations and Improvements for 2016", *Proc. Evian Workshop on LHC Beam Operations*, pp. 123–129, 2015.

[148] C. Bracco, "The New Injection Protection Dump TDIS", 2019.

[149] V. Kain, "Machine Protection and Beam Quality during the LHC Injection Process", Ph.D. dissertation, Vienna Tech. University, 2005. [Online]. Available: http://cds.cern.ch/record/902813?ln=en

[150] C. Bracco, "Injection : Hadron Beams", *lecture given at the CAS–CERN Accelerator School: Beam Injection, Extraction and Transfer,*, 2017. [Online]. Available: https://cas.web.cern.ch/sites/cas.web.cern.ch/files/lectures/erice-2017/bracco-hadron.pdf

[151] Lechner A. et al., "Energy Deposition Studies for Fast Losses during LHC Injection Failures", Geneva, Switzerland, Tech. Rep., 2013.

[152] F.-X. Nuiry, "Low-Z material R&D application for Beam Intercepting Devices (BID) at CERN", in *13th Int. Work. on Spallation Materials Technology*, Chattanooga, USA, 2016.

[153] A. Bertarelli, A. Lafuente, F. Carra, and P. Gradassi, "TDI thermo-mechanical simualtions: Boron Nitride versus Graphite", in *235th LHC machine commitee*, Geneva, Switzerland, 2015.

[154] G. Filacchioni, E. Casagrande, U. De Angelis, G. De Santis, and D. Ferrara, "Effects of strain rate on tensile properties of TZM and Mo–5% Re", *Journal of nuclear materials*, vol. 307, pp. 705–709, 2002.

[155] G. Mazzacano, "Impedance study on HL-LHC's collimation and protection system", in *Master Thesis*, 2017. [Online]. Available: https://cds.cern.ch/record/2301609

[156] J. Jimenez, "Vacuum requirements for the LHC", CERN, Tech. Rep., 2003.

[157] G. Skripka and G. Iadarola, "Buildup studies for the LHC TDIS", 2018. [Online]. Available: https://indico.cern.ch/event/707491

[158] P. L. Roux, R. Billen, and J. Mariethoz, "THE LHC FUNCTIONAL LAYOUT DATABASE AS FOUNDATION OF THE CONTROLS SYSTEM", in *Proceedings of ICALEPCS07*, 2007, pp. 526–528.